Thèse n° 9796

Model-independent measurement of charm mixing parameters in $D^0 \to K_S^0 \pi^+ \pi^-$ decays

Présentée le 21 octobre 2022

Faculté des sciences de base
Laboratoire de physique des hautes énergies OS
Programme doctoral en physique

pour l'obtention du grade de Docteur ès Sciences

par

Surapat EK-IN

Acceptée sur proposition du jury

Prof. P. Ricci, président du jury
Prof. O. Schneider, directeur de thèse
Dr M. Williams, rapporteur
Dr J. Brodzicka, rapporteuse
Prof. D. Sgalaberna, rapporteur

École polytechnique fédérale de Lausanne

2022

To my family
In loving memory of our father…

The secret of life, though,
is to fall seven times and
to get up eight times.
—Paulo Coelho, The Alchemist

Acknowledgements

The sound of the métro M1 passing, the smell of sacred lotus and jujube, the taste of Madeira rum aged in a brandy cask, and here I am, sitting in front of my favourite working station. “The end is part of a journey”, this thought comes to my mind while thinking back to the past four years of my PhD where I have met amazing people. I would like to take a few pages to describe how thankful I am.

My deepest gratitude goes to Prof. Olivier Schneider, my thesis director, for allowing me to do this thesis at the LPHE. He put his trust in me to work independently and provided constructive suggestions whenever I needed them, despite his busy schedule. It has been a pleasure to work with such an enthusiastic and passionate professor.

I could not have undertaken this journey without Tara Nanut, my mentoring supervisor. Her passion for Charm physics has inspired me to dive deep into the field. She always supported me without any hesitations. I would like to thank her for not only spending time answering any queries I had, even if the discussion lasted from minutes to several hours, but also for being my mental support when I went through a difficult time during the Covid period. Her dedication is priceless and deserves my greatest appreciation.

I am also grateful to Maurizio Martinelli. It has been such a pleasure to work with an experienced Charm physicist who provided very helpful advice. It was such an honour to work alongside people in the KsPiPi analysis group. I have learnt a lot from Nathan Jurik, Sascha Stahl, and Mark Williams who always gave constructive comments and trigger helpful discussion in our biweekly meeting. Many thanks to all of the colleagues in Charm working whom I worked with when I was a liaison between working groups.

The atmosphere in the LPHE is a truly unique working environment. This would not be possible without the senior members of the lab: Prof. Aurelio Bay, Dr. Frédéric Blanc, Dr. Guido Haefeli, Prof. Tatsuya Nakada, and Prof. Lesya Shchutska. This sincere appreciation also expands to Esther Hofmann and Corinne Craman who help us with administrative tasks and other advice.

Every day at the LPHE was full with interesting discussions during coffee and lunch breaks with past and present members: Maria Elena Stramaglia, Michel De Cian, Axel Kuonen, Olivier Girard, Maria Vieites Diaz, Violaine Bellée, Anna Mascellani, Preema Pais, Brice Maurin, Guido Andreassi, Guillaume Pietrzyk, Sara Celani, Veronica Kirsebom, Vladimir Macko, Sebastian

Schulte, Elisabeth Niel, Ettore Zaffaroni, Marteen Van Dijk, Aravindhan Venkateswaran, Elena Graverini, Ana Bárbara Rodrigues Cavalcante, Jennifer Frieden, Paul De Bryas, Lucas Russell, Alison Tully, and Renato Quagliani.

I will never forget the time when I turned my chair around in the "coolest" BSP 613.1 office to Carina and Marie. It has never been boring with interesting random discussions about everything. Days seem quite fast and would not be completed without a gym session with fellow boys: Lino, and Serhii who always push the session to the limit with "Encore uneeee!!". I would also like to give my special thanks to Pavol and Sonia who have been amazing flatmates during the last few months.

The Association of Thai Students in Switzerland (ATSS) makes me feel at home and has always been an emotional support for me. I'd like to give my special gratitude to P'Top, with whom we bonded over any discussions we had whether they are about physics, coding, hiking, skiing, or even life lessons we have learnt.

Once a year, my motivation and appreciation in life are refilled with nostalgic conversations with my high school friends. They remind me of how far I have come and encourage me to achieve my goals.

This endeavour would not have been possible without Peter and Chok who are always there whenever I need you guys. We have travelled to many places where we share precious time, especially on a helicopter ride with you, Pete.

A long-distance relationship seems difficult to many people. Fafa, you make it so effortless. From the cold of Siberia, the hot desert in Dubai, to a scenic road trip in Iceland, distance is just a number. You put a smile on my face during my time of grief, even though the path ahead seems impossible. You encourage me to achieve it.

I am deeply indebted to my family. This journey could have been only a dream without their support. Thanks for always believing in my ability to be successful in life. And hey Dad, I know you are quite far away now, I hope that you are proud of me.

Lastly, to all who make this journey memorable,

Thank you.

Lausanne, August 19, 2022 S. E.

Abstract

This thesis presents a measurement of charm mixing and CP-violation parameters using $D^0 \to K_S^0\pi^+\pi^-$ decays. These mixing parameters include the mass and decay-width differences of the mass eigenstates of the D^0–$\overline{D}^0$ system. A search for Charge–Parity violation is performed through measurements of D^0–$\overline{D}^0$ mixing and of the interference between mixing and decay amplitudes. The dataset consists of events reconstructed in pp collisions collected by the LHCb experiment during the operation of the Large Hadron Collider (LHC) from 2016 to 2018. This sample corresponds to an integrated luminosity of 5.4 fb^{-1}. The D^0 decays are selected in semileptonically decays of b hadrons. The results are expressed in terms of the CP-averaged mixing parameters and CP-violating differences as

$$\begin{aligned}
x_{CP} &= [\ +4.29 \pm 1.48\,(\text{stat}) \pm 0.26\,(\text{syst})] \times 10^{-3}\,,\\
y_{CP} &= [+12.61 \pm 3.12\,(\text{stat}) \pm 0.83\,(\text{syst})] \times 10^{-3}\,,\\
\Delta x &= [\ -0.77 \pm 0.93\,(\text{stat}) \pm 0.28\,(\text{syst})] \times 10^{-3}\,,\\
\Delta y &= [\ +3.01 \pm 1.92\,(\text{stat}) \pm 0.26\,(\text{syst})] \times 10^{-3}\,,
\end{aligned}$$

where the first uncertainty is statistical and the second is systematic. They correspond to the mixing and CP-violation parameters

$$\begin{aligned}
x &= 0.46^{+0.15}_{-0.16} \times 10^{-2}\,,\\
y &= 1.24^{+0.32}_{-0.33} \times 10^{-2}\,,\\
|q/p| &= 1.21^{+0.21}_{-0.15}\,,\\
\phi &= -0.132^{+0.088}_{-0.120}\ \text{rad.}
\end{aligned}$$

The value of x deviates from zero with a significance of almost 3σ. These results are complementary to and consistent with previous measurements and with the current world-average values. They represent an independent and complementary knowledge of the charm-mixing parameters. A combination with the recent LHCb analysis of $D^{*+} \to D^0(\to K_S^0\pi^+\pi^-)\pi^+$ decays is also reported.

Keywords: particle physics, LHCb, LHC, charm mixing, CP violation, multibody decay

Résumé

Cette thèse présente une mesure des paramètres de mélange de charme et de violation de CP à l'aide de désintégrations $D^0 \to K_S^0\pi^+\pi^-$. Ces paramètres de mélange incluent les différences de masse et de largeur de décroissance des états propres de masse du système D^0–$\overline{D}^0$. La recherche de la violation de charge–parité est effectuée par des mesures dan mélange D^0–$\overline{D}^0$ et de l'interférence entre les amplitudes de mélange et de désintégration.
Les données de événements sont reconstruits dans les collisions pp enregistées par l'expérience LHCb auprès du Large Hadron Collider (LHC) de 2016 à 2018. Cet echantillon correspond à une luminosité de 5.4 fb^{-1}. Les désintégrations des méson D^0 sont sélectionnées dans des désintégrations semileptoniques de hadrons b. Les résultats sont exprimés en termes de paramètres de mélange moyennés sur CP et de différences violant CP comme

$$\begin{aligned}
x_{CP} &= [\ +4.29 \pm 1.48\,(\text{stat}) \pm 0.26\,(\text{syst})] \times 10^{-3}\,,\\
y_{CP} &= [+12.61 \pm 3.12\,(\text{stat}) \pm 0.83\,(\text{syst})] \times 10^{-3}\,,\\
\Delta x &= [\ -0.77 \pm 0.93\,(\text{stat}) \pm 0.28\,(\text{syst})] \times 10^{-3}\,,\\
\Delta y &= [\ +3.01 \pm 1.92\,(\text{stat}) \pm 0.26\,(\text{syst})] \times 10^{-3}\,,
\end{aligned}$$

où la première incertitude est statistique et la seconde systématique. Ils correspondent aux paramètres de mélange et de violation CP

$$\begin{aligned}
x &= 0.46^{+0.15}_{-0.16} \times 10^{-2}\,,\\
y &= 1.24^{+0.32}_{-0.33} \times 10^{-2}\,,\\
|q/p| &= 1.21^{+0.21}_{-0.15}\,,\\
\phi &= -0.132^{+0.088}_{-0.120}\ \text{rad}.
\end{aligned}$$

La valeur de x s'écarte de zéro avec une signification de presque 3σ. Ces résultats sont complémentaires et compatibles avec les mesures précédentes et les valeurs moyennes mondiales actuelles. Ils représentent une mesure indépendante et complètent la connaissance des paramètres de mélange de charme. Une combinaison avec la récente analyse LHCb des désintégrations $D^{*+} \to D^0(\to K_S^0\pi^+\pi^-)\pi^+$ est également rapportée.

Mots-clés : physique des particules, LHCb, LHC, mélange de charme, violation de CP, désintégration a plusieurs corps

Zusammenfassung

Die Suche nach CP-Verletzung wird mittels der Messungen von CP-verletzenden Parametern durchgeführt, welche sich in den Konstitutionen von D^0-Flavour-Zuständen und Zerfallsamplituden unterscheiden. Die Daten sind von pp-Kollisionen rekonstruiert worden. Die Kollisionen wurden während des Betriebes des Large Hadron Colliders (LHC) von 2016 bis 2018 gesammelt, was einer integrierten Leuchtkraft von 5.4 fb^{-1} entspricht. Der D^0-Zerfall wird durch den semileptonischen Zerfall der b-Hadron in $\overline{B} \to D^0 \mu^- \overline{\nu}_\mu X$ erhalten. Die interessanten Parameter werden als CP-gemittelte Michungswerte und CP-verletzende Unterschiede

$$
\begin{aligned}
x_{CP} &= [\ +4.29 \pm 1.48\,(\text{stat}) \pm 0.26\,(\text{syst})] \times 10^{-3}\,,\\
y_{CP} &= [+12.61 \pm 3.12\,(\text{stat}) \pm 0.83\,(\text{syst})] \times 10^{-3}\,,\\
\Delta x &= [\ -0.77 \pm 0.93\,(\text{stat}) \pm 0.28\,(\text{syst})] \times 10^{-3}\,,\\
\Delta y &= [\ +3.01 \pm 1.92\,(\text{stat}) \pm 0.26\,(\text{syst})] \times 10^{-3}\,.
\end{aligned}
$$

ausgedrückt und erhalten, wobei die erste Unsicherheit statistisch und die zweite symptomatisch ist. Die Parameter entsprechen den Misch- und CP-Verletzungsparametern

$$
\begin{aligned}
x &= 0.46^{+0.15}_{-0.16} \times 10^{-2}\,,\\
y &= 1.24^{+0.32}_{-0.33} \times 10^{-2}\,,\\
|q/p| &= 1.21^{+0.21}_{-0.15}\,,\\
\phi &= -0.132^{+0.088}_{-0.120}\ \text{rad}.
\end{aligned}
$$

Der Wert von x weicht mit einer Signifikanz von 3σ von Null ab. Die Messungen ergänzen früheren Messungen und und stimmen mit den aktuellen Weltdurchschnittswerten überein. Sie sind eine unabhängige Messung und ergänzen die bisherigen Kenntnisse der Charm-Mixing-Parameter. Zusätzlich wird eine Kombination mit der vor kurzem publizierten LHCb-Analyse $D^{*+} \to D^0(\to K^0_S \pi^+\pi^-)\pi^+$ diskutiert.

Schlüsselwörter: Teilchenphysik, LHCb, LHC, Charmemischung, CP-Verletzung, Mehrkörperzerfall

บทคัดย่อ

วิทยานิพนธ์นี้ได้ทำการนำเสนอการวัดค่าการสั่นของอนุภาคชาร์มและพารามิเตอร์การละเมิดสมมาตรโดยอิงจากการสลายตัว $D^0 \to K_S^0\pi^+\pi^-$ ค่าพารามิเตอร์ดังกล่าว ได้รวมถึงมวลและความกว้างของการสลายตัวใน Mass eigenstates ของระบบ D^0–$\overline{D}^0$ เพื่อค้นหาการละเมิดสมมาตรของ Charge–Parity โดยการวัดในระบบการสั่น D^0–$\overline{D}^0$ และแอมพลิจูดของการสลายตัว ชุดข้อมูลประกอบด้วยการชนกันของโปรตอน pp ซึ่งถูกเก็บและรวบรวมจากการทดลองโดยเครื่อง LHCb ระหว่างการทำงานของ Large Hadron Collider (LHC) ตั้งแต่ปี 2559 ถึงปี 2561 รวมทั้งสิ้นเป็นข้อมูลขนาด $5.4\,\mathrm{fb}^{-1}$ การสลายตัวของ D^0 ถูกเลือกในการสลายตัวแบบเซมิแลปตอนิกของฮาดรอน b ผลลัพธ์แสดงในรูปของค่าเฉลี่ยของพารามิเตอร์การผสม CP และพารามิเตอร์ที่ละเมิดความสมมาตร CP

$$
\begin{aligned}
x_{CP} &= [\ +4.29 \pm 1.48\,(\mathrm{stat}) \pm 0.26\,(\mathrm{syst})] \times 10^{-3}\,,\\
y_{CP} &= [+12.61 \pm 3.12\,(\mathrm{stat}) \pm 0.83\,(\mathrm{syst})] \times 10^{-3}\,,\\
\Delta x &= [\ -0.77 \pm 0.93\,(\mathrm{stat}) \pm 0.28\,(\mathrm{syst})] \times 10^{-3}\,,\\
\Delta y &= [\ +3.01 \pm 1.92\,(\mathrm{stat}) \pm 0.26\,(\mathrm{syst})] \times 10^{-3}\,,
\end{aligned}
$$

โดยที่ความไม่แน่นอนแรกเป็นสถิติและความไม่แน่นอนแรกที่สองเป็นจากระบบ ซึ่งสอดคล้องกับ พารามิเตอร์การสั่นของชาร์มและพารามิเตอร์การละเมิดสมมาตร CP

$$
\begin{aligned}
x &= 0.46^{+0.15}_{-0.16} \times 10^{-2}\,,\\
y &= 1.24^{+0.32}_{-0.33} \times 10^{-2}\,,\\
|q/p| &= 1.21^{+0.21}_{-0.15}\,,\\
\phi &= -0.132^{+0.088}_{-0.120}\ \mathrm{rad}.
\end{aligned}
$$

ค่าของ x นั้นมีการเบี่ยงเบนจากศูนย์โดยมีค่าความมั่นใจ 3σ โดยผลลัพธ์สอดคล้องกับการวัดครั้งก่อนและค่าเฉลี่ยจากผลการทดลองทั่วโลกในปัจจุบัน ผลของการทดลองนี้เป็นตัวแทนของการวัดอิสระและสนับสนุนการวัดพารามิเตอร์การสั่นในระบบของชาร์ม วิทยานิพนธ์รายงานการรวมกับการวิเคราะห์ LHCb ล่าสุดของ $D^{*+} \to D^0(\to K_S^0\pi^+\pi^-)\pi^+$ ที่สลายตัวด้วย

คำสำคัญ: ฟิสิกส์ของอนุภาค, LHCb, LHC, การสั่นในระบบของชาร์ม, การละเมิดสมมาตร CP, การสลายตัวหลายตัว

Contents

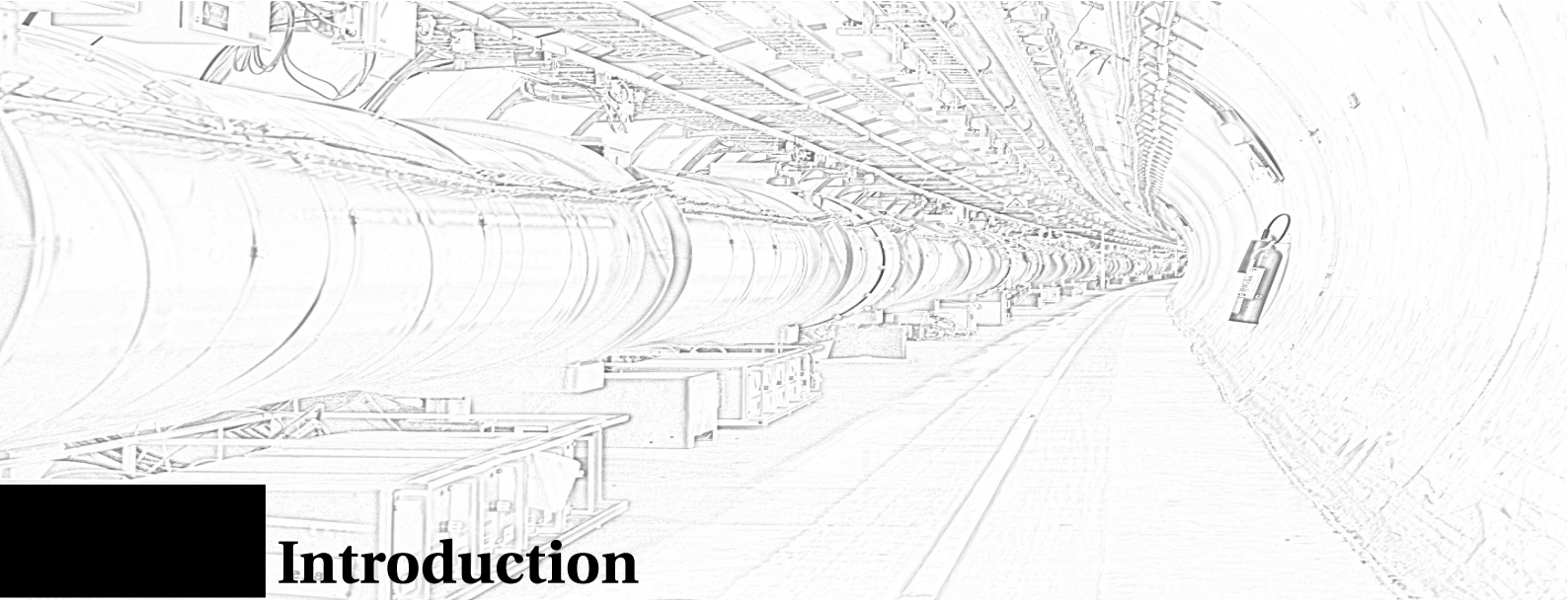

Introduction

"Physics" is derived from an ancient greek word φύσις meaning "Nature". It is one of the oldest branches of natural science which studies the behaviour of matter, its interaction through space and time, and the related entities of energy and force. Physics describes a wide range of phenomena, from tiny constituents of matter to astronomical objects of galaxies. The goal of this academic discipline is to connect observables to root causes, and link them together. Advancement in the field often leads to novel technologies which drastically transfrom our society.

Particle physics studies the fundamental constituents of matter, called elementary particles. It investigates the irreducibly smallest detectable particles and their interactions. The core theory in the field is known as "The Standard Model". It describes the Universe as a composition of basic building blocks of fundamental particles and three forces. The model has successfully explained the results of all lab experiments and predicted a wide variety of phenomena. However, it is not complete. There are hierarchy problems that the model fails to describe. In particular, it does not explain the imbalance between the number of particles and antiparticles in the early Universe that led to the matter-dominated Universe in which we live today.

To understand this, scientists have come together and built ambitious particle accelerators in search for answers and to expand knowledge in the field. The largest one is the Large Hadron Collider (LHC). The machine accelerates bunches of protons and collides them at high energy to imitate the environment at the beginning of the Universe, which is unimaginably hot and dense. The collisions produce massive particles, the properties of which are probed to increase our understanding of the Universe. One of the largest experiments installed at the LHC is the LHCb experiment, specialized in the search for asymmetric behaviours of matter and anti-matter.

This thesis aims at the study of behaviours of matter and anti-matter from data collected by the LHCb experiment. In the Standard Model, transition between matter and anti-matter occurs in the phenomenon called "neutral particle oscillation". A neutral meson can change to its anti-matter counterpart and vice-versa. The properties of such systems has been evolving rapidly in the past two decades thanks to vast amounts of high quality data available from particle physics experiments. Composite particles containing charm quarks provide unique opportunities of studying a weak decay of an up-type quark in a bound state.

The scope of this thesis is the measurement of parameters governing the particle oscillation (mixing) of a particle constituted of a charm quark and an anti-up quark, known as the D^0 meson, and its anti-particle $\overline{D}^0$. The D^0–$\overline{D}^0$ mixing was recently observed in 2012 [1]. The precise measurement of the corresponding parameters has been established and developed with significant contributions from this thesis work:

- Model-indepedent measurement of charm mixing parameters in $\overline{B} \to D^0(\to K^0_S\pi^+\pi^-)\mu^-\overline{\nu}_\mu X$ decays [2,3];
- Observation of the mass difference between the neutral charm-Meson eigenstates [4,5];
- Measurement of charm-mixing and CP-violation parameters using a time-dependent amplitude analysis of semileptonically-tagged $D^0 \to K^0_S\pi^+\pi^-$ decays [6].

The first of those contributions is the main study described in this document. Chapter 1 introduces the theoretical frameworks of the Standard Model and of the state-of-the-art in particle-antiparticle oscillation. Chapter 2 presents the experimental environment of the LHC and the LHCb detector. The data analysis is described in Chapters 3–5. Possible flaws in the analysis are evaluated in Chapter 6. Then the result is combined with previous measurements in Chapter 7. Chapter 8 summarises impacts on the experimental status and prospect for the future measurements. Chapter 9 concludes this thesis.

In addition, during the first year of PhD studies, the author has contributed to the development of the SciFi tracker technology through testbeam activities. An analysis software was developed to process and reconstruct the stream of data from the STiC readout board [7] to monitor and improve the performance of the detector [8]. The author also contributed to explore an alternative approach in a real-time tracking algorithm as a preparation for the start of LHCb data-taking in Run 3 period (2022–2024) [9].

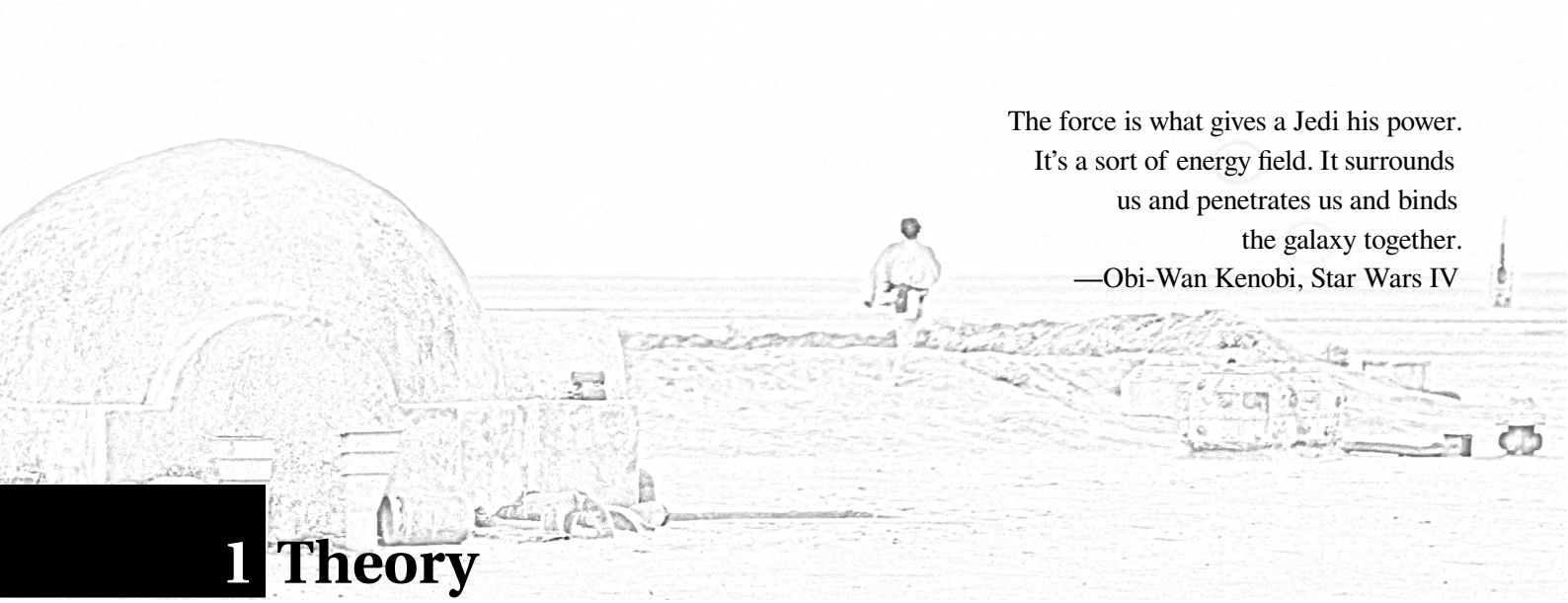

The force is what gives a Jedi his power.
It's a sort of energy field. It surrounds
us and penetrates us and binds
the galaxy together.
—Obi-Wan Kenobi, Star Wars IV

1 Theory

This chapter describes the theoretical aspects related to this thesis. Particle physics is established around the so-called "Standard Model", where elementary particles and their interactions are studied. This model, discussed in Section 1.1, has limitations in describing the matter–antimatter asymmetry observed in the Universe. The core subject of this thesis, presented in Section 1.2, is a study of the particle–antiparticle oscillation of the D^0 meson, a neutral meson containing a charm quark, and a search for asymmetries in the D^0–$\overline{D}^0$ system. Section 1.3 introduces the model-independent method employed to measure the oscillation parameters. More details about the Standard Model can be found in Refs. [10–14].

1.1 Standard Model

The Standard Model (SM) of particle physics describes the known fundamental particles and their interactions in a single framework. The fundamental particles are excitations of quantum fields that fill all space. The fields exist everywhere in space even if there are no particles. Their lowest-energy state, or the zero-point energy may or may not have a zero values. The fields are fluctuating, that is not at their lowest energy level. If a field is confined in a particular region and possesses a discrete energy spectrum, it results in a "particle". What makes a particle unique is how it interacts with specific fields. These interactions determine their intrinsic properties like mass, electric charge, colour charge, weak hypercharge, lepton number, baryon number, lepton family number, and spin.

The model provides boundary conditions (confined regions) that lead to a particular set of existing particles. This is built upon an idea of "symmetry" which means that the properties of particles remain unchanged under a certain transformation or operation. Mathematically the symmetries are described within group theory. The underlying groups of the SM comprise three Lie groups:

- $SU(3)_C$ is the group of the special unitary 3×3 matrices describing the strong force field; C stands here for the colour charge of the field; its properties are described by quantum

chromodynamics (QCD);

- $SU(2)_L$ is the group of the special unitary 2×2 matrices describing the weak force field; L refers to the coupling to left-handed currents;
- $U(1)_Y$ is a unitary group made of all complex numbers with a modulus of 1, describing the electromagnetic field; Y refers to the hypercharge.

The SM is formulated as a non-abelian, local gauge-invariant theory under the direct product on these three groups $G_{SM} = SU(3)_C \otimes SU(2)_L \otimes U(1)_Y$ [16]. The gauge-invariant theory is a type of quantum field theory where the dynamics of a system (the Lagrangian $\mathscr{L}$) does not change (is invariant) under the G_{SM} transformations. In this framework, the model establishes a total of twelve gauge (spin-1) bosons, one scalar (spin-0) boson, and twelve fermions and their anti-fermions (spin-$^1/_2$). The bosons (fermions) obey the Bose-Einstein (Fermi-Dirac) statistics. These particles have the following properties:

Gauge bosons

- 8 massless gluons are the strong-force carriers that bind quarks together to form hadrons. Any quark combination forming a hadron must be colourless. There are mesons ($q\overline{q}$), baryons (qqq), *etc.*.
- 3 weak bosons, W^+, W^-, and Z, are the weak-force carriers, which describe flavour-changing processes and decays of particles.
- 1 massless photon is the electromagnetic-force carrier.

Fermions

- 6 quarks and antiquarks. They interact through all of the three forces. They are categorised into "up-type" (up (u), charm (c), and top (t)) and "down-type" (down (d), strange (s), and beauty (b)) quarks, which have electric charge of $+^2/_3$ and $-^1/_3$, respectively.
- 6 leptons and antileptons. They interact only through the weak and electromagnetic forces. The charged leptons are the electron (e), muon (μ), and tau (τ) with electric charge of -1, each with a neutral lepton partner, called the ν_e, ν_μ, and ν_τ neutrinos.

The fermions can be alternatively grouped into 3 generations. The sole scalar boson in the SM is the Higgs particle which has been observed in 2012 [17, 18]. It is the product of the self-excitation of the Higgs field. Massive particles in the SM acquire their masses through their interactions with the Higgs field. The field is responsible for the spontaneous symmetry breaking of the $SU(3)_C \otimes U(1)_Y$ group, parametrised by the Higgs boson mass and its vacuum expectation value, and leading to massive $W^\pm$ and Z weak bosons [19–21]. All known fundamental particles and force-carriers are illustrated and summarised in Figure 1.1.

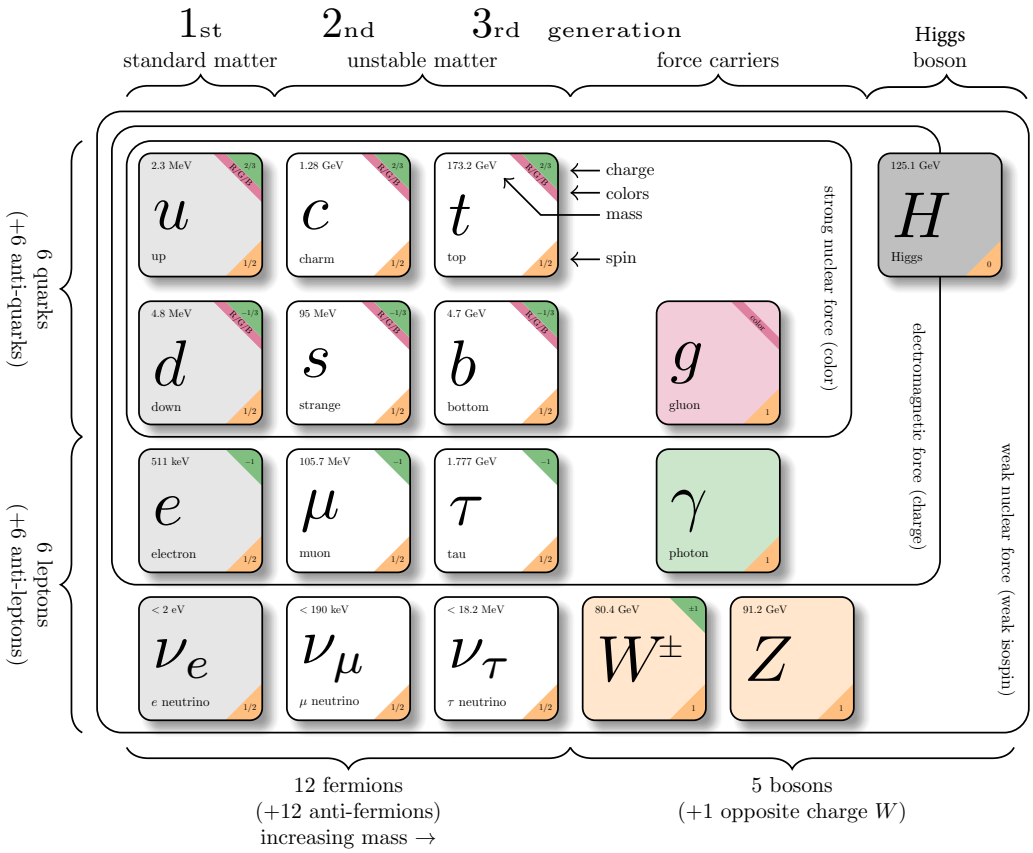

Figure 1.1 – Overview of the Standard Model and its fundamental particles [23].

The Lagrangian of the SM can be written in a compact representation as [22]

$$\mathscr{L}_{\mathrm{SM}} = \underbrace{-\frac{1}{4}F_{\mu\nu}F^{\mu\nu}}_{\substack{\text{Gauge boson}\\ \text{couplings}}} + \underbrace{i\overline{\psi}\not{D}\psi}_{\substack{\text{Fermion}\\ \text{dynamics}}} + \underbrace{\psi_i y_{ij}\psi_j\phi + h.c.}_{\substack{\text{Fermion}\\ \text{masses}}} + \underbrace{\left|D_\mu\phi\right|^2}_{\substack{\text{Weak boson}\\ \text{masses}}} - \underbrace{V(\phi)}_{\substack{\text{Higgs dynamics}\\ \text{and mass}}} \quad . \tag{1.1}$$

Despite the incredible success of the SM in describing and predicting many phenomena observed through various experiments in the last half of century, the model is not adequate to explain some fundamental phenomena, for example [24, 25]:

- Gravity - The SM does not include the gravitational force which is one of the main forces we, as humans, experience in everyday life. The model fails to integrate General Relativity without breaking down under some conditions.
- Strong *CP* problem - There is no restriction in the SM to violate the Charge–Parity symmetry. Such violation has been observed widely in weak interactions, but no violation has been observed in the strong interaction so far [26].

- Matter-antimatter asymmetry - The observable Universe is made almost exclusively of matter. Where did the antimatter go [27, 28]?
- Dark matter and dark energy - The observed velocity of spiral galaxy arms is not consistent with the velocity predicted from the luminous mass distribution according to the gravitational law. However, the presence of additional non-luminous (dark) matter would be able to explain the observations [29, 30]. Also, the Universe is observed to expand at an accelerated rate, for which a form of energy that exerts a negative, repulsive pressure, unlike gravity, is required. There is no proven theory that can explain these phenomena [31].

This thesis focuses on the "matter-antimatter asymmetry" problem. In absense of asymmetry, equal amounts of matter and antimatter should have been produced in the early Universe. These would have annihilated completely and not evolved to form galaxies, stars, or even biological systems like us. In the SM, the only mechanism responsible for inducing an asymmetry is through flavour-changing processes and Charge-Parity (*CP*) violation, which are discussed in Sections 1.1.1 and 1.1.2. In spite of these, the amount of asymmetry accounted for in the SM is much smaller than the observed one [32, 33]. Experiments such as the Large Hadron Collider beauty (LHCb) experiment, specialised in precision measurements to explore tiny differences in behaviour between matter and antimatter, may observe a discrepancy from the SM predictions and provide insights to theoretical frameworks to better understand the matter-antimatter asymmetry problem.

1.1.1 Discrete symmetries

In the SM, there are three discrete symmetries which describe non-continuous transformations of a system.

- The charge symmetry C is the symmetry under the charge conjugation transformation, which replaces a particle with its anti-particle.
- The parity symmetry P is the symmetry under parity transformation, which is equivalent to the reflection by a mirror.
- The time reversal symmetry T is the symmetry under the time reversal transformation, which reverses the time direction of a state.

The simultaneous transformation under charge conjugation, parity, and time reversal is a fundamental symmetry of physical laws that every physical phenomenon must obey. This is known as the CPT theorem [34, 35].

The strong and electromagnetic forces respect all three discrete symmetries. The weak force, however, violates all three. The P violation was observed by Wu in the β decay of Cobalt-60 [36]. In 1964, *CP* violation was discovered in neutral kaon decays [37]. This triggered a new effort in particle physics where additional *CP* violation in the weak interaction is looked for.

1.1.2 Quark flavour changing transitions

As mentioned in Section 1.1, there are 6 distinct types of quarks with different properties. The different types are denoted as "flavours". In the weak interaction, a quark can change its flavour through an exchange of a $W^{\pm}$ boson. The interaction results in a transition from an up-type to a down-type left-handed chiral quark state and vice-versa. This flavour-changing mechanism is governed by the Cabibbo-Kobayashi-Maskawa (CKM) matrix which represents the transition amplitude between quark flavours [38, 39]. This is a consequence of the Yukawa interaction between spinor massless quark fields with the scalar Higgs field [14]. The CKM matrix (V_{CKM}) is composed of 9 elements V_{ij} representing the transition between quarks j and i:

$$V_{\text{CKM}} \equiv \begin{pmatrix} V_{ud} & V_{us} & V_{ub} \\ V_{cd} & V_{cs} & V_{cb} \\ V_{td} & V_{ts} & V_{tb} \end{pmatrix}. \tag{1.2}$$

This 3×3 matrix is required to be unitary, *e.g.* $V^*_{\text{CKM}} V_{\text{CKM}} = 1$, if there exists no other quark flavour. From this condition, only four independent parameters are required to parametrise the CKM matrix. The matrix can be parametrised in terms of three real angles and one complex physical phase which is known as the Kobayashi-Maskawa phase (KM phase). This phase represents the sole known CP-violating source in the SM. Among many proposed parametrisations of the CKM matrix, the Wolfenstein parametrisation [40] is one of the most popular choices in the phenomenological applications. It rewrites V_{CKM} as a power series of $\lambda \approx |V_{us}| \approx 0.225$ as follows (to $\mathcal{O}(\lambda^3)$) [14]:

$$V_{CKM} = \begin{pmatrix} 1 - \frac{1}{2}\lambda^2 & \lambda & A\lambda^3(\rho - i\eta) \\ -\lambda & 1 - \frac{1}{2}\lambda^2 & A\lambda^2 \\ A\lambda^3[1 - (\rho + i\eta)] & -A\lambda^2 & 1 \end{pmatrix}, \tag{1.3}$$

where A, λ, ρ, and η are the four real parameters to be determined from experiments. This parametrisation provides a manifest and transparent explanation of the smallness of the CP-violating phase as it is embedded in the complex term $\rho \pm i\eta$ appearing at the order of λ^3.

The CKM unitarity condition

$$V^*_{ud} V_{ub} + V^*_{cd} V_{cb} + V^*_{td} V_{tb} = 0 \tag{1.4}$$

leads to a so-called unitarity triangle in the complex plane defined by $\overline{\rho}\ \left(= \rho\left(1 - \lambda^2/2 + \ldots\right)\right)$ and $\overline{\eta}\ \left(= \eta\left(1 - \lambda^2/2 + \ldots\right)\right)$, as shown in Figure 1.2. This position of the apex and three angles of the unitarity triangle can be written in terms of the elements in the CKM matrix as

$$\overline{\rho} + i\overline{\eta} = -\frac{V_{ud}V^*_{ub}}{V_{cd}V^*_{cb}}, \quad \alpha = \arg\left(-\frac{V_{td}V^*_{tb}}{V_{ud}V^*_{ub}}\right), \quad \beta = \arg\left(-\frac{V_{cd}V^*_{cb}}{V_{td}V^*_{tb}}\right), \quad \gamma = \arg\left(-\frac{V_{ud}V^*_{ub}}{V_{cd}V^*_{cb}}\right). \tag{1.5}$$

The ultimate goal in flavour physics is to measure a variety of weak decays to constrain the V_{ij} complex numbers and determine the amount of the CP violation in the Standard Model.

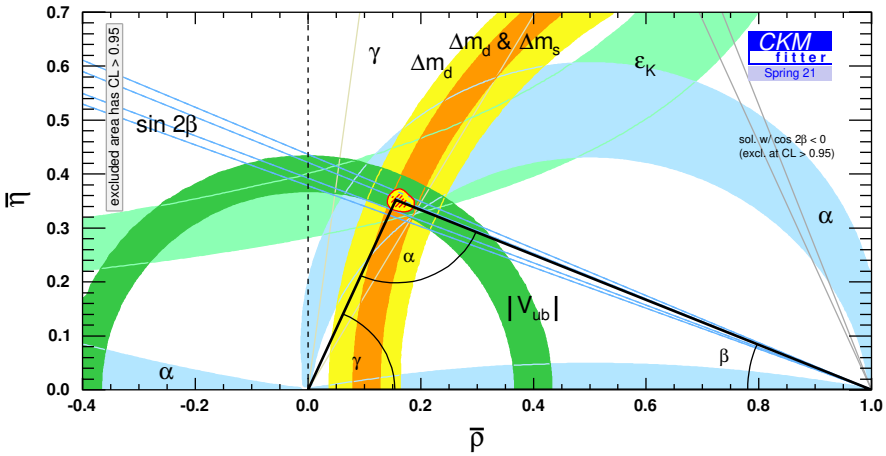

Figure 1.2 – The world averages related to the unitarity triangle as of Spring 2021 [41].

1.2 Particle oscillation and $D^0 \to K_S^0 \pi^+ \pi^-$

Quark flavour oscillation is the transition between a neutral flavoured meson and its antiparticle. In the SM, this transition is mediated by charged weak interactions, involving the exchange of two virtual W bosons as shown by the Feynman diagrams of Figure 1.3.[1] The oscillation occurs because quark mass terms cannot be simultaneously diagonalised with weak coupling terms. This leads to distinct mass and flavour eigenstates [14]. The mass eigenstates can be written as linear combinations of the flavour eigenstates as

$$|D_{1,2}\rangle = p|D^0\rangle \pm q|\overline{D}^0\rangle, \tag{1.6}$$

where p and q are complex parameters which satisfy the normalisation condition $|p|^2+|q|^2 = 1$. The states $|D_{1,2}\rangle$ refer to the CP even (D_1) and odd (D_2) mass eigenstates with eigenvalues $\omega_{1,2} = m_{1,2} - \frac{1}{2}\Gamma_{1,2}$. The $m_{1(2)}$ and $\Gamma_{1(2)}$ observables are the mass and decay width of the $D_{1(2)}$ state. The oscillation can be described by two dimensionless parameters,

$$x = (m_1 - m_2)c^2/\Gamma\,, \tag{1.7}$$

$$y = (\Gamma_1 - \Gamma_2)/(2\Gamma)\,, \tag{1.8}$$

where $\Gamma = (\Gamma_1 - \Gamma_2)/2$ is the average decay width. The p and q parameters are used to quantify CP violation in mixing and interference between mixing and decay. A deviation of $|q/p|$ from unity would indicate CP violation in mixing [14], while the phase $\phi_f \equiv \arg(q\overline{A}_f/pA_f)$ is tied to CP violation in interference between mixing and decay. If CP is conserved in the decay amplitude A_f ($\overline{A}_f$) of the D^0 ($\overline{D}^0$) to the common fixed state f, the CP-violating phase is final-state independent: $\phi_f \approx \phi \equiv \arg(q/p)$.

[1] All Feynman diagrams in this thesis are generated based on Ref. [42].

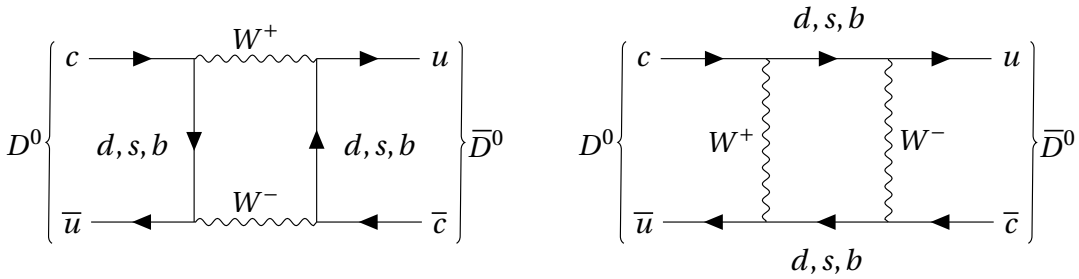

Figure 1.3 – Feynman diagrams of the D^0–$\overline{D}^0$ mixing process in the SM.

Oscillations in the K- and B-meson systems are well-established [14, 43–45]. The evidence and observation of D^0–$\overline{D}^0$ oscillations were reported much later, by the BaBar [46], Belle [47] and LHCb [1] collaborations, because of the small oscillation probability governed by the sizes of the x and y parameters.

The short-distance contribution to x and y from the diagrams shown in Figure 1.3 amounts to around $10^{-6} - 10^{-5}$ due to the small values of the light-quark masses [48]. The main contribution comes from non-perturbative quantum chromodynamics (QCD) processes through intermediate states such as K^-K^+ or $\pi^-\pi^+$ that enhance these parameters up to the order of a percent [49]. This so-called long-distance contribution is challenging to calculate. In addition, potential physics beyond the SM may affect these parameters. For example, an undiscovered massive particle may enter the process and enhance/degrade the oscillation rate. Measurements of these parameters are sensitive to probe physics beyond the SM [50]. CP violation in the charm sector has been experimentally confirmed much later than in the K [37] and B [51, 52] meson systems. To date, only a single observation with significance $> 5\sigma$ exists [53], measuring the difference in time-integrated CP violation asymmetries in the decays $D^0 \to K^-K^+$ and $D^0 \to \pi^-\pi^+$. There has been no sign of CP violation in a time-dependent analysis so far.

Table 1.1 shows the evolution of the world average between 2018 and 2021 of the mixing and CP-violating parameters x, y, $|q/p|$, and ϕ in the D^0–$\overline{D}^0$ system. The precision on these parameters has been improving rapidly in the last 4 years. Recently, the mass parameter x has been measured to significantly differ from zero in a single analysis [5]. This measurement has a

Table 1.1 – World averages of x, y, $|q/p|$, and ϕ computed by HFLAV [57].

Parameter		2018 [54]	2019 [55]	2021 [56]
x	$[10^{-2}]$	$0.36^{+0.21}_{-0.16}$	$0.39^{+0.11}_{-0.12}$	$0.409^{+0.048}_{-0.049}$
y	$[10^{-2}]$	$0.67^{+0.06}_{-0.13}$	$0.651^{+0.063}_{-0.069}$	$0.615^{+0.056}_{-0.055}$
$\lvert q/p \rvert$		$0.94^{+0.17}_{-0.07}$	$0.969^{+0.050}_{-0.045}$	0.995 ± 0.016
ϕ		$-0.13^{+0.17}_{-0.26}$	$-0.068^{+0.079}_{-0.080}$	-0.044 ± 0.021

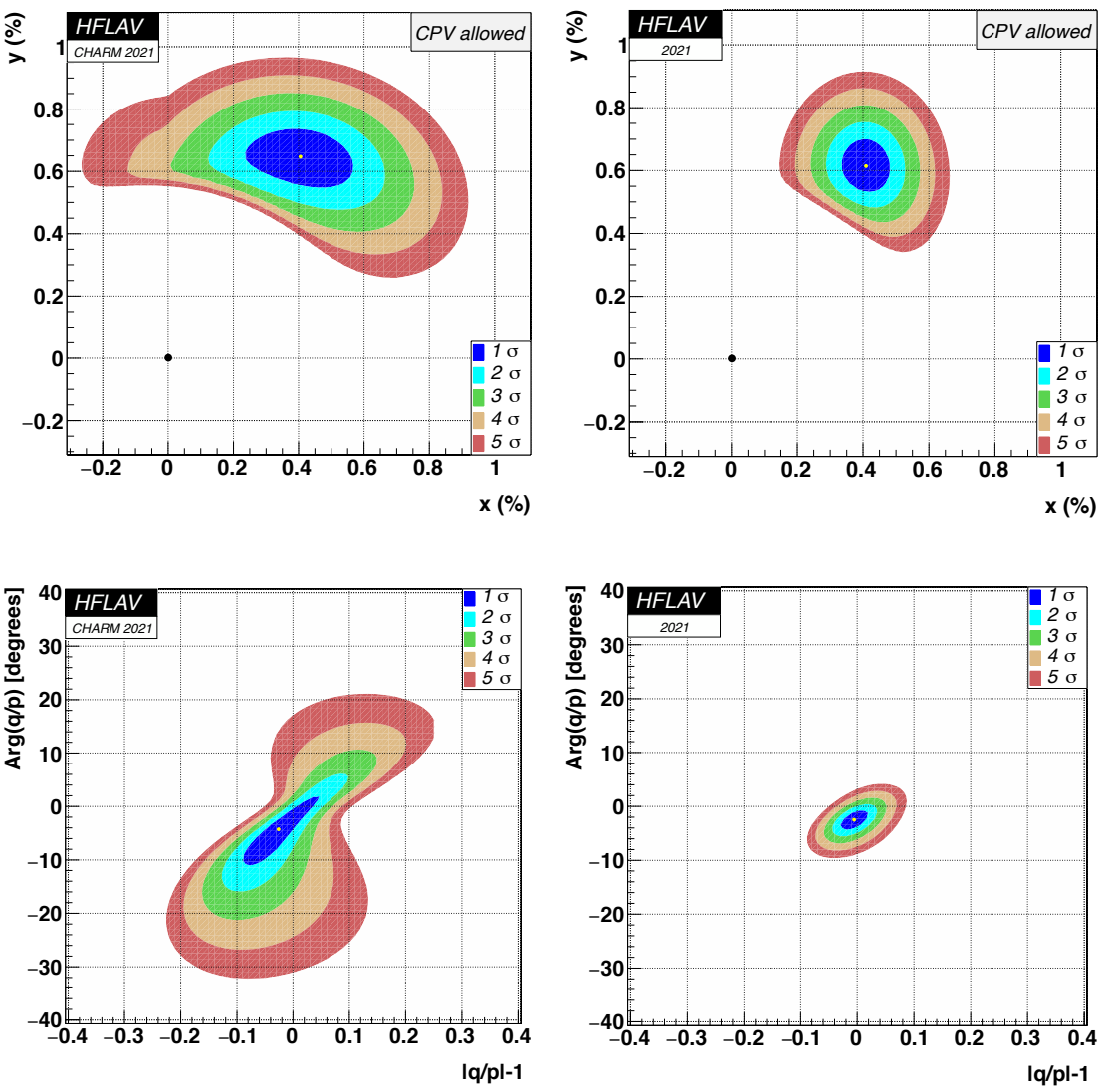

Figure 1.4 – Charm mixing (top) and *CP* violating parameters (bottom) from HFLAV averages without (left) and with (right) the results of Ref. [5].

major impact on the world average values as illustrated in Figure 1.4. The main contribution to the significant improvement stems from the novel model-independent method, the so-called "bin-flip" method, applied to the $D^0 \to K^0_S \pi^+ \pi^-$ decays collected by the LHCb collaboration.

The decay $D^0 \to K^0_S \pi^+ \pi^-$ to a self-conjugated final state provides direct access to both the charm-mixing and *CP*-violating parameters. The decay can proceed with either a Cabibbo-favoured (CF) path through the intermediate resonance $K^{*-}\pi^+$ or a doubly-Cabibbo-suppressed (DCS) path via $K^{*+}\pi^-$ as illustrated in Figure 1.5 (right). These are described by the Feynman diagrams of Figure 1.6. Each of the two processes populates a specific region in the Dalitz plot, as can be seen in Figure 1.5 (left). The Dalitz plot is a two-dimensional distribution that represents the phase space of a three-body decay [58]. The decays proceeding through the

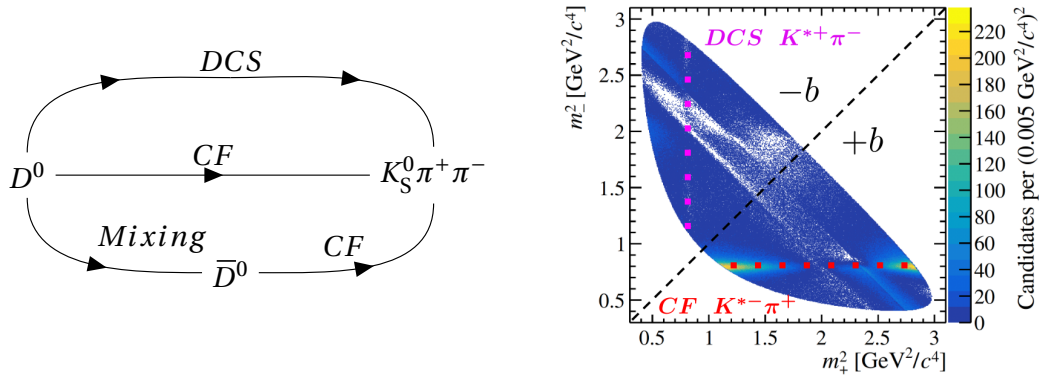

Figure 1.5 – (Left) D^0 decay paths to the $K^0_S\pi^+\pi^-$ final state. (Right) $D^0 \to K^0_S\pi^+\pi^-$ Dalitz plot generated based on the 2008 BaBar amplitude model [59].

CF path dominate in the lower part of the Dalitz plot, where the square of the invariant mass of $K^0_S\pi^+$ (m^2_+) is larger than that of $K^0_S\pi^-$ (m^2_-). The decays through the DCS path populate the upper part of the plot where m^2_+ is smaller than m^2_-. The ratio of events in these two regions of the Dalitz plot does not change with time in the absence of mixing. In the presence of mixing however, the D^0 mesons that have undergone mixing and decay via the CF path populate the same region as non-mixed mesons decaying via the DCS path. Measuring the time evolution of the ratio between the events in those regions gives access to the mixing parameters. Separating the data sample by the production flavour of the D^0 meson further allows the measurement of CP-violating parameters.

There are two main approaches to perform the analysis of the $D^0 \to K^0_S\pi^+\pi^-$ decay: model-dependent and model-independent. The model-dependent approach describes the $D^0 \to K^0_S\pi^+\pi^-$ decay as a superposition of intermediate resonances. The decay amplitude varies as a function of D^0 decay time and decay structure in the Dalitz plot phase space. This amplitude also depends on the mixing and the CP-violating parameters, which can therefore be extracted from a fit to the data sample. However, the data sample is plagued by instrumental effects. The drawback of this approach is the need to establish the correct amplitude model for the decay, also accounting for the instrumental effects. These effects are usually challenging to model precisely even if a simulated sample is available. Examples of amplitude models are described in Refs. [60–62].

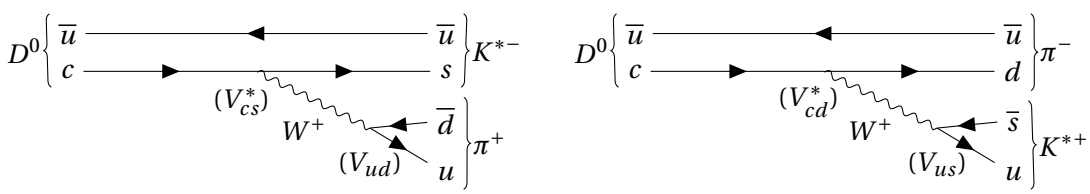

Figure 1.6 – Feynman diagrams for the $D^0 \to K^0_S\pi^+\pi^-$ decay: (left) Cabibbo favoured (CF) path (right) Doubly Cabibbo suppressed (DCS) path.

On the other hand, the model-independent approach probes the parameters without the need of modelling the decay amplitude. In the so-called bin-flip method, described in Section 1.3, the instrumental effects are suppressed by forming ratios of signal yields between two regions of the Dalitz plot located symmetrically on either side of the bisector defined by $m_+^2 = m_-^2$. This only relies on the assumption that the effect is also symmetric, such that it cancels in the ratio. Furthermore, this method is data-driven, meaning that information from a simulated sample is not required.

At LHCb, flavour-tagged D^0 mesons are mainly produced at the pp collision point in the strong decay $D^{*+} \to D^0\pi^+$ (Prompt) and in semileptonic b-hadron decays $\overline{B} \to D^0\mu^-\overline{\nu}_\mu X$ (SL). The topologies of these decay chains are illustrated in Figure 1.7. In the Prompt case, the D^0 flavour is determined from the charge of the accompanying pion, while in the SL case the charge of the muon is used. In 2019, the bin-flip method was applied on both samples of D^0 decays using the data collected by LHCb during 2011–2012. This led to the first evidence of the non-zero value of the mass parameter x [63]. Later in 2021, the analysis of $D^{*+} \to D^0\pi^+$ decays in the data collected during 2016–2018 was published and announced the first observation of a non-zero value of x with more than 7σ of significance [5]. In this thesis, the analysis of the $\overline{B} \to D^0\mu^-\overline{\nu}_\mu X$ sample in the 2016–2018 dataset is performed. This measurement is complementary to the above-mentioned analysis of $D^{*+} \to D^0\pi^+$ decays [5] as it uses an independent sample of D^0 mesons covering a wider range of D^0 decay times.

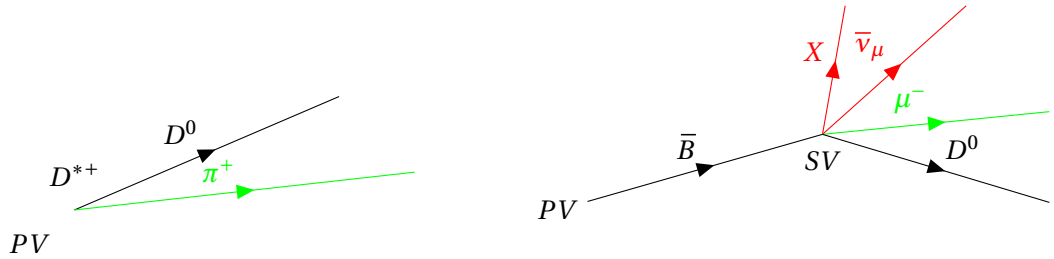

Figure 1.7 – Topology of (left) promptly produced $D^{*+} \to D^0\pi^+$ decays and (right) $\overline{B} \to D^0\mu^-\overline{\nu}_\mu X$ decays. The point where the D^{*+} meson or b hadron is produced is called the primary vertex (PV). The D^{*+} resonance decays promptly at the PV, where the b hadron propagates until it decays at the secondary vertex (SV). Arrows indicate momentum vectors of long-lived particles (green), undetected particles (red), and unstable particles (black).

1.3 The bin-flip method

The analysis is based on the bin-flip method proposed in Ref. [64]. The relevant aspects of the method are summarised from Refs. [2–5, 63, 65].

The bin-flip method is a model-independent approach, optimised for the measurement of the mixing parameter x, which avoids the need for an accurate modelling of the efficiency variation across phase space and decay time. This is achieved by measuring time-dependent ratios of yields in bins symmetric with respect to the Dalitz plot principal bisector.

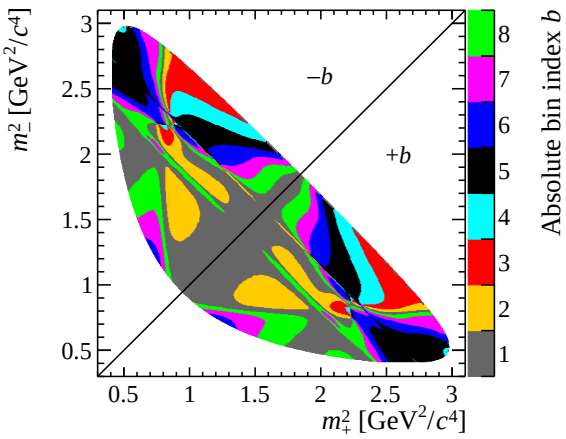

Figure 1.8 – The iso-$\Delta\delta$ binning scheme as proposed by CLEO [60].

1.3.1 Mathematical derivation

The dynamics of the $D^0 \to K_S^0\pi^+\pi^-$ decay can be parametrised by the following two-body invariant masses

$$m_\pm^2 \equiv \begin{cases} m^2(K_S^0\pi^\pm) & \text{for } D^0 \to K_S^0\pi^+\pi^- \text{ decays} \\ m^2(K_S^0\pi^\mp) & \text{for } \overline{D}^0 \to K_S^0\pi^+\pi^- \text{ decays} \end{cases}. \tag{1.9}$$

The two-dimensional distribution of m_-^2 (vertical axis) and m_+^2 (horizontal axis) is called the Dalitz plot. The region where $m_+^2 > m_-^2$ ($m_+^2 < m_-^2$) corresponds to the lower (upper) region of the Dalitz phase space. The function $A_f(m_+^2, m_-^2)$ ($\overline{A}_f(m_-^2, m_+^2)$) represents the amplitude of a D^0 ($\overline{D}^0$) meson decaying to the final state $f = K_S^0\pi^+\pi^-$ as a function of m_+^2 and m_-^2. Due to D^0–$\overline{D}^0$ mixing, the time-dependent amplitudes can be written as

$$T_f(m_+^2, m_-^2; t) = A_f(m_+^2, m_-^2)\, g_+(t) + \overline{A}_f(m_-^2, m_+^2)\, \frac{q}{p}\, g_-(t)\,, \tag{1.10}$$

$$\overline{T}_f(m_+^2, m_-^2; t) = \overline{A}_f(m_+^2, m_-^2)\, g_+(t) + A_f(m_-^2, m_+^2)\, \frac{p}{q}\, g_-(t)\,, \tag{1.11}$$

where $g_\pm(t) = \theta(t) e^{-imt\tau_{D^0}} e^{-t/2} \begin{smallmatrix}\cosh\\ \sinh\end{smallmatrix}(zt/2)$, t is the proper D^0 decay time divided by the average D^0 lifetime τ_{D^0}, $m = (m_1 + m_2)/2$ is the average mass of the neutral D meson eigenstates, θ is the Heaviside function, and $z = -(y + ix)$. Our notation follows the HFLAV convention [57]. The decay amplitudes $A_f(m_+^2, m_-^2)$ and $\overline{A}_f(m_-^2, m_+^2)$ carry weak and strong phases. In the SM, the weak phase appears in the coupling with the W boson. It is CP-odd, meaning that it changes sign between $A_f(m_+^2, m_-^2)$ and $\overline{A}_f(m_-^2, m_+^2)$. On the other hand, the strong phase is CP-even as the phase is the same for $A_f(m_+^2, m_-^2)$ and $\overline{A}_f(m_-^2, m_+^2)$. The source of this phase is dominated by physical rescattering effects via the strong interaction.

The Dalitz phase space is partitioned into disjoint regions ("bins") symmetrically with respect to the principal bisector defined by $m_+^2 = m_-^2$, as illustrated in Figure 1.8 for D^0. These regions preserve nearly constant strong-phase difference between D^0 and $\overline{D}^0$ decay amplitudes as

proposed by CLEO [60]. Positive bin numbers ($+b$) refer to the lower region $m_+^2 > m_-^2$, where the unmixed CF decays dominate. The negative bin numbers ($-b$) refer to the upper region $m_+^2 < m_-^2$, which receives a larger contribution from decays following oscillation. In the case of $\overline{D}^0$, the Dalitz plot is "flipped" version of the D^0 Dalitz plot along its diagonal. The flipping refers to the sign changing from $+b$ to $-b$ and vice-versa.

By integrating over each Dalitz bin b, the yields can be expressed as

$$\begin{aligned} N_b(t) &= \int_b dm_+^2 dm_-^2 \left|T_f(m_+^2, m_-^2; t)\right|^2 \\ &= F_b \left|g_+\right|^2 + \left|\frac{q}{p}\right|^2 \overline{F}_{-b} \left|g_-\right|^2 + 2\sqrt{\overline{F}_{-b} F_b}\,\mathrm{Re}\left(\frac{q}{p} X_b\, g_+^* g_-\right), \end{aligned} \tag{1.12}$$

$$\begin{aligned} \overline{N}_b(t) &= \int_b dm_+^2 dm_-^2 \left|\overline{T}_f(m_+^2, m_-^2; t)\right|^2 \\ &= \overline{F}_b \left|g_+\right|^2 + \left|\frac{p}{q}\right|^2 F_{-b} \left|g_-\right|^2 + 2\sqrt{F_{-b} \overline{F}_b}\,\mathrm{Re}\left(\frac{p}{q} \overline{X}_b\, g_+^* g_-\right), \end{aligned} \tag{1.13}$$

with

$$F_b \equiv \int_b dm_+^2 dm_-^2 \left|A_f(m_+^2, m_-^2)\right|^2, \quad \overline{F}_b \equiv \int_b dm_+^2 dm_-^2 \left|\overline{A}_f(m_+^2, m_-^2)\right|^2, \tag{1.14}$$

$$X_b \equiv \frac{1}{\sqrt{F_b \overline{F}_{-b}}} \int_b dm_+^2 dm_-^2\, A_f^*(m_+^2, m_-^2) \overline{A}_f(m_-^2, m_+^2). \tag{1.15}$$

$\overline{X}_b$ is defined by substituting A_f (F_b) with $\overline{A}_f$ ($\overline{F}_b$) in Equation (1.15). Here F_b and $\overline{F}_b$ are the number of events in the Dalitz bin b at $t = 0$. $\overline{X}_b$ In each Dalitz bin b, the averages between A_f and $\overline{A}_f$ of strong-phase $\Delta\delta_b$ difference and weak-phase difference ϕ_b are embedded in the interference term X_b. By definition, this term has properties $X_{-b} = X_b^*$ and $|X_b| \leq 1$. The method assumes that the D^0 and $\overline{D}^0$ mesons are originally produced in equal numbers, meaning that there is no direct CP violation in the production. This implies $\overline{F}_b = F_b$, $\phi_b = 0$ and $X_b = \overline{X}_b$.

Since the experimental efficiencies may change the yields F_b, we introduce the notation $\tilde{F}_{-b}$ for the yields in presence of efficiencies. The ratio of the yields between the upper part ($-b$) and the lower part ($+b$) at $t = 0$ is

$$\tilde{r}_b \equiv \frac{\tilde{F}_{-b}}{\tilde{F}_b} \equiv \frac{\int_b dm_+^2 dm_-^2\, \epsilon(m_+^2, m_-^2) \left|A_f(m_+^2, m_-^2)\right|^2}{\int_b dm_+^2 dm_-^2\, \epsilon(m_-^2, m_+^2) \left|A_f(m_-^2, m_+^2)\right|^2}, \tag{1.16}$$

where $\epsilon(m_+^2, m_-^2)$ is the efficiency function across the Dalitz plot. If the function is symmetric with respect to the Dalitz-plot bisector, *i.e.* $\epsilon(m_+^2, m_-^2) = \epsilon(m_-^2, m_+^2)$, and constant within bin b, the efficiency cancels completely in the ratio. However, while the latter assumption may not be usually true, it is a good approximation as the efficiency function is already suppressed in the ratio [5, 63]. Therefore, this method does not require a precise modelling of $\epsilon(m_+^2, m_-^2)$. In this analysis, efficiency corrections are performed to minimise the variation within each bin b.

For sufficiently small mixing parameters ($|z|t \ll 1$), $g_{\pm}(t)$ can be approximated up to $\mathcal{O}(z^2)$. The method divides the D^0 decay time in bins with an index j. Then the event yields in each Dalitz bin b and decay time bin j can be written as

$$\begin{aligned} N_{bj} &= \int_j dt N_b(t) \\ &\approx F_b \left[1 + \frac{1}{4}\langle t^2\rangle_j \operatorname{Re}\left(z^2\right)\right] + \frac{1}{4}\langle t^2\rangle_j |z|^2 \left|\frac{q}{p}\right|^2 F_{-b} + \langle t\rangle_j \sqrt{F_{-b}F_b} \operatorname{Re}\left(\frac{q}{p} X_b z\right), \end{aligned} \tag{1.17}$$

$$\begin{aligned} \overline{N}_{bj} &= \int_j dt \overline{N}_b(t) \\ &\approx F_b \left[1 + \frac{1}{4}\langle t^2\rangle_j \operatorname{Re}\left(z^2\right)\right] + \frac{1}{4}\langle t^2\rangle_j |z|^2 \left|\frac{p}{q}\right|^2 F_{-b} + \langle t\rangle_j \sqrt{F_{-b}F_b} \operatorname{Re}\left(\frac{p}{q} X_b z\right), \end{aligned} \tag{1.18}$$

where $\langle t\rangle_j$ ($\langle t^2\rangle_j$) is the average (squared) decay time of unmixed decays in units of τ_{D^0} in the D^0 decay time bin j. The ratios can be formed as

$$R^+_{bj} = \frac{N_{-bj}}{N_{bj}} \approx \frac{r_b \left[1 + \frac{1}{4}\langle t^2\rangle_j \operatorname{Re}\left(z^2\right)\right] + \frac{1}{4}\langle t^2\rangle_j |z|^2 \left|\frac{q}{p}\right|^2 + \langle t\rangle_j \sqrt{r_b} \operatorname{Re}\left(X_b^* \frac{q}{p} z\right)}{\left[1 + \frac{1}{4}\langle t^2\rangle_j \operatorname{Re}\left(z^2\right)\right] + \frac{1}{4}\langle t^2\rangle_j |z|^2 r_b \left|\frac{q}{p}\right|^2 + \langle t\rangle_j \sqrt{r_b} \operatorname{Re}\left(X_b \frac{q}{p} z\right)}, \tag{1.19}$$

$$R^-_{bj} = \frac{\overline{N}_{-bj}}{\overline{N}_{bj}} \approx \frac{r_b \left[1 + \frac{1}{4}\langle t^2\rangle_j \operatorname{Re}\left(z^2\right)\right] + \frac{1}{4}\langle t^2\rangle_j |z|^2 \left|\frac{p}{q}\right|^2 + \langle t\rangle_j \sqrt{r_b} \operatorname{Re}\left(X_b^* \frac{p}{q} z\right)}{\left[1 + \frac{1}{4}\langle t^2\rangle_j \operatorname{Re}\left(z^2\right)\right] + \frac{1}{4}\langle t^2\rangle_j |z|^2 r_b \left|\frac{p}{q}\right|^2 + \langle t\rangle_j \sqrt{r_b} \operatorname{Re}\left(X_b \frac{p}{q} z\right)}, \tag{1.20}$$

where the + (−) superscript refers to the D^0 ($\overline{D}^0$) initial flavour. As we are forming the ratio in which the efficiency is cancelled, these ratios should be similar between D^0 and $\overline{D}^0$. Otherwise, there is a sign of CP violation in D^0–$\overline{D}^0$ mixing.

It should be noted that the term related to $(q/p)^{\pm 1} z$ may degrade the sensitivity to $|q/p|$ as the mixing term $|z|$ is quite small. The quantity $(q/p)^{\pm 1} z$ is parametrised as a function of z_{CP} and Δz:

$$\left(q/p\right)^{\pm 1} z \equiv z_{CP} \pm \Delta z, \tag{1.21}$$

With this definition,

$$z^2 = (z_{CP} + \Delta z)(z_{CP} - \Delta z) = z_{CP}^2 - \Delta z^2, \qquad \left(\frac{q}{p}\right)^2 = \frac{z_{CP} + \Delta z}{z_{CP} - \Delta z}, \tag{1.22}$$

Then Equations (1.19) and (1.20) can be combined and written as

$$R^{\pm}_{bj} \approx \frac{r_b + \frac{1}{4} r_b \langle t^2\rangle_j \operatorname{Re}\left(z_{CP}^2 - \Delta z^2\right) + \frac{1}{4}\langle t^2\rangle_j |z_{CP} \pm \Delta z|^2 + \sqrt{r_b}\langle t\rangle_j \operatorname{Re}\left[X_b^*(z_{CP} \pm \Delta z)\right]}{1 + \frac{1}{4}\langle t^2\rangle_j \operatorname{Re}\left(z_{CP}^2 - \Delta z^2\right) + r_b \frac{1}{4}\langle t^2\rangle_j |z_{CP} \pm \Delta z|^2 + \sqrt{r_b}\langle t\rangle_j \operatorname{Re}\left[X_b(z_{CP} \pm \Delta z)\right]}. \tag{1.23}$$

The results are expressed in terms of the CP-averaged mixing parameters

$$x_{CP} = -\mathrm{Im}\,(z_{CP}) = \frac{1}{2}\left[x\cos\phi\left(\left|\frac{q}{p}\right| + \left|\frac{p}{q}\right|\right) + y\sin\phi\left(\left|\frac{q}{p}\right| - \left|\frac{p}{q}\right|\right)\right], \tag{1.24}$$

$$y_{CP} = -\mathrm{Re}\,(z_{CP}) = \frac{1}{2}\left[y\cos\phi\left(\left|\frac{q}{p}\right| + \left|\frac{p}{q}\right|\right) - x\sin\phi\left(\left|\frac{q}{p}\right| - \left|\frac{p}{q}\right|\right)\right], \tag{1.25}$$

and of the CP-violating differences

$$\Delta x = -\mathrm{Im}\,(\Delta z) = \frac{1}{2}\left[x\cos\phi\left(\left|\frac{q}{p}\right| - \left|\frac{p}{q}\right|\right) + y\sin\phi\left(\left|\frac{q}{p}\right| + \left|\frac{p}{q}\right|\right)\right], \tag{1.26}$$

$$\Delta y = -\mathrm{Re}\,(\Delta z) = \frac{1}{2}\left[y\cos\phi\left(\left|\frac{q}{p}\right| - \left|\frac{p}{q}\right|\right) - x\sin\phi\left(\left|\frac{q}{p}\right| + \left|\frac{p}{q}\right|\right)\right]. \tag{1.27}$$

In this analysis, the Dalitz space is divided into 8 pairs of bins as proposed by CLEO [60], such that the strong-phase difference between the D^0 and $\overline{D}^0$ amplitudes is nearly constant in each bin. The binning scheme is depicted in Figure 1.8. The data is then further divided into 10 equipolulous bins of the measured D^0 decay time:

$$[0.00, 0.155, 0.285, 0.42, 0.57, 0.74, 0.94, 1.20, 1.58, 2.22, 20.00]\,\tau_{D^0}, \tag{1.28}$$

where τ_{D^0} is the world-average value of the D^0 lifetime [14]. The mixing and CP-violating parameters (x, y, $|q/p|$, and ϕ) are determined through a joint fit of the $R^{\pm}_{bj}$ expressions to the measured yield ratios.

1.3.2 External inputs

As seen in Equation (1.23), the bin-flip method needs external knowledge of the quantities X_b defined in Equation (1.15), which are related to the strong-phase differences between the D^0 and $\overline{D}^0$ decays.

In the limit of no direct CP violation, X_b can be written as $X_b \equiv c_b - i s_b$ where c_b and s_b are the amplitude-weighted averages of the cosine and sine of the strong-phase difference over the Dalitz bin $\pm b$. These coefficients can be written as

$$c_b \equiv \frac{1}{\sqrt{F_b F_{-b}}}\int_b dm_+^2\, dm_-^2\, \left|A_f(m_+^2, m_-^2)\right| \left|A_f(m_-^2, m_+^2)\right| \cos[\Delta\delta(m_+^2, m_-^2)], \tag{1.29}$$

$$s_b \equiv \frac{1}{\sqrt{F_b F_{-b}}}\int_b dm_+^2\, dm_-^2\, \left|A_f(m_+^2, m_-^2)\right| \left|A_f(m_-^2, m_+^2)\right| \sin[\Delta\delta(m_+^2, m_-^2)], \tag{1.30}$$

where $\Delta\delta(m_+^2, m_-^2) = \delta(m_+^2, m_-^2) - \delta(m_-^2, m_+^2)$ and $\delta(m_+^2, m_-^2)$ is the phase of $A_f(m_+^2, m_-^2)$.

There are different binning schemes developed by the CLEO collaboration to measure these coefficients. The iso-$\Delta\delta$ binning scheme [60] is chosen as it minimises the variation of the strong-phase difference over the Dalitz bin. A total of $n = 8$ bins are defined in each Dalitz

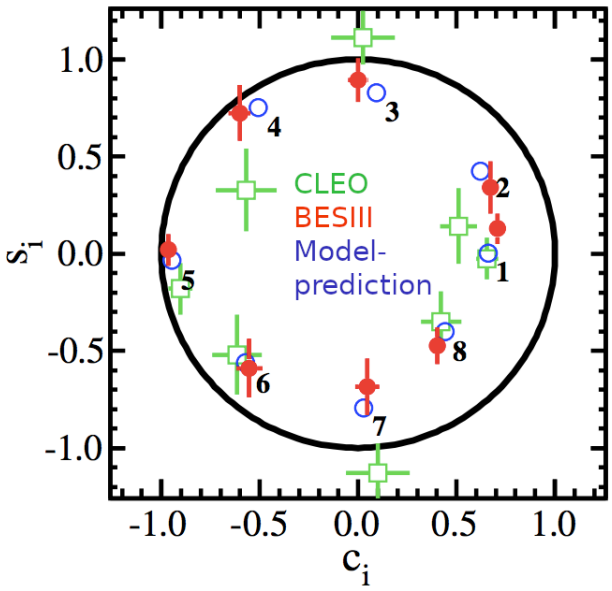

Figure 1.9 – Comparison (taken from Ref. [66]) of the c_b and s_b values measured by (open, green square) CLEO [60] and (red, filled circle) BESIII [66] collaborations, along with (open, blue circle) the prediction from a recent Belle amplitude model [61]. The values are shown for the CLEO iso-$\Delta\delta$ binning of the $D^0 \to K^0_S\pi^+\pi^-$ Dalitz plot [60].

sub-phase space such that

$$2\pi(b-3/2)/n < \Delta\delta(m^2_+, m^2_-) < 2\pi(b-1/2)/n, \quad b = 1, ..., n. \tag{1.31}$$

The iso-$\Delta\delta$ scheme, shown in Figure 1.8, is available as a look-up table consisting of a grid of (m^2_+, m^2_-) points spaced 0.0054 GeV$^2/c^4$ apart in both m^2_+ and m^2_-.

The coefficients c_b, and s_b are obtained from the combination of measurements by the CLEO and BESIII collaborations. Those measurements are performed in e^+e^- collisions at the $\psi(3770)$ resonance where the pairs of quantum-entangled $D^0\overline{D}^0$ are produced from the $\psi(3770)$ decay. This leads to precise measurements of these strong-phase differences. Figure 1.9 presents a comparison between these measured values and the recent Belle amplitude models [61]. This shows a general consistency between these measurements and the amplitude model. The combined values used in this analysis are shown in Table 1.2 together with the corresponding correlations in Table 1.3. These are used as direct inputs to the fit as explained in Section 5.3.

The ratios at $t = 0$ (r_b) are also shown in Table 1.2 but they are not used in the fit because they are affected by the efficiency function as discussed in Section 1.3.1. Note that the efficiency variation within each Dalitz bin b also affects (c_b, s_b). Since the bins are defined to correspond to a nearly constant strong-phase difference $\Delta\delta(m^2_+, m^2_-)$, the efficiency has minimal effect on the (c_b, s_b), but not on r_b.

Table 1.2 – Values of r_b, c_b, and s_b for the CLEO iso-$\Delta\delta$ binning scheme [60] obtained from the combination of the measurements performed by CLEO [60] and BESIII [66]. The uncertainty contains both statistical and systematic contributions.

b	r_b	c_b	s_b
1	0.477 ± 0.014	0.699 ± 0.020	0.091 ± 0.063
2	0.233 ± 0.013	0.643 ± 0.036	0.300 ± 0.110
3	0.304 ± 0.017	0.001 ± 0.047	1.000 ± 0.075
4	0.667 ± 0.050	-0.608 ± 0.052	0.660 ± 0.123
5	0.614 ± 0.028	-0.955 ± 0.023	-0.032 ± 0.069
6	0.207 ± 0.019	-0.578 ± 0.058	-0.545 ± 0.122
7	0.103 ± 0.008	0.057 ± 0.057	-0.854 ± 0.095
8	0.218 ± 0.009	0.411 ± 0.036	-0.433 ± 0.083

Table 1.3 – Correlation coefficients (in %) between the c_b and s_b parameters, containing both statistical and systematic effects, as obtained from the combination of CLEO [60] and BESIII [66] measurements using the CLEO iso-$\Delta\delta$ binning scheme [60].

	c_2	c_3	c_4	c_5	c_6	c_7	c_8	s_1	s_2	s_3	s_4	s_5	s_6	s_7	s_8
c_1	1	12	9	12	12	16	5	2	1	0	1	1	1	1	2
c_2		4	6	9	8	8	9	2	1	−1	1	3	1	0	1
c_3			4	10	8	14	13	1	−4	18	3	−2	4	6	4
c_4				5	6	7	11	3	−1	1	3	4	2	0	2
c_5					4	11	12	5	1	3	1	−1	4	1	7
c_6						8	11	5	2	1	0	0	2	1	5
c_7							9	7	3	2	0	1	0	−2	6
c_8								4	2	0	−1	0	1	0	4
s_1									−8	2	−7	6	4	0	−3
s_2										−6	−8	16	−7	5	8
s_3											1	3	1	38	13
s_4												−12	7	8	9
s_5													−11	6	−5
s_6														−14	−4
s_7															4

1.3.3 Sensitivity

To examine the sensitivity of the bin-flip method, Equation (1.23) can be approximated by keeping only the first order term in the decay time $\langle t \rangle_j$ with the condition $\langle t \rangle_j \sqrt{r_b}\,\mathrm{Re}\,(X_b z) \ll 1$ assuming CP symmetry,

$$R^{\pm}_{bj} \approx \frac{r_b + \langle t \rangle_j \sqrt{r_b}\,\mathrm{Re}\left(X_b^* z\right)}{1 + \langle t \rangle_j \sqrt{r_b}\,\mathrm{Re}\,(X_b z)} \approx r_b - \langle t \rangle_j \sqrt{r_b}\left[(1 - r_b) c_b\, y - (1 + r_b) s_b\, x\right]. \tag{1.32}$$

The r_b values are generally around 0.5, as shown in Table 1.2, making the term $(1 - r_b)$ multiplying y smaller than the term $(1 + r_b)$ multiplying x. This leads to a reduced sensitivity related to the parameters associated with the width difference (y_{CP} and Δy) with respect to the sensitivity to the parameters associated with the mass difference (x_{CP} and Δx).

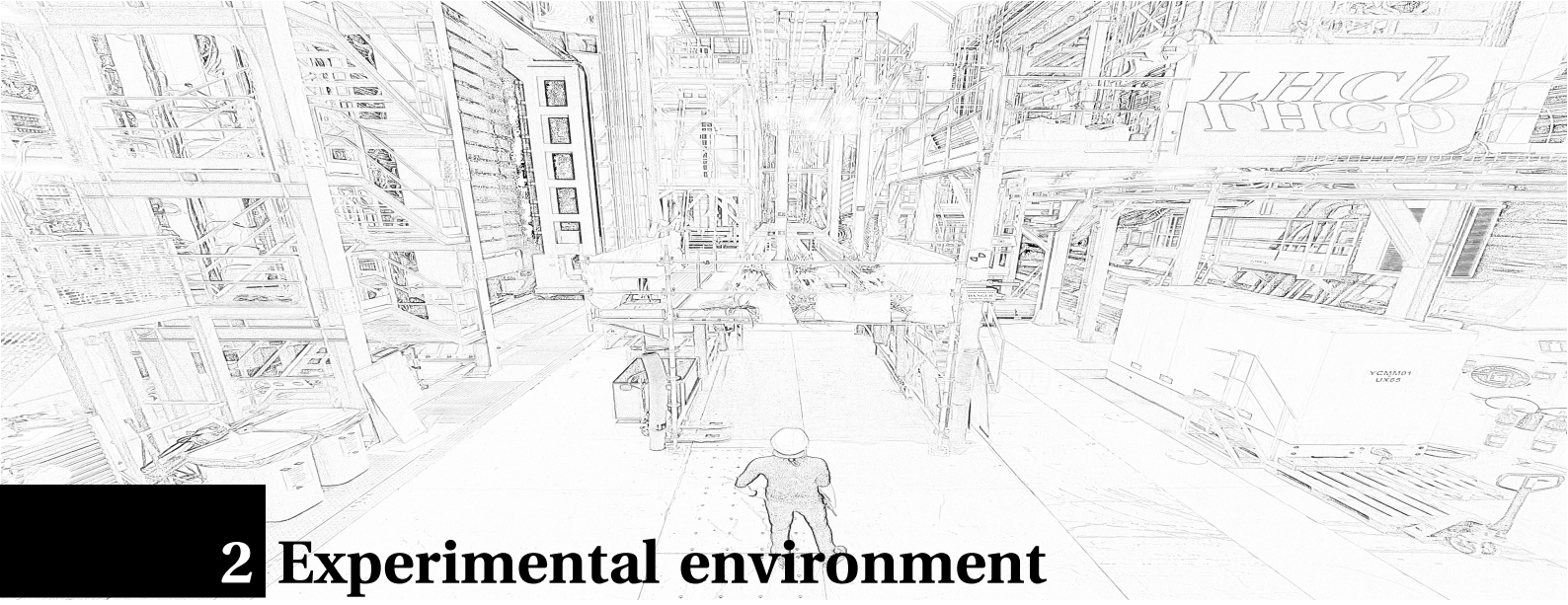

2 Experimental environment

This thesis is based on the dataset collected by the LHCb detector during the operation of the Large Hadron Collider (LHC) from 2016 to 2018. A brief overview of the LHC and details about the detector are summarised in this chapter.

2.1 The Large Hadron Collider at CERN

The European Organization for Nuclear Research (*Conseil européen pour la recherche nucléaire*, CERN) is a research organisation hosting the current largest particle physics laboratory in the world. It operates particle accelerators and computing infrastructures for research in the field.

The largest current accelerator is the Large Hadron Collider (LHC) situated in the suburbs of Geneva on the Swiss-Franco border. It is part of the CERN accelerator complex as shown in Figure 2.1. The main purpose of the LHC is to explore and study predictions of different theories in particle physics. It is a hadron synchrotron accelerator, located in a circular tunnel of 27 kilometres of circumference. The machine is operating around 100 metres below the surface to shield harmful radiation with the earth's crust [68]. The LHC is designed to accelerate two proton beams and collide them at a maximum energy of 14 TeV in the centre of mass [69]. To reach this high energy, the beams are progressively accelerated by a series of particle accelerators (as of August 2018):

- The Linear accelerator (LINAC) 2 boosts protons extracted from hydrogen gas to 50 MeV.
- The Proton Synchrotron Booster (Booster) accelerates the protons up to 1.4 GeV.
- The Proton Synchrotron (PS) accelerates them further to 25 GeV.
- The Super Proton Synchrotron (SPS) gives the protons an energy of 450 GeV.
- The LHC, fed with protons from the SPS in two counter-rotating beams, provides the final energy.

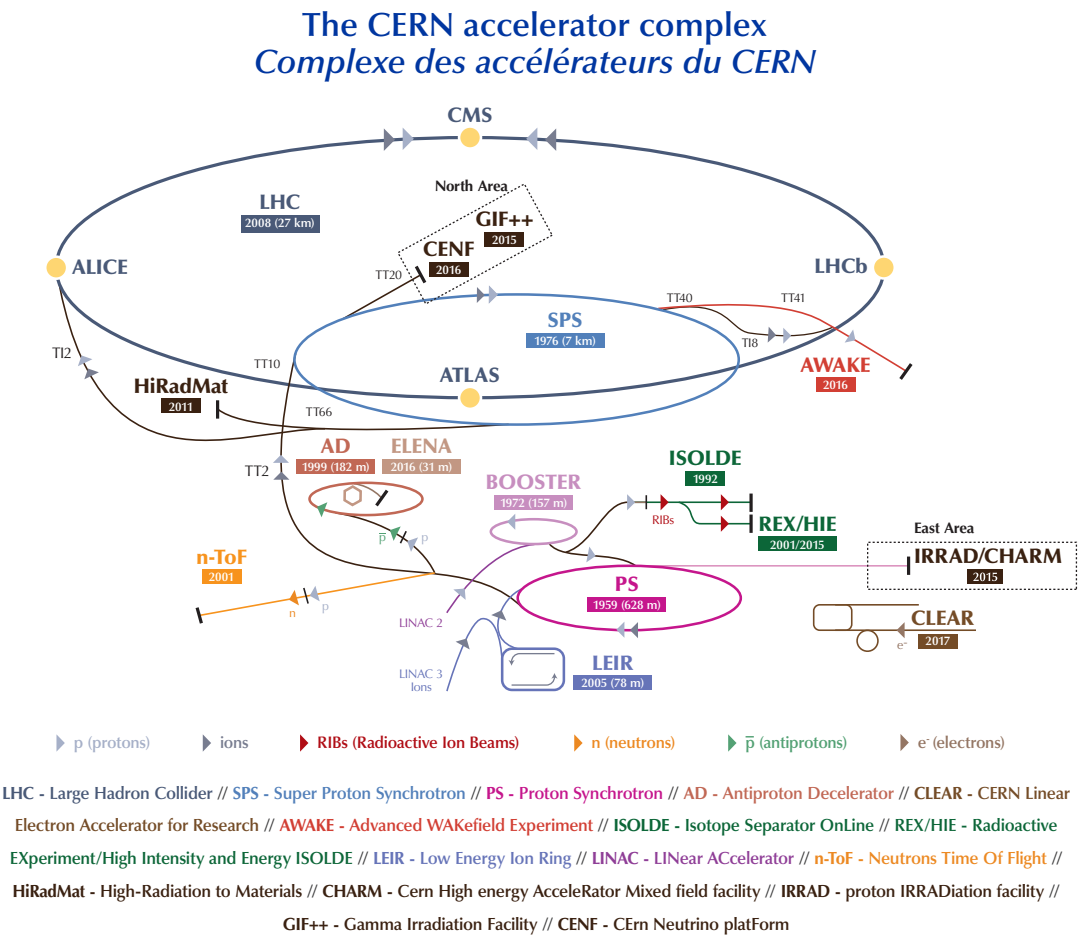

Figure 2.1 – The CERN accelerator complex as of August 2018 [67].

The LHC operates with a nominal number of proton bunches of 2808 per beam, where each bunch consists of about 10^{11} protons. Once the protons have been accelerated to the required energy, the two counter-rotating beams are focused to collide at four collision points where the ALICE, ATLAS, CMS, and LHCb detectors are located.

An important characteristics of particle accelerators is the instantaneous luminosity. It is defined as the rate of produced events of a certain type divided by the corresponding production cross-section. The integral of the instantaneous luminosity over time is known as the integrated luminosity. This quantity determines the size of the collected data sample available for analysis.

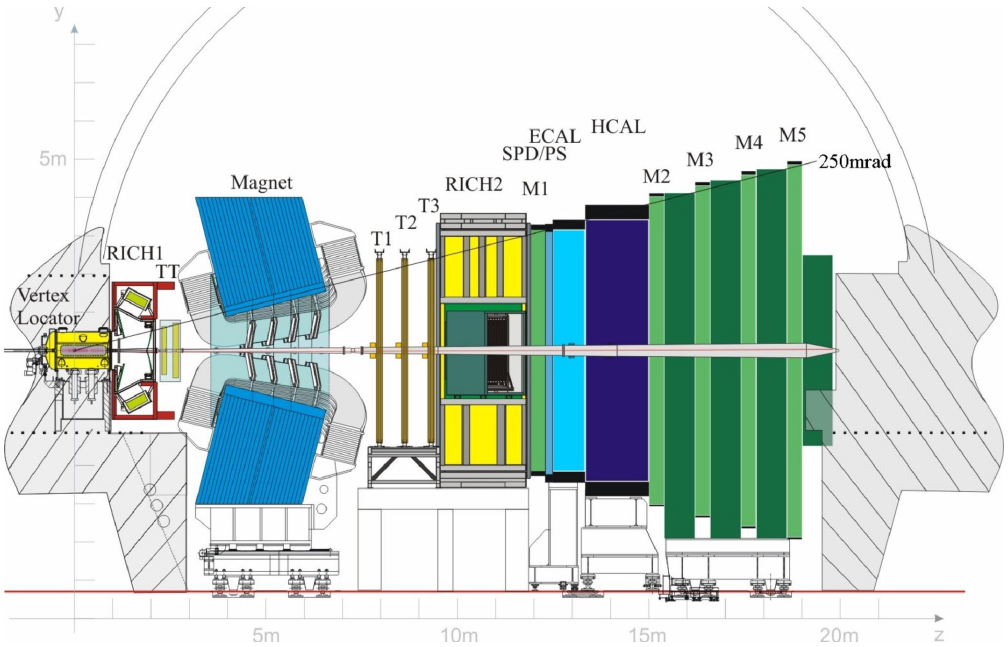

Figure 2.2 – Schematic side view of the LHCb detector [70].

2.2 The LHCb detector

The LHCb detector is a single-arm forward spectrometer dedicated to search for new physics interactions in the decay of particles containing a beauty or charm quark. The detector covers a region close to the LHC beam pipe. The geometrical acceptance is expressed in terms of the pseudorapidity

$$\eta = -\ln\left[\tan\left(\frac{\theta}{2}\right)\right], \tag{2.1}$$

where θ is the angle between the momentum of a produced particle and the beam axis (z axis). The LHCb detector covers the range $2 < \eta < 5$, which is optimised for b-hadron production at the LHC. The $b\bar{b}$ production cross-section in this region is higher than in the range $0 < \eta < 2$. After a quark is produced, it hadronises to form hadrons due to colour confinement which prevents a quark to exist individually.

The distinguishing feature of the experiment is the choice to operate at low pile-up with almost constant luminosity during the data-taking period. This is controlled by a luminosity levelling procedure [71]. The pile-up is defined as the average number of simultaneous collisions in a bunch crossing. At the LHCb detector, this is around 3 depending on the year and running conditions. Operating at low pile-up simplifies event topology and avoids confusion caused by a large number of overlapping interactions. This leads to a clean event reconstruction and more efficient computing performance. Figure 2.2 presents a sketch of the LHCb detector. It is composed of different subdetectors forming the tracking and particle identification systems.

The LHCb detector collected available data for physics analysis during *Run 1* (2010–2012)

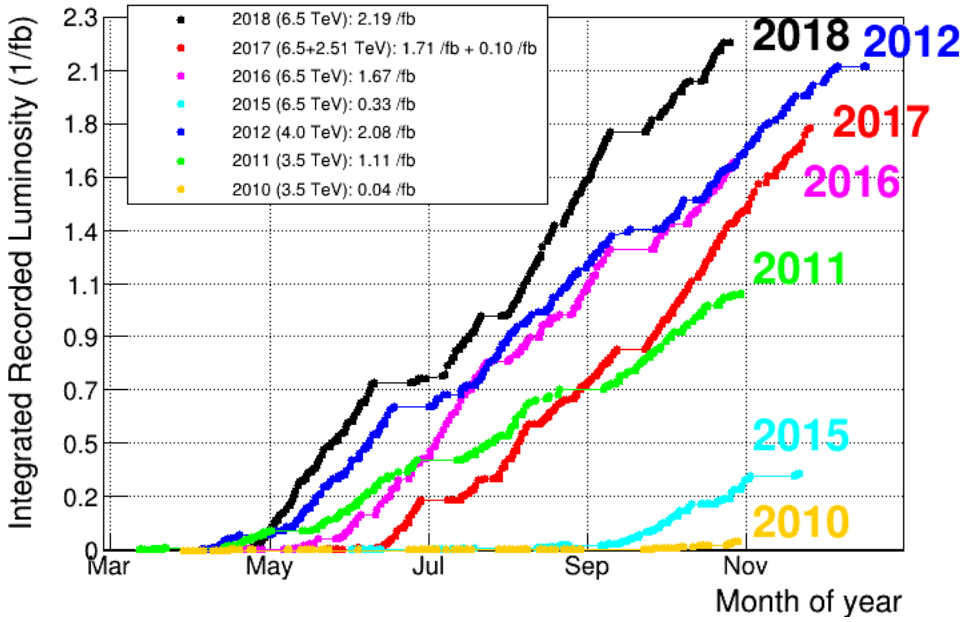

Figure 2.3 – Integrated luminosity as recorded by the LHCb detector [72].

at a centre-of-mass energy of $\sqrt{s} = 7 - 8\,\text{TeV}$ and *Run 2* (2015–2018) at $\sqrt{s} = 13\,\text{TeV}$. The corresponding luminosity is reported in Figure 2.3.

2.2.1 Tracking system

The LHCb tracking system consists of the VErtex LOcator (VELO), the LHCb dipole magnet, and four tracking stations. The VELO is placed close to the collision point. A first tracking station, Tracker Turicensis (TT), is situated upstream of the dipole magnet and three tracking stations (T1, T2, T3) are placed downstream. These three stations use silicon microstrip detectors as their inner tracker (IT), which is the same technology as for the VELO and TT, while straw-tubes are used in the outer tracker (OT).

Vertex Locator (VELO)

The VErtex LOcator (VELO) is a silicon micro-strip detector placed around the collision point. It covers ~ 1 metre along the beam line. It aims at a precise reconstruction of the primary vertices (PV) and secondary vertices (SV) in the event. The precise identification of these vertices are crucial as the b- and c-hadrons are formed at the PV and decay at the SV. The VELO is designed as two sets of semicircular sensors perpendicular to the beam. It is built from 21 modules to measure the azimuthal angle (Φ) and radial distance (R) of a particle transversing the sensors.

The detector can be operated in two configurations. During a data acquisition run, the two

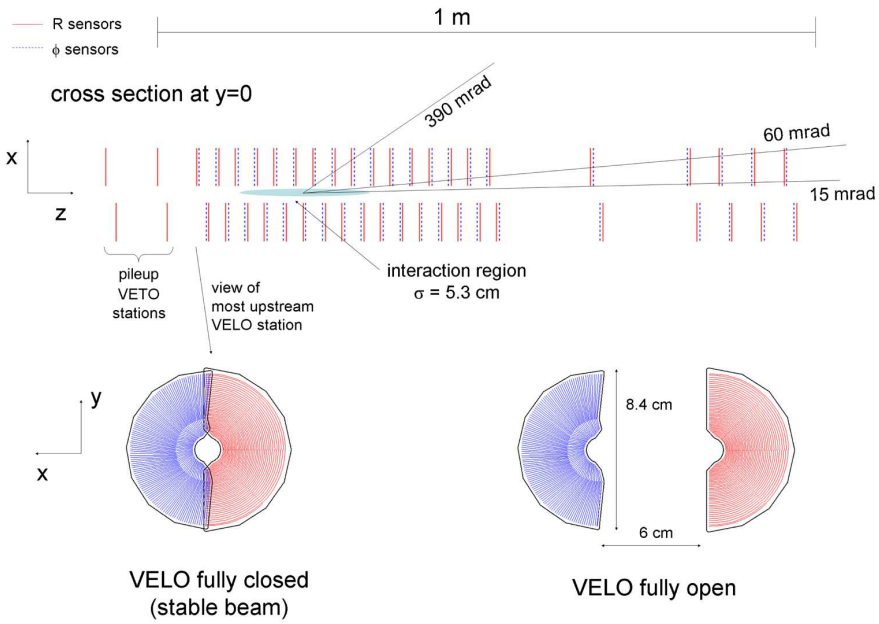

Figure 2.4 – Layout of the VELO circular modules [70].

parts are moved toward each other, leaving an aperture in the centre of the VELO for the LHC proton beam. The closest channels of the detectors are about 8 mm from the beamline. To reduce radiation damage and prolong the lifetime of the detector, these two halves are separated outside of the data acquisition runs [74, 75].

Tracking stations

The tracking stations are modules to track the passage of a particle traversing the detector.

The Tracker Turicensis (TT) consists of four silicon micro-strip layers with an active area of 8.4 m^2, covering between 2.0 and 4.9 in pseudorapidity. The system is held in an insulated volume at 5 °C. The four layers are rotated in the xy plane by 0°, +5°, −5°, and 0° with respect to the vertical direction as shown in Figure 2.5, in order to enable stereo reconstruction. This system provides a measurement of the momentum $\vec{P}$ of charged particles through their curvature. The momentum resolution depends on hit and track reconstruction as well as the magnetic field.

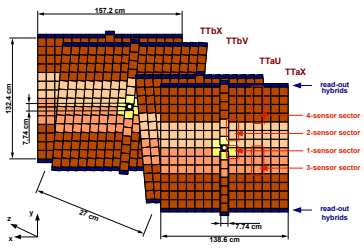

Figure 2.5 – Layout of the Tracker Turicensis [76].

The Inner Tracker (IT) and Outer Tracker (OT) stations are the three downstream tracking modules (T1–T3) after the LHCb magnet, as presented in Figure 2.2. The IT uses silicon micro-strip layers like the TT. It is built close to the beam pipe where the occupancy of charged

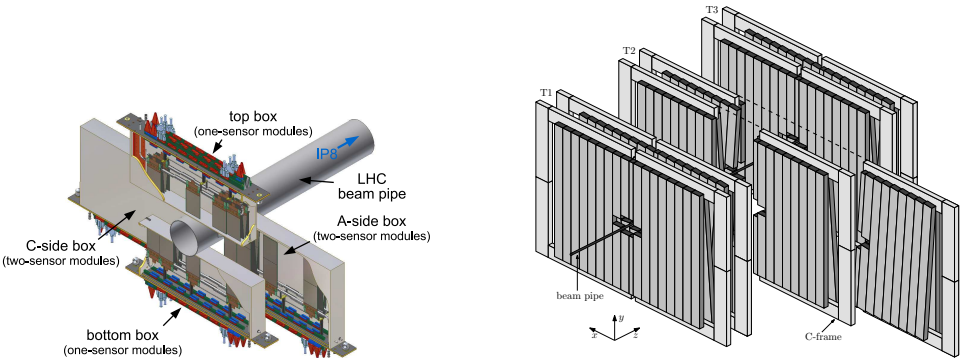

Figure 2.6 – Layout of the (left) Inner Tracker [70] and (right) Outer Tracker [77].

particles is large. The IT detects around 20% of the charged particle passing through the stations while covering only 1.3% of the total surface area. The geometrical acceptance of this region is $3.4 < \eta < 5.0$ in the xz plane and $4.5 < \eta < 4.9$ in the yz plane. On the other hand, the OT is constructed around the IT. It is a drift tube detector with a mixture of Argon (70.0%), CO_2 (28.5%), and O_2 (1.5%) gas. Each tracking station is a combination of four layers of IT and OT modules with orientations similar to the ones in TT. Figure 2.6 shows the configurations of IT and OT.

The LHCb dipole magnet

The charge and momentum of a particle determine its curvature under the influence of a magnetic field. At the LHCb detector, a non-superconducting dipole magnet is used and placed between TT and T1. It generates an integrated magnetic field of 4 Tm for tracks of 10 m length in the xz plane. The field is mainly vertical and the polarity of the magnet is inverted regularly (with configurations called MagUp and MagDown) during the data acquisition, to study the instrumental asymmetries as the performance of the detector is not symmetric along the x axis. Figure 2.7 shows the LHCb magnet as well as the vertical field along the beam axis.

Track reconstruction

Different types of tracks are reconstructed in the LHCb detector as shown in Figure 2.7:

- A VELO track is reconstructed from VELO hits only.
- A Long track is reconstructed in the whole tracking system.
- An Upstream track is similar to a Long track but the track is bent out of the detector before the three tracker stations.
- A Downstream track is similar to a Long track, but the track is not seen in the VELO.
- A T track is reconstructed using only hits in the three downstream tracking stations.

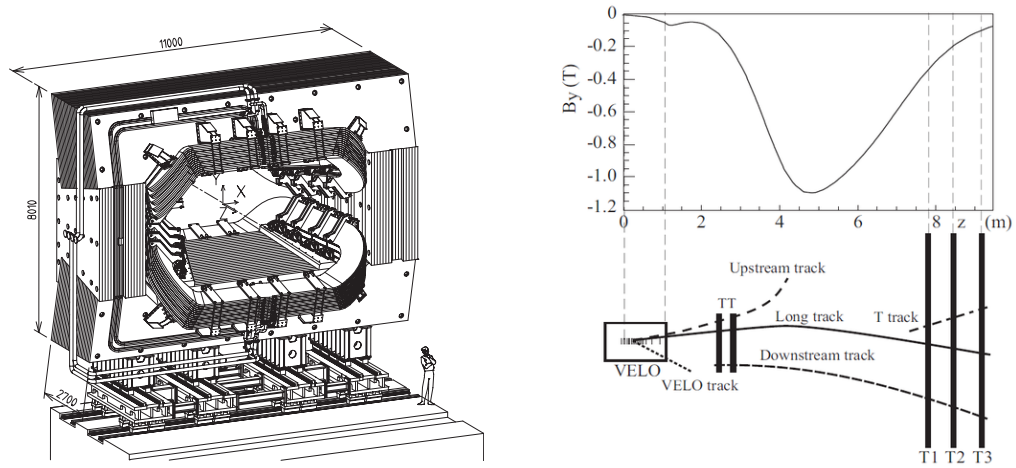

Figure 2.7 – (Left) Drawing of the LHCb dipole magnet. (Right) Vertical magnetic field in the MagDown configuration at the location of the different tracking stations. The different track types are also shown [70].

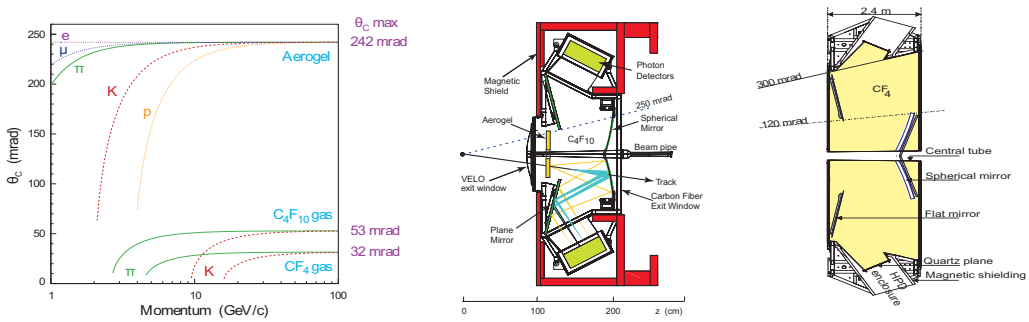

Figure 2.8 – (Left) Cherenkov angle as a function of the particle momentum in aerogel, CF_4, and C_4F_{10}. Designs of (middle) RICH1 and (right) RICH2. Figures taken from Ref. [70].

2.2.2 Particle identification

The unique fundamental requirement of the LHCb detector is the Particle IDentification (PID) to distinguish different particle types from their interactions in different parts of the detector. This PID system is composed of two Ring Imaging Cherenkov Detectors (RICH), an electromagnetic calorimeter (ECAL), a hadronic calorimeter (HCAL), and muon stations.

Ring Imaging Cherenkov Detectors (RICH)

The RICH detectors are photodetectors constructed to capture Cherenkov radiation from high energy particles propagating faster than the speed of light in a medium. The relation between the particle velocity, βc, and the angle of Cherenkov light with respect to the particle's velocity θ_C is

$$\beta = \frac{1}{n \cos\theta_C}, \tag{2.2}$$

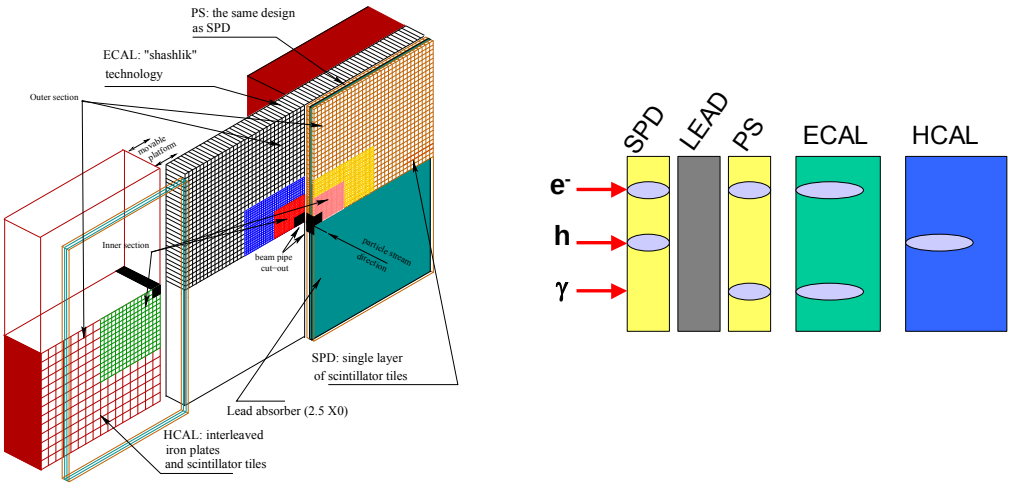

Figure 2.9 – (Left) Schematic view of the calorimeter system [78]. (Right) Signatures of an electron e, a hadron h, and a photon γ in the calorimeter system [79].

where n is the refractive index of the medium. The information obtained from the RICH detectors plays an important role in particle identification, since charged particles with different masses lead to different relations between the Cherenkov angle and the particle momentum, as shown in Figure 2.8 (left). To optimise for the sensitivity in distinguishing kaons from pions for the whole momentum spectrum, two RICH detectors are deployed. One is located after the VELO (RICH1) and another one after the downstream trackers (RICH2), as shown in Figure 2.2. RICH1 covers momenta ranging from ~ 1 to 60 GeV/c with C_4F_{10} radiator (the aerogel was removed before *Run 2* started). CF_4 radiator is used in RICH2 to cover the high momentum range from ~ 15 GeV/c up to more than 100 GeV/c.

Calorimeters

The calorimeter system is designed to absorb particles and measure their energies. Photons, electrons and hadrons can be identified by the calorimeter system, which consists of a scintillating pad detector (SPD), a preshower detector (PS), an electromagnetic calorimeter (ECAL) and a hadronic calorimeter (HCAL) as shown in Figure 2.9 (left).

The SPD and PS are made of scintillators. They provide fast particle identification and background rejection during online data acquisition. The SPD is placed in front of the PS separated by a lead converter. Particles interacting electromagnetically lose their energy by inducing electromagnetic showers in the ECAL. Hadrons, which can interact through the strong interaction, deposit their energy in the hadronic calorimeter (HCAL). The ECAL (HCAL) is arranged with alternating layers of scintillator and lead (iron). The signature of each long-lived particle (electron e, hadron h, and photon) in terms of energy deposition in the calorimeter system is shown in Figure 2.9 (right).

Muon system

The main process for an electron to produce an electromagnetic shower in the calorimeters is Bremsstrahlung. It is electromagnetic radiation emitted when a charged particle is accelerated. The emission power is inversely proportional to the square of the mass of the charged particle.

Since the muon mass is 200 times the electron mass, a muon deposits much less energy than electrons in the calorimeters. It is also a lepton, insensitive to the strong interaction. Muon chambers are placed at the very end of the detector to detect muons. In LHCb, these chambers are composed of alternating layers of iron and multiwire proportional chambers to detect ionisation of the gas inside the chambers. The chambers form five stations (M1–M5) located after the calorimeters except M1, as shown in Figure 2.10.

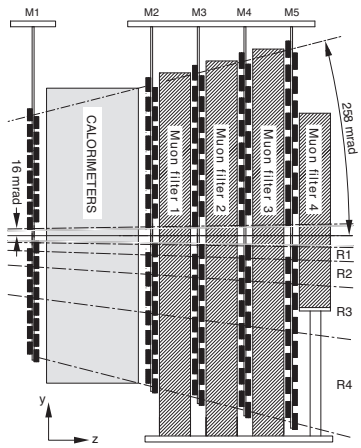

Figure 2.10 – Layout of the muon stations [70].

The triple gas electron multiplier (GEM) technology is used to cope with the harsh environment close to the beam pipe in the M1 station due to high particle rate. This station is designed for a precise position measurement (alignment) before the multiple scattering in the calorimeters.

2.2.3 Trigger system

In general, particle physics experiments are searching for events that have a relatively low probability to be produced. Collisions at the interaction point inside the LHCb detector occur at a rate of 40 MHz. Due to the limited computing facilities, the event rate that can be recorded is around a few kHz. The trigger system is designed to reduce the rate by rejecting background events. It decides whether events occurring in the detector should be stored or not. This is done in several stages:

- **The Level-0 (L0) trigger** is a hardware-based trigger. It rapidly selects events that have muons or high transverse energy particles from collisions by using information from the VELO, the calorimeters, and the muon chambers. This reduces the readout rate down to 1 MHz.
- **The High Level Trigger 1 (HLT1)** is the first stage of the software-based triggers. The HLT1 partially reconstructs events where a few tracks are chosen based on their transverse momenta and impact parameters (IP). This stage reduces the event rate further to around 50 kHz.
- **The High Level Trigger 2 (HLT2)** is the second stage of the software-based triggers. After a positive decision of HLT1, data is transferred to disk with detector calibrations applied. At this stage, a full event reconstruction of tracks and vertices is performed. Events are categorised and selected based on their matching criteria with the topology of decay channels of interest. The event rate is reduced to 12.5 kHz.

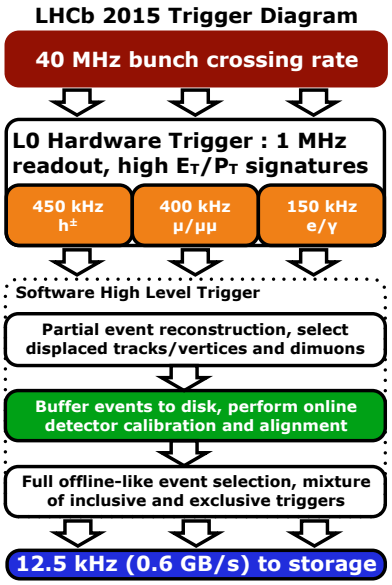

Figure 2.11 – Flowchart of the trigger system in the Run 2 data-taking period [80].

Figure 2.11 illustrates the event rate reduction from the collision rate to the storage rate. The funtionalities of each trigger level are shown in Figure 2.12.

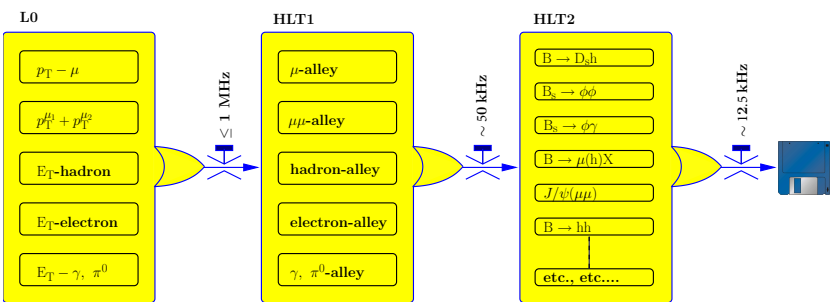

Figure 2.12 – Trigger selections at each stage [70].

2.3 Analysis environment

The official LHCb software stack is used to process data from online and offline streams as well as to perform simulation. Data processing is centralised and automated to transform raw collision data to tabular data format for further analysis. The analysis software is written in the PYTHON and C++ programming languages with several packages.

2.3.1 The LHCb software

The LHCb software is built on top of the GAUDI framework, developed between collaborations at CERN [81, 82]. Figure 2.13 presents a data flow of the LHCb software stack. The main frameworks are:

- GAUSS: This framework provides an interface for Monte Carlo (MC) simulation including particle interaction in the collisions and their passage through the detector. Details of the simulation process are described further in Section 3.2.
- BOOLE: After the interactions are simulated with GAUSS, events are digitised to imitate the detector responses.
- MOORE: Events, from real collisions or simulation, are processed at the HLT stage in this framework.
- BRUNEL: Offline reconstructions are performed in this framework. The full track reconstruction and particle identification are applied, and processed data are loaded onto Data Summary Tapes (DSTs) which is a not-only Structured Query Language (NoSQL) database.
- DAVINCI: This software provides analysis packages to Extract, Transform, and Load (ETL) process from the DSTs file format to a ROOT tabular file format [83, 84]. Physics-related quantities are constructed in this framework.

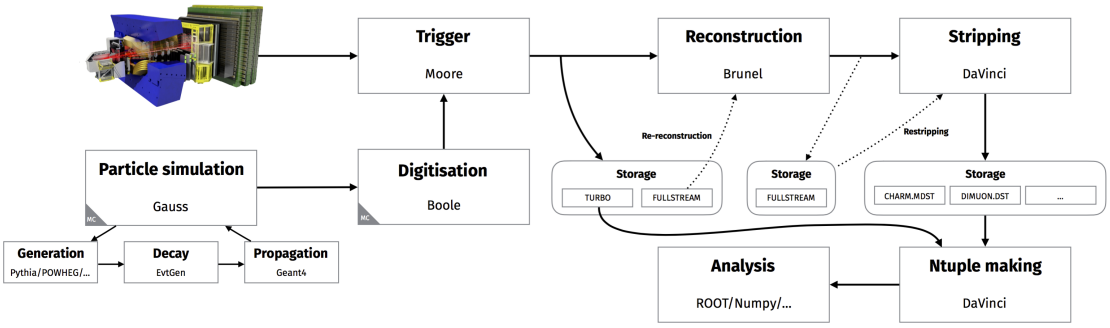

Figure 2.13 – Data flow through the LHCb software stack during the Run 2 data-taking period.

2.3.2 Analysis production

The LHCb analysis production package is developed as part of the Data Processing & Analysis (DPA) Project [85, 86]. The goal of the package is to reduce duplication of processed data from the DaVinci framework, as analysts may independently produce similar data. Computing infrastructure usages inside the LHCb collaboration could be wasted due to this [87].

The package provides an interface to perform the ETL procedure within the Stripping framework (as part of DaVinci) and Turbo stream [88] (as part of the trigger system) to produce the ROOT data format. The data are processed with the Ganga [89] software interfaced with the Worldwide LHC Computing Grid (WLCG) where computing and storage infrastructures are provided [90].

The author contributed in the development of data processing of the following decay channels [91]:

- $D^{*+} \to D^0(\to K^0_S H^+ H^-)\pi^+$,
- $\overline{B} \to D^0(\to K^0_S H^+ H^-)\mu^- \overline{\nu}_\mu X$,

where H refers to either a kaon or a pion. Only D^0 decays to $K^0_S \pi^+ \pi^-$ final states are used in this thesis.

2.3.3 Analysis dependencies

After the data has been processed and stored in the ROOT file format, the analysis is performed with Python [92] and C++ [93] programming languages depending on tasks and available packages. In general, the tasks that require intensive computational resources are written in C++ while the others are in Python. The package dependencies utilised in this thesis are the following:

- LHCb repositories: BinflipFitter [94], AdetPiPi [95], and GammaCombo [96].
- Analysis framework: Root [83, 84], and RooFit [97]
- Data manipulation: `NumPy` [98], and `Pandas` [99].
- Visualisation: `Matplotlib` [100], and Root [83, 84]
- Statistics and machine learning: `SciPy` [101], `scikit-learn` [102], and `hep-ml` [103].

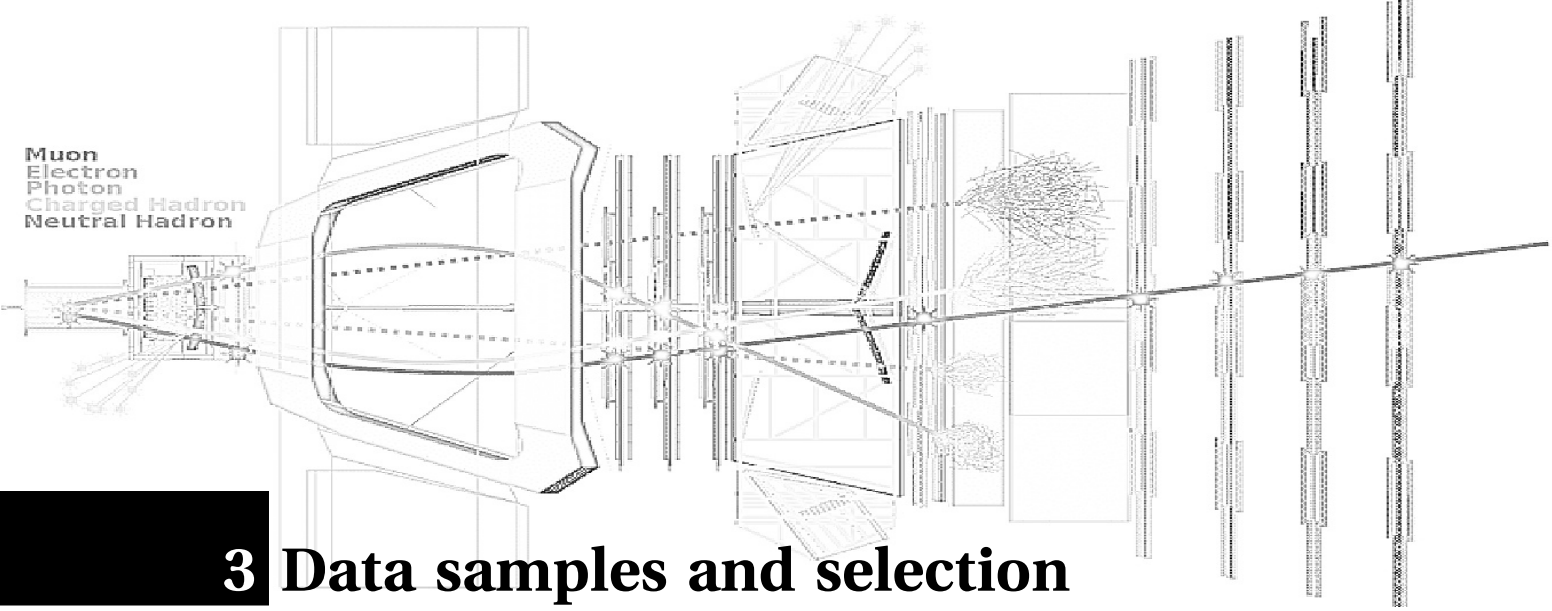

3 Data samples and selection

The analysis is performed using the 5.4 fb^{-1} sample of pp collisions collected by LHCb during 2016–2018. These data correspond to centre-of-mass energy of $\sqrt{s} = 13$ TeV. Note that the 2015 data is not included as there is a different selection on the transverse momentum of the muon. If these data were included, a separate dedicated multivariate analysis (see Section 3.1.2) would be needed. Considering the small sample size and hence limited impact on the measurement, the 2015 data are excluded from the analysis.

This chapter is organised in two parts. The analysis strategy with collision data is summarised in Section 3.1. This part outlines the data cleaning process and signal-to-background ratio optimisation utilising multivariate analysis. Section 3.2 describes the simulated sample generated with a Monte-Carlo technique.

3.1 Analysis of collision data

Data is processed to select and reconstruct events depending on topology, kinematics, and detector response from the LHCb detector as explained in Chapter 2. In general, the procedure consists of the following steps

1. Trigger selection — selection criteria to retain interesting events at trigger level.
2. Stripping selection — set of preselections to match the topology of the studied decay chain.
3. Preprocessing and multivariate analysis — data cleaning and preparation for signal and background event classification with multivariate analysis.
4. Simple rectangular cuts and clone candidate rejection — post-processing to select interest kinematic regions and reject potential copious background.
5. Multi-candidate removed — random selection of one single candidate per event.

To minimize bias on the measurement, the efficiency of each selection is investigated on the simulated sample to check that it does not introduce artificial asymmetry between the two

sides of the Dalitz plot or induce correlation between the Dalitz coordinates and the D^0 decay time.

3.1.1 Trigger, stripping and offline selections

We select exclusively $D^0 \to K^0_S \pi^+\pi^-$ candidates with the topology of a b hadron decaying to $D^0\mu^-\overline{\nu}X$, where X can be any combination of particles. The K^0_S candidates are reconstructed in the $\pi^+\pi^-$ decay mode and categorised as LL or DD, where L (D) refers to a daughter pion reconstructed as a long (downstream) track with (without) hits in the vertex locator. These $\overline{B} \to D^0(\to K^0_S\pi^+\pi^-)\mu^-\overline{\nu}_\mu X$ candidates are reconstructed by the `stripping` line `b2D0MuXK-sPiPi{DD,LL}CharmFromBSemiLine`. The `stripping` selection reconstructs a candidate from the full raw sub-detector data. This line has requirements applied in the offline selection summarised in Table 3.1 and is motivated as follows:

- Minimum p and p_T: reduce combinatorial background which comes from random combinations of tracks.
- Impact parameters: accept a good impact parameter (IP), the distance of closest approach of the track to a reference point. The primary vertex (PV), where the protons collide, is chosen as the reference point.
- Track quality: accept a well-reconstructed track with a good track χ^2/ndf.
- Vertex quality: accept a well-reconstructed vertex from a fit of reconstructed tracks assumed to come from a common vertex.
- Mass region: select a mass region of a set of reconstructed particles to reduce combinatorial bacground. The selection also aims at keeping sideband candidates for the representing background kinematic in multivariate selections. This is related to the ADAMASS variable computed as the absolute difference between the measured mass and the PDG reference value.
- DIRA: restrict the cosine of the angle between the particle's momentum and the vector pointing from the primary vertex to the secondary vertex (DIRA). These two vectors must point in the same direction.
- Ghost probability: avoid selecting a false track which is misrecognised by the tracking algorithm.
- Flight distance: reduce the background from unrelated decays. This is applied on K^0_S to reduce background from $D^0 \to \pi^+\pi^-\pi^+\pi^-$ decays.
- Difference in origin and decay vertices: accept a decay which has a topology pointing toward detector. This is denoted as $\Delta_{\mathrm{Vtx},z}(X)$ for the difference between vertices along the z axis (beam-pipe direction) of a particle X.
- TISTOS triggers: preselect interesting events during the online data aquisition.

Table 3.1 – Stripping selection requirements for $\overline{B} \to D^0(\to K^0_S\pi^+\pi^-)\mu^-\overline{\nu}_\mu X$.

Particle	Variable	Requirement
$\pi^\pm$ of K^0_S	Track χ^2/ndf	< 4
	Momentum	> 2 GeV/c
	IPχ^2 w.r.t. PV	> 4(DD), > 9(LL)
	Track ghost probability	< 0.5 (LL)
	Tranverse momentum	> 250 MeV/c (LL)
K^0_S	ADAMASS	< 64 MeV/c^2(DD), < 35 MeV/c^2(LL)
	Vertex-fit χ^2/ndf	< 6
	cos(DIRA)	> 0.99
	Flight distance χ^2	> 100
	Momentum	> 3000 MeV/c (DD), > 2000 MeV/c (LL)
	Tranverse momentum	> 250 MeV/c
	Vertex fit χ^2/ndf	< 25
$\pi^\pm$ of D^0	Track χ^2/ndf	< 4
	Track ghost probability	< 0.5
	Momentum	> 2 GeV/c
	Transverse momentum	> 250 MeV/c
	IPχ^2 w.r.t. PV	> 4
D^0	$m(K^0_S\pi^+\pi^-)$	$[1.785, 1.945]$ GeV/c^2
	$\sum p_T$	> 1.4 GeV/c
	Transverse momentum	> 2.0 GeV/c
	Vertex-fit χ^2/ndf	< 6.0
	$\Delta_{\mathrm{Vtx},z}(D^0)$	> -10.0 mm
μ^-	Track χ^2/ndf	< 4
	Track ghost probability	< 0.5
	Momentum	> 3 GeV/c
	Transverse momentum	> 800 MeV/c
	IPχ^2 w.r.t. PV	> 4.0
$\overline{B}$	Vertex-fit χ^2/ndf	< 6.0
	Visible mass $D^0\mu^-$	> 2500 MeV/c^2
		< 6000 MeV/c^2
	DIRA	> 0.999
	$m(D^0\mu^-)$	< 6200 MeV/c^2
	$\Delta_{\mathrm{Vtx},z}(D^0)$	> -9999 mm
TisTos	`Hlt1_*Track*Decision_TOS || Hlt2Topo*Decision_TOS` ‖ `Hlt2_*SingleMuon*Decision_TOS || Hlt2Global_TIS`	

Table 3.2 – Trigger lines used to select $\overline{B} \to D^0(\to K_S^0\pi^+\pi^-)\mu^-\overline{\nu}_\mu X$ candidates.

Trigger Level	Trigger line
L0	Mu_L0MuonDecision_TOS
HLT1	Mu_Hlt1TrackMuonDecision_TOS Mu_Hlt1TrackMuonMVADecision_TOS
HLT2	B_TopoMu_(2,3,4)-Body_Decision_TOS

In the TISTOS method candidates are classified depending on their trigger information as Triggered On Signal (TOS), Triggered Independent of Signal (TIS), and Triggered On Both (TOB) [104]. A particle candidate is TOS when it fires a particular trigger line. If the event is still triggered when the candidate is removed, the particle candidate is considered to be TIS for that trigger selection. Events classified as TOB require the candidate and the rest of the event together to be triggered. Neither of the candidate and the rest of the event are classified as TOS nor TIS. The method is implemented together with trigger selections to identify which trigger lines are fired relevent to the signal. It is applied in Tables 3.1 and 3.2.

The online selection requires at least one displaced, high transverse momentum muon at the hardware-trigger level (`Mu_L0Muon_TOS`) At the first stage of software-trigger, the μ track must be selected by the muon tracking algorithm or by a multivariate analysis developed specifically for extracting a well-defined muon track (`Mu_Hlt1TrackMuonDecision_TOS OR Mu_Hlt1TrackMuonMVADecision_TOS`). The topological selection is performed by a multivariate algorithm to distinguish n-body decays of a b hadron, designed for $n = 2, 3$, and 4 [105]. These `HLT2` triggers select a set of tracks which contain at least a muon track (`B_TopoMu_-(2,3,4)-Body_TOS`). This line also requires the $D^0\mu^-$ origin vertex to be consistent with the decay of a b hadron. The candidates are required to have at least one of the `TopoMu` trigger. Events are required to have at least one trigger line fired at each level. The trigger requirements are summarised in Table 3.2.

3.1.2 Background suppression with MVA

The $\overline{B} \to D^0(\to K_S^0\pi^+\pi^-)\mu^-\overline{\nu}_\mu X$ candidates are refitted using `DecayTreeFitter` [106] (DTF). The DTF is a progressive least square fit (Kalman's filter) involving multiple decay vertices. This technique allows to define the kinematics of the particles in the decay chain and determine their correlations in the decay chain.

In this fit, we constrain the K_S^0 mass. The D^0 mass and D^0 decay time are reconstructed using these refitted values from the DTF. The D^0 mass constraint is further added to compute the Dalitz-plot coordinates. The values for the K_S^0 and D^0 mass constraints are taken from the Particle Data Group (PDG) [14]. In both cases, the fit is required to converge. The $D^0\mu^-$ system is required to have an invariant mass less than 4900 MeV/c^2. We select only candidates with a reconstructed D^0 decay time larger than -1 ps. A value of 1 ps corresponds to around 2.5 times the D^0 average lifetime. These selections are summarised in Table 3.3.

Table 3.3 – Preselection applied to $\overline{B} \to D^0(\to K^0_S\pi^+\pi^-)\mu^-\overline{\nu}_\mu X$ candidates before implementing multivariate analysis.

	Cut variable	Accepted region	Description
B	$m(D^0\mu)$	> 2500 MeV/c^2 < 4900 MeV/c^2	Visible mass
	DTFKS VCHI2NDOF	> 0	DTF with K^0_S mass constraint must converge
	DTFD0KS VCHI2NDOF	> 0	DTF with D^0 and K^0_S mass constraints must converge
D^0	Decay time	$> -2.5\tau_{D^0}$	D^0 decay time must be larger than -1 ps.

The $K^0_S\pi^+\pi^-$ invariant mass distribution after preselection is presented in Figure 3.1. We model the invariant mass distribution of the $D^0 \to K^0_S\pi^+\pi^-$ signal using a Johnson S_U function to account for asymmetric tails. The Johnson S_U distribution is defined as [107]

$$\mathscr{J}(x|\mu,\sigma,\delta,\gamma) = \frac{1}{N_{\mathscr{J}}} \frac{e^{-\frac{1}{2}\left[\gamma + \delta \sinh^{-1}\left(\frac{x-\mu}{\sigma}\right)\right]^2}}{\sqrt{1+\left(\frac{x-\mu}{\sigma}\right)^2}}, \tag{3.1}$$

where δ and γ are tail parameters, while μ is the mean of the distribution, σ expresses the dispersion of the core, and $N_{\mathscr{J}}$ is a normalization. The combinatorial background distribution is modelled with a first-order Chebyshev polynomial. The fit results are displayed in Figure 3.1. A pull plot, which defined as the difference between the data and the fit model normalised by data uncertainty, is also shown.

The sample is contaminated with combinatorial background which is further suppressed using a multivariate analysis (MVA). The signal distributions of the variables used in the MVA are extracted through the sPlot technique [108] following a fit to the D^0 invariant mass distribution of Figure 3.1. In this technique, a distribution of interest is extracted by considering 2 sets

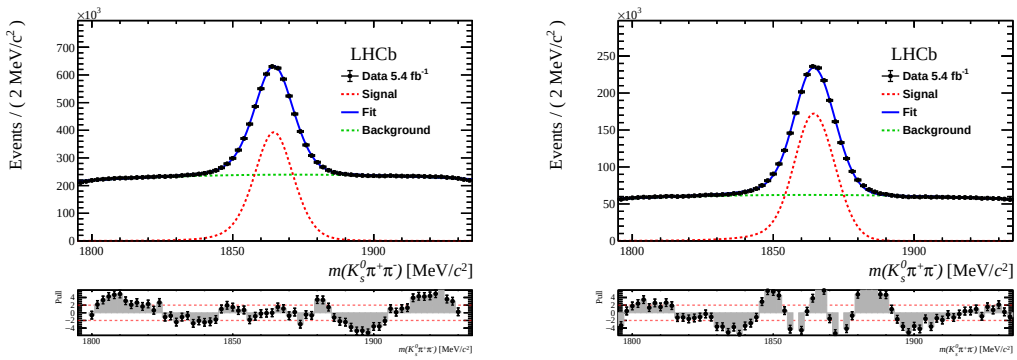

Figure 3.1 – $K^0_S\pi^+\pi^-$ invariant mass distributions before applying the multivariate selection, shown separatly for DD (left) and LL (right), with fit results superimposed.

of variables: discriminating variables and control variables. A discriminating variable is a variable for which the distributions of all the sources of events are known while a control variable is a variable for which the distributions of some sources of events are unknown. This technique performs a maximum likelihood fit with the aim to obtain the signal distribution of a control variable independently of the known properties of the control variable itself. The technique uses fitting parameters in the signal distribution as the discriminating variables to compute a correlation between signal and background in the merged distribution. As such, a metric, so-called `sWeight`, is computed. This weight represent how likely the event comes from the signal distribution.

Table 3.4 – Discriminating variables used in the multivariate analysis.

Particle	Variable	Description
B	DTFKS_VCHI2NDOF	χ^2 of the DTF vertex fit per degree of freedom.
	B_MCORR	Corrected B mass $m_{\text{corr}} = \sqrt{m^2(D^0\mu^-) + p_\perp^2(D^0\mu^-)} + p_\perp(D^0\mu^-)$ where $m(D^0\mu^-)$ and $p_\perp(D^0\mu^-)$ are the invariant mass and transverse momentum of the $D^0\mu^-$ system.
	log(acos(B_DIRA))	log(acos(DIRA)) where DIRA is the cosine of the angle between the particle's momentum and the vector pointing from the primary vertex and the secondary vertex.
	log(B_IPCHI2)	$\log(\chi^2_{\text{IP}})$ where χ^2_{IP} is the χ^2 difference between the primary vertex fits when the B candidate is added and excluded from the fit.
	log(B_FD)	log(FD) where FD is the B flight distance.
	log(B_FDCHI2)	$\log(\chi^2_{\text{FD}})$ where χ^2_{FD} is a quality of above flight distance divided by its uncertainty.
	log(B_ENDVTX_CHI2/B_ENDVTX_NDOF)	$\log(\chi^2_{\text{DV}}/\text{ndof})$ where χ^2_{DV} is the χ^2 of the B decay vertex.
	log(B_PVTX_CHI2)	$\log(\chi^2_{\text{PV}})$ where χ^2_{PV} is the χ^2 of the B origin vertex.
μ	D0_PT	Transverse momentum
D^0	mu_PT	Transverse momentum

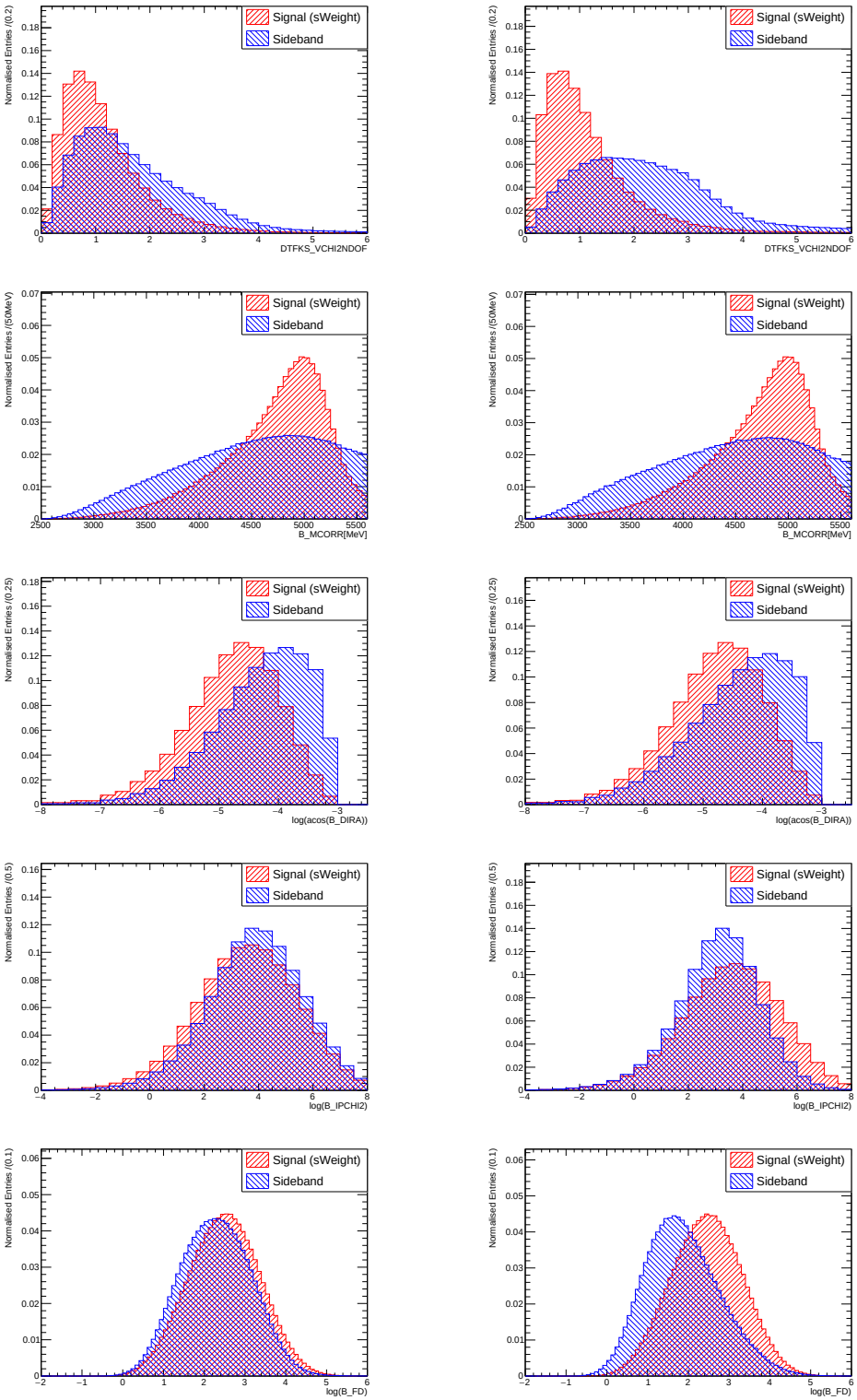

Figure 3.2 – Distributions of the MVA variables from the training samples of signal (red) and background (blue) for events reconstructed with different K_S^0 types, DD (left) and LL (right).

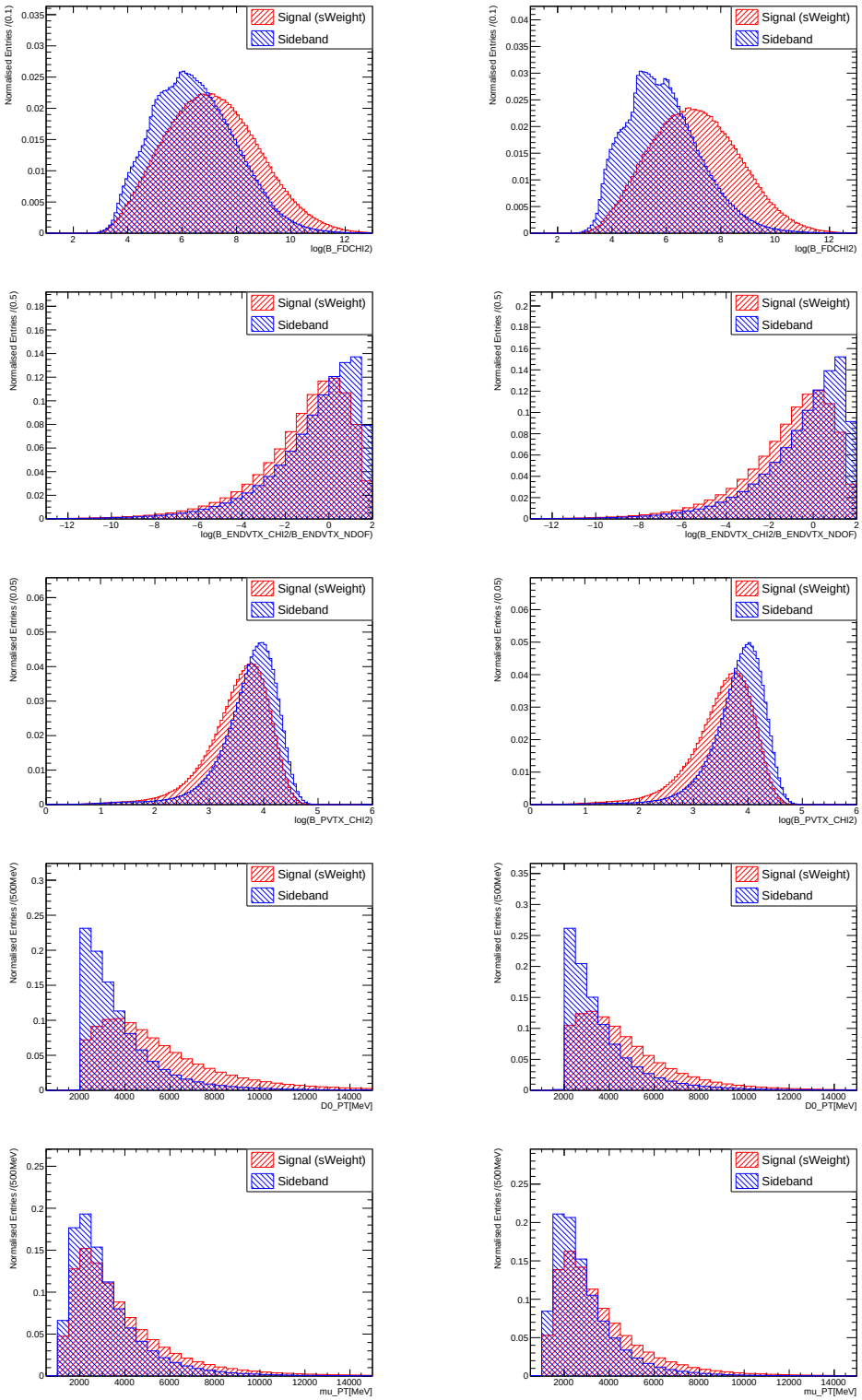

Figure 3.3 – Distributions of the MVA variables from the training samples of signal (red) and background (blue) for events reconstructed with different K_S^0 types, DD (left) and LL (right).

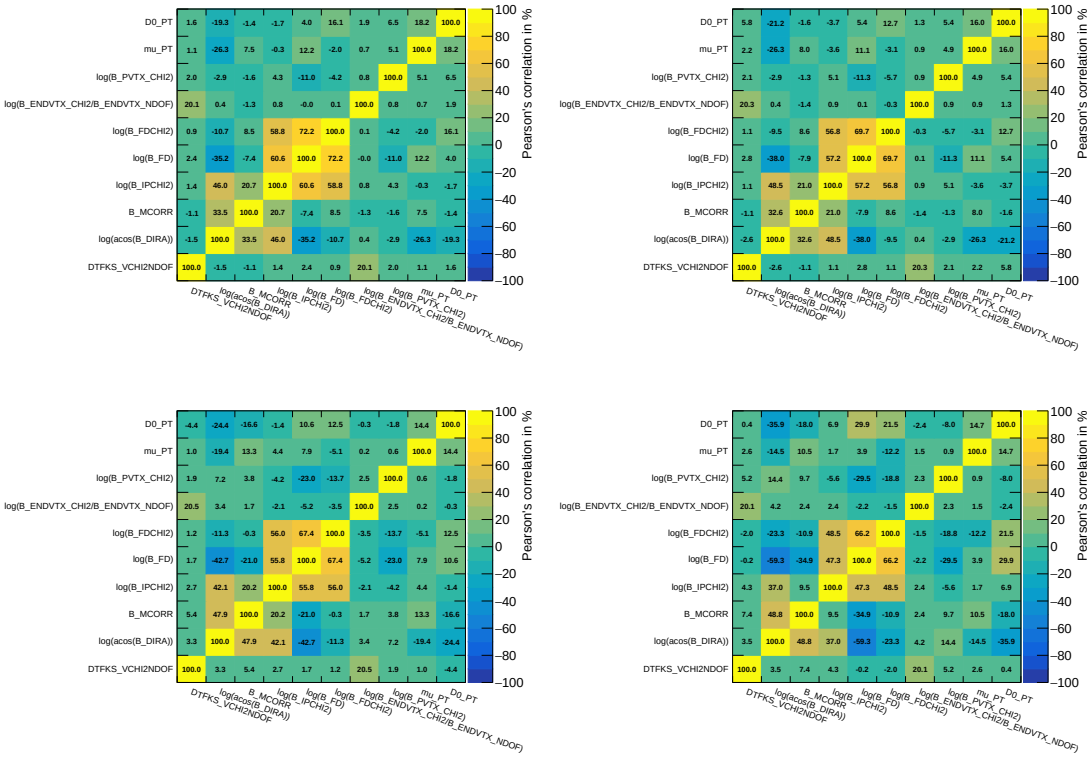

Figure 3.4 – Correlation between variables implemented in the MVA for signal (Top) background (bottom) and separately for K_S^0 type DD (left) LL (Right).

The multivariate analysis is implemented to reduce combinatorial background contamination in the data sample. Topological and kinematic variables are employed, including vertex qualities, b-hadron flight distance, the D^0 and μ^- transverse momenta as explained in Table 3.4. Some of these variables are modified with natural logarithm ($\log_e$ expressed as only log). The distributions of these variables are shown in Figures 3.2 and 3.3 for background-subtracted (`sWeighted`) signal and background from the invariant mass sideband defined as $m_{D^0} \in [1805, 1820] \cup [1910, 1925]$ MeV/c^2. The Pearson correlation coefficients are presented in Figure 3.4. To assess the effect of the correlations, we decorrelate these variables with a Principle Component Analysis (PCA). The performance of the uncorrelated version is not different from that of the correlated one. We thus conclude that the correlations are not degrading the performance of the MVA and hence do not apply the decorrelation procedure. In addition, these correlations are not significantly different between data-taking years.

A decision-tree classifier is implemented to distinguish between signal and background. However, the classifier alone randomly defines rules on each variable without considering how much weight should be put on each test node. To enhance this weak classifier, a gradient boosting algorithm is used. This algorithm considers remaining errors of the classifier and builds a second classifier such as to minimize the error [109]. A drawback of this technique

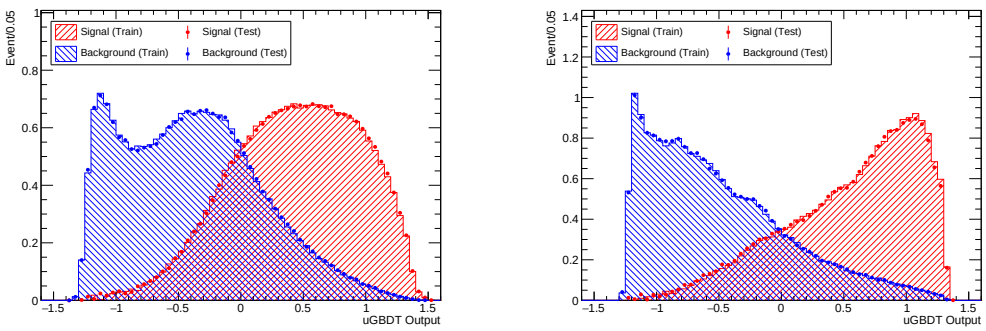

Figure 3.5 – Distributions of the BDT output variable from the training (hatched histograms) and testing (points with error bars) samples of signal (red) and background (blue) for events reconstructed with different K_S^0 types, DD (left) and LL (right).

may be undesired correlations between variables. For example, the output from this boosted decision tree (BDT) may be correlated with the D^0 decay time or the Dalitz-plot coordinates. This is expected to be under control by adding uniform regularisation to the tree model. This regularisation prevents the BDT prediction to be correlated with the D^0 decay time or the Dalitz-plot coordinates. This is known as the uBoost algorithm, which is implemented using the *hep_ml* package [110].

The combined data is divided randomly into 6 subsamples for cross validation in the MVA training process. This procedure controls the overtraining of the MVA model. The MVA is trained on each subsample, and the MVA hyperparameters are tuned such that the 6 MVA classifiers have the same distribution (according to a Kolmogorov test). Then the MVA trained on the first sample is applied it to the other 5 subsamples. Figure 3.5 presents the distributions of the BDT output variable. These distributions for signal and background are well separated and show no sign of overtraining.

The relevance parameter, which shows how much each MVA variable contributes to the classifier, is presented in Table 3.5 for DD and LL samples. It is defined as the normalised total reduction of the loss function brought by that feature. It is also known as the Gini importance or mean decrease in impurity [111]. Roughly speaking, the relevance of each variable is defined as a relative of how the sample can be split by the decision tree considering that variable comparing with the rest. It can be seen that `B_MCORR` has the best discriminating power.

The performance of the BDT can be quantified by using the area under Receiver Operating Characteristic (ROC) curve or AUROC. This is a relation between true positive (signal efficiency) and false positive (background efficiency). Then we test our classifier by excluding variables with the smallest relevance, *i.e.* the flight distance (`log(B_FD)`) and the B decay vertex quality (`log(B_ENDVTX_CHI2/B_ENDVTX_NDOF)`). We compare the AUROCs in 4 cases: default, default without `log(B_FD)`, default without `log(B_ENDVTX_CHI2/B_ENDVTX_NDOF)`,

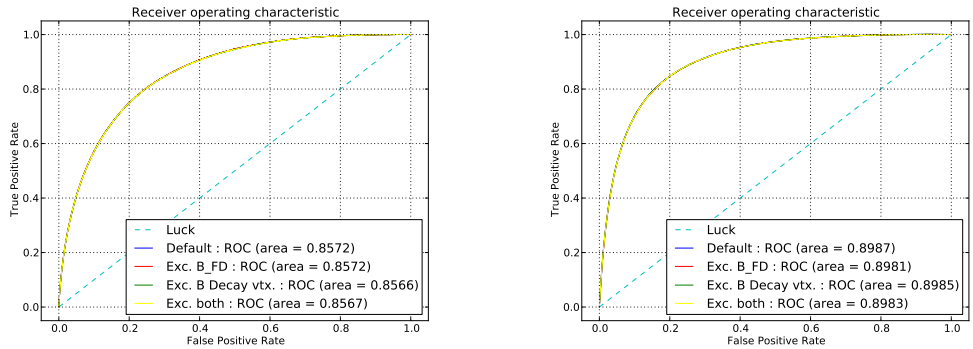

Figure 3.6 – Comparison of Receiver Operating Characteristic (ROC) curves for different MVA variable sets with different K_S^0 types, DD (left) and LL (right). The areas under the ROC curves (AUROC) are reported in the legends.

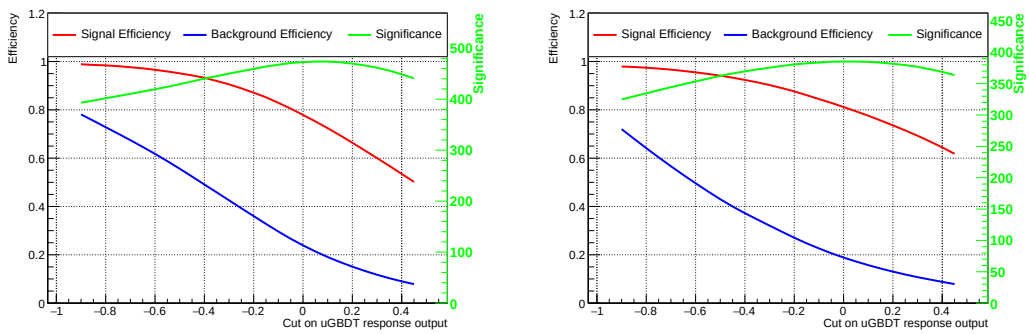

Figure 3.7 – Significance (green line), signal efficiency (red line) and, background efficiency (blue line) as a function of the BDT output requirement shown separately for DD (left) and LL (right). These plots show only 1/6 of all data.

and default without both variables. The ROC curves are shown in Figure 3.6 separately for the two K_S^0 types. Excluding `log(B_ENDVTX_CHI2/B_ENDVTX_NDOF)` leads to a slight degradation of the BDT performance in the DD sample. A similar effect can be seen in the LL sample if `log(B_FD)` is excluded. For simplicity, we decide to keep both variables in the MVA training.

The requirement on the BDT variable is optimised using the signal significance, defined as $S/\sqrt{S+B}$ where S and B are the numbers of signal and background events in the whole D^0 mass region.

These numbers are obtained from binned maximum likelihood fits of the D^0 mass distribution. The optimal point is computed in each subsample and for each BDT. The optimal BDT requirements are found to be around 0.1 for both types of K_S^0, as shown in Figure 3.7. The mass distribution of $K_S^0\pi^+\pi^-$ after the BDT requirement is shown in Figure 3.8. For simplicity, the optimal cut is chosen at this point and applied to the whole sample.

Table 3.5 – Average relative contribution of the discriminating variables in the classifier trained with the DD and LL samples.

Variable	Relevance [%]	
	DD	LL
B_MCORR	31.4	30.1
D0_PT	18.5	10.8
DTFKS_VCHI2NDOF	13.8	24.5
log(B_PVTX_CHI2)	11.7	10.7
log(B_FDCHI2)	6.1	10.3
log(acos(B_DIRA))	5.9	0.9
log(B_IPCHI2)	5.7	1.4
mu_PT	3.5	7.7
log(B_ENDVTX_CHI2/B_ENDVTX_NDOF)	2.7	0.3
log(B_FD)	0.6	3.2

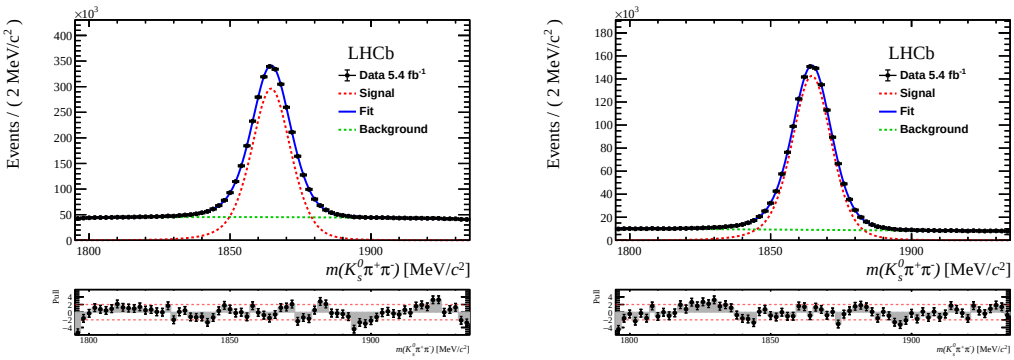

Figure 3.8 – $K^0_S\pi^+\pi^-$ invariant mass distribution after BDT selection at the optimal point shown separately for DD (left) and LL (right).

3.1.3 Additional selection

We apply some additional selection after the MVA. Only candidates with positive D^0 decay times are retained. In case of multiple candidates in an event, only one candidate is chosen randomly after clone tracks have been removed. Two tracks in the same event are considered to be clones (*i.e.* a copy of each other) if they satisfy one of the following two criteria:

$$\text{Clone type I}: \quad |t_{x1} - t_{x2}| < 0.0004 \quad \text{and} \quad |t_{y1} - t_{y2}| < 0.0002 \tag{3.2}$$

$$\text{Clone type II}: \quad |t_{x1} - t_{x2}| < 0.0005 \quad \text{and} \quad |t_{y1} - t_{y2}| < 0.0005 \tag{3.3}$$

$$\text{and} \quad |q_1/p_1 - q_1/p_2| < 10^{-6}$$

where t_{xi}, t_{yi} are the slopes in the xz and xy planes, q_i is the electric charge (± 1), and p_i is the reconstructed momentum of track i [112]. This clone removal does not affect the efficiency as a function of the helicity angle studied in Chapter 4. The DD (LL) sample contains around

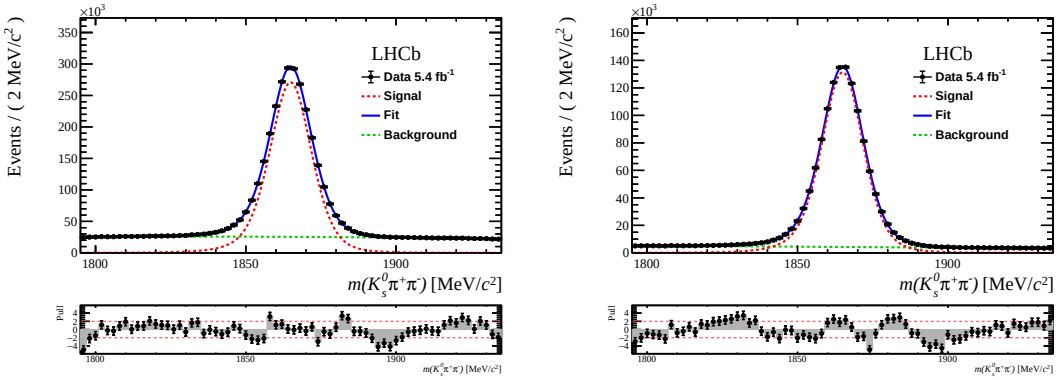

Figure 3.9 – $K^0_S\pi^+\pi^-$ invariant mass distribution of the DD (left) and LL (right) candidates after all selection requirements. The curves show the results of a fit with signal (red) and combinatorial background (green) components.

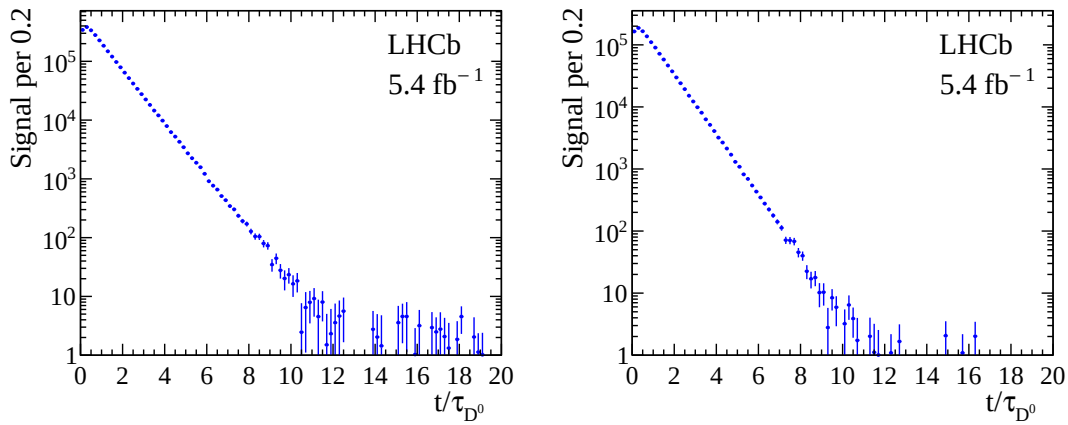

Figure 3.10 – D^0 decay time distribution of the DD (left) and LL (right) candidates after all selection requirements and background subtraction using `sWeight`.

4.6% (3.5%) of multiple candidates in which 2% (3%) contain clone tracks.

Figure 3.9 shows the $D^0 \to K^0_S\pi^+\pi^-$ invariant mass distribution after applying the full selection. The sample contains approximately 3.7 million candidates, of which 2.5 (1.2) millions are of the DD (LL) type. The signal-to-background ratio is significantly improved with respect to Figure 3.1.

The D^0 decay time and Dalitz-plot distributions are shown in Figures 3.10 and 3.11, after background subtraction with the `sWeights` from the fit of Figure 3.9.

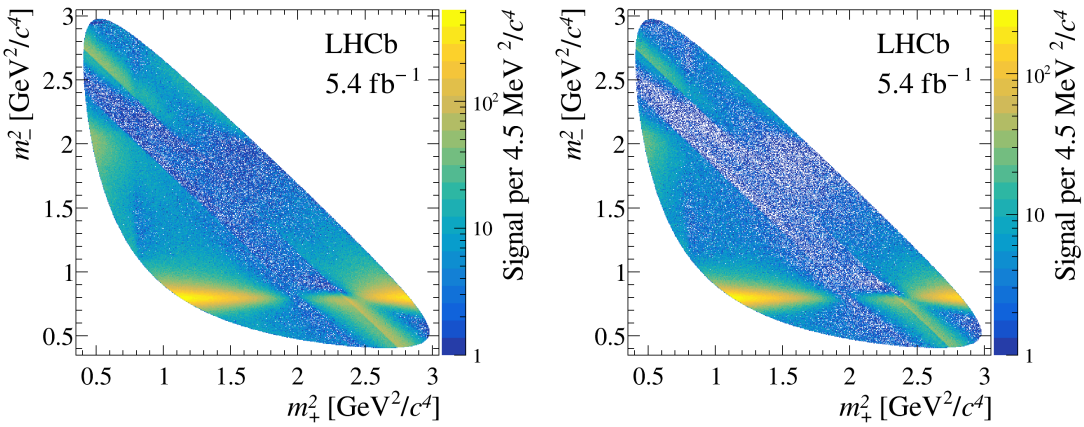

Figure 3.11 – $D^0 \to K_S^0\pi^+\pi^-$ Dalitz plot of the DD (left) and LL (right) candidates after all selection requirements and background subtraction using `sWeight`.

3.2 Simulated samples

Experiments in particle physics require statistical modelling to study the physical processes occurring in collisions and the interactions of the final-state particles in the detector. Monte Carlo simulation (MC) is a repeated random sampling to examine a process with a deterministic pattern. This is implemented to predict distributions of the processes of interest.

In this analysis, MC samples provide expected distributions of the $\overline{B} \to D^0(\to K_S^0\pi^+\pi^-)\mu^-\overline{\nu}_\mu X$ decay. The objectives of using simulated samples are to model reconstruction efficiencies, as a function of Dalitz plot coordinates and decay time. This part is explained in Chapter 4, including the decorrelation process of Section 4.4. The MC efficiency maps are ingredients for generating pseudoexperiments to validate the analysis and study systematic uncertainties as detailed in Chapter 6. Since this analysis relies mainly on data-driven modelling, we only use the MC samples which are available for the inclusive $B^- \to D^0(\to K_S^0\pi^+\pi^-)\mu^-\overline{\nu}_\mu X$ decay, where X is any combination of particles.

The samples are produced centrally within the LHCb collaboration using LHCb software. The production line is coordinated as follows:

1. pp collisions are generated with the PYTHIA 8 generator [113] with a specific LHCb configuration [114]. Hadronisation and fragmentation processes are also included in the generation. Only events with a B^- produced within 400 mrad of the z axis are kept.
2. The B^- decay chain is controlled by EVTGEN [115]. In particular, this analysis uses only a phase-space model for the $D^0 \to K_S^0\pi^+\pi^-$ decay. This means that the production is uniform over the $\left(m^2\left(K_S^0\pi^+\right), m^2\left(K_S^0\pi^-\right)\right)$ Dalitz plane.
3. During the decay of a b hadron to charged particles, energy may be released via a photon. This process is generated by the PHOTOS package [116].

4. The interaction of the particles in the detector material is simulated with GEANT4 [117, 118].
5. To produce an event in the same format as the raw data from a real collision, the detector response is digitized by BOOLE [119].
6. In simulation, the performance of the tracking system is overestimated. In particular, the charged track momentum resolution is better than in collision data. This is corrected by momentum smearing to weight the simulated sample in agreement with the collision data.
7. To ensure that the simulated sample contains only signal candidates, each reconstructed particle in the decay chain is associated with the corresponding true particle of the true decay chain (truth-matching).

After the generation, the MC samples are processed as in the same way as collision data, including the selection of candidates explained in this chapter. We present the number of MC candidates passing each step of the selection in Table 3.6.

Table 3.6 – Number of candidates retained in the $\overline{B} \to D^0(\to K_S^0\pi^+\pi^-)\mu^-\overline{\nu}_\mu X$ MC samples at each step of the selection.

	2016		2017		2018	
Selection	DD	LL	DD	LL	DD	LL
Stripping	2081732	843973	2992666	1181819	2974806	1401227
Truth-matching	1720498	711749	2462368	994762	2452904	1146224
Trigger selection	1111276	451450	1619849	646666	1605725	749865
Preselection	1081414	439183	1583213	631608	1432127	554352
MVA selection	904506	376228	1318320	539495	1193599	473778
Positive lifetime	831740	348818	1211093	499964	1096544	439177
Signal candidates	829527	348772	1207045	499889	1092786	439112

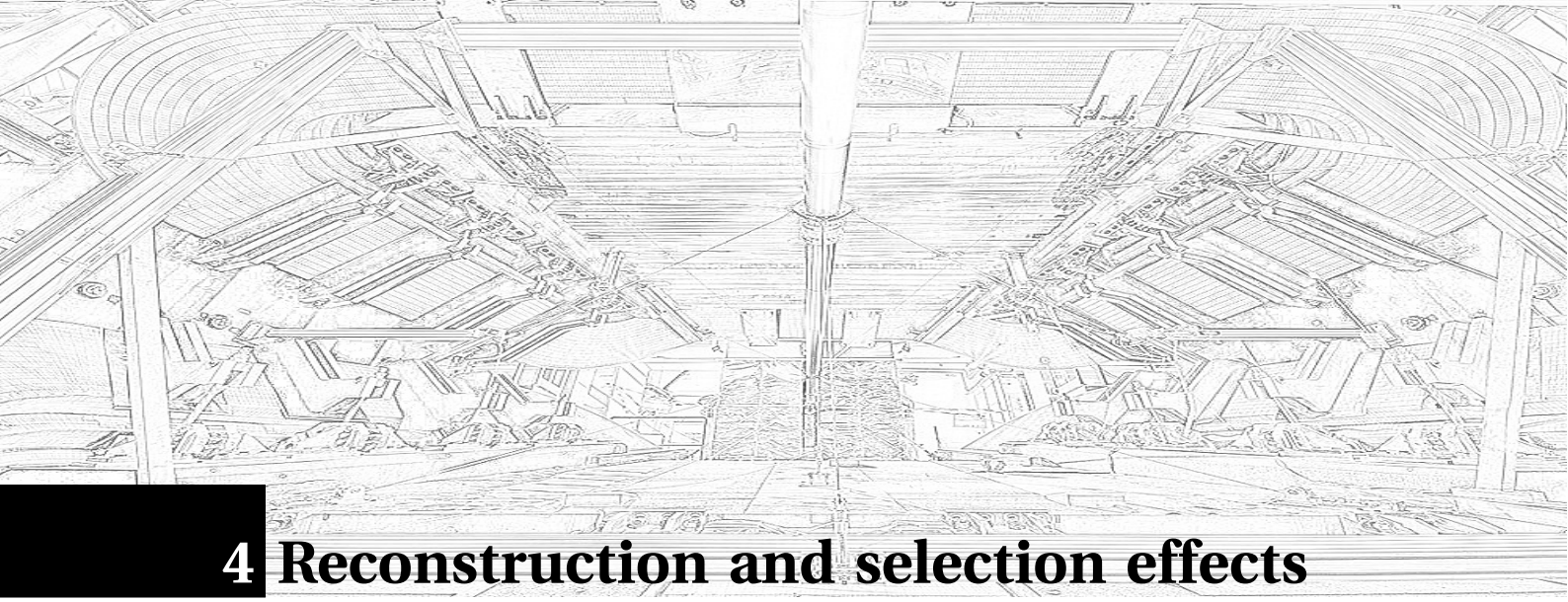

4 Reconstruction and selection effects

In this chapter, the precision and performance of the reconstruction and selection on parameters of interest are discussed. These effects can degrade the basic assumption of the analysis method and may lead to unwanted biases.

We study the reconstruction efficiency as a function of the Dalitz plot coordinates and of the D^0 decay time. Resolution studies of these coordinates are also included. The bin-flip method is designed such that the efficiency effects between two symmetric bins of the Dalitz plot with respect to the diagonal is suppressed in the ratio. However, efficiency variations in each Dalitz bin may result in degraded sensitivity. To minimise efficiency effects, we apply corrections to the data as explained in this Chapter. The corrections also quantify the experimental effects and will be used as ingredients for generating pseudoexperiments (toys) data. Such data is essential for the estimation of the systematic uncertainties in Chapter 6.

The DD and LL samples have significantly different efficiencies as a function of the Dalitz plot and of the D^0 decay time. These efficiencies are therefore modelled separately. This chapter is organised in 3 subsections. The resolutions on the Dalitz coordinates and D^0 decay time are modelled in Section 4.1. The efficiencies are studied in Sections 4.2 and 4.3. While a correlation between the Dalitz coordinates and the D^0 decay time is not expected in this analysis, a potential bias may be caused by such correlation as shown in Section 6.3. The source of this correlation as well as a decorrelation procedure on the data sample are studied and presented in Section 4.4.

4.1 Resolution on decay time and Dalitz-plot coordinates

Resolution effects on Dalitz plot coordinates and D^0 decay time may cause the migration of an event from one bin to another. This possibly induces a small bias on the measurements. In the Run 1 analysis [63], this effect was found to be negligible as the resolution is smaller than the bin width.

We determine the resolutions with MC samples. The resolution is defined as the width of the

distribution of the difference between a reconstructed quantity and its generated value. As the resolution will be implemented in toy generation, we implement a fit of the resolution on the Dalitz coordinates and D^0 decay time distribution. The resolution is modelled with a combination of Johnson S_U and Gaussian distributions. The Johnson S_U function is defined in Equation (3.1). The Gaussian distribution is allowed to have a different mean $\mu + \Delta\mu$. The total probability distribution as a function of a variable x is then

$$\wp_{\text{sig}}(x) = f_1 \mathscr{J}(x|\mu,\sigma,\delta,\gamma) + (1-f_1)\mathscr{G}(x|\mu+\Delta\mu,\sigma_g)\,. \tag{4.1}$$

The results of the fits are presented in Table 4.1 and Figures 4.1 and 4.2, separately for D^0 decay time resolution, Dalitz positive $\left(m^2\left(K_S^0\pi^+\right)\right)$ and negative $\left(m^2\left(K_S^0\pi^-\right)\right)$ coordinates and K_S^0 DD and K_S^0 LL types. These PDFs will be used to simulate pseudoexperiments (toys). There is also a similar effect from the K_S^0 mass constraint which induces an anti-correlation between the resolutions of the two Dalitz plot coordinates. In the $B^- \to D^0(\to K_S^0\pi^+\pi^-)\mu^-\overline{\nu}_\mu X$ simulation, this is found to be -0.66 (-0.59) for the DD (LL) case as presented in Figure 4.3, which is consistent with the Run 1 analysis [63].

Table 4.1 – Resolution fit parameters for the D^0 decay time resolution (in units of the average D^0 lifetime), and the two Dalitz coordinates. Note that $\Delta\mu$, μ, and σ have units of GeV^2/c^4 for $m^2\left(K_S^0\pi^+\right)$ and $m^2\left(K_S^0\pi^-\right)$. Others are dimensionless.

	Parameter	D^0 decay time	$m^2\left(K_S^0\pi^+\right)\left[\text{GeV}^2/c^4\right]$	$m^2\left(K_S^0\pi^-\right)\left[\text{GeV}^2/c^4\right]$
DD	f_1	0.959 ± 0.004	0.730 ± 0.005	0.722 ± 0.005
	$\Delta\mu$	-0.027 ± 0.002	0.00059 ± 0.00004	0.00061 ± 0.00004
	σ_g	0.062 ± 0.002	0.00635 ± 0.00002	0.00639 ± 0.00002
	δ	1.131 ± 0.004	0.889 ± 0.005	0.886 ± 0.005
	γ	0.133 ± 0.002	0.103 ± 0.002	0.105 ± 0.002
	μ	0.0108 ± 0.0005	0.00016 ± 0.00001	0.00017 ± 0.00001
	σ	0.180 ± 0.001	0.00418 ± 0.00003	0.00415 ± 0.00003
LL	f_1	0.982 ± 0.004	0.655 ± 0.006	0.650 ± 0.006
	$\Delta\mu$	-0.021 ± 0.004	0.00035 ± 0.00004	0.00021 ± 0.00004
	σ_g	0.046 ± 0.005	0.00477 ± 0.00002	0.00484 ± 0.00002
	δ	1.309 ± 0.006	0.796 ± 0.006	0.789 ± 0.006
	γ	0.110 ± 0.004	0.134 ± 0.003	0.136 ± 0.003
	μ	0.0071 ± 0.0007	0.00012 ± 0.00001	0.00016 ± 0.00001
	σ	0.195 ± 0.002	0.00276 ± 0.00003	0.00271 ± 0.00003

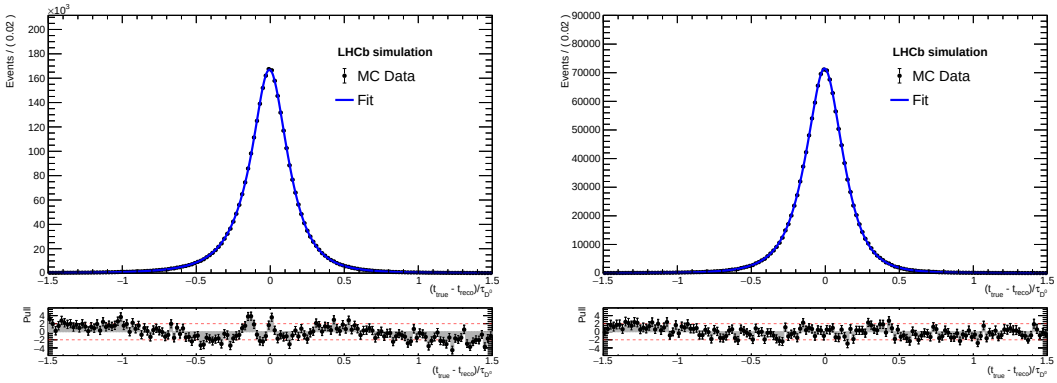

Figure 4.1 – Distribution of the difference between the reconstructed and true D^0 decay time (in units of the average D^0 lifetime) in a simulated sample where the K_S^0 candidates are reconstructed in the DD (left) and LL (right) category. The fitted resolution function is shown.

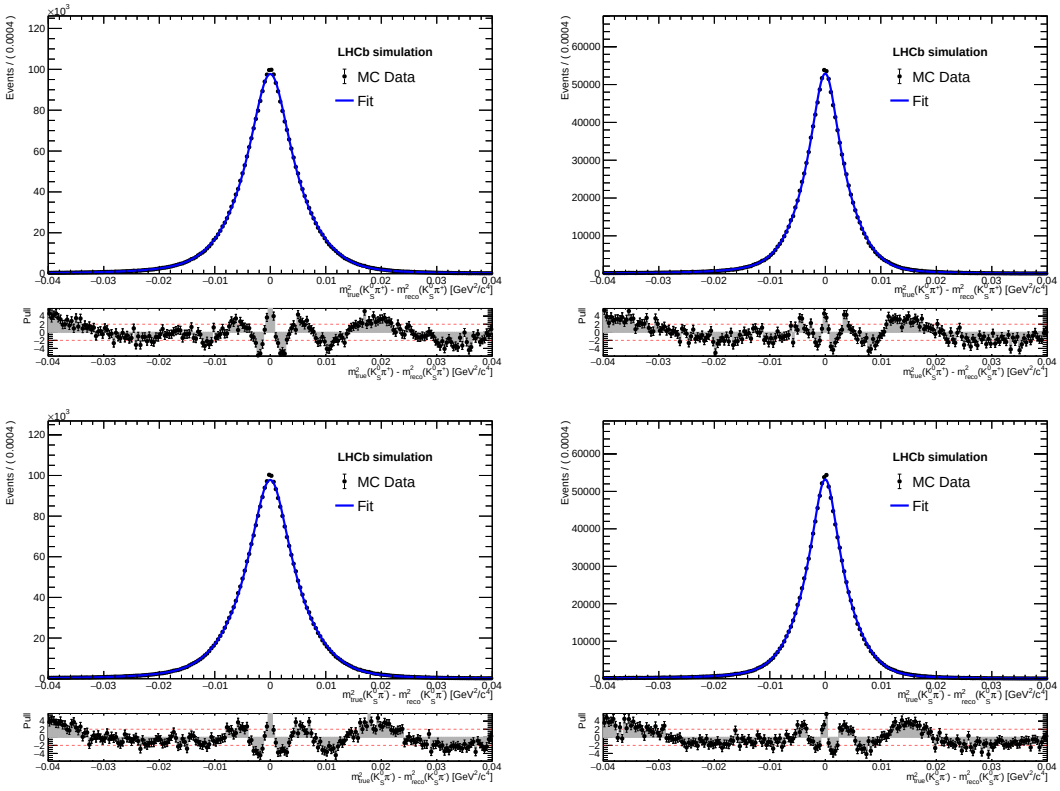

Figure 4.2 – Distribution of the difference between the reconstructed and true Dalitz plot coordinate $m^2\left(K_S^0\pi^+\right)$ (top) and $m^2\left(K_S^0\pi^-\right)$ (bottom), in a simulated sample where the K_S^0 candidates are reconstructed in the DD (left) and LL (right) category and positive (top), negative (bottom). The fitted resolution function is shown.

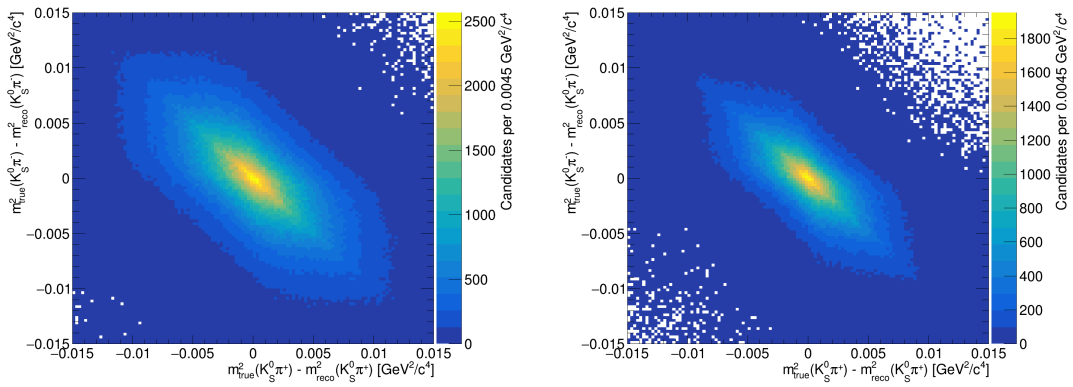

Figure 4.3 – Two-dimensional distribution of the differences between the reconstructed and true Dalitz plot coordinates in a simulated sample where the K^0_S candidates are reconstructed in the DD (left) and LL (right) category.

4.2 Efficiency as a function of decay time

The distribution of the true D^0 decay time is expected to be an exponential function. In experiment, the distribution is affected by the precision of the detector, such that each measured value is Gaussian distributed. The probability density function (PDF) of the distribution of the reconstructed D^0 decay time is expected to be that exponential function convoluted with the resolution function of Figure 4.1. The reconstruction efficiency as a function of D^0 decay time is called here the decay-time acceptance. This efficiency is estimated as the ratio between the reconstructed distribution and the expected one. This can be determined with two different approaches: a toy-data driven method and a MC modelling method.

4.2.1 Toy-data model

The toy-data driven method compares the reconstructed, background-subtracted (with sWeights) D^0 decay-time distribution to the exponential distribution convolved with the resolution. We generate a pseudo-experiment (toy) sample according to the Belle amplitude model [61]. The D^0 decay time distribution in this toy is fitted with exponential distribution. Then, this distribution is convolved with the decay time resolution as explained in Section 4.1 to model an expected decay time distribution with the detector effect.

The decay-time acceptance is formed as the ratio between the sWeighted collision data and the exponential distribution convolved with the resolution. Locally weighted scatterplot smoothing (LOWESS) regression is implemented on the resulting histogram to obtain a smooth parametrisation. LOWESS is a non-parametric regression method which smoothes a distribution by combining multiple regression models [120]. Each value of the LOWESS function y_k at point x_k is obtained using weighted least squares of its neighbour points (x_i, y_i). The weight for (x_i, y_i) is inversely proportional to the distance between that point and (x_k, y_k).

Figure 4.4 presents the decay-time acceptance obtained from this method for 2016 data-taking year. The other data-taking years are presented in Appendix A.1. The degraded efficiency at low decay times is mostly caused by the displacement requirements on the D^0 final state particles. Since the decay-time acceptance is symmetric with respect to the Dalitz-plot bisector, we expect that its effect will almost completely cancel in the bin-flip approach of forming the ratio between signal yields in symmetric Dalitz-plot bins. The effect is therefore neglected in the analysis and a systematic uncertainty is assigned in Section 6.3.

The efficiency at high D^0 decay time is larger in the DD sample because of the reconstruction of the downstream track. As the K_S^0 meson has an average $c\tau$ around 26 mm which is more than half of the radius of the VELO sub-detector, the K_S^0 daughters tend to be reconstructed outside the VELO. They are more likely to be reconstructed as downstream tracks. Therefore the efficiency drop at large D^0 decay times is less pronounced in the DD case than in the LL case.

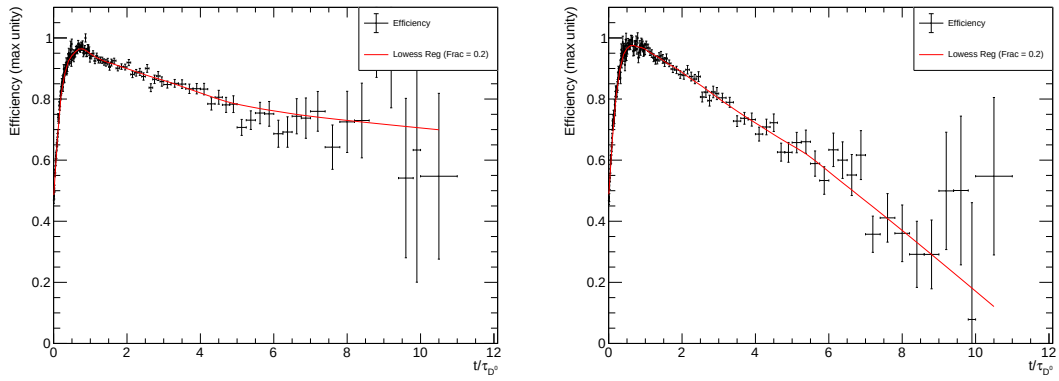

Figure 4.4 – D^0 decay time acceptance in the $\overline{B} \to D^0(\to K_S^0\pi^+\pi^-)\mu^-\overline{\nu}_\mu X$ sample obtained by forming the ratio between the observed D^0 decay-time distribution (`sWeight`) and an exponential function fitted from toy data shown separately for the DD (left) and LL (right) cases and for data taken in 2016. The raw ratios (black points) are smoothed with the LOWESS algorithm (red curves).

4.2.2 MC model

To validate the decay time acceptance, another method is performed. The simulated samples described in Section 3.2 can be used to model the decay-time acceptance function. The expected decay time distribution ($\theta(t-t_0)$) is an exponential with the known D^0 lifetime convolved with the resolution function obtained in Section 4.1. It is affected by an acceptance function ($\epsilon(t)$) and can be parametrised as

$$f(t) = \theta(t-t_0)\epsilon(t) \tag{4.2}$$

$$\epsilon(t) = \left(\frac{(t-t_0)^n}{(1+a(t-t_0)^n)}\right)e^{\beta t} \tag{4.3}$$

where t_0 is fixed at -0.3 like in the Run 1 analysis [63] as it indicates the shift to the negative D^0 decay time due to the resolution. The other parameters, a, n, and β, are extracted from a fit. We present the fit to $f(t)$ with a corresponded decay-time acceptance (ϵ(t)) for 2016 data-taking year as an example in Figure 4.5. The acceptances for other data-taking years are presented in Appendix A.1.

4.2.3 Comparison

A comparison of the decay-time acceptance obtained from these two methods is shown in Figure 4.6 where all the data-taking years are combined. The MC and toy-data models provide consistent results at D^0 low decay time. At high decay time, the toy-data model tends to decline faster than the MC model. As the toy-data model relies on the yield of observed signal in data, the uncertainties of this efficiency increases, and the method is unreliable at high decay-time as seen in Figure 4.4.

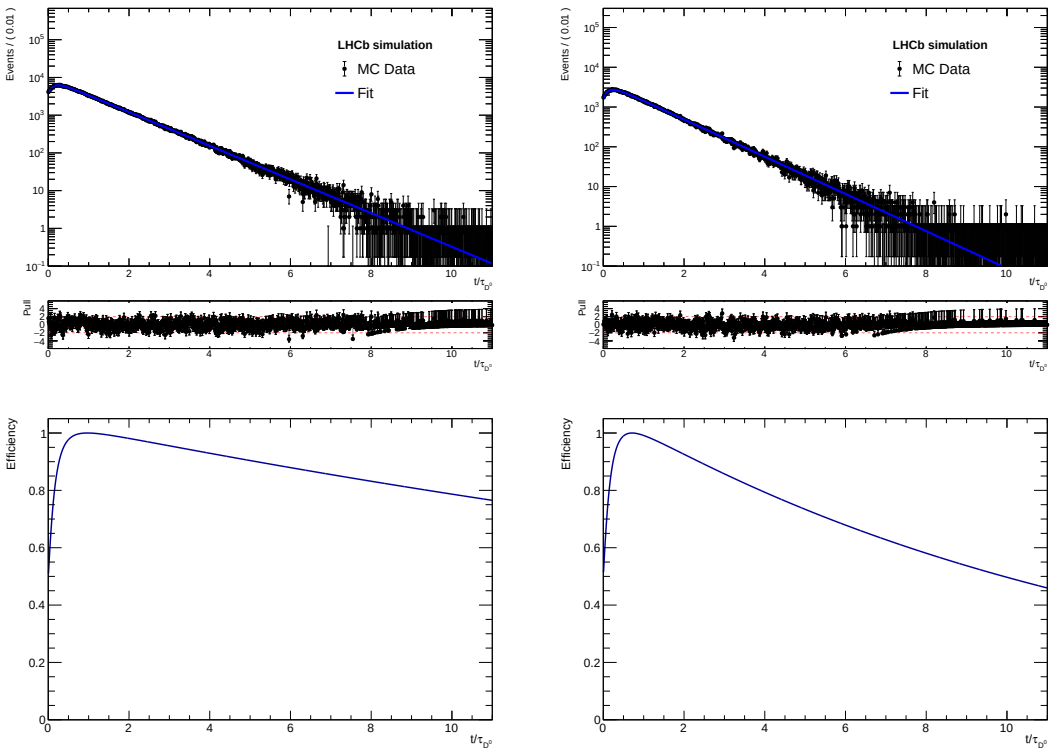

Figure 4.5 – Reconstructed D^0 decay time distribution in a simulated sample of $\overline{B} \to D^0(\to K^0_S\pi^+\pi^-)\mu^-\overline{\nu}_\mu X$ decays for the year 2016 with fit superimposed (top) and corresponding acceptance function (bottom), for K^0_S reconstructed in the DD (left) and LL (right) categories.

To further check the origin of this discrepancy, we utilise the reweighted MC as studied in the amplitude analysis of the same decay (see Section 6.2 of Ref. [6] and Ref. [62] for more details). The D^0 decay time acceptance is derived from this reweighted sample using the MC method described above. The result is also shown in Figure 4.6. The agreement with the toy-data model is improved by the weights, though it is still unsatisfactory at high decay times. We further study the stability of the analysis using different decay time acceptances to correct the data in Chapter 6.

By construction of the bin-flip method, the efficiency is cancelled in the ratio and it does not affect significantly the measurement. This is studied further on toys in Section 6.3, where we test the effects of using different efficiency functions. Therefore, the discrepancies between the methods and the choice of a particular model carry negligible effects on the final result. We opt for using the MC model in the toy generation to estimate systematics.

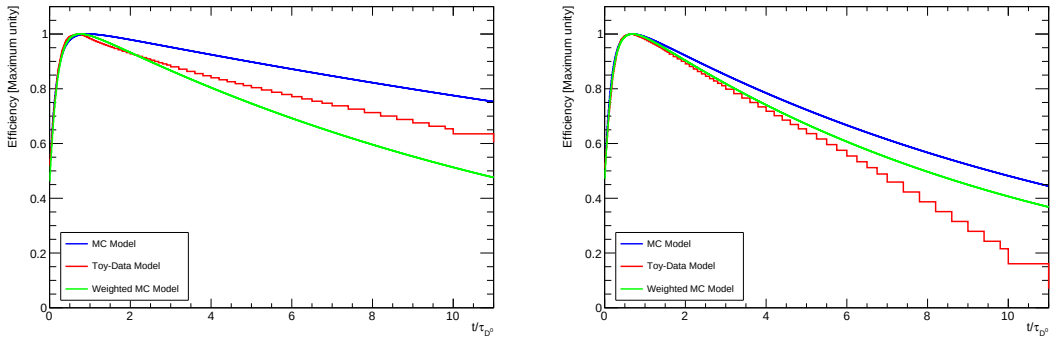

Figure 4.6 – D^0 decay time acceptance functions obtained from the MC model (solid blue curve), toy-data model smoothed with LOWESS (solid red curve), and the weighted MC model (solid green curve) for K_S^0 reconstructed in the DD (left) and LL (right) categories.

4.3 Efficiency variation over the Dalitz plot

To a good extent, the effects from efficiency variation over the Dalitz plane cancel in forming the ratio of yields in kinematically identical regions of phase space. However it is important that the efficiency variation does not significantly change the average strong-interaction phases, for which external measurements are used. The variation in each Dalitz bin may result in bias toward the measurements. Here, we model the reconstruction efficiency over the Dalitz phase space which will be used to correct for the effect and estimate systematic uncertainties in Chapter 6.

The efficiency is determined using the simulated $\overline{B} \to D^0(\to K_S^0\pi^+\pi^-)\mu^-\overline{\nu}_\mu X$ sample as a function of the so-called squared Dalitz plot coordinates defined as the square of the invariant mass of the two daughter pions from the D^0 decay, $m^2(\pi^+\pi^-)$ and the cosine of the helicity angle of these pions, $\cos\theta_{\pi^+\pi^-}$, defined as an angle between a momentum vector of $\pi^+\pi^-$ in D^0 rest frame and a momentum vector of a D^0 daughter pion in $\pi^+\pi^-$ rest frame.

In the simulation, the generated D^0 decays are uniformly distributed in Dalitz phase space $\left(m^2\left(K_S^0\pi^+\right), m^2\left(K_S^0\pi^-\right)\right)$, and therefore not in squared Dalitz phase space $(m^2(\pi^+\pi^-), \cos\theta_{\pi^+\pi^-})$. In order to represent the original distribution of $(m^2(\pi^+\pi^-), \cos\theta_{\pi^+\pi^-})$, which is needed as the dominator of the efficiency, an independent fast simulation is run.

The efficiency is parametrised as a two-dimensional polynomial

$$\begin{aligned}\epsilon(m^2(\pi^+\pi^-), \cos\theta_{\pi^+\pi^-}) = {} & q_0 \cdot m^4(\pi^+\pi^-) + q_1 \cdot m^2(\pi^+\pi^-) \\ & + q_2 \cdot m^2(\pi^+\pi^-)\cos^2\theta_{\pi^+\pi^-} + q_3 \cdot \cos^2\theta_{\pi^+\pi^-} + q_4 \\ & + q_5 \cdot \cos\theta_{\pi^+\pi^-} + q_6 \cdot \cos\theta_{\pi^+\pi^-} m^2(\pi^+\pi^-),\end{aligned} \tag{4.4}$$

where the terms with coefficients q_5 and q_6 represent a reconstruction asymmetry between the two pions. Equation (4.4) is fitted on the simulated data. The fit parameters are shown

Table 4.2 – Parameters of the Dalitz plot acceptance function of Equation (4.4), as determined from fits to simulated $\overline{B} \to D^0(\to K^0_S \pi^+\pi^-)\mu^-\overline{\nu}_\mu X$. The values of the parameters q_0, q_1, q_2, q_3, and q_4 do not change when q_5 and q_6 are fixed to zero.

	Parameter	2016	2017	2018
DD	q_0	-0.051 ± 0.005	-0.042 ± 0.004	-0.045 ± 0.004
	q_1	0.169 ± 0.009	0.156 ± 0.007	0.163 ± 0.007
	q_2	0.156 ± 0.007	0.155 ± 0.006	0.157 ± 0.006
	q_3	-0.187 ± 0.006	-0.179 ± 0.005	-0.179 ± 0.005
	q_4	0.777 ± 0.004	0.765 ± 0.003	0.762 ± 0.003
	q_5	0.009 ± 0.003	0.004 ± 0.003	0.001 ± 0.003
	q_6	-0.007 ± 0.004	-0.004 ± 0.003	-0.001 ± 0.003
LL	q_0	0.050 ± 0.006	0.061 ± 0.005	0.056 ± 0.005
	q_1	0.016 ± 0.011	0.003 ± 0.010	-0.003 ± 0.010
	q_2	0.171 ± 0.009	0.174 ± 0.008	0.180 ± 0.008
	q_3	-0.222 ± 0.008	-0.228 ± 0.007	-0.227 ± 0.007
	q_4	0.680 ± 0.005	0.694 ± 0.004	0.661 ± 0.004
	q_5	0.003 ± 0.004	0.001 ± 0.003	0.000 ± 0.003
	q_6	-0.000 ± 0.005	-0.003 ± 0.004	0.003 ± 0.004

in Table 4.2 for each data-taking year, assuming a symmetric efficiency between the two pions ($q_5 = q_6 = 0$). Figure 4.7 show an example fit function of the 2016 data-taking year as well as the corresponding pull plots. For the 2017 and 2018 data-taking years, they are presented in Appendix A.2 These show that in Equation (4.4) is a good parametrisation of the Dalitz efficiency. The simulated samples are also fit without constraining q_5 and q_6 to test for reconstruction asymmetry effects. These coefficients are compatible with zero as shown in Table 4.2. Figure 4.8 shows a combined Dalitz efficiency without asymmetric terms. This is used for toy generation. A separated test with the asymmetric terms is also generated to study a bias in Section 6.4.

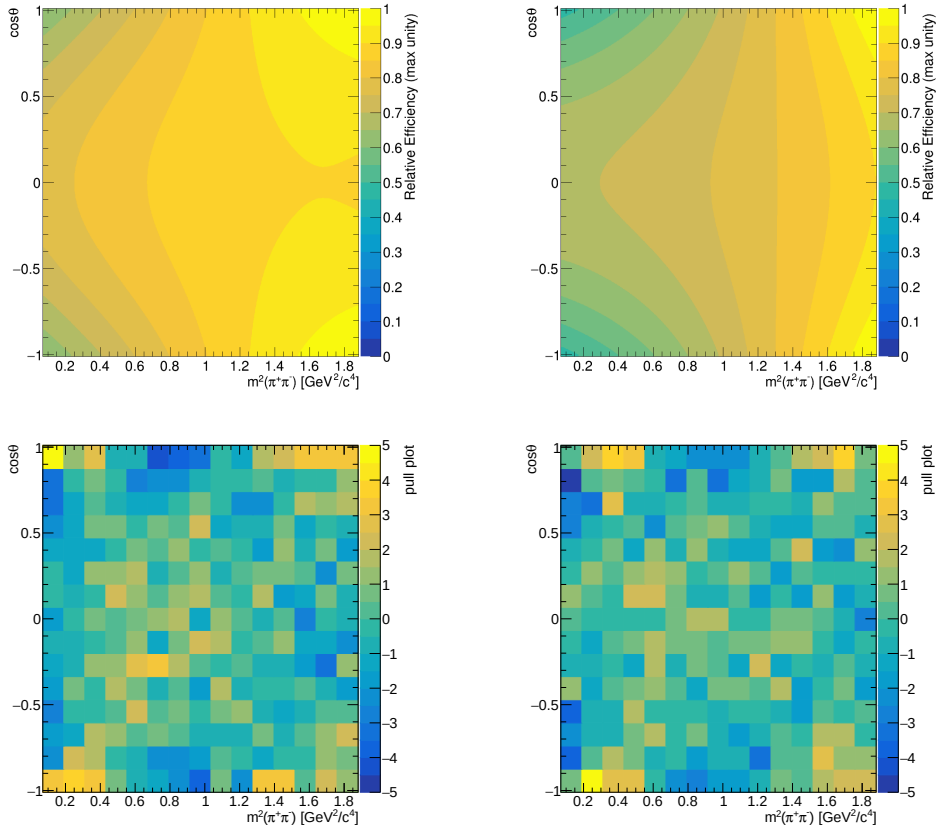

Figure 4.7 – (Top) Efficiency function of Equation (4.4) in the plane $(m^2(\pi^+\pi^-), \cos\theta_{\pi^+\pi^-})$ for the parameters of Table 4.2 year 2016 (with $q_5 = q_6 = 0$), separately for reconstructed K_S^0 in the DD (left) and LL (right) categories. (Bottom) Corresponding pull plots with respect to the simulated sample for the 2016 data-taking year.

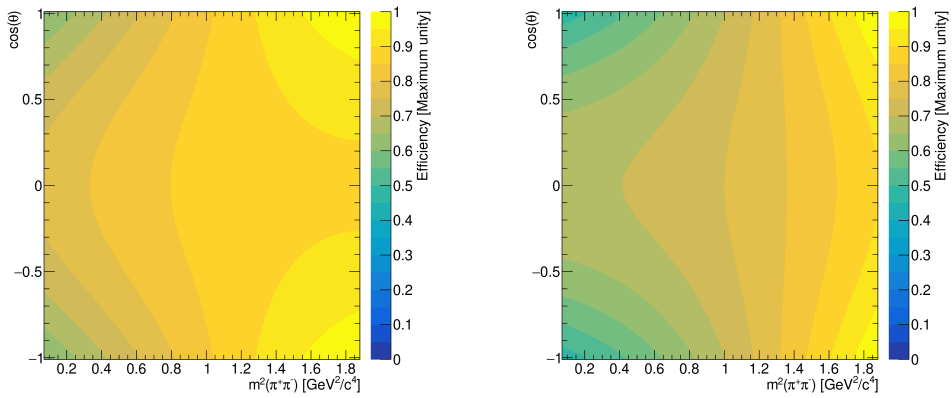

Figure 4.8 – Weighted average of Dalitz acceptances in the simulated $\overline{B} \to D^0(\to K_S^0\pi^+\pi^-)\mu^-\overline{\nu}_\mu X$ sample from Figures 4.7, A.4 and A.5, shown separately for the K_S^0 reconstructed in the DD (left) and LL (right) categories.

4.4 Correlations between the D^0 decay time and Dalitz coordinates

4.4.1 Correlation induced by topological trigger lines

An important assumption of the analysis method is that there are no experimentally-induced correlations between the decay time and the Dalitz-plot coordinates, such that it is possible to integrate separately over the Dalitz bins (to obtain the decay-time-independent coefficients r_b and X_b) and in bins of decay time. An experimentally-induced correlation can mimic the correlation from the mixing effect. This introduces a bias on the measured parameters as shown later in Section 6.3.

The Run 1 analysis however shows correlations for the prompt sample [63]. While the Run 1 analysis did not find significant correlations in the semileptonic sample, they are revealed in this analysis thanks to higher statistics and higher signal-to-background ratio. Here, we notice that the topological trigger `HLT2TopoMu` causes the correlations both in data and simulation.

Note that, due to the known small values of the mixing parameters [57] and the $D^0 \to K^0_S\pi^+\pi^-$ amplitude model [61], the correlation presented in the $m^2(\pi^+\pi^-)$ and D^0 decay time caused by the mixing effect is negligible at the current sample size. This was also the case in the analysis of the $D^{*+} \to D^0(\to K^0_S\pi^+\pi^-)\pi^+$ sample [63]. Therefore, the correlation observed in this section is induced by instrumental effects only.

<u>Data</u>

To identify the source of the induced correlation, we examine both data and simulation in normalised yields as a function of Dalitz phase space and D^0 decay time. Data are analysed similar to what is explained in Chapter 3 but using different trigger combinations. In that Chapter, the `HLT2TopoMu` 2, 3, and 4 body decay triggers are used simultaneously (see Table 3.2). We separate here the `HLT2TopoMu` triggers to check how severe a correlation is caused by any individual trigger.

The topological HLT2 trigger lines require that 2, 3 or 4 tracks form a single displaced vertex. In the case of $\overline{B} \to D^0(\to K^0_S\pi^+\pi^-)\mu^-\overline{\nu}_\mu X$, one of the tracks is required to be a muon, the others must come from the D^0 decay. Hence, the selection favours configurations where the D^0 decays close to the b-hadron vertex, *i.e.* the efficiency is larger at low decay time and decreases at high decay time. Other potential hazard is the MVA selection. However this selection does not introduce further correlation between variables. It even reduces this correlation slightly.

This correlation can be observed in 1D relation between normalised signal yields in each Dalitz bin as a function of D^0 decay time bin as shown in Figure 4.9. If there is no correlation between these variables, the normalised yields in each phase space bin should be equal. However, it is not the case when one can notice the variation of the yields in one bin of Dalitz as a function of the D^0 decay time. Figures 4.10 and 4.11 present the correlation in $(m^2(\pi^+\pi^-), t/\tau_{D^0})$ and $(|\cos\theta_{\pi^+\pi^-}|, t/\tau_{D^0})$, respectively. This correlation can induce a large bias in the measurement

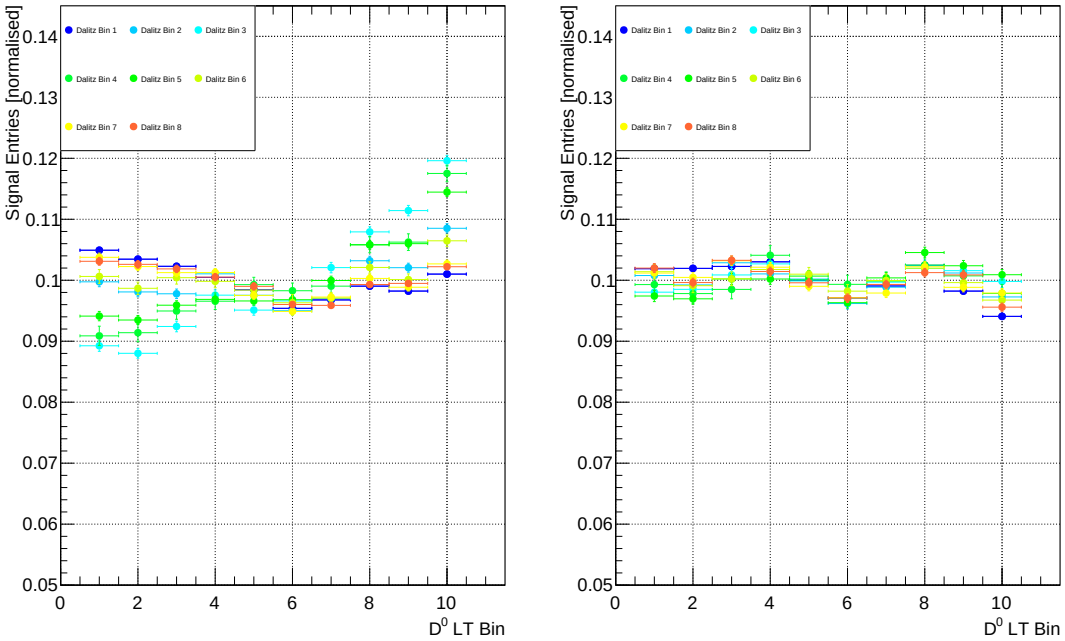

Figure 4.9 – Signal yields of the collision data in each Dalitz bin as a function of the D^0 decay time bin, separately for reconstructed K_S^0 in the DD (left) and LL (right) categories.

of the charm-mixing parameters as studied in the Run 1 analysis [63] and needs to be corrected for.

Figure 4.12 presents the correlations in $(m^2(\pi^+\pi^-), t/\tau_{D^0})$ phase space when the `HLT2TopoMu2` line is fired independently of other `HLT2TopoMu`, likes *i.e.* `(L0Muon && HLT1Track(Muon || MuonMVA ) && HLT2TopoMu2)`. It shows the signal yields normalised to all events in each $m^2(\pi^+\pi^-)$ bin as a function of D^0 decay time bins. Figure 4.13 presents the similar effect but the phase space is binned according to the CLEO Dalitz binning scheme. A similar effect is also observed when we study on `HLT2TopoMu3` and `HLT2TopoMu4` as shown in Figures 4.14–4.17.

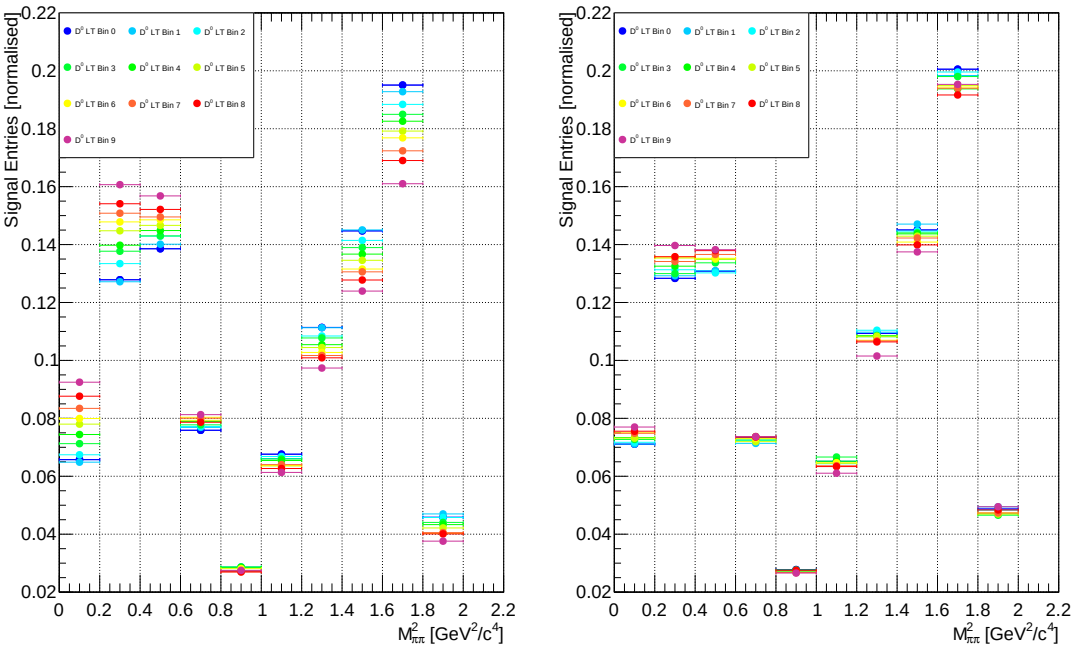

Figure 4.10 – Signal yields of the collision data in each D^0 decay time bin as a function of $m^2(\pi^+\pi^-)$, separately for reconstructed K^0_S in the DD (left) and LL (right) categories.

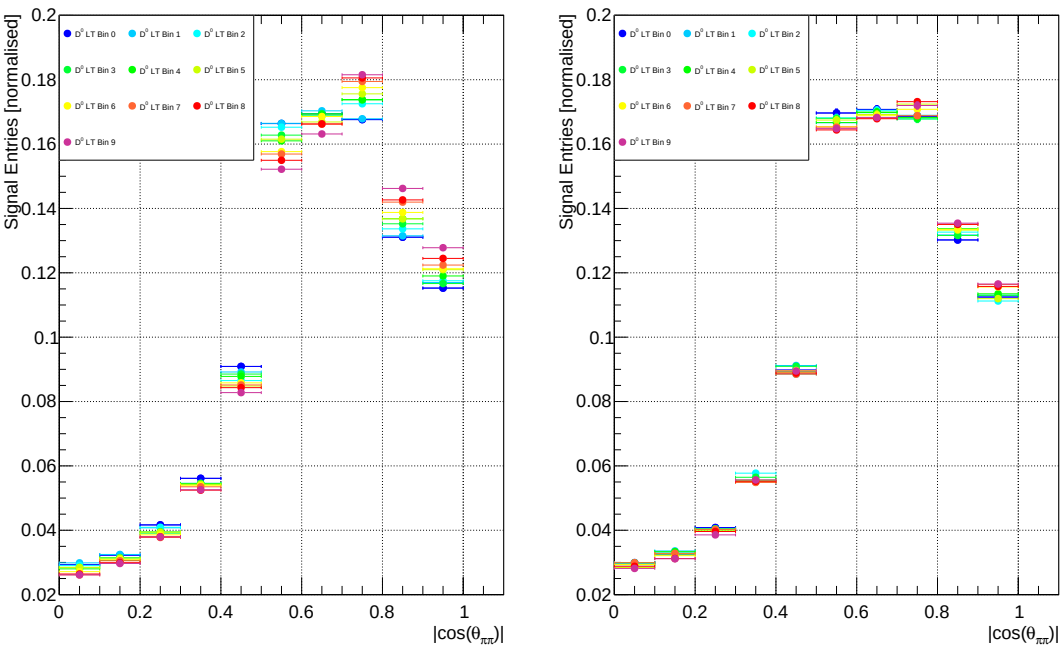

Figure 4.11 – Signal yields of the collision data in each D^0 decay time bin as a function of $|\cos\theta_{\pi^+\pi^-}|$, separately for reconstructed K^0_S in the DD (left) and LL (right) categories.

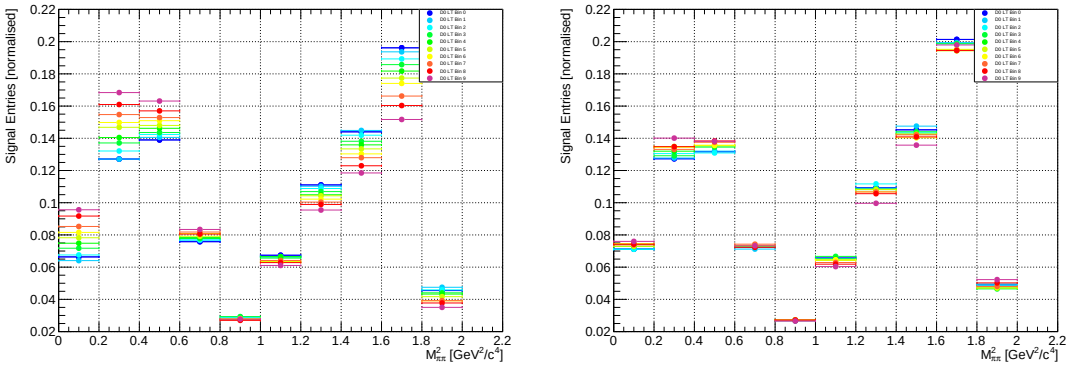

Figure 4.12 – Signal yields in each D^0 decay time as a function of $m^2(\pi^+\pi^-)$ bin when the trigger line HLT2TopoMu2 is fired, separately for reconstructed K^0_S in the DD (left) and LL (right) categories.

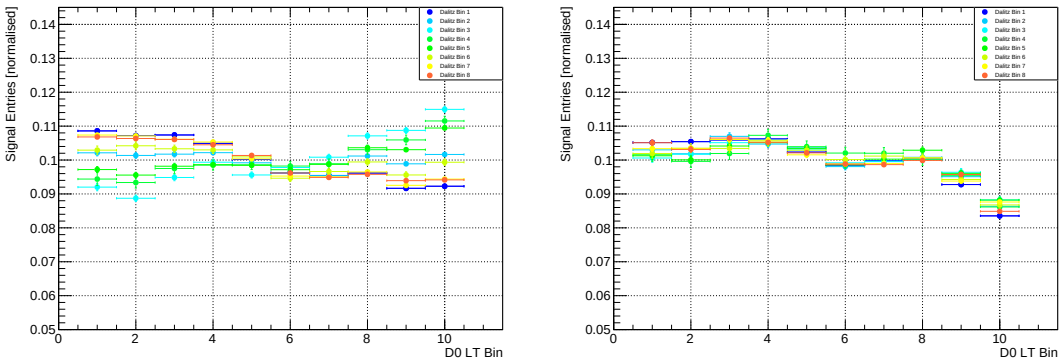

Figure 4.13 – Signal yields in each Dalitz bin as a function of D^0 decay time bin when the trigger line HLT2TopoMu2 is fired, separately for reconstructed K^0_S in the DD (left) and LL (right) categories.

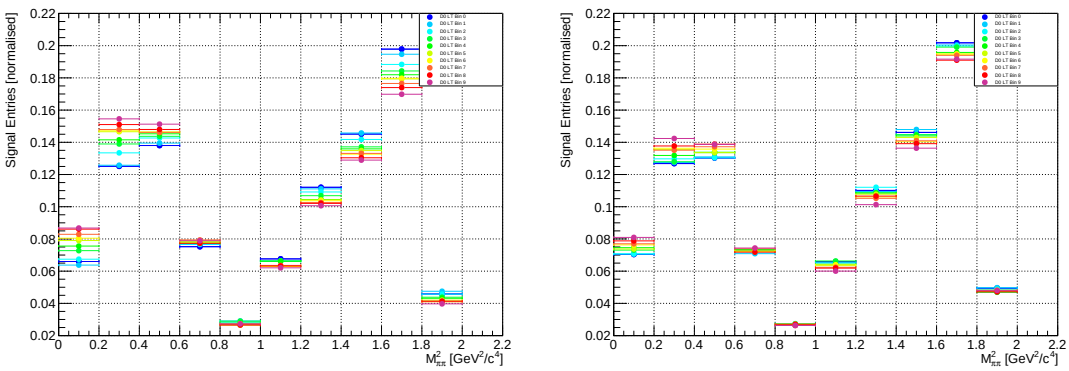

Figure 4.14 – Signal yields in each D^0 decay time as a function of $m^2(\pi^+\pi^-)$ bin when the trigger line HLT2TopoMu3 is fired, separately for reconstructed K^0_S in the DD (left) and LL (right) categories.

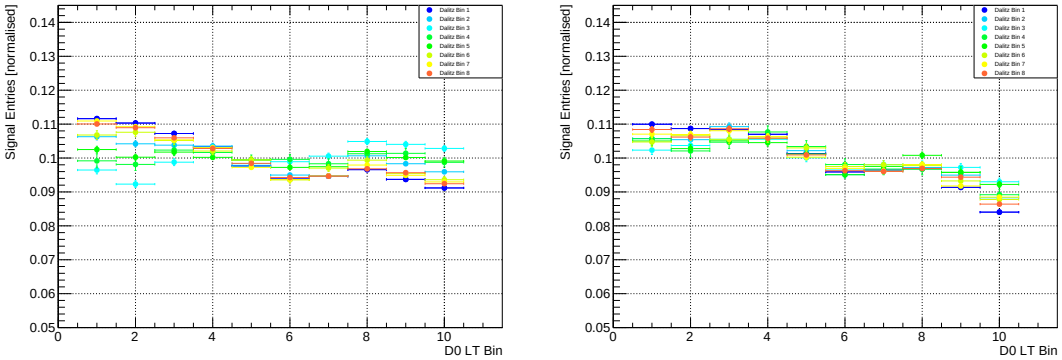

Figure 4.15 – Signal yields in each Dalitz bin as a function of D^0 decay time bin when the trigger line `HLT2TopoMu3` is fired, separately for reconstructed K_S^0 in the DD (left) and LL (right) categories.

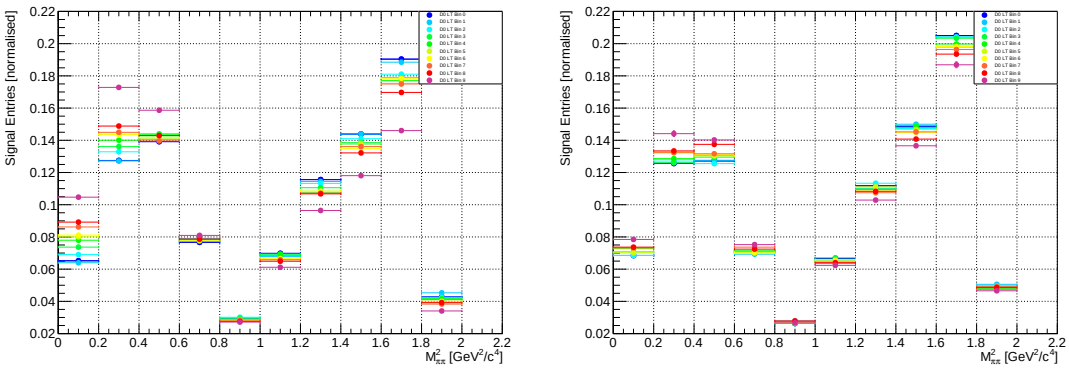

Figure 4.16 – Signal yields in each D^0 decay time as a function of $m^2(\pi^+\pi^-)$ bin when the trigger line `HLT2TopoMu4` is fired, separately for reconstructed K_S^0 in the DD (left) and LL (right) categories.

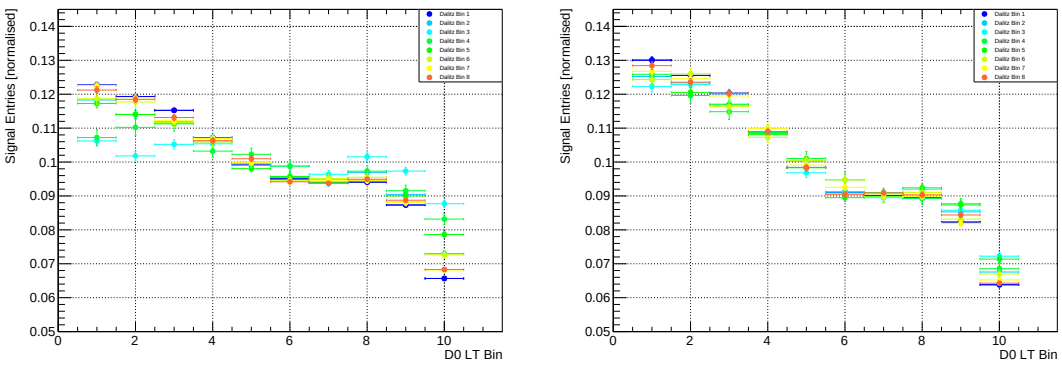

Figure 4.17 – Signal yields in each Dalitz bin as a function of D^0 decay time bin when the trigger line `HLT2TopoMu4` is fired, separately for reconstructed K_S^0 in the DD (left) and LL (right) categories.

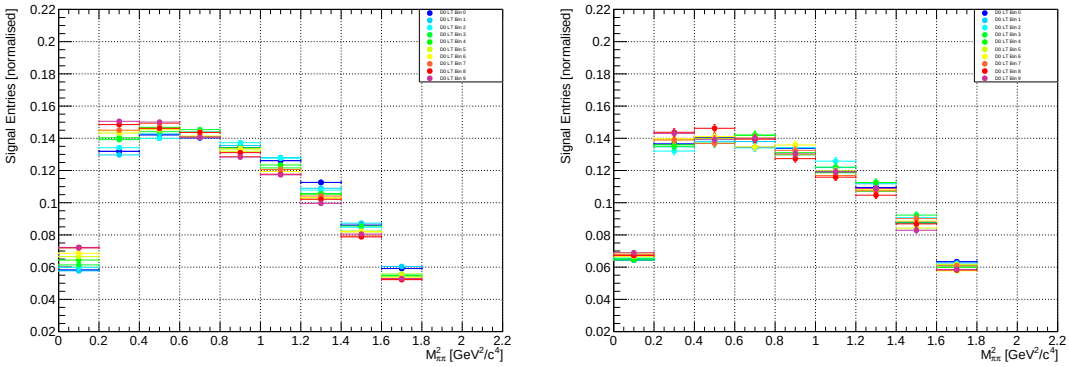

Figure 4.18 – MC signal yields in each D^0 decay time as a function of $m^2(\pi^+\pi^-)$ bin, separately for reconstructed K^0_S in the DD (left) and LL (right) categories.

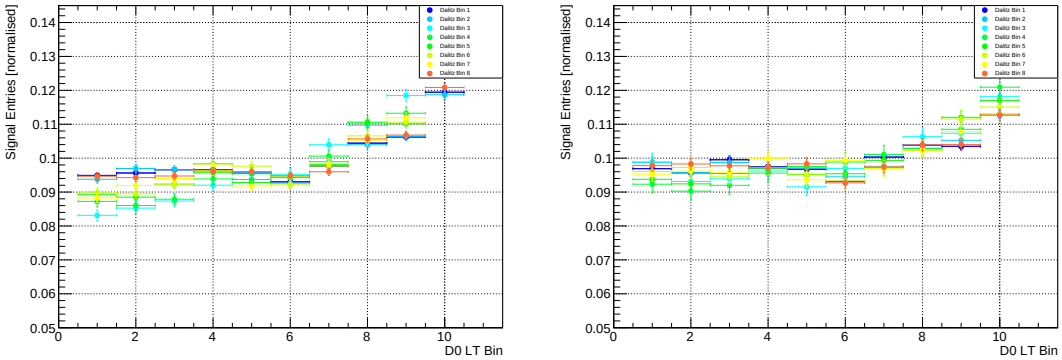

Figure 4.19 – MC signal yields in each Dalitz bin as a function of D^0 decay time bin, separately for reconstructed K^0_S in the DD (left) and LL (right) categories.

<u>MC</u>

The same study is performed on simulated $\overline{B} \to D^0(\to K^0_S\pi^+\pi^-)\mu^-\overline{\nu}_\mu X$ samples. Figures 4.18 and 4.19 present the correlation in $(m^2(\pi^+\pi^-), t/\tau_{D^0})$ space and signal yields normalised to all events in each Dalitz bin as a function of D^0 decay time bin. Note that this is phase-space Monte Carlo sample, hence, there is no resonant structure in the plots. The can be seen that the efficiency at low D^0 decay time (blue shade) is smaller than the efficiency at high D^0 decay time (red shade) at low $m^2(\pi^+\pi^-)$, but this is swapped at high $m^2(\pi^+\pi^-)$. This effect is consistent with data as shown earlier in Figure 4.10.

4.4.2 Decorrelation strategy

The process for decorrelating the variable is based on the procedure performed in the Run 1 analysis, where each candidate was weighted with decorrelation factor at a given $(m^2(\pi^+\pi^-), t/\tau_{D^0})$ point. This data-driven decorrelation has the disadvantage that it cannot distinguish between the correlation induced by the trigger selections and by mixing. A study in the $D^{*+} \to D^0(\to K^0_S\pi^+\pi^-)\pi^+$ [5] shows that this introduces a bias, especially on y_{CP}.

Keeping the mentioned weaknesses of the data-driven approach in mind, we add a first step to the method: the efficiency is extracted from the simulated sample because it is generated without the mixing effect, and an inverse correction is applied to the data. This provides us direct access to the correlation induced only from the trigger selection effects. In the prompt sample [5], such a procedure using the MC was not possible as the available prompt MC sample is not statistically large enough to represent the data. Therefore, a fully data-driven approach was applied as a correction, while for generating the effect in the toys a reweighter was used. However, the weights extracted from that method may not be optimal in the case of the semileptonic sample, as the statistics is much smaller than in the prompt sample - almost one order of magnitude difference. The simulated semileptonic samples have a yield comparable to the yields observed in the data (see Table 3.6 and Figure 3.9). Using the information available from MC thus seems appropriate.

4.4.3 Efficiency correction using simulated samples

Due to the limited yields in the simulated sample of each data-taking year, fitting the Dalitz plot as a function of D^0 decay time may not be optimal in terms of precision. The efficiency correction is extracted using yields in a binning of $(m^2(\pi^+\pi^-),\ t/\tau_{D^0}, |\cos\theta_{\pi^+\pi^-}|)$. Then each dimension is binned weighted to the efficiency as described in Sections 4.2 and 4.3. The map of each data-taking year is used to correct for efficiency effects in data.

Figures 4.24 and 4.25 present the relative signal yields in $(m^2(\pi^+\pi^-), t/\tau_{D^0})$ and $(|\cos\theta_{\pi^+\pi^-}|, t/\tau_{D^0})$ after applying efficiency correction from MC. The correlation is significantly reduced, but there is still a small noticable correlation left. This is taken care of in the next section.

4.4.4 Data-driven decorrelation

Since the efficiency extracted from the simulated sample may not be sufficient to account fully for the correlation effect, a further decorrelation method utilising the data is needed. We examine the correlation using a decorrelation factor (ϵ_{ij}) as a function of D^0 decay time in the D^0 decay time unit (t/τ_{D^0}) and $m^2(\pi^+\pi^-)$ defined as

$$\epsilon_{ij} = \frac{n_{ij}}{\sum_l n_{il}} \Bigg/ \frac{\sum_k n_{kj}}{\sum_{k,l} n_{kl}} \ , \tag{4.5}$$

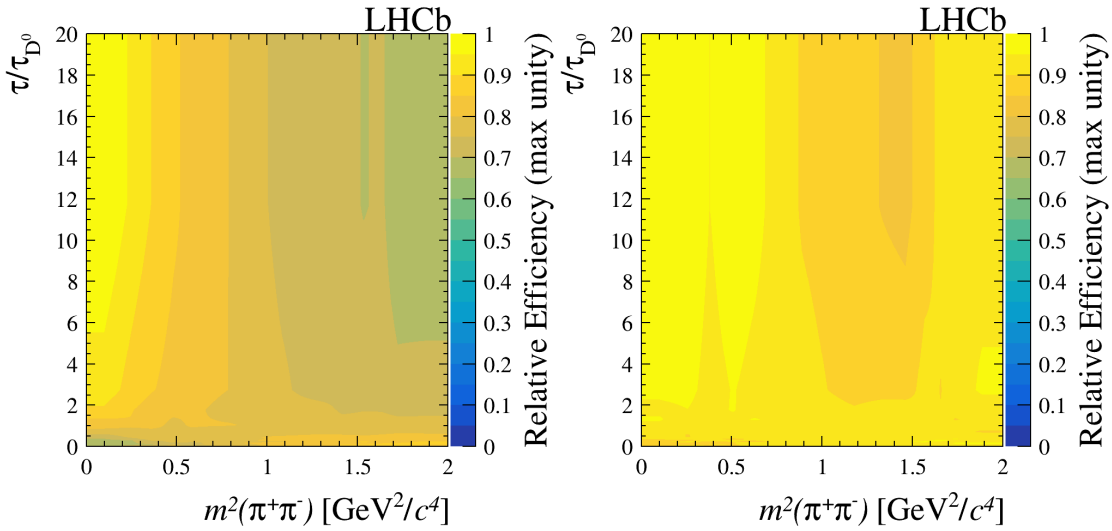

Figure 4.20 – Relative efficiency in the collision data as a function of D^0 decay time and $m^2(\pi^+\pi^-)$, determined from $\overline{B} \to D^0(\to K^0_S\pi^+\pi^-)\mu^-\overline{\nu}_\mu X$ candidates and smoothed using bilinear interpolation, separately for (left) LL and (right) DD candidates.

where $i(j)$ runs over bins in $m^2(\pi^+\pi^-)$ (t/τ_{D^0}). n_{ij} is the signal yield extracted with the fit model in each bin ij. The bins are chosen as to be equipopulous in $m^2(\pi^+\pi^-)$. The overall map of ϵ_{ij} are smoothed using bilinear interpolation and scaled to the maximum value. The benefit of using Equation (4.5) is that the factor ϵ_{ij} is uniform if there is no correlation between these variables.

Figure 4.20 shows the results separately for the LL and DD cases without the efficiency correction from the simulated sample. These plots show a variation which suggests there exists a correlation between the Dalitz-plot coordinates and D^0 decay time. As $|\cos\theta_{\pi^+\pi^-}|$ also correlates with $m^2(\pi^+\pi^-)$, this variation is also found in the $|\cos\theta_{\pi^+\pi^-}|$ and t/τ_{D^0} space as shown in Figure 4.21.

The efficiency corrrection from the simulated is applied. This results in the reduced variation as shown in Figure 4.22. Inverse of this map (decorrelation factor) is applied per candidates depending on their position in $(m^2(\pi^+\pi^-), t/\tau_{D^0})$ space to eliminate the remaining correlation. The final maps are presented in Figure 4.23. Figures 4.26 and 4.27 present the $(m^2(\pi^+\pi^-), t/\tau_{D^0})$ and $(|\cos\theta_{\pi^+\pi^-}|, t/\tau_{D^0})$ after applying the data-driven correction on top of MC correction. This shows that this decorrelation procedure is able to diminish the correlation effectively. We use these combined weights on the data sample and extract yield in each Dalitz bin and D^0 decay time to fit with the bin-flip method in the next chapter. The correlation obtained from the simulated sample and the data-driven decorrelation are combined and also further used in Chapter 6. The resulting correlation map is included to generate realistic toys which is used in estimating the systematic uncertainties.

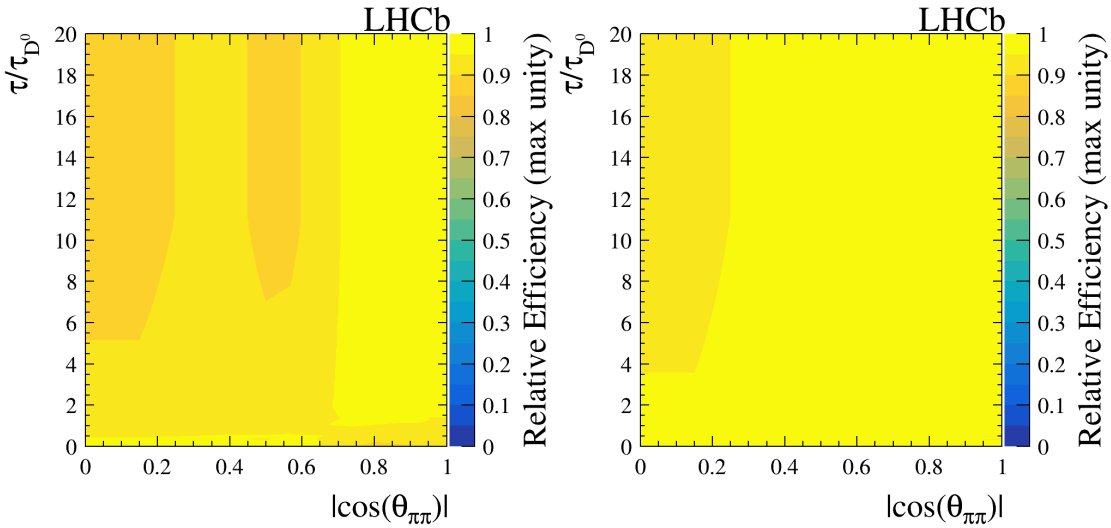

Figure 4.21 – Relative efficiency in the collision data as a function of D^0 decay time and $|\cos\theta_{\pi^+\pi^-}|$, determined from $\overline{B} \to D^0(\to K_S^0\pi^+\pi^-)\mu^-\overline{\nu}_\mu X$ candidates and smoothed using bilinear interpolation, separately for (left) LL and (right) DD candidates.

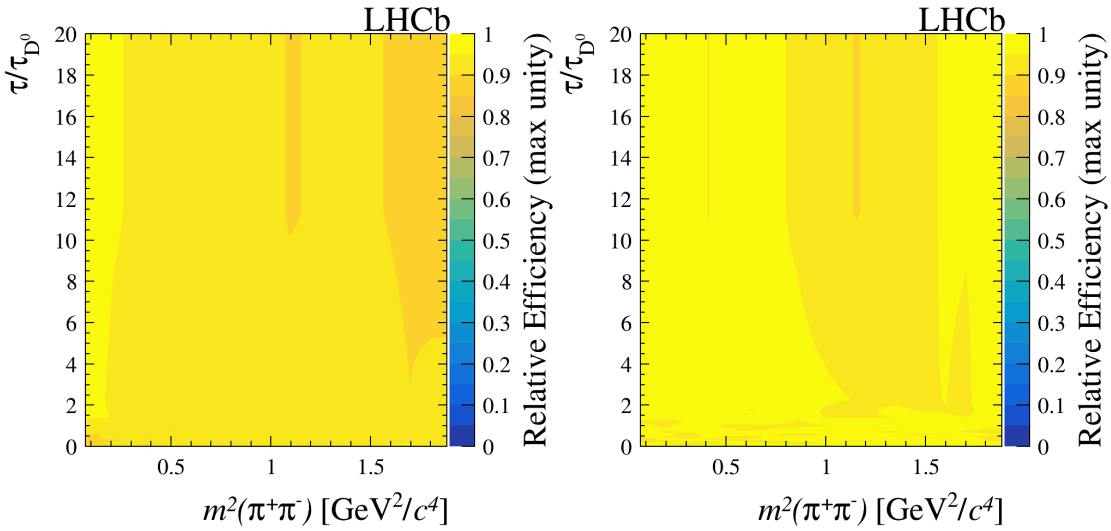

Figure 4.22 – Relative efficiency in the collision data as a function of D^0 decay time and $m^2(\pi^+\pi^-)$, determined from $\overline{B} \to D^0(\to K_S^0\pi^+\pi^-)\mu^-\overline{\nu}_\mu X$ candidates and smoothed using bilinear interpolation, separately for (left) LL and (right) DD candidates after the efficiency correction from MC.

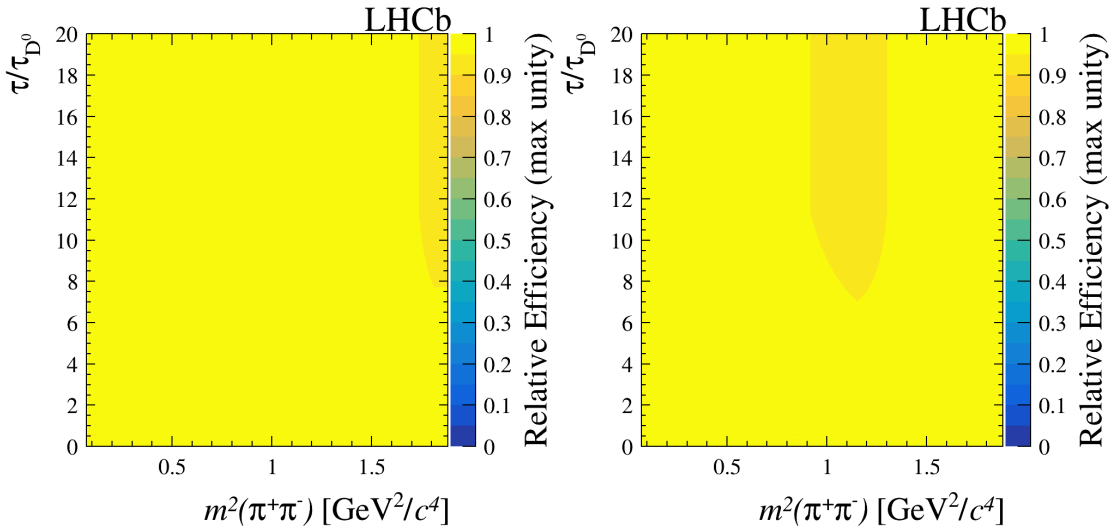

Figure 4.23 – Relative efficiency in the collision data as a function of D^0 decay time and $m^2(\pi^+\pi^-)$, determined from $\overline{B} \to D^0(\to K_S^0\pi^+\pi^-)\mu^-\overline{\nu}_\mu X$ candidates and smoothed using bilinear interpolation, separately for (left) LL and (right) DD candidates after the efficiency correction from MC and data-driven decorrelation.

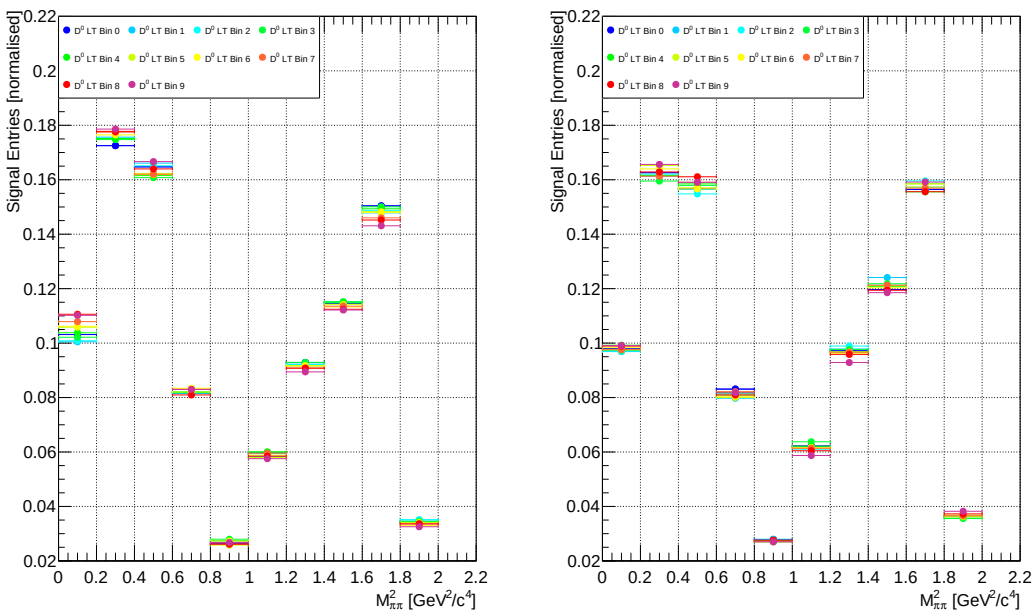

Figure 4.24 – Efficiency-corrected signal yields in each D^0 decay time as a function of $m^2(\pi^+\pi^-)$ bin, separately for reconstructed K_S^0 in the DD (left) and LL (right) categories.

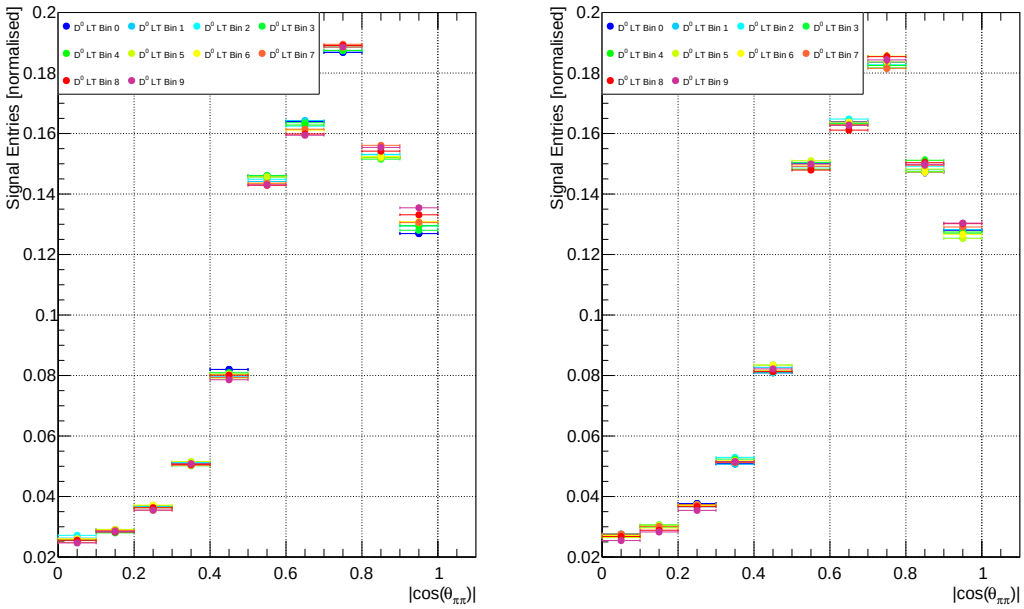

Figure 4.25 – Efficiency-corrected signal yields in each D^0 decay time as a function of $|\cos\theta_{\pi^+\pi^-}|$ bin, separately for reconstructed K_S^0 in the DD (left) and LL (right) categories.

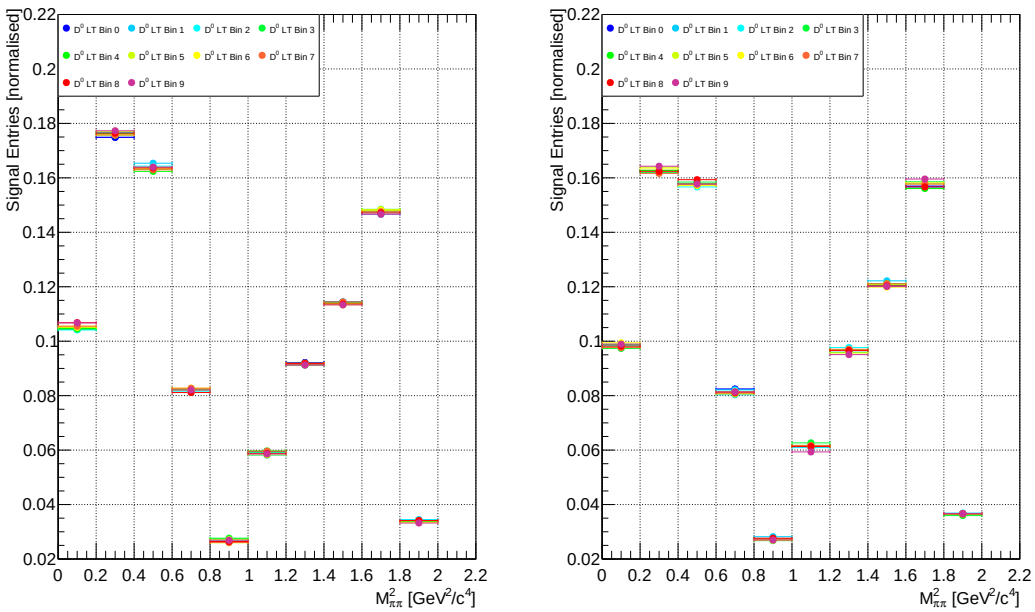

Figure 4.26 – Efficiency-correlation-corrected signal yields in each D^0 decay time as a function of $m^2(\pi^+\pi^-)$ bin, separately for reconstructed K_S^0 in the DD (left) and LL (right) categories.

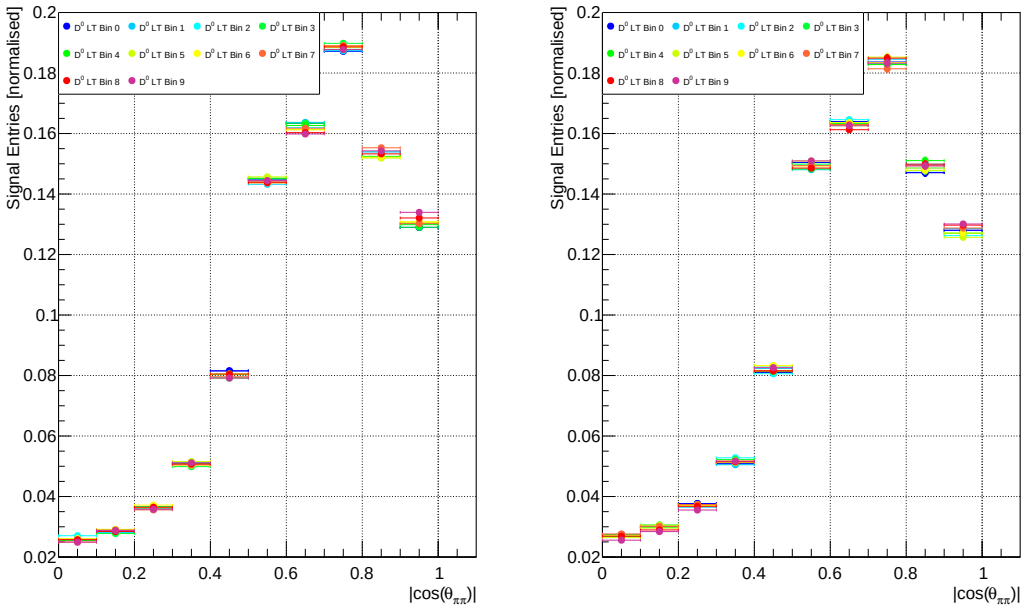

Figure 4.27 – Efficiency-correlation-corrected signal yields in each D^0 decay time as a function of $|\cos\theta_{\pi^+\pi^-}|$ bin, separately for reconstructed K_S^0 in the DD (left) and LL (right) categories.

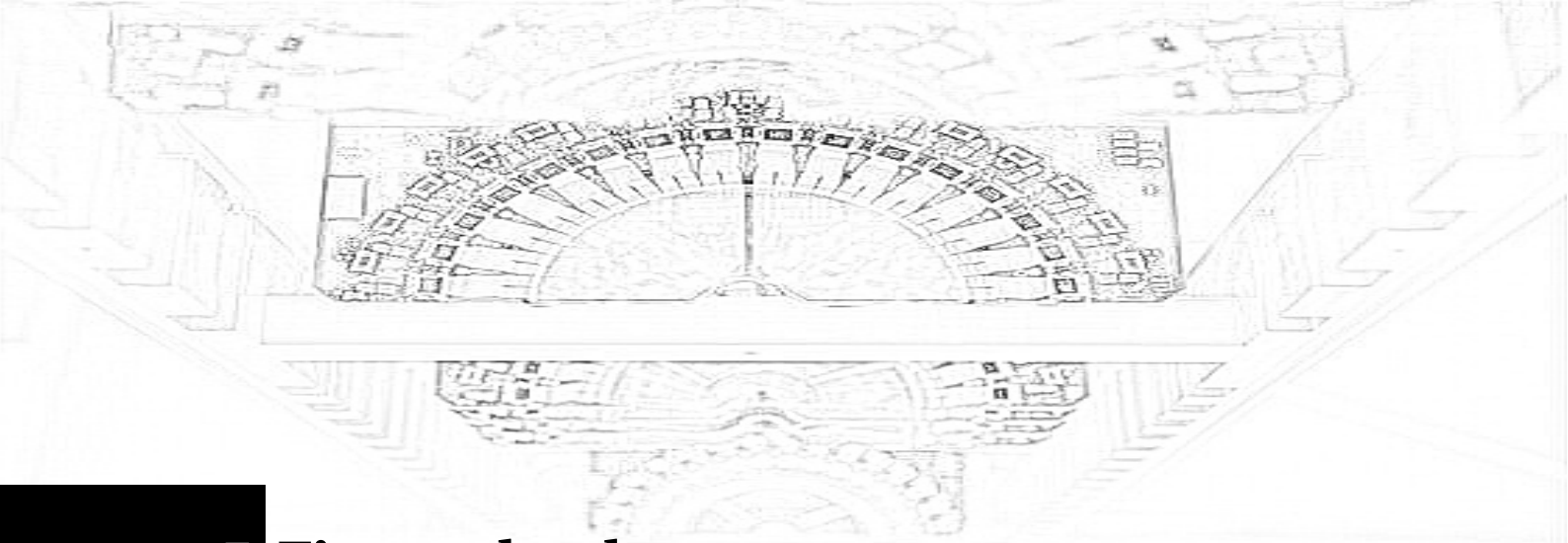

5 Fits to the data

In this chapter, the data are divided into sub-samples according to K^0_S types, D^0 meson flavour, Dalitz-plot position and decay time. For simplicity, the samples from the different years are merged together. Cross-checks are performed to validate this approach, and verify that the change is negligible when treating the different years separately.

For each decay-time bin, the average decay time and average squared decay time is then determined in Section 5.2. The decay-time dependence of the ratio of signal yields symmetric with respect to the Dalitz-plot bisector is fit to determine the mixing and CP-violation parameters, as described in Section 5.3. The analysis requires the strong-phase differences as external inputs from CLEO and BESIII [66]. We study impacts on the measurements implementing different inputs in Section 5.4.

5.1 Determination of $\overline{B} \to D^0(\to K^0_S\pi^+\pi^-)\mu^-\overline{\nu}_\mu X$ signal yields

The signal yields are determined from fits to the invariant mass distribution of the $K^0_S\pi^+\pi^-$, weighted following Section 4.4, in the range $[1795, 1935]$ MeV/c^2. We model the invariant mass distribution of the $D^0 \to K^0_S\pi^+\pi^-$ signal using the sum of a Johnson S_U distribution and a bifurcated Gaussian. The Johnson S_U distribution is defined in Equation (3.1). The bifurcated Gaussian is a Gaussian distribution with a mean parameter μ and asymmetric variance parameters characterised by widths denoted as σ_L for the left side and σ_R for the right side:

$$\mathscr{B}(x|\mu,\sigma_L,\sigma_R) = \frac{1}{N_{\mathscr{B}}} e^{-\frac{(x-\mu)^2}{2\sigma^2}} \begin{cases} \sigma = \sigma_L & \text{if } x < \mu, \\ \sigma = \sigma_R & \text{if } x > \mu, \end{cases} \tag{5.1}$$

These two distributions are constrained to have the same μ parameter. The full signal distribution function is

$$\wp_{\text{sig}}(M(K^0_S\pi^+\pi^-)) = f_1\,\mathscr{J}\,(M(K^0_S\pi^+\pi^-)|\mu,\sigma,\delta,\gamma) + (1-f_1)\cdot\mathscr{B}(M(K^0_S\pi^+\pi^-)|\mu,\sigma_L,\sigma_R), \tag{5.2}$$

where f_1 is the fraction of the signal distributed by the Johnson distribution. The combinatorial background distribution is modelled with Chebyshev polynomial up to second order:

$$\wp_{\text{bkg}}(x|c_0, c_1) \quad = \quad \frac{1}{N_{\mathscr{P}}}\left(c_1(2x^2-1)+c_0x+1\right). \tag{5.3}$$

The total fit function is then

$$\begin{aligned}\wp_{\text{tot}}(M(K_S^0\pi^+\pi^-)) = N\wp_{\text{sig}}(M(K_S^0\pi^+\pi^-)|f,\mu,\sigma,\delta,\gamma,\sigma_L,\sigma_R)\\ + N_{\text{bkg}}\wp_{\text{bkg}}(M(K_S^0\pi^+\pi^-)|c_0,c_1)\,,\end{aligned} \tag{5.4}$$

where N (N_{bkg}) is the number of signal (background) decays. For the LL sample, a first-order polynomial is sufficient to describe the background, so we set $c_1 = 0$. As the K_S^0 mass constraint induces a drop of candidates at the edge of the $K_S^0\pi^+\pi^-$ distribution, in the DD sample, a second-order term polynomial is needed.

The $K_S^0\pi^+\pi^-$ distribution is fitted separately for different K_S^0 samples and upper and lower part of Dalitz coordinate as shown in Figure 5.1 with fitted parameters presented in Table 5.1. Signal and background yields are also fitted separately for data-taking year and magnet polarities, MagUp (up) and MagDown (dw) to test for further stability of the models.

To obtain a yield in each Dalitz and D^0 decay time bin, a fit is performed in each bin where δ,σ,σ_L are constrained to the fitted parameters of the whole sample as shown in Table 5.1. This is to avoid correlation between fitted parameters which could bias the fit result. The other parameters are left free to account for a mass shift between bins due to resonant content. We minimise the fluctation of a fit in each pair of positive and negative Dalitz bin by utilising a signal PDF from fitting in the positive ($m^2\left(K_S^0\pi^+\right)$) part of the Dalitz bin to the negative ($m^2\left(K_S^0\pi^-\right)$) part. Note that, the fits in Table 5.1 are not used further.

Overall, there are (8 Dalitz bins) × (10 decay time bins) × (2 sides of Dalitz plot) × (2 D^0 flavours) × (2 K_S^0 categories) = 640 fits. In the case where some free parameters are not stable or converge outside a given range, they are constrained to that value and the fit is reperformed. As a result, all fits are converged. Yields, reported in Appendix B, are used to form a ratio, and mixing parameters are fitted in Section 5.3.

Table 5.1 – Fit parameters of the $K_S^0\pi^+\pi^-$ invariant mass of $\overline{B} \to D^0(\to K_S^0\pi^+\pi^-)\mu^-\overline{\nu}_\mu X$ candidates shown in Figure 5.1. Note that σ_L, σ_R, μ, and σ have units of MeV/c^2. c_0 and c_1 have units of $\left(\text{MeV}/c^2\right)^{-1}$ and $\left(\text{MeV}/c^2\right)^{-2}$, respectively. Others are dimensionless.

Parameter	DD		LL	
	Negative Dalitz	Positive Dalitz	Negative Dalitz	Positive Dalitz
σ_L	7.030 ± 0.082	6.915 ± 0.046	6.74 ± 0.25	6.873 ± 0.030
σ_R	7.135 ± 0.052	7.152 ± 0.043	7.082 ± 0.093	7.139 ± 0.049
δ	1.2000 ± 0.0095	1.313 ± 0.022	1.564 ± 0.014	1.207 ± 0.027
γ	0.1449 ± 0.0097	0.1654 ± 0.0079	0.151 ± 0.011	0.1715 ± 0.0038
μ	1865.204 ± 0.019	1865.345 ± 0.028	1865.595 ± 0.053	1865.362 ± 0.021
σ	9.14 ± 0.26	9.97 ± 0.15	11.514 ± 0.097	9.20 ± 0.14
f_1	0.472 ± 0.052	0.5587 ± 0.0083	0.75 ± 0.57	0.535 ± 0.015
c_0	-0.05295 ± 0.0018	-0.07629 ± 0.0020	-0.20535 ± 0.0033	-0.23167 ± 0.0044
c_1	-0.03278 ± 0.0054	-0.04316 ± 0.0047	0 (fixed)	0 (fixed)
N_{bkg}	828689 ± 3951	907343 ± 3880	122895 ± 697	174862 ± 1527
N_{sig}	613865 ± 4012	1892536 ± 3999	293445 ± 685	927873 ± 1663

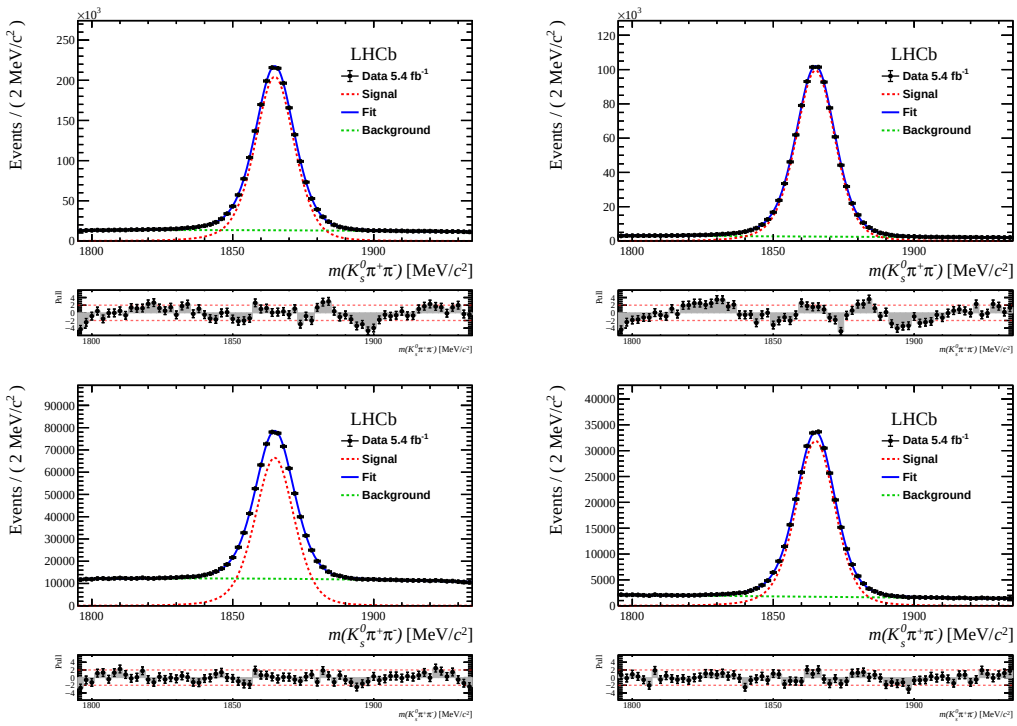

Figure 5.1 – $K_S^0\pi^+\pi^-$ distribution of $\overline{B} \to D^0(\to K_S^0\pi^+\pi^-)\mu^-\overline{\nu}_\mu X$ candidates from the DD (left) and LL (right) samples populating the positive (top) and negative (negative) Dalitz-plot sides.

Table 5.2 – Values of $\langle t \rangle$ and $\langle t^2 \rangle$ in unit of an averaged D^0 decay time, calculated for each K_S^0 sample.

Time bin	D^0				$\overline{D}^0$			
	DD		LL		DD		LL	
	$\langle t \rangle$	$\langle t^2 \rangle$	$\langle t \rangle$	$\langle t^2 \rangle$	$\langle t \rangle$	$\langle t^2 \rangle$	$\langle t \rangle$	$\langle t^2 \rangle$
0	0.0823	0.0087	0.0825	0.0088	0.0824	0.0087	0.0826	0.0088
1	0.2199	0.0497	0.2202	0.0499	0.2200	0.0498	0.2204	0.0500
2	0.3517	0.1252	0.3522	0.1255	0.3516	0.1252	0.3518	0.1253
3	0.4933	0.2452	0.4934	0.2453	0.4934	0.2453	0.4933	0.2452
4	0.6528	0.4285	0.6527	0.4284	0.6528	0.4285	0.6526	0.4283
5	0.8359	0.7020	0.8365	0.7030	0.8363	0.7027	0.8362	0.7026
6	1.0641	1.1379	1.0647	1.1392	1.0643	1.1382	1.0639	1.1375
7	1.3773	1.9089	1.3774	1.9090	1.3783	1.9117	1.3770	1.9080
8	1.8643	3.5091	1.8622	3.5012	1.8646	3.5100	1.8631	3.5045
9	3.1790	11.0380	3.1159	10.4815	3.1768	11.0129	3.1214	10.5476

5.2 Determination of $\langle t \rangle$ and $\langle t^2 \rangle$

We construct statistically pure decay-time distributions of D^0 mesons by subtracting the background using `sWeights` derived from the mass fits of candidates in each Dalitz and D^0 decay time bin.

Only candidates in the lower half of Dalitz plot are used, which is dominated by D^0 that do not oscillate. The decay time of each candidate is weighted with the product of the `sWeights` used to subtract the background and the efficiency in Section 4.4. The product of these weights in each candidate i is denoted as w_i. The decay-time resolution is neglected as its effect is treated as a systematic uncertainties in Section 6.3. The average decay time and squared decay time are calculated as

$$\langle t \rangle_j = \frac{\sum_i w_i \, t_i}{\sum_i w_i} \quad \text{and} \quad \langle t^2 \rangle_j = \frac{\sum_i w_i \, t_i^2}{\sum_i w_i} \,, \tag{5.5}$$

where the sum goes over all the candidates populating the decay time bin j and w_i is the weight assigned to candidate i with decay time t_i in the averaged D^0 decay time unit. The obtained values are listed in Table 5.2. These are used in Equation (1.20).

5.3 Determination of mixing parameters

The mixing and CP-violating parameters are determined using a least squares fit that compares the decay-time evolution (with a binning index j) of signal yields ($N_{\pm bjk}$) observed in the Dalitz bins $-b$ and $+b$, along with their uncertainties ($\sigma_{\pm bjk}$), as determined from the previous

described mass distribution fits in the DD and LL samples (with an index k). With the expected value of the ratio $R_{\pm bj}$ as reported in Equation (1.23), the χ^2 is defined as

$$\chi^2 = \sum_b^8 \sum_j^{10} \sum_{k=\mathrm{LL,DD}} \left[\frac{(N^+_{-bjk} - N^+_{+bjk} R^+_{bj})^2}{(\sigma^+_{-bjk})^2 + (\sigma^+_{+bjk} R^+_{bj})^2} + \frac{(N^-_{-bjk} - N^-_{+bjk} R^-_{bj})^2}{(\sigma^-_{-bjk})^2 + (\sigma^-_{+bjk} R^-_{bj})^2} \right] + \chi^2_X \tag{5.6}$$

is minimized, where the Gaussian penalty term

$$\chi^2_X = \sum_b^8 \sum_{b'}^8 \left(X^{\mathrm{ext}}_b - X_b\right) (V^{-1}_{\mathrm{ext}})_{bb'} \left(X^{\mathrm{ext}}_{b'} - X_{b'}\right) \tag{5.7}$$

where the superscript on $N_{\pm bjk}$, $\sigma_{\pm bjk}$, and $R_{\pm bjk}$ refers to as a flavour of D^0: positive sign (+) for D^0 and negative sign (−) for $\overline{D}^0$.

We perform separate fits to the data, for LL and DD K^0_S candidates, as well as a simultaneous fit to the combined sample, either assuming different or common values of ratios of the zero D^0 decay time ($t = 0$) in each Dalitz bin b (r_b) between the two samples. The X_b are constrained by the external inputs on the parameters through the Gaussian penalty term χ^2_X with the combined values X^{ext}_b from the CLEO and BESIII measurements [66] as presented in Table 1.2. The covariance matrix V_{ext}, shown in Table 1.3, resulting from the sum of the statistical and systematic covariance matrices are included in the χ^2. Since the ratio r_b in each Dalitz bin b depends on the remaining efficiency variation after efficiency correction in Chapter 4, it is different depending on the K^0_S types. However, these efficiencies are corrected when the candidates are weighted as explained in Section 4.4. In this fit, the r_b parameters are shared between K^0_S samples.

To search for *CP* violation, we fit with and without assuming *CP* symmetry. In the first fit, the *CP*-violating parameters Δx and Δy are constrained to zero. The mixing parameters x_{CP} and y_{CP} are then equal to x and y respectively. In the second fit, all four parameters are determined from the fits. These two hypotheses are tested and justified by χ^2/ndf from each scenario. In all cases, the statistical uncertainties estimated by the fit include the systematic uncertainty

Table 5.3 – Results of the fit to the $\overline{B} \to D^0(\to K^0_S \pi^+\pi^-)\mu^-\overline{\nu}_\mu X$ sample. The reported uncertainties include the statistical component and the contribution due to the uncertainties in the strong phase inputs.

Parameter		No *CP* violation	*CP* violation allowed	Correlations		
				y_{CP}	Δx	Δy
x_{CP}	$[10^{-3}]$	4.30 ± 1.48	4.29 ± 1.48	0.085	−0.011	−0.009
y_{CP}	$[10^{-3}]$	12.89 ± 3.12	12.61 ± 3.12		−0.001	−0.050
Δx	$[10^{-3}]$	–	-0.77 ± 0.93			0.070
Δy	$[10^{-3}]$	–	3.01 ± 1.92			
χ^2/ndf		282/310	278/308			

due to the finite precision of the external inputs from CLEO and BESIII measurements.

The filled values of the oscillation parameter: x_{CP}, y_{CP}, Δx and Δy were kept blinded until the entire analysis procedure was finalised, reviewed, and approved by the LHCb collaboration. The blinding was meant to avoid any bias from the analyst. The blinding was implemented by adding random numbers to the results, extracted from a uniform distribution in the range $[-10 \times 10^{-3}, +10 \times 10^{-3}]$.

The results of the simultaneous fit to the DD and LL sample with common r_b are shown in Table 5.3, and projections of the fit are shown in Figure 5.2. Results of the same fit, but with separated r_b are shown in Appendix B.2. The projections show the CP-averaged ratio as well as the difference in D^0 and $\overline{D}^0$ as a function of decay time. The results are compatible with the current world average [57] and with the analysis on the $D^{*+} \to D^0(\to K^0_S\pi^+\pi^-)\pi^+$ sample [5]. The fits show deviations of x_{CP} from 0 by almost 3σ of significance. There is no evidence for CP violation.

Figure 5.3 shows the central values and two-dimensional 68.3%, 95.5%, and 99.7% confidence regions in the (x_{CP}, y_{CP}) and $(\Delta x, \Delta y)$ planes. The full set of results, including all nuisance parameters, is also reported in Table 5.4.

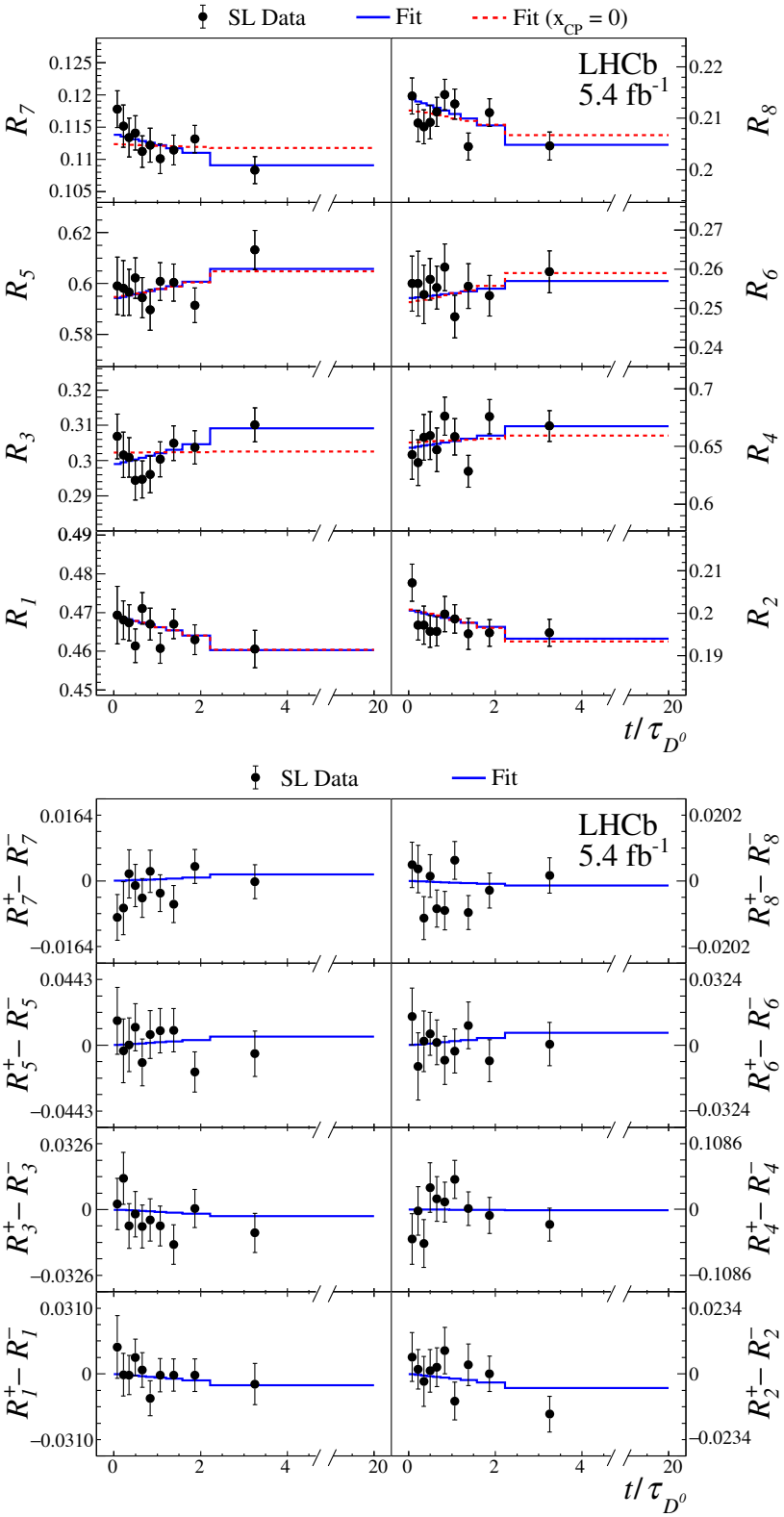

Figure 5.2 – Projections of the fit allowing for *CP* violation: (top) *CP*-averaged ratio and (bottom) difference of D^0 and $\overline{D}^0$ yield ratios as functions of decay time for the different Dalitz bins.

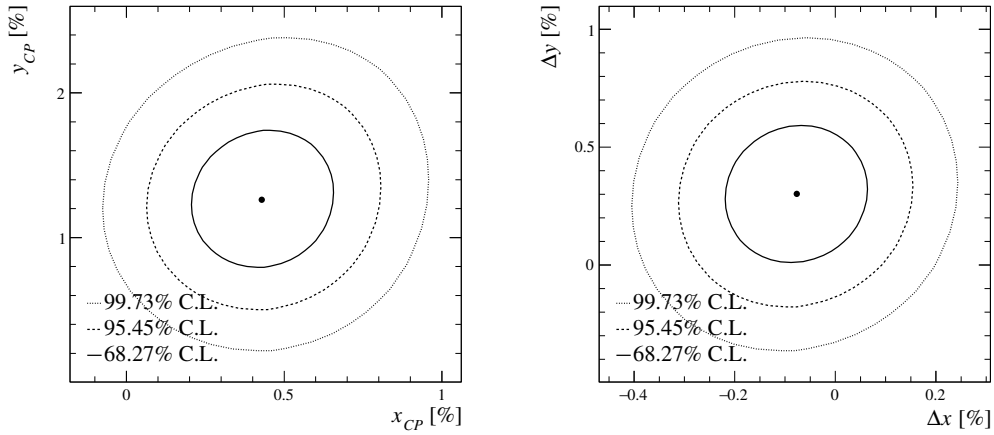

Figure 5.3 – Two-dimensional 68.3%, 95.5%, and 99.7% confidence-level contours on the mixing and *CP*-violation parameters determined from the fit with *CP* violation allowed.

Table 5.4 – Numerical results from the bin-flip fit to the data separately for no CP violation and allowed one. The ratios r_b are shared between DD and LL samples.

Parameter	No *CP* violation	Indirect *CP* violation allowed
c_1	0.700 ± 0.020	0.700 ± 0.020
c_2	0.643 ± 0.036	0.646 ± 0.036
c_3	0.003 ± 0.047	0.008 ± 0.047
c_4	-0.607 ± 0.052	-0.605 ± 0.052
c_5	-0.955 ± 0.023	-0.954 ± 0.023
c_6	-0.577 ± 0.058	-0.573 ± 0.058
c_7	0.064 ± 0.056	0.072 ± 0.056
c_8	0.412 ± 0.036	0.414 ± 0.036
s_1	0.092 ± 0.062	0.093 ± 0.062
s_2	0.303 ± 0.108	0.308 ± 0.108
s_3	0.995 ± 0.074	1.002 ± 0.075
s_4	0.650 ± 0.122	0.652 ± 0.122
s_5	-0.030 ± 0.068	-0.026 ± 0.068
s_6	-0.546 ± 0.121	-0.543 ± 0.120
s_7	-0.864 ± 0.093	-0.856 ± 0.094
s_8	-0.434 ± 0.082	-0.431 ± 0.082
r_1	0.4692 ± 0.0016	0.4692 ± 0.0016
r_2	0.2008 ± 0.0014	0.2008 ± 0.0014
r_3	0.2988 ± 0.0020	0.2988 ± 0.0020
r_4	0.6485 ± 0.0052	0.6485 ± 0.0052
r_5	0.5939 ± 0.0027	0.5940 ± 0.0027
r_6	0.2525 ± 0.0020	0.2526 ± 0.0020
r_7	0.1139 ± 0.0010	0.1139 ± 0.0009
r_8	0.2140 ± 0.0011	0.2139 ± 0.0011

5.4 Impact of external inputs

The uncertainties presented in Table 5.3 include both the statistical uncertainty and the uncertainty from the external inputs though the Gaussian penalty term of Equation (5.7).

To decouple the impact of these factors and quantify the pure statistical uncertainty, the external inputs (c_b, s_b) are fixed to their central values and the fits are repeated. The difference in quadrature of the uncertainties obtained from these two fits is taken as the impact of the external inputs on the measurements. The precision on these inputs affects the uncertainties significantly as the CLEO measurement has the least precision. The result is improved when the measurement is combined together with the inputs from the BESIII measurement. Figure 5.4 shows the pull plot of (c_b, s_b) from the fits with different inputs. The result from the combined inputs has the lowest uncertainty, hence it propagates to the measurement the least, providing the lowest contribution to the statistical uncertainty. Therefore, the combination measurement is used in the fit to measure the oscillation parameters. Results are presented in Table 5.5.

Table 5.5 – Uncertainties from the external strong phase inputs in units of 10^{-3} from the CP-violation-allowing fit in which the (c_b, s_b) parameters are fixed to their values returned by the default fit, in comparison with the default fit where (c_b, s_b) are Gaussian constrained to the combination of the strong phase inputs from combined BESIII and CLEO. Here we report the difference in quadrature of these fit uncertainties, separately for DD and LL K^0_S categories. Combined fit with separated and shared r_b are also reported.

Fit uncertainties	DD	LL	Comb.	Comb. (Shared r_b)
$\sigma(x_{CP})$	0.49	0.54	0.30	0.32
$\sigma(y_{CP})$	1.06	0.61	0.67	0.68
$\sigma(\Delta x)$	0.19	0.20	0.16	0.16
$\sigma(\Delta y)$	0.31	0.30	0.21	0.21

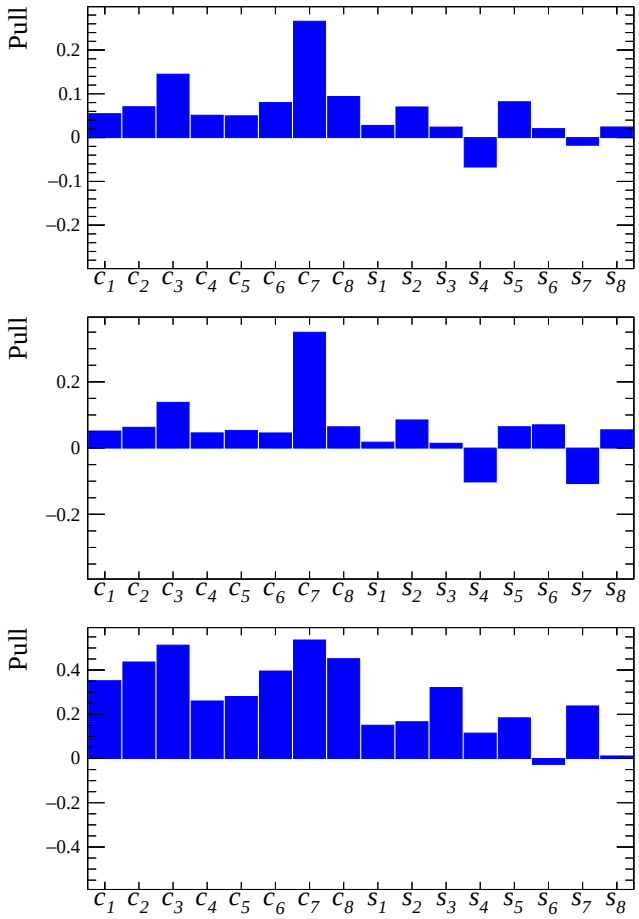

Figure 5.4 – Pulls of the measured strong phases with respect to the central values used in the constraints, for fits performed using (top) combined BESIII and CLEO inputs, (middle) BESIII inputs only, (bottom) CLEO inputs only where r_b is shared between samples.

6 Systematic uncertainties

Possible systematic uncertainties on the measurement of charm-mixing parameters are evaluated on pseudoexperiment (toy) data. The toy data is generated with the mixing and *CP*-violating parameters set to the measured values, as described in Section 6.1. The general strategy to compute the systematic uncertainties from toys is explained in Section 6.2.

As discussed in Section 5.4, the analysis is limited by the precision of the external strong-phase difference inputs. This contributes to the fit in addition to the statistics of the data. Other sources of possible systematic effects are considered and studied in detail here. The following contributions are studied in Sections 6.3–6.6 : reconstruction and selection effects (*e.g.*, imperfection in the efficiency correction, finite resolutions in decay time and Dalitz-plot coordinates, *etc.*); detection and reconstruction asymmetry of the D^0 daughter pions; unrelated $D^0\mu$ combination in the $\overline{B} \to D^0(\to K^0_S\pi^+\pi^-)\mu^-\overline{\nu}_\mu X$ sample. All sources of systematics are combined and summarised in Section 6.7.

6.1 Pseudoexperiments

The systematic uncertainties are estimated on at least 1000 pseudoexperiments for each systematic contribution. The events are generated by sampling the decay-time-dependent decay rate using the Belle model [61] to describe the amplitudes at $t = 0$. Table 6.1 reports the values of c_b and s_b corresponding to the Belle model used in the generation; in order to be self-consistent, these values substitute the central values of the externally measured strong phase differences when implementing the constraints to these parameters in the fit to the pseudoexperiments. In the generation, the mixing and *CP*-violating parameters are included according to the world-average values as $x = x_{CP} = 0.4\%$, $y = y_{CP} = 0.6\%$, and $|q/p| = 1$, $\phi = 0$ (or $\Delta x = \Delta y = 0$) [14].

The combinatorial background component in $K^0_S\pi^+\pi^-$ mass distribution is included in the pseudoexperiments according to the signal-to-background ratio found in data as shown in Figure 5.1 of Section 5.1. The Dalitz coordinate and decay time dependence is simulated as of

Table 6.1 – Values of r_b, c_b and s_b resulting from the Belle model [61], used to generate the pseudoexperiments in $\overline{B} \to D^0(\to K_S^0\pi^+\pi^-)\mu^-\overline{\nu}_\mu X$.

b	r_b	c_b	s_b
1	0.457705	0.662123	0.00338361
2	0.199015	0.621737	0.423018
3	0.292177	0.0932084	0.827948
4	0.635612	-0.505907	0.751153
5	0.602885	-0.947815	-0.0344837
6	0.242069	-0.574707	-0.561769
7	0.103822	0.0271415	-0.794396
8	0.205713	0.442	-0.401914

the signal's, but the D^0 flavour is randomly assigned.

Phase space and decay-time acceptance effects derived in Chapter 4 are included and fluctuated within the statistical uncertainties observed in data. The distributions of the signal and background are generated according to the PDFs described in Chapter 5. The toy data can then be processed in exactly the same manner as the real data:

- Apply the efficiency correction weight. This weight includes both MC correlation weight and efficiency weight from Dalitz phase space and decay-time.
- Calculate and apply a decorrection weight on each toy with the same method used in the real data.
- Determine yields in each Dalitz and decay-time bin via a fit to the $K_S^0\pi^+\pi^-$ distribution.
- Calculate $\langle t \rangle_j$ and $\langle t^2 \rangle_j$ via `sWeights` derived from a fit to the $K_S^0\pi^+\pi^-$ distribution.
- Perform the fit for the mixing and *CP* violation parameters.

Samples are generated separately for each of the K_S^0 types, and processed separately up until the last step when all samples are combined to determine the mixing and *CP*-violation parameters (just like for the data) separately for different K_S^0 types. Biases of these parameters from the generated values are then used to assign the systematic uncertainties. While the systematic uncertainty is set using the biases of the fit to the combined sample, the biases are also studied when fitting the individual K_S^0 samples separately.

6.2 General strategy

The general strategy for assigning the systematic uncertainties is to include the systematic effect under consideration in the toy, and then analyse it with the default method which in general ignores all of these effects (after the correlation removal). The default toy includes both the systematic and statistical uncertainties. The statistical uncertainties are suppressed by performing a reference fit to the same dataset where systematic effect under consideration removed or corrected for. This is done by applying correction factors to the yields and $\langle t^2 \rangle$

which would, on average, bring them into agreement with purely reference distributions. The difference between the default fit and the reference fit (residual) is fitted with Gaussian distribution, as well as its uncertainty. From this we can estimate the average bias caused by the systematic effect.

One of the systematic uncertainties under consideration is that due to the acceptance and resolution effects. However, in order to have toys which represent the data and to be sure to assess the true effect of the different systematic sources under a realistic setting, the acceptance and reconstruction effects are included in all studies presented in this section. To avoid double counting of the bias from acceptance and resolution, this baseline bias is included as a systematic uncertainty once, and then the effect of the additional systematic uncertainty sources is calculated with respect to it. Systematic uncertainties are reported with respect to the baseline bias.

Similarly, for the detection asymmetry systematic, the $\pi^+\pi^-$ asymmetry estimated in Section 6.4 is incorporated to the Dalitz efficiency map in Section 4.3. The resulting efficiency map is used to generate toys instead of the default one. For the systematics associated to the PDF choice, the reference fit is performed using the PDF used to generate the dataset, which is different from the default PDF. The systematics due to the unrelated $D^0\mu$ combination is estimated on an independent sample of $D^0 \to K\pi$ decays. The rate of wrong combinations is injected in the toys. The systematics is computed comparing to those of the reference fit where the mistag is removed. Table 6.11 reports a summary of all the contributions to the final uncertainties.

6.3 Acceptance and resolution effects

The reconstruction and selection effects are discussed in detail in Chapter 4. The efficiency models constructed in Dalitz coordinates and D^0 decay time phase space are incorporated and added to the toy data. These also cover resolutions of Dalitz coordinates and D^0 decay time and their experimentally-induced correlations.

The resolutions are incorporated by smearing the Dalitz-coordinate and decay-time values according to the fit distributions described in Section 4.1. The efficiency effects (including their correlations) are incorporated using an accept-reject method. The event is accepted if a random number generated between 0 and 1 is below the efficiency. To generate the realistic toys, the efficiency is included with the following product: $((m^2(\pi^+\pi^-), \tau_{D^0}, \cos\theta_{\pi^+\pi^-})$ model of the MC efficiency) $\times$ $((m^2(\pi^+\pi^-), \tau_{D^0})$ from data-driven correlations). phase-space integrated decay-time acceptance to generate realistic toys. Each of these components are those described in Chapter 4. We inject statistical uncertainty observed in data to the efficiency map to avoid using the exact same efficiency map to generate toys and correct for the efficiency.

The resulting systematic uncertainties are calculated as outlined above, and are shown for the combined fit with different and shared r_b, as well as for each of the individual samples, in

Table 6.2. Systematic uncertainties are also evaluated in different situations to understand the source of the bias and its dependencies. In the first part of Table 6.2 where the nominal systematic uncertainty in this section is shown, there exists biases in Δx and Δy due to the correlation between resolutions of Dalitz coordinates. This essentially comes from the K_S^0 mass constraint. The bias on the combined fit with shared r_b, which is ultimately what is used for the measurement, is considered as the systematic uncertainty. This bias comes from a fit on residual distribution with Gaussian distribution with parameters (μ, σ). They are reported as $\mu \pm \sigma$ of the Gaussian. The standard error on the Gaussian parameters are negligible since toys are generated with sufficient amount. Then we take the quadratic sum of μ and σ. The value is reported in Table 6.11 of the final systematics in the end of this chapter in Section 6.7.

The remaining parts of Table 6.2 present additional studies of the systematics under different conditions, serving as cross-checks. In the second part, we test whether the measurement is changed if the decay time efficiency is modelled on the Toy-data method as explained in Section 4.2. Even if there is an inconsistency between decay time acceptance from different methods, the systematic uncertainties from using two different models are consistent and do not bias the measurement. As suggested from this table, the bias from the inaccurate description of the decay time efficiency is not significant as expected from the construction of the bin-flip method. In the third part of this table, we also show that there is a huge bias, especially in y_{CP}, if the efficiency is not corrected for. In the fourth part, the generated toys are decorrelated using information from the simulated sample. The systematic uncertainty is compatible with the first case where the data-driven weight is also applied on top. This indicates that the weight derived from MC sample is sufficient to account for the correlation between decay time and Dalitz coordinate.

Table 6.2 – Systematic uncertainties in units of 10^{-3} due to reconstruction and selection effects in different scenarios. The first part presents the nominal uncertainty from this source, while the parts present different cross-checks.

Parameter	DD	LL	Comb.	Comb. (Shared r_b)
		Nominal systematic uncertainty		
$\sigma(x_{CP})$	$+0.045 \pm 0.045$	$+0.035 \pm 0.045$	$+0.042 \pm 0.042$	$+0.042 \pm 0.041$
$\sigma(y_{CP})$	-0.773 ± 0.064	-0.813 ± 0.060	-0.790 ± 0.051	-0.790 ± 0.051
$\sigma(\Delta x)$	-0.274 ± 0.022	-0.278 ± 0.023	-0.277 ± 0.020	-0.277 ± 0.020
$\sigma(\Delta y)$	$+0.230 \pm 0.047$	$+0.238 \pm 0.047$	$+0.235 \pm 0.042$	$+0.236 \pm 0.042$
	as above, but with the D^0 decay time efficiency from the Toy-Data model			
$\sigma(x_{CP})$	-0.011 ± 0.046	-0.025 ± 0.047	-0.011 ± 0.042	-0.012 ± 0.042
$\sigma(y_{CP})$	-0.753 ± 0.068	-0.756 ± 0.070	-0.755 ± 0.054	-0.755 ± 0.055
$\sigma(\Delta x)$	-0.288 ± 0.025	-0.291 ± 0.025	-0.290 ± 0.023	-0.290 ± 0.022
$\sigma(\Delta y)$	$+0.125 \pm 0.047$	$+0.124 \pm 0.051$	$+0.122 \pm 0.043$	$+0.122 \pm 0.043$
		Efficiencies not corrected for		
$\sigma(x_{CP})$	-1.145 ± 1.327	$+0.483 \pm 0.387$	-0.335 ± 0.993	-0.465 ± 0.856
$\sigma(y_{CP})$	$+22.547 \pm 1.140$	$+13.201 \pm 0.723$	$+19.079 \pm 1.045$	$+18.793 \pm 0.995$
$\sigma(\Delta x)$	-0.293 ± 0.128	-0.326 ± 0.074	-0.308 ± 0.100	-0.308 ± 0.098
$\sigma(\Delta y)$	$+0.299 \pm 0.397$	$+0.449 \pm 0.317$	$+0.337 \pm 0.290$	$+0.325 \pm 0.286$
		Applied weight only from MC sample		
$\sigma(x_{CP})$	$+0.045 \pm 0.042$	$+0.035 \pm 0.043$	$+0.042 \pm 0.040$	$+0.043 \pm 0.040$
$\sigma(y_{CP})$	-0.777 ± 0.066	-0.813 ± 0.061	-0.792 ± 0.050	-0.791 ± 0.049
$\sigma(\Delta x)$	-0.284 ± 0.022	-0.289 ± 0.022	-0.285 ± 0.022	-0.285 ± 0.023
$\sigma(\Delta y)$	$+0.248 \pm 0.048$	$+0.255 \pm 0.046$	$+0.251 \pm 0.044$	$+0.251 \pm 0.045$

6.4 $\pi^+\pi^-$ detection asymmetry

The reconstruction efficiency of the $\pi^\pm$ tracks may vary depending on their charges and momenta. This effect is induced by the asymmetric tracking reconstruction efficiency. In $D^0 \to K^0_S\pi^+\pi^-$, this affects the efficiency across the Dalitz plot with respect to its bisector and introduces an artificial asymmetry between D^0 and $\overline{D}^0$. The asymmetry induces a bias on the measurement of the CP-violating parameters Δx and Δy.

We estimate the asymmetry in the $D^0 \to K^0_S\pi^+\pi^-$ sample using two Cabibbo-favoured D_s^+ decays: $D_s^+ \to \pi^+\pi^+\pi^-$ and $D_s^+ \to \phi(\to K^+K^-)\pi^+$. These D_s^+ decays are selected with requirements as close as possible to those for the $D^0 \to K^0_S\pi^+\pi^-$ selection. A weighting procedure is implemented to equalise the kinematic distributions of the D_s^+ and D^0 samples in each bin of $m^2(\pi^+\pi^-)$, $|\cos\theta_{\pi^+\pi^-}|$ and D^0 decay time.

The detection asymmetry of a decay f ($A_{\text{meas}}(f)$) can be measured from the raw asymmetry, which is defined as the difference between the yields found for that decay and its conjugate. In the case of $f = D_s^+ \to \pi^+\pi^+\pi^-$, this asymmetry receives contributions from the $\pi^+\pi^-$ detection asymmetry ($A_{\text{det}}(\pi^+\pi^-)$), the pion detection asymmetry ($A_{\text{det}}(\pi^+)$), the D_s^+ production asymmetry ($A_{\text{prod}}(D_s^+)$), and the asymmetry from the hardware trigger selections on the D_s^+ ($A_{\text{trig}}(D_s^+)$).

These contributions of the asymmetry are similar to the case where $f = D_s^+ \to \phi(\to K^+K^-)\pi^+$, except there is no $A_{\text{det}}^{K^+K^-}$ contribution. Indeed, the K^+K^- detection asymmetry vanishes as the self-conjugate $\phi \to K^+K^-$ decay lead to identical phase-space for the two kaons. Hence, the asymmetries from these two decays in the first order approximation can be expressed as

$$A_{\text{meas}}(D_s^+ \to \pi^+\pi^+\pi^-) = A_{\text{det}} + A_{\text{det}}(\pi^+) + A_{\text{prod}}(D_s^+) + A_{\text{trig}}(D_s^+) \tag{6.1}$$

$$A_{\text{meas}}(D_s^+ \to \phi(\to K^+K^-)\pi^+) = A_{\text{det}}(\pi^+) + A_{\text{prod}}(D_s^+) + A_{\text{trig}}(D_s^+) \tag{6.2}$$

where one of the same sign pions of the decay $D_s^+ \to \pi^+\pi^+\pi^-$ is associated randomly with the π^-, and the other same sign pion corresponds to the pion in $D_s^+ \to \phi(\to K^+K^-)\pi^+$. The latter pion is referred to as the bachelor pion. The difference in asymmetries between these two channels is

$$A_{\text{det}}^{\pi^+\pi^-} = A_{\text{meas}}(D_s^+ \to \pi^+\pi^+\pi^-) - A_{\text{meas}}(D_s^+ \to \phi(\to K^+K^-)\pi^+) \tag{6.3}$$

These asymmetries vary over the phase-space and kinematic distributions of D_s^+. Reconstruction efficiencies between these two channels are also different and affect the detection asymmetry. The reweighting procedure is implemented to account for these nuisance asymmetries.

The triggers used in this analysis only consists of a trigger on a muon track in which its kinematic distribution is symmetric with respect to Dalitz bisector. The asymmetry is expected to be generally small, and the efficiency cancels in the ratio.

Table 6.3 – HLT2 requirements to select $D_s^+ \to \phi(\to K^+K^-)\pi^+$ and $D_s^+ \to \pi^+\pi^+\pi^-$ candidates.

Particle	Variable	$D_s^+ \to \phi(\to K^+K^-)\pi^+$	$D_s^+ \to \pi^+\pi^+\pi^-$
D_s^+	Mass	$\in [1889, 2049]$ MeV/c^2	$\in [1889, 2049]$ MeV/c^2
	Flight distance χ^2	> 100	> 100
	arccos(DIRA)	< 14.1 mrad	< 10.0 mrad
	D_s^+ decay time	> 0.2 ps	> 0.2 ps
	Vertex χ^2	< 6	< 6
$h^\pm$	3 of 3 with IPχ^2	> 4	> 4
	3 of 3 with p_T	> 250 MeV/c	> 250 MeV/c
	2 of 3 with IPχ^2	> 10	> 10
	2 of 3 with p_T	> 400 MeV/c	> 400 MeV/c
	1 of 3 with IPχ^2	> 50	> 50
	1 of 3 with p_T	$1 >$ GeV/c	> 1 GeV/c
	$\sum p_T$	> 3.2 GeV/c	> 3.2 GeV/c
$\pi^\pm$	DLL$_{K\pi}$	< 5	< 3 (2016)
			< 1 (2017–2018)
K^+	DLL$_{K\pi}$	> 5	-

Table 6.4 – Offline requirements to select for $D_s^+ \to \phi(\to K^+K^-)\pi^+$ and $D_s^+ \to \pi^+\pi^+\pi^-$ candidates.

Particle	Variable	$D_s^+ \to \phi(\to K^+K^-)\pi^+$	$D_s^+ \to \pi^+\pi^+\pi^-$
D_s^+	Mass	$\in [1910, 2038]$ MeV/c^2	$\in [1910, 2038]$ MeV/c^2
	IPχ^2	< 50	< 10
	IP	< 40 µm	
	p_T	$\in [2.9, 17.5]$ GeV/c	$\in [2.9, 17.5]$ GeV/c
	η	$\in [2.1, 4.35]$	$\in [2.1, 4.35]$
	L0	D_L0Global_TIS	D_L0Global_TIS
	(p_T, η)	$p_T(D_s^+) < (5 - \eta(D_s^+)) \times 10000$ MeV/c	
ϕ	$\lvert m(K^+K^-) - m_\phi^{PDG}\rvert$	< 5 MeV/c^2	-
Bachelor π^+	DLL$_{K\pi}$	< 0	< 0
	IPχ^2	-	> 12
	p_T	> 250 MeV/c	> 250 MeV/c
	η	$\in [2, 4.5]$	$\in [2, 4.5]$
$\pi^\pm$ of $\pi^+\pi^-$	p_T	-	> 275 MeV/c^2
	IPχ^2	-	> 12

6.4.1 Trigger and selection requirements

Trigger requirements on the D_s^+ samples are made similar to help match kinematic distributions between these samples. The HLT2 and offline requirements are presented in Tables 6.3 and 6.4. At hardware trigger level (L0), we require a global trigger independently of the D_s^+ signal (D_L0Global_TIS). HLT1 requirements for $\overline{B} \to D^0(\to K_S^0\pi^+\pi^-)\mu^-\overline{\nu}_\mu X$ are applied on the muon candidate, independently of the $\pi^+\pi^-$ pair, as mentioned in Table 3.2. The bachelor pions of the D_s^+ samples are treated similarly to this muon candidate and the Hlt1TrackMVADecision_TOS trigger is required on these pions. This trigger line is similar to Hlt1TrackMuonMVADecision_TOS, but it does not require the track to be identified as a muon.

The particle identification (PID) relies on the $\mathtt{DLL}_{K\pi}$ variable, which is the log of the likelihood ratio for the kaon mass hypothesis for the track relative to the pion mass hypothesis. The requirements on this variable for the $\pi^\pm$ tracks depends on data-taking year as shown in Table 6.3. This requirement $\mathtt{DLL}_{K\pi} < 0$ is appiled further in the offline selection in Table 6.4. PID requirements do not exist in the $\overline{B} \to D^0(\to K_S^0\pi^+\pi^-)\mu^-\overline{\nu}_\mu X$ selection. The possible asymmetry effect induced by the mismatched selection is parametrised as

$$\begin{aligned} A_{\text{det}}(\pi^+\pi^-) &= A_{\text{det,PID}}(\pi^+\pi^-) - A_{\text{PID}}(\pi^+\pi^-) \\ A_{\text{PID}}(\pi^+\pi^-) &= \frac{\epsilon_{\text{PID}}(\pi^+) - \epsilon_{\text{PID}}(\pi^-)}{\epsilon_{\text{PID}}(\pi^+) + \epsilon_{\text{PID}}(\pi^-)} \end{aligned} \tag{6.4}$$

where ϵ_{PID} is a PID efficiency evaluated from PIDCalib2 [121] depending on the charge, momentum, and pseudorapidity of the pion and kaon tracks and averaged over on the kinematic distributions of the pion for each data-taking year and magnet polarity.

6.4.2 Reweighting of the D_s^+ candidates

After the selections, the D_s^+ samples are reweighted to match the kinematic distributions of the $\overline{B} \to D^0(\to K_S^0\pi^+\pi^-)\mu^-\overline{\nu}_\mu X$. The procedure is divided into 4 steps. As the first step, a simple binned reweighting is implemented to match angular distributions of the $\pi^+\pi^-$ pair. Then a Gradiant Boosting reweighting algorithm [103] is used to obtain an unbinned parametrisation of the correlations. The algorithm calculates weights to bring an original data sample into agreement with a target data sample. The following steps are implemented:

1. The angular distribution ϕ of the $\pi^+\pi^-$ pairs in the $D_s^+ \to \pi^+\pi^+\pi^-$ are weighted to the signal $\pi^+\pi^-$ ϕ distributions using a 8×8 binned weighting procedure.
2. The p_T and η distributions of each pion in the $\pi^+\pi^-$ pair are weighted to the signal $\pi^+\pi^-$ distributions using the Gradiant Boosting Decision Tree (GBDT) reweighting,
3. The p_T and η distributions from the previous step are reweighted using binned weighter.
4. The p_T and η distributions of the D_s^+ and the bachelor pion of the $D_s^+ \to \phi(\to K^+K^-)\pi^+$ are weighed to the weighed $D_s^+ \to \pi^+\pi^+\pi^-$ candidates.

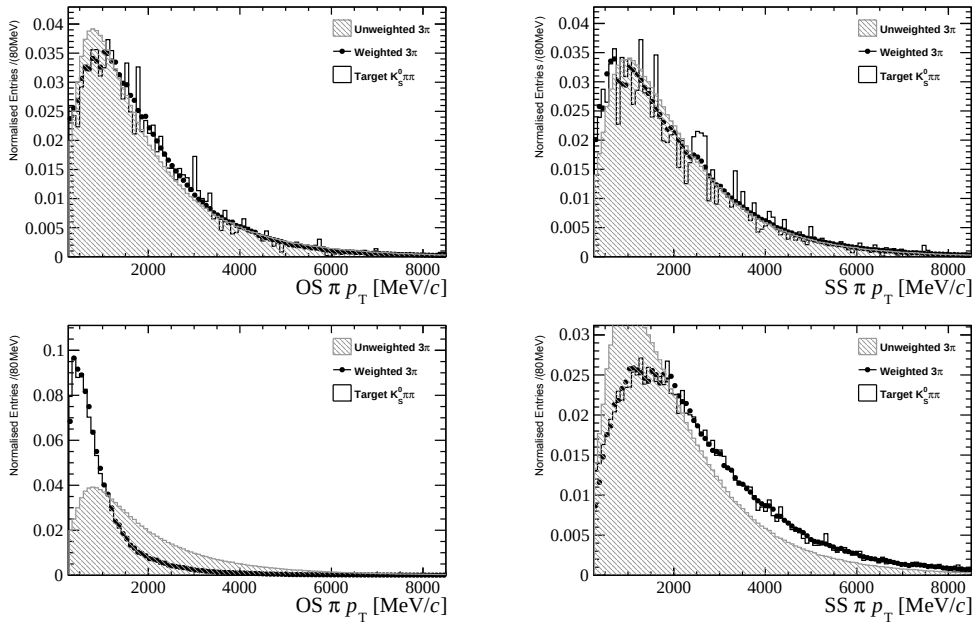

Figure 6.1 – Transverse momentum distributions of the opposite-sign (left) and same-sign (right) pion of the $\pi^+\pi^-$ pair for $D_s^+ \to \pi^+\pi^+\pi^-$ candidates before (hatched histogram) and after (data points) the reweighting procedure. The target distribution is given by (open histogram) $\overline{B} \to D^0(\to K_S^0\pi^+\pi^-)\mu^-\overline{\nu}_\mu X$ candidates. The top row shows candidates with small decay time ($t/\tau_{D^0} < 0.35$) and close to the Dalitz diagonal ($|\cos\theta_{\pi^+\pi^-}| < 0.25$), the bottom row shows candidates with large decay time ($t/\tau_{D^0} > 1.5$) and close to the edge of the kinematically allowed region ($|\cos\theta_{\pi^+\pi^-}| > 0.75$).

Events with weights larger than 10 times the average weight are discarded to stabilise the procedure. These events are accounted for less than 0.5% of the overall sample size. Figure 6.1 shows examples of $D_s^+ \to \pi^+\pi^+\pi^-$ distributions weighted to the $\overline{B} \to D^0(\to K_S^0\pi^+\pi^-)\mu^-\overline{\nu}_\mu X$ distributions. The effective yield of $D_s^+ \to \pi^+\pi^+\pi^-$ ($D_s^+ \to \phi(\to K^+K^-)\pi^+$) after the reweighting procedure varies between 25% and 60% (70% and 90%) of the original yield. These variation depends on Dalitz and decay time bins.

6.4.3 Determination of $\pi^+\pi^-$ detection asymmetry

The D_s^+ asymmetries are obtained from yields of fits to the mass distribution of the $D_s^+ \to \pi^+\pi^+\pi^-$ and $D_s^+ \to \phi(\to K^+K^-)\pi^+$ candidates. The signal shape is described by a sum of Gaussian and a Crystal-Ball distributions. The background shape is described by an exponential distribution. Figure 6.2 presents an example of a mass fit in one Dalitz region and decay time bin. As mentioned in Section 6.4.1, the asymmetry may be contaminated by different PID requirements which are not applied on the $\overline{B} \to D^0(\to K_S^0\pi^+\pi^-)\mu^-\overline{\nu}_\mu X$ selection. After subtraction of the PID asymmetry, the $\pi^+\pi^-$ detection asymmetry is shown in Figure 6.3 as a function of ($|\cos\theta_{\pi^+\pi^-}|, \tau$) and ($m^2(\pi^+\pi^-), |\cos\theta_{\pi^+\pi^-}|$). Figure 6.4 presents the weight average asym-

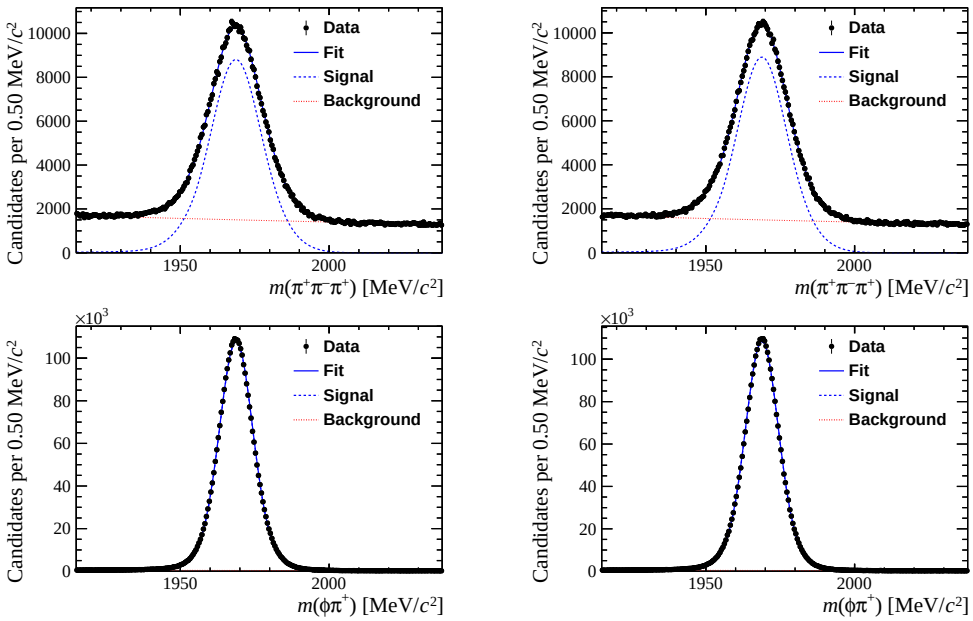

Figure 6.2 – $D_s^+ \to \pi^+\pi^+\pi^-$ (top) and $D_s^+ \to \phi(\to K^+K^-)\pi^+$ (bottom) mass distributions reweighted to $\overline{B} \to D^0(\to K_S^0\pi^+\pi^-)\mu^-\overline{\nu}_\mu X$ in phase space $|\cos\theta_{\pi^+\pi^-}| > 0.75$ and $t/\tau_{D^0} > 1.5$, shown separately for D_s^+ (left) and D_s^- (right), with fit results superimposed.

metry values of the combined data-taking years in each bin of $(|\cos\theta_{\pi^+\pi^-}|, \tau)$ and $(m^2(\pi^+\pi^-), |\cos\theta_{\pi^+\pi^-}|)$. Observed asymmetry in each data-taking year is reported in Appendix C. The obtained asymmetry, which represents the asymmetry on the $\overline{B} \to D^0(\to K_S^0\pi^+\pi^-)\mu^-\overline{\nu}_\mu X$, seems to be independent of Dalitz region and D^0 decay time. It is also compatible with zero.

6.4.4 Determination of systematic uncertainty

To incorporate the detection asymmetry measured in the D_s^+ sample, we multiply the efficiency determined in Sections 4.2.2 and 4.3 by

$$r(m^2(\pi^+\pi^-), |\cos\theta_{\pi^+\pi^-}|, \tau_{D^0}, \text{flavour}) = \begin{aligned} &1 + (\text{flavour} \times \text{sign}(|\cos\theta_{\pi^+\pi^-}|) \\ &\times A_{\text{det}}(\pi^+\pi^-; m^2(\pi^+\pi^-), |\cos\theta_{\pi^+\pi^-}|, \tau_{D^0})) \end{aligned} \tag{6.5}$$

where flavour is the flavour of D^0: $+1$ for D^0 and -1 for $\overline{D}^0$. The sign of $|\cos\theta_{\pi^+\pi^-}|$ is ± 1. $A_{\text{det}}(\pi^+\pi^-; m^2(\pi^+\pi^-), |\cos\theta_{\pi^+\pi^-}|, \tau_{D^0})$ is obtained from combining the asymmetry map of $(m^2(\pi^+\pi^-), |\cos\theta_{\pi^+\pi^-}|)$ of Figure 6.3 (top) injecting a time-dependence from a fit to $(|\cos\theta_{\pi^+\pi^-}|, t/\tau_{D^0})$ as shown in Figure 6.4. This assumes that the main effect of the time-dependence comes from only $|\cos\theta_{\pi^+\pi^-}|$. Then toys are rerun. The resulting systematic uncertainties are reported in Table 6.5 , where acceptance and resolution effects have been removed. There are little biases found on the measurement.

This asymmetry is smaller than what is observed in the prompt analysis [5]. The systematic

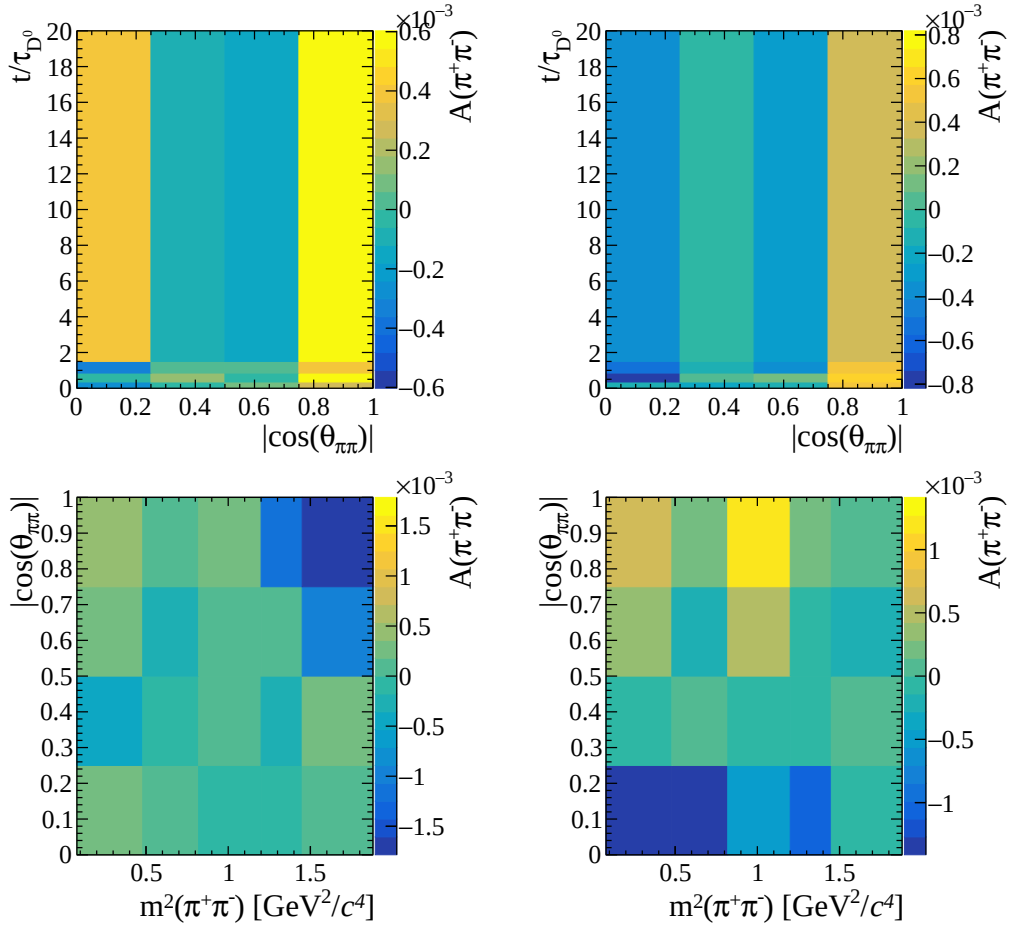

Figure 6.3 – Observed track detection asymmetry as a function of (top) ($|\cos\theta_{\pi^+\pi^-}|$, t/τ_{Dz}) and (bottom) ($m^2(\pi^+\pi^-)$, $|\cos\theta_{\pi^+\pi^-}|$), for the DD (left) and LL (right) categories. All data-taking years have been combined.

effects shown in the first part of Table 6.5 are quite small compared to the statistical uncertainty. Thus, a correction for this systematic effect is not necessary. The result from this procedure is taken as the nominal systematic uncertainties from this source.

As a cross-check, the systematic due to the detection asymmetry is estimated using asymmetric term from parametrised squared Dalitz plot as explained in Section 4.3. The asymmetry is added to the toy by using Equation (4.4) with the non-zero asymmetric terms. The terms are added from the fit as presented in Table 4.2 with Gaussian smearing to account for the uncertainties. The toys are rerun. The resulting systematics is reported in the second part of Table 6.5. The uncertainties are small compared to the statistical uncertainties.

Overall, systematics from detection asymmetries derived from different procedures are consistent and smaller than statistical uncertainties. We thus conclude that the systematic from this source is under control.

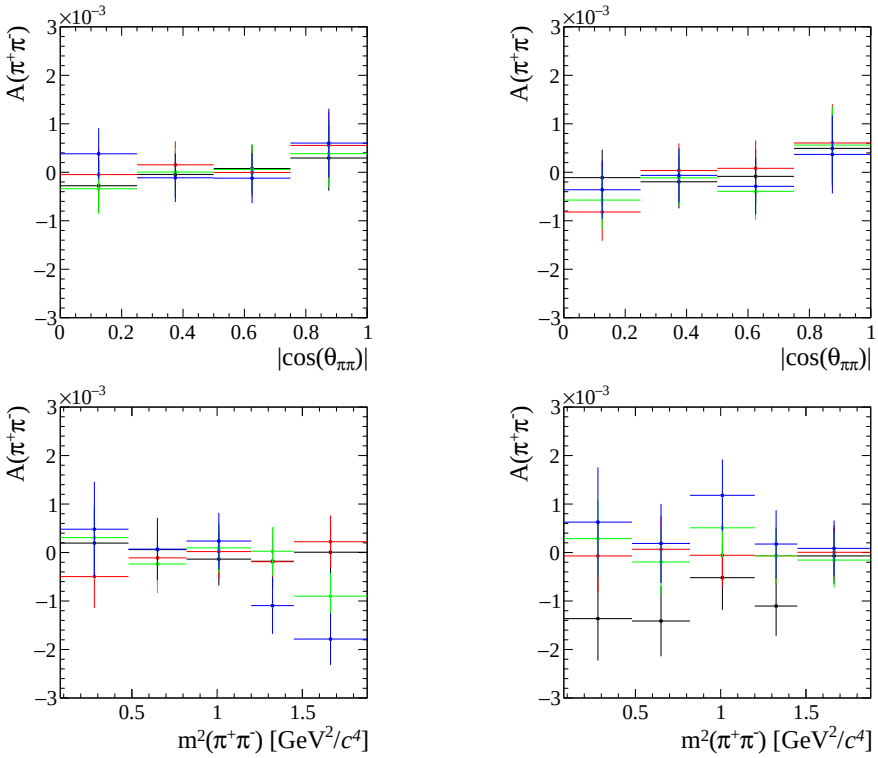

Figure 6.4 – Observed track detection asymmetry as a function of $|\cos\theta_{\pi^+\pi^-}|$ for each bin in t/τ_{D^0} (top) and as a function of $m^2(\pi^+\pi^-)$ for each bin in $|\cos\theta_{\pi^+\pi^-}|$ (bottom), separately for the DD (left) and LL (right) categories. The black, red, green, and blue points correspond to the bins in t/τ_{D^0} and $|\cos\theta_{\pi^+\pi^-}|$ in ascending order.

Table 6.5 – Systematic uncertainties in units of 10^{-3} resulting from detection asymmetries. The systematics uncertainties are with respect to acceptance and resolution effects. The first part of the table corresponds to the nominal method from which the systematic uncertainty of this source is estimated; the second parts represent cross-checks with the MC method.

Parameter	DD	LL	Comb.	Comb. (Shared r_b)
		Track asymmetry from reweighted D_s^+ samples		
$\sigma(x_{CP})$	$+0.060 \pm 0.017$	$+0.061 \pm 0.014$	$+0.060 \pm 0.016$	$+0.060 \pm 0.015$
$\sigma(y_{CP})$	$+0.027 \pm 0.022$	$+0.017 \pm 0.014$	$+0.024 \pm 0.017$	$+0.024 \pm 0.018$
$\sigma(\Delta x)$	-0.011 ± 0.012	-0.013 ± 0.010	-0.012 ± 0.010	-0.012 ± 0.010
$\sigma(\Delta y)$	-0.090 ± 0.015	-0.090 ± 0.010	-0.089 ± 0.012	-0.089 ± 0.012
		Asymmetry from MC		
$\sigma(x_{CP})$	-0.063 ± 0.015	-0.065 ± 0.013	-0.064 ± 0.015	-0.064 ± 0.015
$\sigma(y_{CP})$	-0.085 ± 0.020	-0.087 ± 0.018	-0.083 ± 0.017	-0.083 ± 0.017
$\sigma(\Delta x)$	$+0.035 \pm 0.010$	$+0.034 \pm 0.009$	$+0.034 \pm 0.008$	$+0.034 \pm 0.008$
$\sigma(\Delta y)$	$+0.016 \pm 0.014$	$+0.015 \pm 0.012$	$+0.015 \pm 0.012$	$+0.015 \pm 0.012$

6.5 Mass-fit models

In the bin-flip method, the ratio $R^{\pm}_{bj}$ is formed between yields in mirror Dalitz bins. The analysis is expected to be insensitive to the choice of a fit model. Indeed, any deviations that appears in the numerator is also present in the denominator of the ratio.

However, a possible systematic bias from implementing a specific PDF model to obtain the yields is examined by considering an alternative mass-fit model. The systematic uncertainty from the mass fit is estimated by changing the signal model explained in Section 5.1 from the Johnson distribution to Crystal ball function. The Crystal Ball distribution is defined as

$$\mathscr{C}(x|\mu,\sigma,\alpha,n) = \mathscr{N}_{\mathscr{C}} \cdot \begin{cases} \exp\left(-\frac{(x-\mu)^2}{2\sigma^2}\right) & \text{if } \frac{x-\mu}{\sigma} > -\alpha \\ A \cdot \left(B - \frac{x-\mu}{\sigma}\right)^{-n} & \text{if } \frac{x-\mu}{\sigma} \leq -\alpha \end{cases} \tag{6.6}$$

where

$$\begin{aligned} A &= \left(\frac{n}{|\alpha|}\right)^n \cdot \exp\left(-\frac{\alpha^2}{2}\right) \\ B &= \frac{n}{|\alpha|} - |\alpha| \end{aligned} \tag{6.7}$$

and $\mathscr{N}_{\mathscr{C}}$ is a normalization factor. This distribution consists of a Gaussian core with mean parameter μ and standard deviation σ and low-end decay tail with parameters α and n. Note that α is larger than zero. So the signal PDF is then

$$\wp_{\text{sig}}(M(K^0_S\pi^+\pi^-)) = f_1\mathscr{C}(M(K^0_S\pi^+\pi^-)|\mu,\sigma,\alpha,n) + (1-f_1)\mathscr{B}(M(K^0_S\pi^+\pi^-)|\mu,\sigma_L,\sigma_R);. \tag{6.8}$$

Then, the sensitivity of the background model is further validated with an alternative simple polynomial model:

$$\mathscr{P}(x|a_0) = \frac{1}{\mathscr{N}_1}(a_0x+1) \tag{6.9}$$

$$\mathscr{P}(x|a_0,a_1) = \frac{1}{\mathscr{N}_2}\left(a_1x^2 + a_0x + 1\right). \tag{6.10}$$

The signal shape in the latter case is kept to similar to the signal model in Section 5.1. The total PDFs are implemented separately to fit on the same toy generated in Section 6.3. As a priori, the alternative joint model is fit on the combined bin data as shown in Figure 6.5. This shows that this alternative model can describe the D^0 mass distribution. Table 6.7 presents the resulting estimated systematics uncertainties which for each of the individual samples, as well as for the combined fit for alternative signal, alternative background model, and joint alternative fit models.

Since the polynomial distribution may be unstable, PDF used for toy generations and fit are inverted to further test the stability, *i.e.* the joint alternative PDF model is used to generate toys and the mass distribution is fit with the default model. This is shown in the last row of

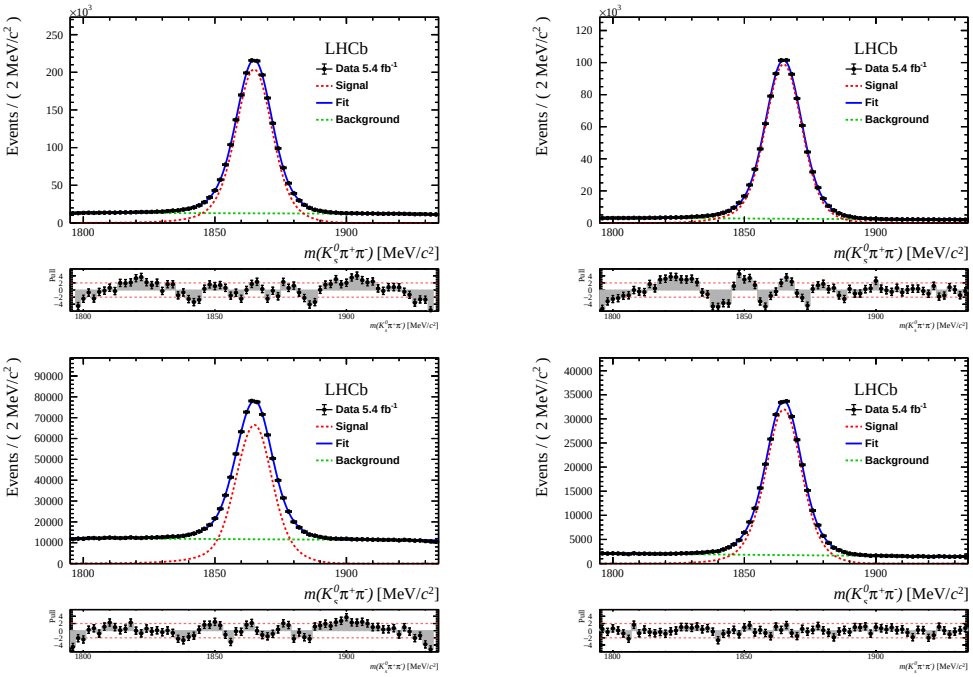

Figure 6.5 – $K^0_S\pi^+\pi^-$ invariant mass distribution of the DD (left) and LL (right) candidates after all selection requirements. The curves show the results of a fit with the joint alternative model with signal (red) and combinatorial background (green) components.

Table 6.6 – Fit parameters of the $K^0_S\pi^+\pi^-$ invariant mass of $\overline{B} \to D^0(\to K^0_S\pi^+\pi^-)\mu^-\overline{\nu}_\mu X$ candidates as shown in Figure 6.5. Note that μ, σ, $\Delta\mu$, σ_L, and σ_R have units of MeV/c^2. a_0 and a_1 have units of $\left(\text{MeV}/c^2\right)^{-1}$ and $\left(\text{MeV}/c^2\right)^{-2}$, respectively. Others are dimensionless.

Parameter	DD		LL	
	Negative Dalitz	Positive Dalitz	Negative Dalitz	Positive Dalitz
α	1.220 ± 0.017	1.470 ± 0.011	1.660 ± 0.034	4.64 ± 0.71
μ	1865.489 ± 0.016	1864.155 ± 0.013	1864.424 ± 0.094	1864.820 ± 0.011
n	10.00	10.00	10.00	10.00
σ	10.179 ± 0.050	11.443 ± 0.035	10.21 ± 0.20	6.429 ± 0.022
$\Delta\mu$	-0.4680 ± 0.021	0.787 ± 0.015	0.654 ± 0.094	2.451 ± 0.044
σ_L	6.468 ± 0.021	6.231 ± 0.014	5.89 ± 0.11	15.05 ± 0.14
σ_R	5.879 ± 0.021	6.277 ± 0.013	5.906 ± 0.100	10.676 ± 0.086
f_1	0.4143 ± 0.0033	0.3496 ± 0.0021	0.447 ± 0.026	0.7396 ± 0.0052
$a_0\left[\times 10^{-4}\right]$	-2.81 ± 0.73	-3.30 ± 0.50	-4.487 ± 0.020	-4.621 ± 0.012
$a_1\left[\times 10^{-8}\right]$	-0.13 ± 5.82	0.00 ± 6.54	0 (fixed)	0 (fixed)
N_{bkg}	816927 ± 1051	888754 ± 1289	123147 ± 567	184007 ± 663
N_{sig}	625537 ± 999	1911136 ± 1581	293200 ± 701	918679 ± 1083

Table 6.7. The numbers are biases with respect to the bias from resolution and selection effects. The systematic with this row is used and assigned as the final systematic from the fit model.

Table 6.7 – Systematic uncertainties in units of 10^{-3} resulting from possible mis-modelling of the mass PDF's. The systematics uncertainties are with respect to acceptance and resolution effects.

Parameter	DD	LL	Comb.	Comb. (Shared r_b)
		Alternative signal model		
$\sigma(x_{CP})$	$+0.003 \pm 0.011$	$+0.003 \pm 0.011$	$+0.005 \pm 0.011$	$+0.005 \pm 0.011$
$\sigma(y_{CP})$	-0.139 ± 0.018	-0.126 ± 0.021	-0.133 ± 0.015	-0.133 ± 0.016
$\sigma(\Delta x)$	-0.019 ± 0.007	-0.019 ± 0.007	-0.019 ± 0.007	-0.019 ± 0.007
$\sigma(\Delta y)$	$+0.007 \pm 0.011$	$+0.002 \pm 0.014$	$+0.005 \pm 0.012$	$+0.005 \pm 0.012$
		Alternative background model		
$\sigma(x_{CP})$	-0.060 ± 0.025	-0.059 ± 0.025	-0.058 ± 0.020	-0.057 ± 0.021
$\sigma(y_{CP})$	-0.186 ± 0.043	-0.187 ± 0.047	-0.180 ± 0.038	-0.182 ± 0.038
$\sigma(\Delta x)$	-0.032 ± 0.013	-0.030 ± 0.013	-0.031 ± 0.011	-0.031 ± 0.011
$\sigma(\Delta y)$	$+0.037 \pm 0.023$	$+0.032 \pm 0.031$	$+0.035 \pm 0.020$	$+0.035 \pm 0.020$
		Alternative signal and background model		
$\sigma(x_{CP})$	-0.055 ± 0.024	-0.057 ± 0.024	-0.053 ± 0.020	-0.053 ± 0.019
$\sigma(y_{CP})$	-0.180 ± 0.043	-0.176 ± 0.045	-0.173 ± 0.034	-0.173 ± 0.035
$\sigma(\Delta x)$	-0.030 ± 0.013	-0.029 ± 0.012	-0.030 ± 0.011	-0.030 ± 0.011
$\sigma(\Delta y)$	$+0.035 \pm 0.023$	$+0.033 \pm 0.029$	$+0.034 \pm 0.019$	$+0.034 \pm 0.019$
		Generate with alternative joint model, fit with default model		
$\sigma(x_{CP})$	$+0.023 \pm 0.011$	$+0.030 \pm 0.011$	$+0.024 \pm 0.010$	$+0.024 \pm 0.011$
$\sigma(y_{CP})$	$+0.091 \pm 0.014$	$+0.104 \pm 0.010$	$+0.094 \pm 0.012$	$+0.095 \pm 0.013$
$\sigma(\Delta x)$	-0.006 ± 0.011	-0.006 ± 0.012	-0.007 ± 0.010	-0.007 ± 0.010
$\sigma(\Delta y)$	$+0.005 \pm 0.012$	$+0.006 \pm 0.012$	$+0.005 \pm 0.012$	$+0.005 \pm 0.012$

6.6 Unrelated $D^0\mu^-$ combination

The D^0 or $\overline{D}^0$ flavour is tagged using the charge of the accompanying muon. The main systematic uncertainty in this analysis is expected to come from the mistag probability, *i.e.* the probability that the D^0 flavour is wrongly assigned. The main source of this mistag is unrelated $D^0\mu^-$ combinations where the muon does not come from the same b hadron as the D^0.

In the Run 1 analysis [63], this was estimated using $\overline{B}^0 \to D^{*+}(\to D^0\pi^+)\mu^-\overline{\nu}X$ (DoubleTag, DT) events assuming the same mistag probability in DoubleTag and $\overline{B} \to D^0(\to K^0_S\pi^+\pi^-)\mu^-\overline{\nu}_\mu X$ (SingleTag, ST) events. This DoubleTag sample is reconstructed like the $\overline{B} \to D^0(\to K^0_S\pi^+\pi^-)\mu^-\overline{\nu}_\mu X$ sample, but with an additional pion at the B decay vertex. The pion track is required to be compatible with the tracks originating from the $D^0\mu^-$ vertex

This sample can be representative of the $\overline{B} \to D^0(\to K^0_S\pi^+\pi^-)\mu^-\overline{\nu}_\mu X$ sample if the additional pion track does not affect the mistag probability. We separate the sample into two subsamples: a right-sign ($B \to D^{*+}(\to D^0\pi^+_s)\mu^- X$) and a wrong-sign ($B \to D^{*+}(\to D^0\pi^+_s)\mu^+ X$) subsample where the true flavour of the D^0 is given by the charge of the soft pion (π^+_s) reconstructed at the B decay vertex. The mistag probability is computed as the fraction of $B \to D^{*+}(\to D^0\pi^+_s)\mu^+ X$ within the whole DoubleTag sample.

We study the mistag probability as a function of the quality of the $D^0\pi^+_s\mu^-$ vertex (χ^2_{DV}/ndof). Figure 6.6 presents the mistag probability as a function of the D^0 decay time in the $B \to D^*(\to D^0\pi^+_s)\mu X$ sample, after trigger selection and preselection only. There are no MVA selections applied, but $\chi^2_{\mathrm{DV}}/\mathrm{ndof} < 6$ is required. We use the binning of Equation (1.28). We then tighten the requirement of χ^2_{DV}/ndof to less than 5, 4, 3, and 2. The mistag probabilities in these cases are presented in Figure 6.7. This shows that the average values of the mistag probabilities decrease as the selection is tightened. This implies that the mistag probability depends on this B vertex quality. Because the number of degrees of freedom of the B decay vertex in the DoubleTag is different from the SingleTag due to the additional pion, the χ^2 distributions between the two cases are different. We conclude that the $B \to D^*(\to D^0\pi^+_s)\mu X$ sample is incapable of representing $\overline{B} \to D^0(\to K^0_S\pi^+\pi^-)\mu^-\overline{\nu}_\mu X$ for the mistag estimation.

Therefore a new method for estimating systematic uncertainties due to unrelated $D^0\mu^-$ combinations must be determined. We investigate the possibility of using the $D^0 \to K^-\pi^+$ decay channel in this scope. First, the mistag probability may depend on the D^0 decay time as studied in the semileptonic A_Γ analysis [122]. Such dependency may interfere significantly with the measurement and result in a large bias on the x_{CP} measurement. This is investigated in detail in Section 6.6.1. Then the method to determine the mistag probability is constructed in Section 6.6.2. This is done by comparing the mistag probability between the two D^0 decays, $K^0_S\pi^+\pi^-$ and $K\pi$ in their DoubleTag decay chains. Although the DoubleTag sample is not a suitable representative of the SingleTag, the validation on the mistag procedure is still valid and comparable within each tag. Finally, the mistag probabilities are determined in Section 6.6.3, and systematics due to this source is estimated on toys as explained in Section 6.6.4.

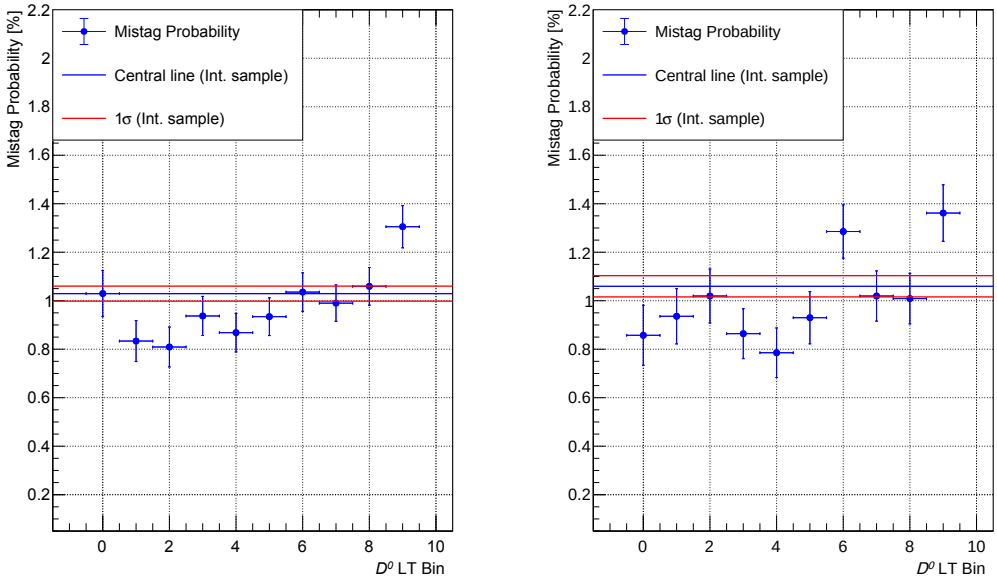

Figure 6.6 – Mistag probability as a function of the D^0 decay time in the $B \to D^*(\to D^0\pi_s^+)\mu X$ sample. Vertex quality of B decay vertex over number of degrees of freedom is required to be lower than 6 ($\chi^2_{\mathrm{DV}}/\mathrm{ndof} < 6$). This cut is applied already in the stripping selection.

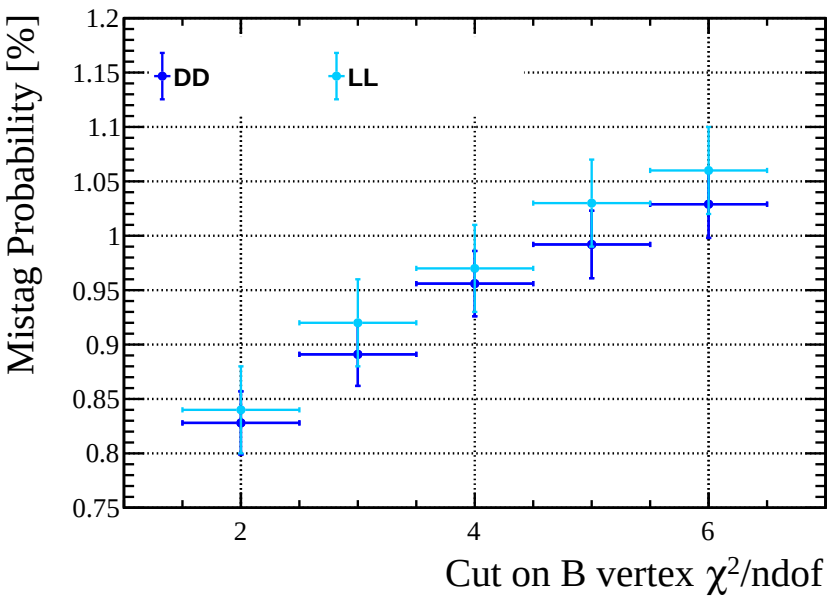

Figure 6.7 – Mistag probability as a function of the D^0 decay time and requirement on $\chi^2_{\mathrm{DV}}/\mathrm{ndof}$ in the $B \to D^*(\to D^0\pi_s^+)\mu X$ sample.

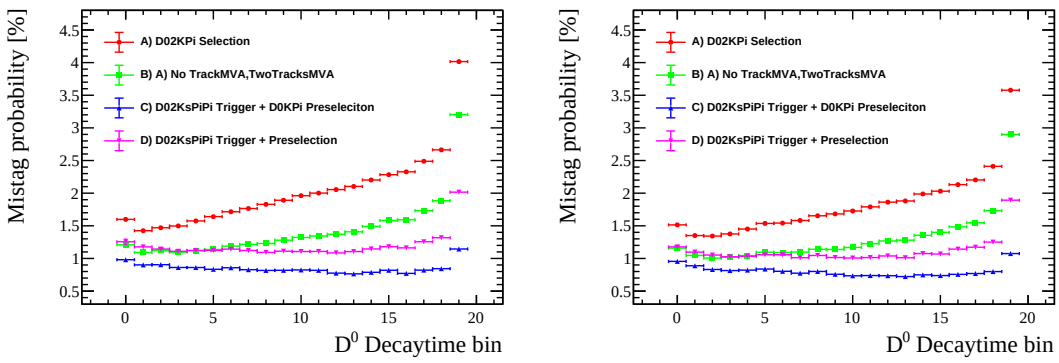

Figure 6.8 – Comparison of the mistag probability in the $\overline{B} \to D^0(\to K^-\pi^+)\mu^-\overline{\nu}_\mu X$ with different trigger requirements and preselections for 2017 (left), 2018 (right).

6.6.1 Decay-time dependence

As a first step, we study the decay-time dependence of the mistag probability in $\overline{B} \to D^0(\to K^-\pi^+)\mu^-\overline{\nu}_\mu X$ channel. In each decay-time bin, we form the ratio between the yields found in the wrong-sign sample over the right-sign sample R_{mistag}. Then we define the mistag probability as

$$\text{Mistag probability} = \frac{R_{\text{mistag}}}{1 + R_{\text{mistag}}} \tag{6.11}$$

Yields are extracted from a fit of the $K^-\pi^+$ invariant mass. This ratio is subtracted by the known values of mixing and Doubly-Cabibbo suppressed (DCS) decay as a function of the D^0 decay time [123]. We use an average decay time for each bin weighted with `sWeight` from the fit on the $K^-\pi^+$ invariant mass to compute the expected fraction of mixed and DCS events. As the statistics is high in this sample, the D^0 decay time binning scheme is changed to

$$\begin{aligned}[0.00, 0.12, 0.21, 0.30, 0.39, 0.48, 0.57, 0.66, 0.76, 0.87, 0.99, 1.10, 1.25,\\ 1.40, 1.60, 1.80, 2.00, 2.20, 2.52, 3.00, 15.00, 20.00]\,\tau_{D^0}\end{aligned} \tag{6.12}$$

The binning scheme is similar to the one used in the semileptonic A_Γ analysis [122]. In that analysis, the probability is found to be dependent on the D^0 decay time. However, the A_Γ analysis uses different sets of online selections which consider all tracks in the B decay chain (namely `B_HLT1TrackMVADecision_TOS` and `B_HLT1TwoTracksMVADecision_TOS`) while this analysis utilises only on a muon track (`mu_HLT1TrackMuonDecision_TOS` and `mu_HLT1TrackMuonMVADecision_TOS`). In addition, the topological trigger is also applied as shown in Table 3.2. Figure 6.8 presents a comparison between different scenarios of trigger and preselections on this control channel in 2017 and 2018 data-taking years. Note that the 2016 data-taking year is not available for this sample. Only online selection and preselections are appiled here. The `B_HLT1TrackMVADecision_TOS` and `B_HLT1TwoTracksMVADecision_TOS` tend to enhance the time-dependency, while the `B_HLT2TopoMu{2,3,4}Decision_TOS` seem to flatten the dependency. The difference in preselections between this analysis and

the A_Γ analyses only adjust the offset of the mistag. The trends are consistent among the data-taking years. Therefore, the mistag probability in our case is not time dependent and a single value can be used. This hypothesis is additionally tested further on.

6.6.2 Determination of method and cross-check on $D^0 \to K^-\pi^+$ channel

To validate whether the mistag probability in the $K\pi$ channel is a representative of the mistag probability in $K^0_S\pi^+\pi^-$, we analyse both channels in their DoubleTag samples. The $D^0 \to K^-\pi^+$ channel has benefits such that one can estimate mistag both through a DoubleTag sample as well as directly from SingleTag, by comparing the sign of the kaon and muon after accounting for DCS and mixing effects. It is discovered that the mistag probability as determined on the DoubleTag sample is not representative of the mistag probability on the SingleTag sample in the previous section.

In the DoubleTag $K^0_S\pi^+\pi^-$ final state, samples are acquired from the stripping line `b2DstarMuXKsPiPi{DD,LL}CharmFromBSemiLine`. The selection is similar to the one described in Chapter 3 but with the additional requirement that the slow pion ($\pi^-{}_s$) comes from the same vertex as the D^0. The DoubleTag $K\pi$ final state is obtained from `Turbo` line, similar to the SingleTag $K\pi$. The `Turbo` line allows to perform candidate selections during online event reconstruction without storing the full raw sub-detector data. This is different from `stripping` where the candidates are reconstructed offline [88]. The mistag probability between the DoubleTag and SingleTag samples is not directly comparable as discussed. The mistag in the DoubleTag sample is determined from the charges of the accompanying particles (soft pion and the muon candidate), while in the SingleTag sample, it is determined from the charges of muon and daughter of the D^0.

To test the consistency between different D^0 final states of the DoubleTag samples, the samples are processed with a selection procedure similar to the one described in Chapter 3. Two MVA models trained on different types of K^0_S are used in this analysis. The MVA models, developed in this analysis for DD and LL $\overline{B} \to D^0(\to K^0_S\pi^+\pi^-)\mu^-\overline{\nu}_\mu X$ samples, are applicable to the $\overline{B} \to D^0(\to K^-\pi^+)\mu^-\overline{\nu}_\mu X$ as the models are trained using only topological variables of $\overline{B} \to D^0\mu^-\overline{\nu}_\mu X$ decay as explained in Table 3.4. They are applied independently on the same $K^-\pi^+$ sample. This splits the $\overline{B} \to D^0(\to K^-\pi^+)\mu^-\overline{\nu}_\mu X$ sample to two samples. For consistency, the two samples of $\overline{B} \to D^0(\to K^-\pi^+)\mu^-\overline{\nu}_\mu X$ are denoted as DD and LL depending on the MVA model applied. Multiple candidate and clone rejection are also applied on top of the selections. It should be noted that the selection applied here is similar to the one applied on the $\overline{B} \to D^0(\to K^0_S\pi^+\pi^-)\mu^-\overline{\nu}_\mu X$. This is different from Figure 6.8 where only trigger and preselections are applied. The MVA selection does not induce further D^0 decay time dependency, and also reduces the mistag probabilities.

Any nuisance deviations are treated further with reweighting procedure to match kinematics between $K\pi$ and $K^0_S\pi^+\pi^-$ final states. A Gradient Boosting reweighter [103] is implemented to match the kinematics of the DoubleTag $B \to D^*(\to D^0\pi^+_s)\mu X$ decays followed by $D^0 \to K^-\pi^+$

and $D^0 \to K^0_S\pi^+\pi^-$. Topological variables related to B decay including B decay vertex χ^2, transverse momentum of the μ and D^0 candidate, and D^0 pseudorapidity are used as training variables. We divide each sample in training and testing samples for tuning the reweighter to avoid a possible overtraining. The training variables are described in Appendix D.

The mistag probabilities are determined with Equation (6.11) where the mixing and DCS effects are subtracted in the $K\pi$ final state. Such effects are expected in the $K^0_S\pi^+\pi^-$ channel, but they do not influence the measured mistag probabilities, which come from the soft pion charge. A fit of the distribution of the difference between the $K^0_S\pi^+\pi^-\pi^+_s$ and $K^0_S\pi^+\pi^-$ masses (ΔM) is performed. The Johnson distribution is used for describing the signal. The background is modelled as a two-body phase-space distribution. The mistag probability is defined as a fraction of a wrong sign sample over the total number found in wrong sign and right sign samples.

Figure 6.9 represent comparisons between mistag probability across different samples in the DoubleTag. The mistag probabilities in the DoubleTag samples are consistent between $K^0_S\pi^+\pi^-$ and $K\pi$. This shows that the mistag found on $K\pi$ is representative for $K^0_S\pi^+\pi^-$.

6.6.3 Determination of mistag probability

As discussed in the previous section, the mistag probability is similar within each tag between different D^0 final states. The same procedure is applied to reweigh the $\overline{B} \to D^0(\to K^-\pi^+)\mu^-\overline{\nu}_\mu X$ sample to the $\overline{B} \to D^0(\to K^0_S\pi^+\pi^-)\mu^-\overline{\nu}_\mu X$ sample. The reweighters are trained separately for SingleTag and DoubleTag because the B decay vertex is formed differently in the two samples. The decay vertex of the SingleTag sample is constructed from D^0 and μ, while the DoubleTag has an additional track from a slow pion (π^+_s). This results in different numbers of degrees of freedom between these samples, and hence χ^2 distributions. Figure 6.10 presents the mistag probability as a function of the D^0 decay time. The mistag probability with the LL MVA model is lower than the one with the DD MVA model.

The probabilities fluctuate around the value found in the whole sample within uncertainties which implies that this mistag probability is independent of the D^0 decay time. The linear regressions to the mistag probabilities in Figures 6.9 and 6.10 lead to slope coefficients consistent with zero. Therefore, we decide to use the average values of the mistag probabilities. We estimate the mistag probability for $\overline{B} \to D^0(\to K^0_S\pi^+\pi^-)\mu^-\overline{\nu}_\mu X$ ($\omega_{\mathrm{ST},K^0_S\pi^+\pi^-}$) as the mistag probability for $\overline{B} \to D^0(\to K^-\pi^+)\mu^-\overline{\nu}_\mu X$ ($\omega_{\mathrm{ST},K\pi}$) multiplied by a scale factor obtained as the ratio of the mistag probabilities in the corresponding DoubleTag samples.

$$\omega_{\mathrm{ST},K^0_S\pi^+\pi^-} = \frac{\omega_{\mathrm{DT},K^0_S\pi^+\pi^-}}{\omega_{\mathrm{DT},K\pi}}\omega_{\mathrm{ST},K\pi} \tag{6.13}$$

The scale factors are shown for each years in Table 6.8 and Table 6.9 for the DD and LL categories. Note that the $D^0 \to K^-\pi^+$ sample is not available for the 2016 data-taking year and

that the combined values only include 2017 and 2018 data-taking years. These final mistag probabilities are (0.301 ± 0.016) % for the DD sample and (0.125 ± 0.010) % for the LL sample.

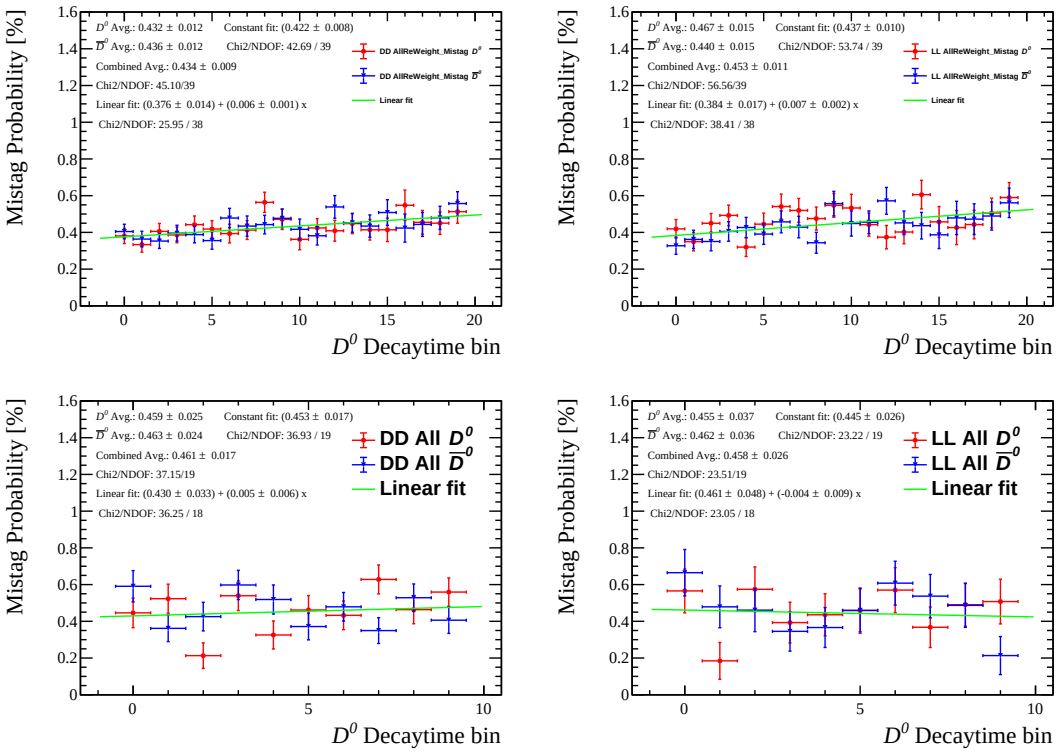

Figure 6.9 – Mistag probability as a function of the D^0 decay time separately for D^0 and $\overline{D}^0$ in the reweighted $\overline{B}^0 \to D^{*+}(\to D^0\pi^+)\mu^- X$ with final state: (Top) $D^0 \to K^-\pi^+$, (Bottom) $D^0 \to K_S^0\pi^+\pi^-$, (Left) K_S^0 DD MVA, (Right) K_S^0 LL MVA.

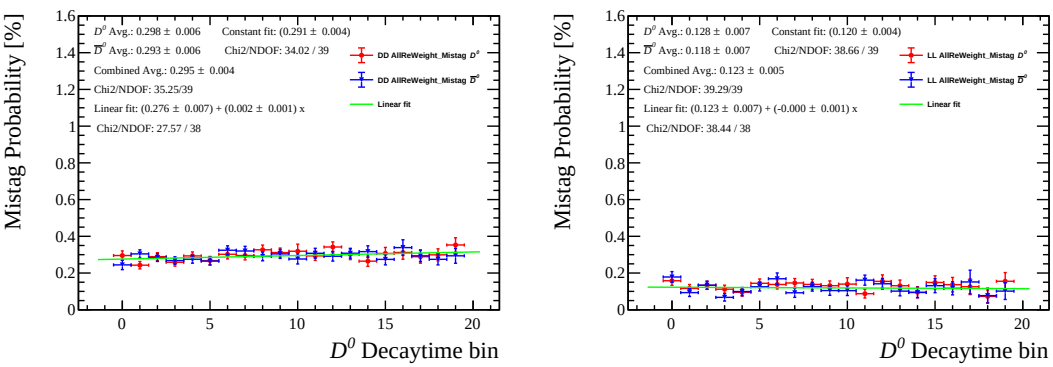

Figure 6.10 – Mistag probability as a function of the D^0 decay time separately for D^0 and $\overline{D}^0$ in the reweighted $\overline{B} \to D^0(\to K^-\pi^+)\mu^-\overline{\nu}_\mu X$ sample. MVA selection is applied with the model trained on K_S^0 DD (left) and K_S^0 LL (right).

Table 6.8 – Mistag probability for $\overline{B} \to D^0\mu^-\overline{\nu}_\mu X$ and $B \to D^*(\to D^0\pi_s^+)\mu X$ with final states $D^0 \to K^-\pi^+$ and $D^0 \to K_S^0\pi^+\pi^-$. The $D^0 \to K^-\pi^+$ sample is reweighted to $D^0 \to K_S^0\pi^+\pi^-$ with the DD K_S^0 category. Scaling factors are also shown for separated and combined years.

Year	D^0 final state	$\overline{B} \to D^0\mu^-\overline{\nu}_\mu X$	$B \to D^*(\to D^0\pi_s^+)\mu X$	Scale factor
2016	$D^0 \to K^-\pi^+$	–	–	-
	$D^0 \to K_S^0\pi^+\pi^-$	–	0.516 ± 0.033	
2017	$D^0 \to K^-\pi^+$	0.307 ± 0.007	0.428 ± 0.013	1.114 ± 0.078
	$D^0 \to K_S^0\pi^+\pi^-$	0.342 ± 0.025	0.477 ± 0.030	
2018	$D^0 \to K^-\pi^+$	0.288 ± 0.007	0.435 ± 0.012	0.943 ± 0.067
	$D^0 \to K_S^0\pi^+\pi^-$	0.271 ± 0.020	0.410 ± 0.027	
2017 - 2018	$D^0 \to K^-\pi^+$	0.295 ± 0.004	0.434 ± 0.009	1.022 ± 0.051
	$D^0 \to K_S^0\pi^+\pi^-$	0.301 ± 0.016	0.444 ± 0.020	

Table 6.9 – Mistag probability for $\overline{B} \to D^0\mu^-\overline{\nu}_\mu X$ and $B \to D^*(\to D^0\pi_s^+)\mu X$ with final states $D^0 \to K^-\pi^+$ and $D^0 \to K_S^0\pi^+\pi^-$. The $D^0 \to K^-\pi^+$ sample is reweighted to $D^0 \to K_S^0\pi^+\pi^-$ with the LL K_S^0 category. Scaling factors are also shown for separated and combined years.

Year	D^0 final state	$\overline{B} \to D^0\mu^-\overline{\nu}_\mu X$	$B \to D^*(\to D^0\pi_s^+)\mu X$	Scale factor
2016	$D^0 \to K^-\pi^+$	–	–	-
	$D^0 \to K_S^0\pi^+\pi^-$	–	0.464 ± 0.048	
2017	$D^0 \to K^-\pi^+$	0.131 ± 0.007	0.465 ± 0.016	1.022 ± 0.103
	$D^0 \to K_S^0\pi^+\pi^-$	0.134 ± 0.015	0.475 ± 0.045	
2018	$D^0 \to K^-\pi^+$	0.120 ± 0.006	0.446 ± 0.014	1.002 ± 0.099
	$D^0 \to K_S^0\pi^+\pi^-$	0.120 ± 0.013	0.447 ± 0.042	
2017 - 2018	$D^0 \to K^-\pi^+$	0.123 ± 0.005	0.453 ± 0.011	1.018 ± 0.072
	$D^0 \to K_S^0\pi^+\pi^-$	0.125 ± 0.010	0.461 ± 0.031	

6.6.4 Determination of systematic uncertainty

The mistag probability determined in Section 6.6.3 are used to generate an ensemble of toy with resolution and efficiencies included. The fraction of random $D^0\mu^-$ combinations of the $D^0\mu^-$ is twice of the mistag probability because a random combination may have the right-sign of $D^0\mu^-$. The PDF of the D^0 decay time resolution is Gaussian with a width of 0.5 τ_{D^0} for mistagged events. This number, 0.5 τ_{D^0}, is taken directly from Run 1 analysis note [65].

We test on the procedure explained above and toys are generated with the averaged mistag probability found in the SingleTag $\overline{B} \to D^0(\to K^-\pi^+)\mu^-\overline{\nu}_\mu X$ with scaling factor from the

DoubleTag. Note that we assume the mistag probability in 2016 data taking year to be equal to the average of the ones in 2017 and 2018. In cases where a smeared event would fall out of decay time acceptance, it is mirrored back in. This measure ensures that the decay-time dependence remains flat, as otherwise lower bins lose mistagged events compared to other bins and cause an artificial decay-time dependence of the mistag. We also present studies with mistag probability set to 0.5% as a comparison to mistag probability estimated in the Run I analysis.

The systematic uncertainties in these cases are shown in Table 6.10 for each individual and combined samples. The values are with respect to resolution and selection effects. The first part of Table 6.10 is taken as systematics uncertainties. The second part presents the resulting uncertainties from higher mistag probabilities. This shows that by increasing the mistag probability mainly has an impact on the measurement on x_{CP} and y_{CP}. For the systematic uncertainty on x_{CP}, is reduced by almost a factor of 4 comparing with the systematics estimated in the analysis of the Run 1 data [63].

Table 6.10 – Systematic uncertainties in units of 10^{-3} resulting from mistag. The systematics uncertainties are with respect to acceptance and resolution effects.

Parameter	DD	LL	Comb.	Comb. (Shared r_b)
	Mistag probability measured on $\overline{B} \to D^0(\to K^-\pi^+)\mu^-\overline{\nu}_\mu X$			
$\sigma(x_{CP})$	-0.241 ± 0.034	-0.243 ± 0.034	-0.236 ± 0.029	-0.236 ± 0.029
$\sigma(y_{CP})$	-0.210 ± 0.067	-0.239 ± 0.068	-0.209 ± 0.058	-0.210 ± 0.058
$\sigma(\Delta x)$	$+0.004 \pm 0.016$	$+0.004 \pm 0.015$	$+0.003 \pm 0.014$	$+0.003 \pm 0.014$
$\sigma(\Delta y)$	-0.042 ± 0.027	-0.039 ± 0.033	-0.042 ± 0.021	-0.042 ± 0.021
	Mistag probability = 0.5%			
$\sigma(x_{CP})$	-0.265 ± 0.045	-0.275 ± 0.047	-0.267 ± 0.038	-0.268 ± 0.038
$\sigma(y_{CP})$	-0.621 ± 0.081	-0.629 ± 0.081	-0.610 ± 0.076	-0.610 ± 0.076
$\sigma(\Delta x)$	-0.001 ± 0.019	-0.001 ± 0.022	-0.001 ± 0.016	-0.001 ± 0.016
$\sigma(\Delta y)$	-0.062 ± 0.036	-0.060 ± 0.046	-0.061 ± 0.030	-0.061 ± 0.030

6.7 Summary of final uncertainties

The uncertainties affecting the measurement is reported in Table 6.11. The total systematic uncertainty is the sum in quadrature of the individual components. The statistical uncertainty includes, by default, also the contribution of the uncertainties on the strong phase inputs. All sources of systematics are considered as uncorrelated.

To test the robustness of the analysis, several cross-checks are performed. The analysis is repeated in subsets of data, dividing the sample by K_S^0 categories, data-taking periods, magnet polarities, and kinematics of the B meson. Variations of the observables x_{CP}, y_{CP}, Δx, and Δy are all compatible within statistical fluctuations. The analysis is generally very robust to any changes in each step. Results from the bin-flip fit are consistent within statistical uncertainties when an alternative method is implemented in the efficiency correction process. Similar compatibility is observed when the selection process is altered, *e.g.* a different procedure is used for the multivariate analysis. These cross-checks further demonstrate the reliability and robustness of the analysis.

Table 6.11 – Summary of the uncertainties in units of 10^{-3} on the measured quantities. The total systematic uncertainty is the sum in quadrature of the individual components. The uncertainties due to the strong phase inputs are (by default) included in the statistical uncertainty. Here, to ease comparison with other sources, we also report the separate contributions due to the strong phase inputs and to the statistics of our data.

Source	x_{CP}	y_{CP}	Δx	Δy
Reconstruction and selection	0.058	0.790	0.278	0.238
Detection asymmetry	0.063	0.031	0.015	0.089
Mass-fit model	0.028	0.096	0.005	0.005
Unrelated $D^0\mu$ combinations	0.244	0.219	0.013	0.051
Total systematic	0.259	0.826	0.278	0.259
Strong phase inputs	0.32	0.68	0.16	0.21
Statistical (w/o phase inputs)	1.45	3.04	0.92	1.91
Statistical	1.48	3.12	0.93	1.92

6.7.1 Systematic correlation matrix

To propagate the fitted parameter to the oscillation parameters x, y, $|q/p|$ and ϕ. The systematic correlation is needed.

For each systematic uncertainty (S), the correlation matrix of the biases is calculated as follows. For each toy, we calculate the residuals of fit parameters i between the fitted one (i_{fit}) and the fit result of the reference fit (i_{ref}) as described in Section 6.2: $\delta_i = i_{fit} - i_{ref}$. The correlation of the residuals is calculated as

$$\rho^S_{\delta_i,\delta_j} = \frac{\mathrm{cov}(\delta_i,\delta_j)}{\sigma_{\delta_i}\sigma_{\delta_j}}, \tag{6.14}$$

where the usual formulae are used for the sample covariance and standard deviation. To calculate a total correlation matrix ($\rho^{total}_{i,j}$), the correlation matrix for each systematic ($\rho^S_{i,j}$) is weighted by its respective biases given above:

$$\rho^{\mathrm{total}}_{i,j}\sigma^{\mathrm{total}}_i\sigma^{\mathrm{total}}_j = \sum_S \rho^S_{\delta_i,\delta_j}\sigma^S_i\sigma^S_j. \tag{6.15}$$

A distinction should be emphasised between the standard deviations of the residuals used in Equation (6.14) marked by σ_{δ_i}, and the total biases used in Equation (6.15) marked by σ^S_i. In Table 6.12, the correlations between the fit variables for the total systematic uncertainties are reported.

Table 6.12 – Systematic correlations between the fitted variables including all systematic effects in $\overline{B} \to D^0(\to K^0_S\pi^+\pi^-)\mu^-\overline{\nu}_\mu X$.

Systematic correlations				
	x_{CP}	y_{CP}	Δx	Δy
x_{CP}	1.00	0.11	-0.25	-0.02
y_{CP}		1.00	-0.05	-0.20
Δx			1.00	0.11
Δy				1.00

7 Combination with the results from the $D^{*+} \to D^0(\to K_S^0\pi^+\pi^-)\pi^+$ analysis

In this chapter, a combination between the $\overline{B} \to D^0(\to K_S^0\pi^+\pi^-)\mu^-\overline{\nu}_\mu X$ (SL) and $D^{*+} \to D^0(\to K_S^0\pi^+\pi^-)\pi^+$ (Prompt) analysis is performed. These two samples cover different regions of the D^0 decay time. The SL analysis is complementary to the Prompt analysis as it covers a wider range of D^0 decay times. We discuss the D^0 decay time coverage of these two samples in Section 7.1.

The ratios r_b at D^0 decay time $t = 0$ are obtained from the bin-flip fit of Equation (1.23) and are different due to efficiency effects as described in Section 1.3.1. This leads to different sets of r_b values for each sample in the bin-flip fits. The chosen combination method is the same as was done in the Run 1 analysis [63]: performing a simultaneous fit with different r_b parameters. We also investigate the potential improvements of aligning r_b at $t = 0$ by correcting efficiencies within each subsample. This allows the parameters to be shared among the two samples. This effort was motivated by the significant improvement in the systematic uncertainty for the analysis of $D^0 \to K^\pm\pi^\mp$ decays when the longer lever arm was exploited [124, 125]. However, it was found that in this analysis the improvements are small and do not justify the effort that would be needed to make the efficiency alignment. This study is detailed in Section 7.2. The combination of the systematic uncertainties of these two analyses is explained in Section 7.3.

7.1 D^0 decay time coverage

The decay time coverages of these two independent samples are different ($t_{\mathrm{SL}} \in [0, 20]\tau_{D^0}$ and $t_{\mathrm{Prompt}} \in [0.3, 8]\tau_{D^0}$). Even if the Prompt sample has higher statistics in the Run 2 dataset, the topology of the decay limits the data acquisition at low D^0 decay time because the D^0 is produced at the primary vertex. The SL sample is acquired by muon trigger selections. Such selections do not place a limit on the D^0 decay time. Therefore, the D^0 decay time coverage in this sample covers the distribution down to zero, even down to negative value, caused by the decay-time resolution.

Figure 7.1 presents the D^0 decay time efficiencies in the SL and Prompt analyses. The SL

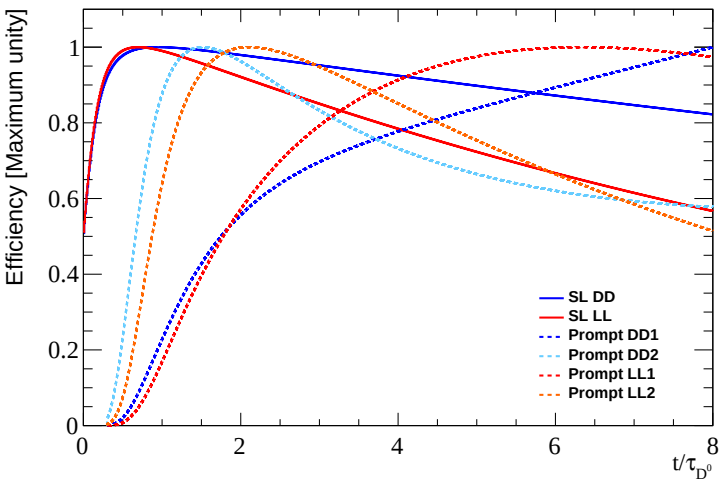

Figure 7.1 – Efficiency as a function of decay time in the SL and Prompt analyses obtained from a fits on simulated samples. The SL efficiencies are obtained from the MC model explained in Figure 4.6. The DD and LL subsamples refers to the K_S^0 types as explained in this note, while DD1, DD2, LL1 and LL2 refers to different trigger categories in the prompt sample from Section 4.2 of Ref. [4].

analysis has higher efficiency at low D^0 decay time as shown in Section 4.2. The prompt sample, on the other hand, covers a narrower decay time range. The DD1 and LL1 analyses have smaller (larger) efficiencies than those for DD2 and LL2 at low (high) D^0 decay time.

7.2 Improvement from shared r_b between samples

As a first step to test whether aligning the r_b leads to a significant improvement of the sensitivity over performing only simultaneous fits with different sets of r_b as done in the Run 1 analysis [63], two different sets of toys are generated with the Belle amplitude model as similar to what is explained in Section 6.1.

These two sets are generated with the same decay time efficiency without any correlations or resolution effects. The SL DD decay time efficiency is used. Since the ratios r_b are affected mainly by the Dalitz efficiency, SL DD and Prompt LL1 Dalitz efficiencies are used to distinguish these two toys.

Table 7.1 shows a comparison of the statistical uncertainties of the SL and Prompt analyses, together with combined fits with or without constraining r_b across the samples. Since the Dalitz efficiencies are known in these toys, they are used to correct for the efficiency effect that causes the differences in r_b. Then the bin-flip fit is performed with constraining r_b between these samples (shared r_b). As noticed from this table, correcting for the efficiency and adding constraints on r_b improves the sensitivity by only around 5%. To implement similar correction

Table 7.1 – Statistical uncertainties in units of 10^{-3} on the measured quantities acquired from the bin-flip fits with different tags and conditions on sets of r_b. The reported uncertainties include the contribution due to the uncertainties in the strong phase inputs.

Analysis	x_{CP}	y_{CP}	Δx	Δy
$\overline{B} \to D^0(\to K^0_S\pi^+\pi^-)\mu^-\overline{\nu}_\mu X$	1.48	3.12	0.93	1.92
$D^{*+} \to D^0(\to K^0_S\pi^+\pi^-)\pi^+$	0.46	1.20	0.18	0.36
Combined with different r_b	0.45	0.89	0.15	0.24
Combined with shared r_b	0.43	0.86	0.14	0.24

and fits on both real SL and Prompt data, large MC samples are required to model more precisely the Dalitz efficiencies. The generation of the needed MC samples would take too much time for little improvement to be gained. Therefore, for the combination we opt for a simultaneous fit with different sets of r_b ratios.

7.3 Combination of systematic uncertainties

The full sets of systematics for both analyses is summarised in Table 7.2. They are combined as follows. Let $x_{\text{comb},i}$ be the combined weighted average values which are linear combinations of mixing and CP-violating parameters ($x_i := x_{CP}, y_{CP}, \Delta x, \Delta y$) from SL $x_{\text{SL},i}$ and Prompt ($x_{\text{p},i}$) samples with weights $w_{\text{SL},i}$ and $w_{\text{p},i}$:

$$x_{\text{comb},i} = w_{\text{SL},i}\, x_{\text{SL},i} + w_{\text{p},i}\, x_{\text{p},i}\,, \tag{7.1}$$

where $w_{\text{SL},i} + w_{\text{p},i} = 1$. For systematics S, the combined uncertainties of a variable x_i between the samples $\sigma^S_{(\text{SL,p}),i}$ can be computed as

$$\left(\sigma^S_{(\text{SL,p}),i}\right)^2 = w^2_{\text{SL},i}\left(\sigma^S_{\text{SL},i}\right)^2 + w^2_{\text{p},i}\left(\sigma^S_{\text{p},i}\right)^2 + 2\, w_{\text{SL},i}\, w_{\text{p},i}\, \rho^S_{\text{p,SL}(i)}\, \sigma^S_{\text{SL},i}\, \sigma^S_{\text{p},i}\,, \tag{7.2}$$

where $\rho^S_{\text{p,SL}(i)}$ is the correlation of a variable x_i between the SL and prompt samples. Considering that covariances between variables x_i and x_j can be combined as a weighted covariance, which can be expressed with the correlation coefficient $\rho^S_{\text{SL,p}(ij)}$ of SL and prompt samples. This leads to the combined variance

$$\text{COV}(x_i, x_j)^S_{\text{SL,p}} = \sum_{ij} w_{\text{SL},i}\, w_{\text{p},i}\, \rho^S_{\text{SL,p}(ij)}\, \sigma^S_{\text{SL},i}\, \sigma^S_{\text{p},i}\,, \tag{7.3}$$

of the systematics S. Then the total combined systematic uncertainties are computed as

$$\begin{aligned}\text{COV}(x_i, x_j)_{\text{SL,p}} = \sum_S (&w_{\text{p},i}\, w_{\text{p},j}\, \rho^S_{\text{p},ij}\, \sigma^S_{\text{p},i}\, \sigma^S_{\text{p},j} + w_{\text{SL},i}\, w_{\text{SL},j}\, \rho^S_{\text{SL},ij}\, \sigma^S_{\text{SL},i}\, \sigma^S_{\text{SL},j} \\ &+ 2\, w_{\text{p},i}\, w_{\text{SL},j}\, \rho^S_{\text{SL,p}(ij)}\, \sigma^S_{\text{p},i}\, \sigma^S_{\text{SL},j})\end{aligned} \tag{7.4}$$

Table 7.2 – Summary of the uncertainties in units of 10^{-3} on the measured quantities of the SL analysis from Table 6.11 and the Prompt analysis (in parenthesis) from Section 9.7 of Ref. [4]. The total systematic uncertainty is the sum in quadrature of the individual components. The uncertainties due to the strong phase inputs are (by default) included in the statistical uncertainty. Here, to ease comparison with other sources, we also report the separate contributions due to the strong phase inputs and to the statistics of our data.

Source	x_{CP}	y_{CP}	Δx	Δy
Reconstruction and selection	0.058(0.199)	0.790(0.757)	0.278(0.009)	0.238(0.044)
Detection asymmetry	0.063(0.016)	0.031(0.032)	0.015(0.009)	0.089(0.122)
Mass-fit model	0.028(0.045)	0.096(0.361)	0.005(0.003)	0.005(0.009)
Unrelated $D^0\mu$ combinations	0.244(0.000)	0.219(0.000)	0.013(0.000)	0.051(0.000)
Secondary charm decays	0.000(0.208)	0.000(0.154)	0.000(0.001)	0.000(0.002)
Total systematic uncertainty	0.259(0.291)	0.826(0.853)	0.278(0.011)	0.259(0.129)
Strong phase inputs	0.32(0.23)	0.68(0.66)	0.16(0.02)	0.21(0.04)
Statistical (w/o phase inputs)	1.45(0.40)	3.04(1.00)	0.92(0.18)	1.91(0.35)
Det. asymm. inputs	0.00(0.00)	0.00(0.00)	0.00(0.04)	0.00(0.08)
Statistical uncertainty	1.48(0.46)	3.12(1.20)	0.93(0.18)	1.92(0.36)

where $\rho^S_{\mathrm{SL},ij}$ ($\rho^S_{\mathrm{p},ij}$) is the systematic correlation in the SL (Prompt) sample as described in Section 6.7.1 (Section 9 of Ref. [4]). $\sigma^S_{\mathrm{SL},i}$ ($\sigma^S_{\mathrm{p},i}$) represents a systematic uncertainty on mixing parameter i for the SL (Prompt) sample. The systematic uncertainties from most sources can be treated as independent. The quantities $w_{\mathrm{SL},i}$ ($w_{\mathrm{p},j}$) are the weights of the SL (Prompt) results in the weighted averages, and are determined to minimise Equation (7.4) using the downhill simplex algorithm [126] from `SciPy` [101]. The detection asymmetries are estimated on the same D^+_s samples. This may induce a certain level of correlation and propagate to the final result. Conservatively, the systematic uncertainties from the detection asymmetry are assumed to be 100% correlated between the SL and Prompt analyses. The correlation appears in the last term of Equation (7.4) as $\rho^S_{\mathrm{p,SL}(ij)}$. Note that this term is zero for the other systematics. The results are presented in Table 7.3, along with the combined results for all systematic sources.

7.3.1 Combined result

Fits are performed as similar to what is described in Section 5.3. A χ^2 is defined as the sum of the SL χ^2 in Equation (5.6) and the prompt χ^2 defined in Equations 39–41 in Section 7.3 of Ref. [4]. Table 7.4 presents the results of the simultaneous fits of $\overline{B} \to D^0(\to K^0_S\pi^+\pi^-)\mu^-\overline{\nu}_\mu X$ and $D^{*+} \to D^0(\to K^0_S\pi^+\pi^-)\pi^+$ assuming *CP* conservation and *CP* violation. The difference in χ^2 between the two fits is used to evaluate the compatibility of our data with the hypothesis of *CP* symmetry.

The results of the fit to the data are shown in Table 7.4, and projections of the fit are shown

Table 7.3 – Summary of the systematic uncertainties in units of 10^{-3} on the measured quantities of the combined sample from Table 7.2 using Equation (7.4). The total systematic uncertainty is the sum in quadrature of the individual components.

Source	x_{CP}	y_{CP}	Δx	Δy
Reconstruction and selection	0.094	0.548	0.009	0.046
Detection asymmetry	0.042	0.031	0.009	0.119
Mass-fit model	0.025	0.181	0.003	0.008
Unrelated $D^0\mu$ combinations	0.136	0.113	0.000	0.005
Secondary charm decays	0.092	0.074	0.001	0.002
Total systematic uncertainty	0.195	0.594	0.013	0.128

Table 7.4 – Results of the combined fit to the $\overline{B} \to D^0(\to K^0_S\pi^+\pi^-)\mu^-\overline{\nu}_\mu X$ and $D^{*+} \to D^0(\to K^0_S\pi^+\pi^-)\pi^+$ sample. The reported uncertainties include the statistical component and the contribution due to the uncertainties in the strong phase inputs.

Parameter		No *CP* violation	*CP* violation allowed	Correlations		
				y_{CP}	Δx	Δy
x_{CP}	$[10^{-3}]$	4.00 ± 0.45	4.00 ± 0.45	0.121	−0.018	−0.016
y_{CP}	$[10^{-3}]$	5.50 ± 1.16	5.51 ± 1.16		−0.012	−0.058
Δx	$[10^{-3}]$	–	-0.29 ± 0.18			0.069
Δy	$[10^{-3}]$	–	0.31 ± 0.35			
χ^2/ndf		1034.683/1110	1031.066/1108			

in Figure 7.2 similar to the fit projections of Section 5.3. Note that the slopes in the Prompt sample are different from those in the SL sample as the projected fits in the Prompt sample are the weighted average of 4 different samples which have different Dalitz efficiencies leading to different r_b ratios. In the SL sample, the efficiency variation between LL and DD is smaller.

The results are dominated by the Prompt sample and compatible with the current world average [57]. The fits show deviations of x_{CP} from 0 exceeding 8σ of significance. There is no evidence for *CP* violation. Figure 7.3 shows the central values and two-dimensional 68.3%, 95.5%, and 99.7% confidence regions in the (x_{CP}, y_{CP}) and $(\Delta x, \Delta y)$ planes.

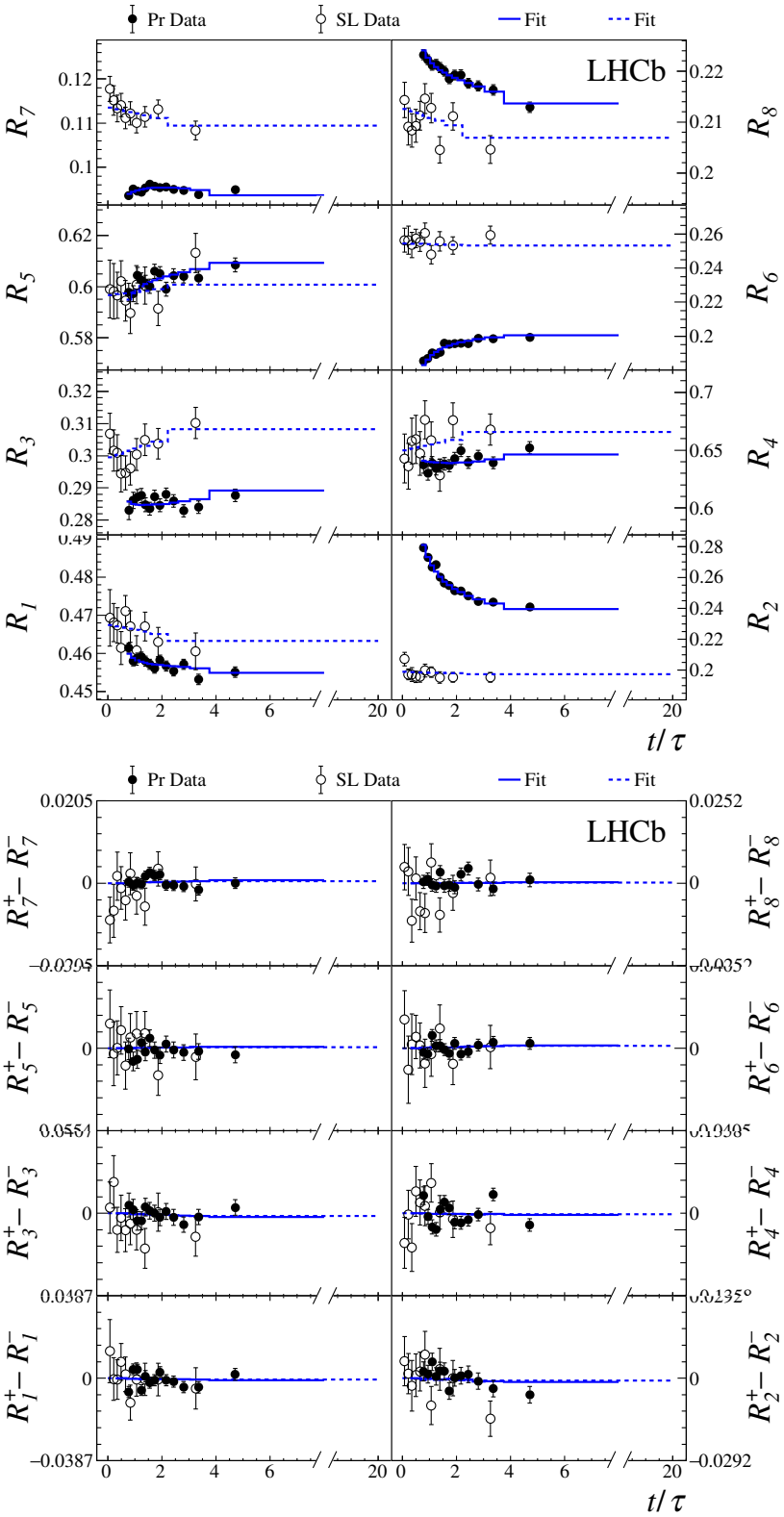

Figure 7.2 – Projections of the combined fit allowing for *CP* violation: (top) *CP*-averaged ratio and (bottom) difference of D^0 and $\overline{D}^0$ yield ratios as functions of decay time for the various Dalitz bins.

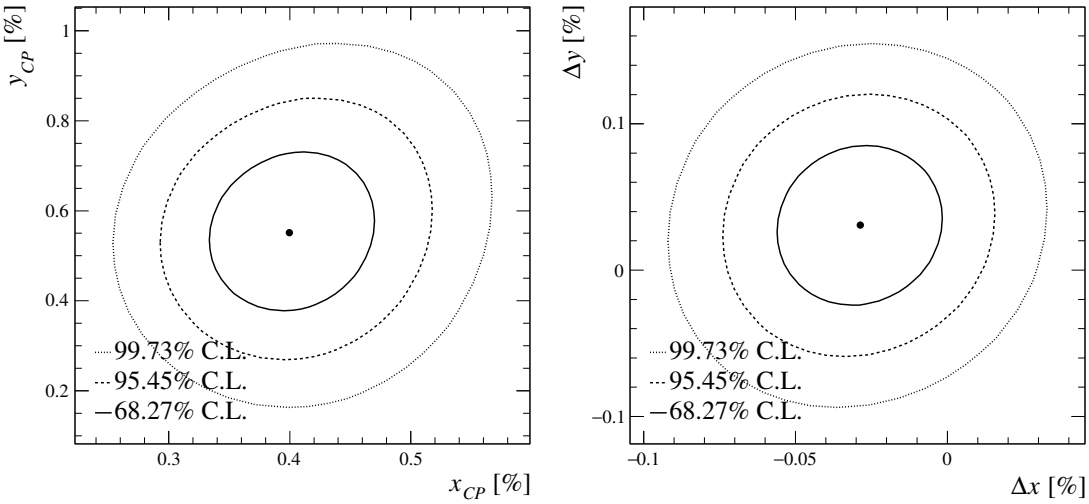

Figure 7.3 – Two-dimensional 68.3%, 95.5%, and 99.7% confidence-level contours on the mixing and *CP*-violation parameters determined from the combined fit with *CP* violation is allowed.

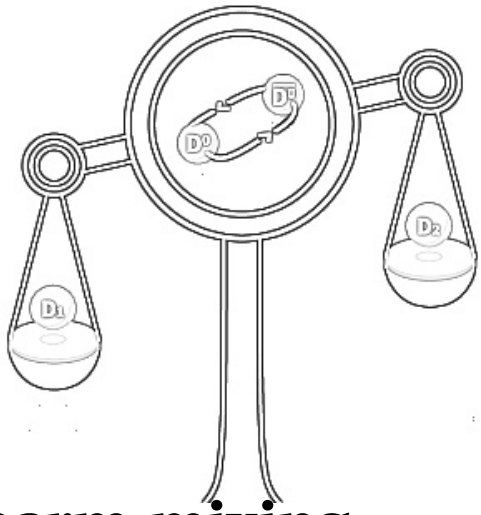

8 Impact on neutral charm mixing

This chapter summarises impacts of the $\overline{B} \to D^0(\to K^0_S\pi^+\pi^-)\mu^-\overline{\nu}_\mu X$ analysis and of its combination with the $D^{*+} \to D^0(\to K^0_S\pi^+\pi^-)\pi^+$ analysis on the mixing and *CP*-violating parameters x, y, $|q/p|$, and ϕ.

8.1 Translation to charm mixing and *CP*-violating observables

From Chapters 5 and 6, the fit results are summarised here together with their statistical (stat) and systematic (syst) uncertainties. We measure $x = 4.30 \pm 1.48\,(\text{stat}) \pm 0.26\,(\text{syst})) \times 10^{-3}$ and $y = 12.89 \pm 3.12\,(\text{stat}) \pm 0.83\,(\text{syst})) \times 10^{-3}$ assuming *CP* symmetry. By allowing for *CP* violation in the bin-flip fit, we obtain

$$
\begin{aligned}
x_{CP} &= [\ +4.29 \pm 1.48\,(\text{stat}) \pm 0.26\,(\text{syst})] \times 10^{-3}\,,\\
y_{CP} &= [+12.61 \pm 3.12\,(\text{stat}) \pm 0.83\,(\text{syst})] \times 10^{-3}\,,\\
\Delta x &= [\ -0.77 \pm 0.93\,(\text{stat}) \pm 0.28\,(\text{syst})] \times 10^{-3}\,,\\
\Delta y &= [\ +3.01 \pm 1.92\,(\text{stat}) \pm 0.26\,(\text{syst})] \times 10^{-3}\,.
\end{aligned}
$$

As the SL sample extends the D^0 decay times close to zero, where the Prompt sample has a limitation due to its decay topology and selection in the triggers, the SL analysis is complementary to and combined with the Prompt analysis [4,5] using simultaneous fits combining their χ^2 as described in Chapter 7. The combination results in $x = 4.00 \pm 0.45\,(\text{stat}) \pm 0.20\,(\text{syst})) \times 10^{-3}$ and $y = 5.50 \pm 1.16\,(\text{stat}) \pm 0.59\,(\text{syst})) \times 10^{-3}$ assuming *CP* symmetry. Allowing for *CP* violation, we measure

$$
\begin{aligned}
x_{CP} &= [+4.00 \pm 0.45\,(\text{stat}) \pm 0.20\,(\text{syst})] \times 10^{-3}\,,\\
y_{CP} &= [+5.51 \pm 1.16\,(\text{stat}) \pm 0.59\,(\text{syst})] \times 10^{-3}\,,\\
\Delta x &= [-0.29 \pm 0.18\,(\text{stat}) \pm 0.01\,(\text{syst})] \times 10^{-3}\,,\\
\Delta y &= [+0.31 \pm 0.35\,(\text{stat}) \pm 0.13\,(\text{syst})] \times 10^{-3}\,.
\end{aligned}
$$

Table 8.1 – Fit results on the $\overline{B} \to D^0(\to K^0_S\pi^+\pi^-)\mu^-\overline{\nu}_\mu X$ sample and combined fit result. One-dimensional confidence-level (CL) intervals for the derived parameters x, y, $|q/p|$, ϕ are presented.

	Parameter		Fit result	Allowed interval 68.3% CL	95.5% CL	99.7% CL
SL	x	$[10^{-2}]$	$0.46^{+0.15}_{-0.16}$	$[0.30, 0.61]$	$[0.16, 0.77]$	$[-0.02, 0.90]$
	y	$[10^{-2}]$	$1.24^{+0.32}_{-0.33}$	$[0.91, 1.56]$	$[0.57, 1.87]$	$[0.35, 2.12]$
	$\lvert q/p\rvert$		$1.21^{+0.21}_{-0.15}$	$[1.06, 1.42]$	$[0.91, 1.80]$	$[0.76, 2.40]$
	ϕ		$-0.132^{+0.088}_{-0.120}$	$[-0.252, -0.044]$	$[-0.47, 0.03]$	$[-0.80, 0.09]$
Combined	x	$[10^{-2}]$	0.401 ± 0.049	$[0.352, 0.450]$	$[0.302, 0.499]$	$[0.250, 0.550]$
	y	$[10^{-2}]$	0.55 ± 0.13	$[0.42, 0.68]$	$[0.29, 0.81]$	$[0.16, 0.94]$
	$\lvert q/p\rvert$		$1.012^{+0.050}_{-0.048}$	$[0.964, 1.062]$	$[0.913, 1.118]$	$[0.86, 1.18]$
	ϕ		$-0.060^{+0.037}_{-0.044}$	$[-0.104, -0.023]$	$[-0.161, 0.014]$	$[-0.24, 0.06]$

The SL and Prompt results are compatible with each other and their combination is compatible with the world-average values [57]. The value of x_{CP} deviates from zero with a significance of 8.1 σ. No evidence of CP violation is observed in both cases.

The results for x_{CP}, y_{CP}, Δx, and Δy are transformed to the mixing and CP-violating parameters x, y, $|q/p|$, and ϕ using Equations (1.24)–(1.26) and taking into account the statistical and systematic corrections explained in Section 5.3 (Section 7.3) using Equations (1.24)–(1.26).

The PLUGIN method [127] is implemented for the transformation. The method is a generalisation of the Feldman-Cousins method [128] where a likelihood-ratio between probability distributions of the measured and best-fit (maximum likelihood) values of these parameters is constructed. Confidence intervals of x, y, $|q/p|$, and ϕ are determined with the likelihood-ratio assuming that the measured correlations are independent of the true values of the parameters. The PLUGIN method uses the maximum likelihood estimator as an estimate of the transformed distribution to determine confidence intervals of x, y, $|q/p|$, and ϕ. This is used in the Prompt analysis [4] as well as the LHCb γ-combination analysis [129]. The SL and combination results are presented in Table 8.1. The table also shows the 68.3%, 95.5%, and 99.7% confidence level intervals for the variables x, y, $|q/p|$, and ϕ.

Figure 8.1 shows the impacts of the measured mixing and CP-violating parameters from the $D^{*+} \to D^0(\to K^0_S\pi^+\pi^-)\pi^+$ [5] analysis, the $\overline{B} \to D^0(\to K^0_S\pi^+\pi^-)\mu^-\overline{\nu}_\mu X$ analysis, and their combination. x is consistent amongst the prompt and SL samples. y is moving closer to the world-average value [57] in the combination. The CP-violating parameters, $|q/p|$ and ϕ are consistent with the world-averages. The combination is dominated by the result of the Prompt analysis, as expected from the much larger statistics.

The results obtained in this analysis are consistent with the current world-average determinations [57]. They complement the knowledge of the charm-mixing parameters. To show the

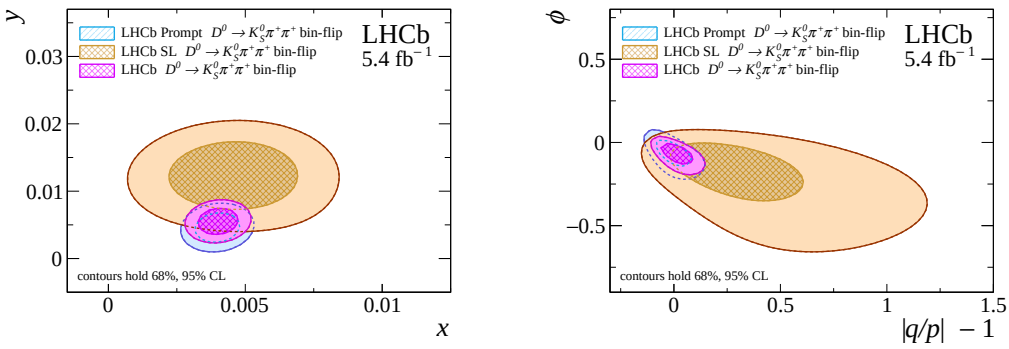

Figure 8.1 – Two-dimensional 68.3% and 95.5% confidence-level contours in the (left) (x, y) and (right) $(|q/p| - 1, \phi)$ planes. Results from $D^{*+} \to D^0(\to K^0_S\pi^+\pi^-)\pi^+$ [4, 5], $\overline{B} \to D^0(\to K^0_S\pi^+\pi^-)\mu^-\overline{\nu}_\mu X$, and their combination are shown.

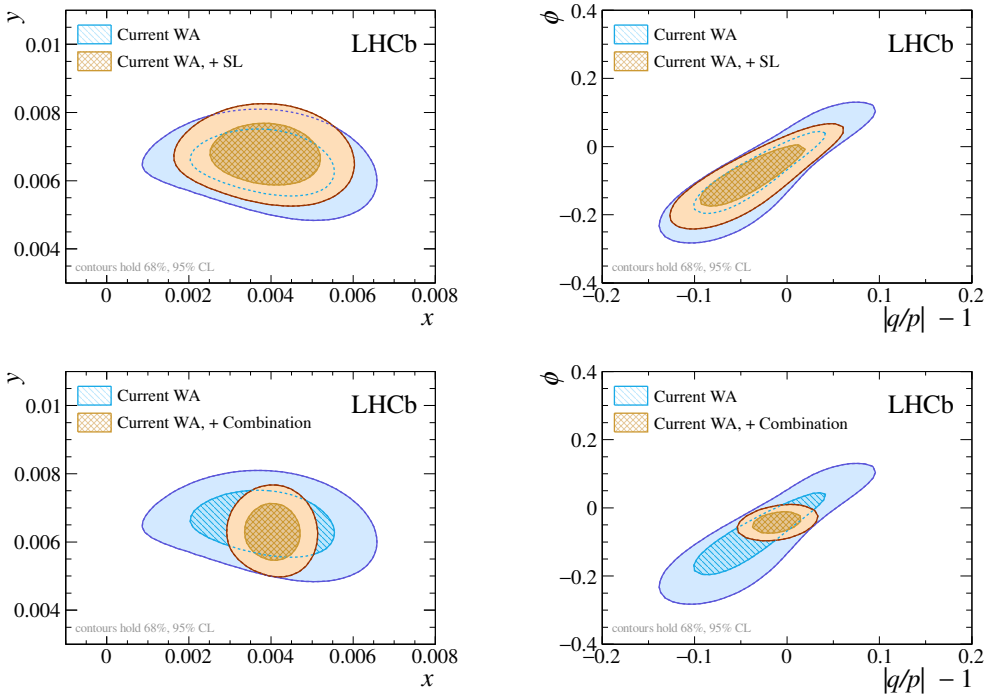

Figure 8.2 – Two-dimensional 68.3% and 95.5% confidence-level contours in the (left) (x, y) and (right) $(|q/p| - 1, \phi)$ planes from a "world-average" combination (without [4, 5]) with and without this new result from (top) $\overline{B} \to D^0(\to K^0_S\pi^+\pi^-)\mu^-\overline{\nu}_\mu X$ (SL) and (bottom) the combination between $\overline{B} \to D^0(\to K^0_S\pi^+\pi^-)\mu^-\overline{\nu}_\mu X$ and $D^{*+} \to D^0(\to K^0_S\pi^+\pi^-)\pi^+$ analyses.

impact, a combination is performed using all measurements in the HFLAV combination dated from 31 March 2019 until June 2021 [130] without the prompt analysis [4, 5]. The results of the HFLAV combination with and without the $\overline{B} \to D^0(\to K^0_S\pi^+\pi^-)\mu^-\overline{\nu}_\mu X$ and the combination between $\overline{B} \to D^0(\to K^0_S\pi^+\pi^-)\mu^-\overline{\nu}_\mu X$ and $D^{*+} \to D^0(\to K^0_S\pi^+\pi^-)\pi^+$ are shown in Figure 8.2.

Table 8.2 – Fit results of the derived parameters x, y, $|q/p|$, ϕ combined with the world average (WA) values with $D^{*+} \to D^0(\to K^0_S\pi^+\pi^-)\pi^+$ (Prompt), $\overline{B} \to D^0(\to K^0_S\pi^+\pi^-)\mu^-\overline{\nu}_\mu X$ (SL) and their combination.

Parameter		WA+Prompt	WA+SL	WA+combined (Prompt + SL)
x	$[10^{-2}]$	0.418 ± 0.051	0.45 ± 0.10	0.414 ± 0.046
y	$[10^{-2}]$	$0.605^{+0.059}_{-0.057}$	0.651 ± 0.065	$0.616^{+0.058}_{-0.056}$
$\|q/p\|$		$0.998^{+0.020}_{-0.019}$	$0.965^{+0.057}_{-0.052}$	0.999 ± 0.019
ϕ		-0.046 ± 0.024	$-0.091^{+0.082}_{-0.089}$	$-0.048^{+0.022}_{-0.023}$

Table 8.2 compares different world average (WA) values results, which include the Prompt [130] results, the SL results, or both. The inclusion of the SL results (in addition to the Prompt results) improves a little the precisions in x, y and ϕ measurements. The precision of $|q/p|$ remains almost unchanged.

8.2 Improvements from Run 1 analysis

The analysis method closely follows the one described in Run 1 [63, 65] to analyse the $\overline{B} \to D^0(\to K^0_S\pi^+\pi^-)\mu^-\overline{\nu}_\mu X$ sample and some methods are partly adpated from the Run 2 Prompt analysis [4, 5]. There are some improvements and necessary differences:

Selection

- The Trigger line on muon candidates `mu_Hlt2SingleMuonDecision_TOS` is excluded since it does not provide a significant improvement over the current `TopoMu` trigger.
- Offline selections are changed from simple cuts in the Run 1 analysis to a multivariate analysis to better select the signal candidates and reject background.
- The range of reconstructed D^0 decay times is changed from $[-0.1, 20]\tau_{D^0}$ to $[0, 20]\tau_{D^0}$ because the signal efficiency below zero is low. The correlation between the Dalitz coordinates and the D^0 decay time changes rapidly in the negative decay time region. Accepting only the positive decay times helps in the correlation modeling.

Efficiency modelling

- In the Run 1 analysis, the efficiency was estimated in the Dalitz phase space of $m^2\left(K^0_S\pi^+\right)$ and $m^2\left(K^0_S\pi^-\right)$. Here, the efficiency is modeled on the squared Dalitz coordinates $\left(m^2(\pi^+\pi^-), \cos\theta_{\pi^+\pi^-}\right)$ to simplify the correction on data.
- An efficiency model as a function of $m^2(\pi^+\pi^-)$, $\cos\theta_{\pi^+\pi^-}$, and D^0 decay time is used in order to correct the data while there was no correction applied in the Run 1 analysis. This suppresses a potential bias that may arise from efficiency variations in each Dalitz bin while the efficiency is assumed to be constant within a bin as described in Section 1.3.1.

Phase-space and decay-time acceptance correlations

- There was no significant correlation in Run 1 analysis. However, as statistics in Run 2 is higher, the correlation is more pronouced and a correlation removal procedure is neccessary.
- The correlation between the Dalitz coordinates and D^0 decay time are eliminated using two-steps procedure through the efficiency correction using the simulated sample and a data-driven decorrelation. This is different from the Run 1 and Run 2 analyses of the $D^{*+} \to D^0(\to K^0_S\pi^+\pi^-)\pi^+$ sample.

Bin-flip fit

- A combination between the CLEO and BESIII measurements of strong phase differences between the D^0 and $\overline{D}^0$ amplitudes (c_b, s_b) [66] are used as external inputs to determine the mixing and *CP* violating parameters. Only the measurement from CLEO [60] was used in the Run 1 analysis.

Systematic uncertainties

- Pseudo-experiments (toys) are generated using the updated Belle 2018 amplitude model [61] instead of the BaBar 2008 amplitude model [60].
- The $\pi^+\pi^-$ detection asymmetry is estimated on two Cabibbo-favoured D_s^+ decays, $D_s^+ \to \pi^+\pi^+\pi^-$ and $D_s^+ \to \phi(\to K^+K^-)\pi^+$, which is aligned with the Run 2 $D^{*+} \to D^0(\to K^0_S\pi^+\pi^-)\pi^+$ analysis. However, the correction to this systematics is not applied like the prompt analysis because no significant asymmetry is observed in $\overline{B} \to D^0(\to K^0_S\pi^+\pi^-)\mu^-\overline{\nu}_\mu X$ sample. This systematic was not evaluated in the Run 1 analysis.
- The mistag probability is determined on the $\overline{B} \to D^0(\to K^-\pi^+)\mu^-\overline{\nu}_\mu X$ sample while the $B \to D^*(\to D^0\pi^+_s)\mu X$, $D^0 \to K^0_S\pi^+\pi^-$ decay chain was used in the Run 1 analysis. This led to a major improvement of the systematics uncertainty due to the unrelated $D^0\mu^-$ combinations. This systematic reduced from 0.90×10^{-3} [63, 65] to around 0.24×10^{-3} in this analysis.

8.3 Future prospect and improvement ideas

Data collected by the LHCb experiment during Runs 1–2 corresponding to an integrated luminosity of $9\,\text{fb}^{-1}$ yields almost 40 millions $D^0 \to K^0_S\pi^+\pi^-$ decays from semileptonic b hadron and prompt $D^*(2010)^+$ production. These samples are analysed and lead to the most precise measurement of the mass parameter x in the charm oscillation system.

The LHCb experiment is scheduled to further collect data for physics analysis starting from 2022. During Run 3 (2022–2025) and Run 4 (2029–2032) an integrated luminosity in excess of $50\,\text{fb}^{-1}$ is planned to be collected. The LHC will operate at high luminosity (HL-LHC) from Run 5 (2035–2038) allowing the experiment to accumulate data up to $300\,\text{fb}^{-1}$ by 2038. Table 8.3 shows the prospects for the cumulative $D^0 \to K^0_S\pi^+\pi^-$ signal yields from $\overline{B} \to D^0(\to$

Table 8.3 – Extrapolated signal yields and statistical precisions (in units of 10^{-3}) on the *CP*-averaged mixing parameters and *CP*-violating differences for the bin-flip analysis on the $\overline{B} \to D^0(\to K^0_S\pi^+\pi^-)\mu^-\overline{\nu}_\mu X$ (SL) and $D^{*+} \to D^0(\to K^0_S\pi^+\pi^-)\pi^+$ (Prompt) samples. The statistical uncertainties on the Run 1–2 row are based on the results of this thesis, Run 1 analysis [63] and the prompt analysis [4, 5]. This table is adapted and scaled from Table 6.3 of Ref. [131].

Sample (lumi $\mathscr{L}$)	Tag	Yield	$\sigma(x_{CP})$	$\sigma(y_{CP})$	$\sigma(\Delta x)$	$\sigma(\Delta y)$
Run 1–2 (9 fb^{-1})	SL	4.7M	1.31	2.80	0.82	1.73
	Prompt	34M	0.45	1.16	0.18	0.35
Run 1–3 (23 fb^{-1})	SL	16M	0.71	1.52	0.44	0.94
	Prompt	190M	0.19	0.49	0.07	0.15
Run 1–4 (50 fb^{-1})	SL	37M	0.47	1.00	0.29	0.62
	Prompt	490M	0.12	0.30	0.05	0.09
Run 1–5 (300 fb^{-1})	SL	230M	0.19	0.40	0.12	0.25
	Prompt	3300M	0.05	0.12	0.02	0.04

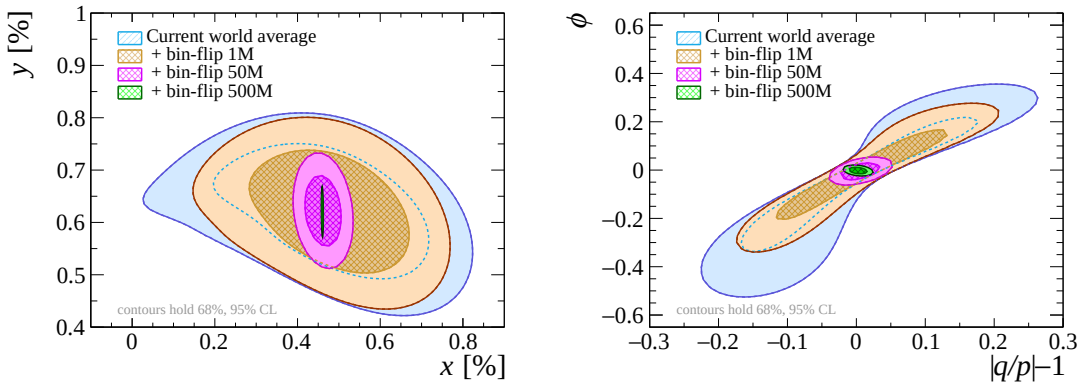

Figure 8.3 – Confidence regions at the (inner, darker filling) 68.3% and (outer, lighter filling) 95.5% confidence level in the two-dimensional space of (left) oscillation parameters (x, y) and *CP*-violating parameters $(|q/p|-1, \phi)$. This showing that the 2018 world average [54] can be improved significantly with data collected by LHCb in future LHC runs. These figures are taken from Ref. [64].

$K^0_S\pi^+\pi^-)\mu^-\overline{\nu}_\mu X$ (SL) and $D^{*+} \to D^0(\to K^0_S\pi^+\pi^-)\pi^+$ (Prompt) samples at the end of each Run with extrapolated statistical uncertainties of x_{CP}, y_{CP}, Δx, and Δy from the combined weighted average of Run 1 [63] and 2 [3, 5] results. The $D^0 \to K^0_S\pi^+\pi^-$ yields are expected to be more than 500M where the sensitivity of the bin-flip method will reach almost 10^{-5}. Figure 8.3 shows the impact of the bin-flip method on the mixing and *CP*-violating parameters with respect to the world average in 2018 for a sample size up to 500 million events.

To prepare for further analysis of the upcoming Run 3 dataset, further improvements could be made based on the development of this analysis on the $\overline{B} \to D^0(\to K^0_S\pi^+\pi^-)\mu^-\overline{\nu}_\mu X$ sample:

Selection

- Development of a TURBO stream [88] for the $\overline{B} \to D^0(\to K^0_S\pi^+\pi^-)\mu^-\overline{\nu}_\mu X$ can be developed with the knowledge from the selection study in this thesis. The TURBO stream performs an analysis in real-time data-taking, bypassing the offline reconstruction. This will lead to a higher reconstruction efficiency with optimised data storage.
- In the MVA selection, additional variables, such as an isolation variable that compares reconstructed tracks of a b candidate with the other unrelated tracks [132], could be added. Preliminary result shows that this leads to improved discriminating power between signal and background.
- The requirement on the K^0_S flight distance χ^2 can be dropped since the K^0_S reconstructed in DD category has a large uncertainty on the decay vertex due to track extrapolation to the K^0_S origin vertex. This leads to low χ^2.
- For the LL category, the transverse momentum requirement can be excluded. The selection is applied on the daughter pions which removes around 30% of the signal.
- Clone track rejection can be improved. Currently, the clone tracks are removed by comparing track slopes within the reconstructed tracks in the $\overline{B} \to D^0(\to K^0_S\pi^+\pi^-)\mu^-\overline{\nu}_\mu X$ decay chain as described in Section 3.1.3. Cross-check is needed to also compare those tracks with the other unrelated tracks in an event.

Efficiency modelling

- The precision on the efficiency model as a function of $m^2(\pi^+\pi^-)$, $\cos\theta_{\pi^+\pi^-}$, and D^0 decay time should be improved by generating more events in the simulation. This is needed in the analysis because the statistics from the Run 3 data-taking (2022–2025) will results in higher event yields where the mixing effect induces significant correlation between Dalitz coordinates and D^0 decay time. The work done in this thesis shows that the efficiency correction from the simulated sample can be used to partly remove the correlation without biasing the measurements.

Bin-flip fit

- The external strong phase inputs will become the main systematic effect and impose an obstacle to the bin-flip method. Currently, only measurements at BESIII provide the most precise determination of these (c_i, s_i) inputs by analysing $D^0\overline{D}^0$ production from the $\psi(3770)$ decay. A future programme at BESIII was proposed but further data-taking has not yet been approved [133].

Systematics

- Other alternative background models, *e.g.* exponential distribution, should be chosen to estimate the systematic uncertainties from the $K^0_S\pi^+\pi^-$ mass fit.

- The source of unrelated $D^0\mu^-$ combinations is well-understood and estimated in this thesis. However, the estimated mistag probabilities could have been accounted for in the bin-flip fit to the yield ratios.

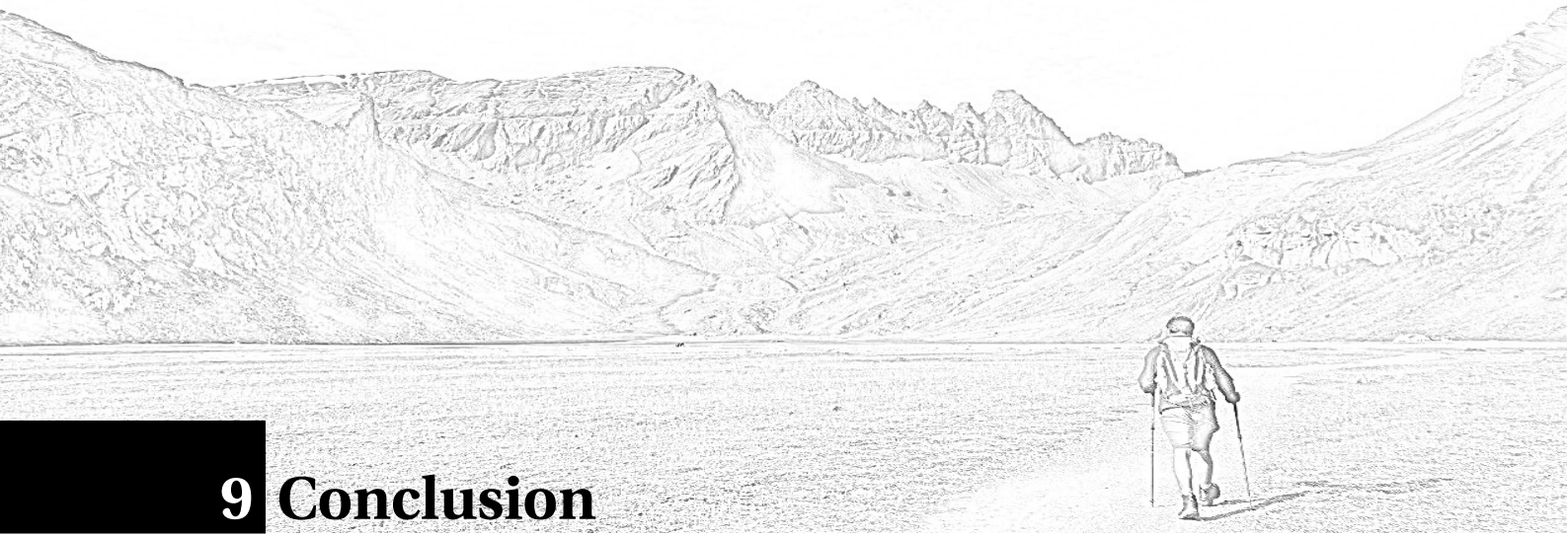

9 Conclusion

This thesis presents a measurement of the charm-mixing and CP-violation parameters using $D^0 \to K^0_S \pi^+ \pi^-$ decays reconstructed in the LHCb Run 2 data with the semileptonic decay of $\overline{B} \to D^0 \mu^- \overline{\nu}_\mu X$ used to identify the charm meson at production as D^0 or $\overline{D}^0$ meson. Signal yields are extracted from fits to the invariant mass distributions of the D^0 meson in various bins of the Dalitz plot and D^0 decay time. The binning of the Dalitz plot is chosen such as to preserve nearly constant values of the strong-interaction phases in each bin, and external constraints for these phases are used. Time-dependent ratios of yields for each pair of Dalitz plot bins symmetric about its bisector are fitted to Equation (1.23) to extract the mixing and CP parameters

$$
\begin{aligned}
x_{CP} &= [\ +4.29 \pm 1.48\,(\text{stat}) \pm 0.26\,(\text{syst})] \times 10^{-3}\,, \\
y_{CP} &= [+12.61 \pm 3.12\,(\text{stat}) \pm 0.83\,(\text{syst})] \times 10^{-3}\,, \\
\Delta x &= [\ -0.77 \pm 0.93\,(\text{stat}) \pm 0.28\,(\text{syst})] \times 10^{-3}\,, \\
\Delta y &= [\ +3.01 \pm 1.92\,(\text{stat}) \pm 0.26\,(\text{syst})] \times 10^{-3}\,,
\end{aligned}
$$

where the first uncertainty is statistical and the second is systematic. These measurements are consistent with the $D^{*+} \to D^0(\to K^0_S \pi^+ \pi^-)\pi^+$ analysis [5] and a combination is performed to maximise the performance. These measurements further confirm the observation of the mass parameter x deviated from zero and push the significance to more than 8σ.

The analysis procedure developed in this work significantly improves the measurements. The information from the simulated sample has the potential to eliminate the correlation between Dalitz plot and D^0 decay time arising from the instrumental effects without biasing the measurement. A novel strategy to estimate systematics from unrelated $D^0\mu^-$ combinations leads to more precise measurements of the mistag probability. This reduces the systematic uncertainty from this source by almost a factor of four comparing to the analysis on the Run 1 dataset. The procedure presented in this thesis could be implemented to improve the measurement of the mixing and CP-violating parameters with the upcoming LHCb Run 3 dataset.

Even if this work contributes to a better understanding of the neutral charm oscillation system, the mystery behind the matter-antimatter asymmetry at the beginning of the Universe still stands. The knowledge developed in this thesis could be employed to study upcoming data from particle physics experiments which may shed light on this problem in the future.

A Data-taking years efficiency

A.1 D^0 decay time

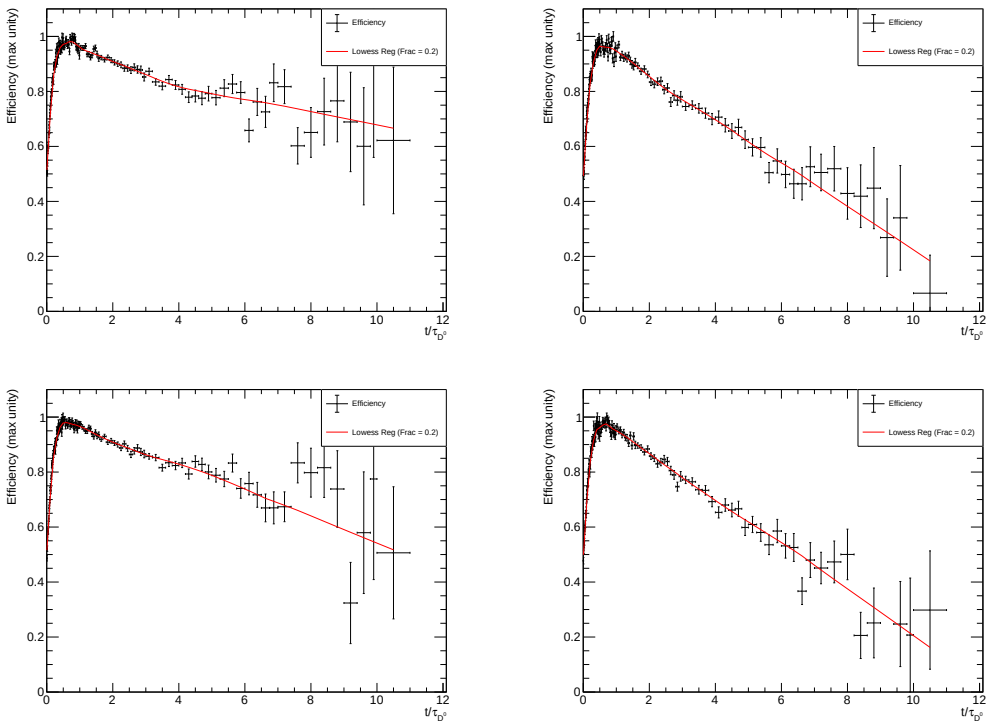

Figure A.1 – D^0 decay time acceptance in the $\overline{B} \to D^0(\to K^0_S\pi^+\pi^-)\mu^-\overline{\nu}_\mu X$ sample obtained by forming the ratio between the observed D^0 decay-time distribution (`sWeight`) and an exponential function fitted from toy data shown separately for DD (left) and LL (right) cases and for data taken in 2017 (top), and 2018 (bottom). The raw ratios (black points) are smoothed with the LOWESS algorithm (red curves).

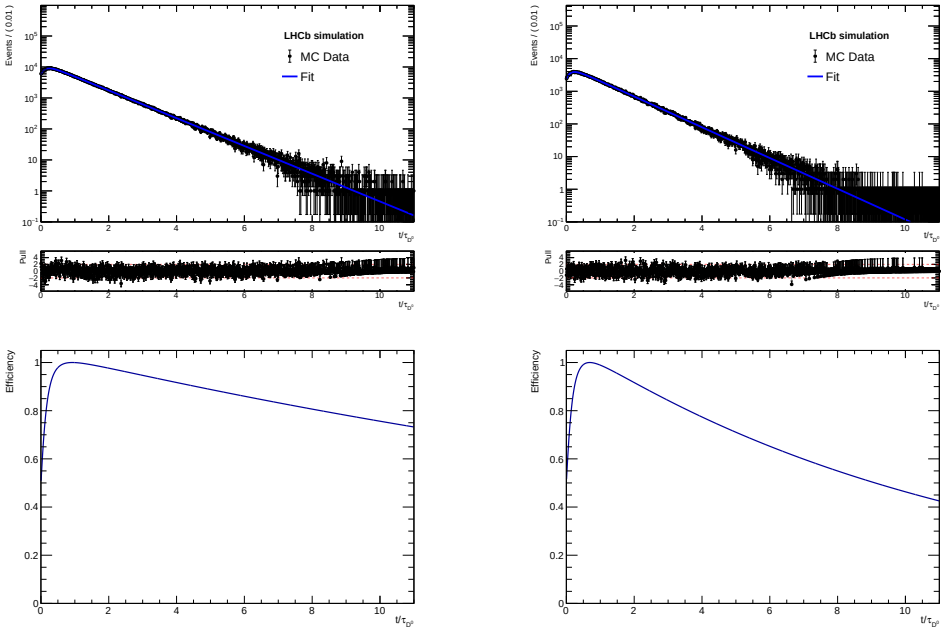

Figure A.2 – Reconstructed D^0 decay time distribution in a simulated sample of $\overline{B} \to D^0(\to K_S^0\pi^+\pi^-)\mu^-\overline{\nu}_\mu X$ decays for the year 2017 with fit superimposed (top) and corresponding acceptance function (bottom), for K_S^0 reconstructed in the DD (left) and LL (right) categories.

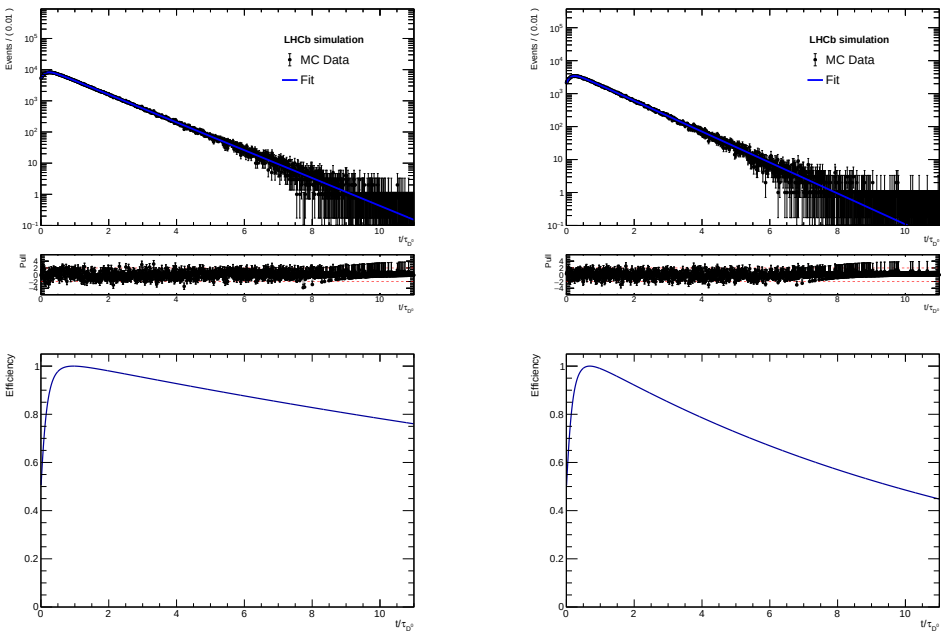

Figure A.3 – Reconstructed D^0 decay time distribution in a simulated sample of $\overline{B} \to D^0(\to K_S^0\pi^+\pi^-)\mu^-\overline{\nu}_\mu X$ decays for the year 2018 with fit superimposed (top) and corresponding acceptance function (bottom), for K_S^0 reconstructed in the DD (left) and LL (right) categories.

A.2 Dalitz coordinates

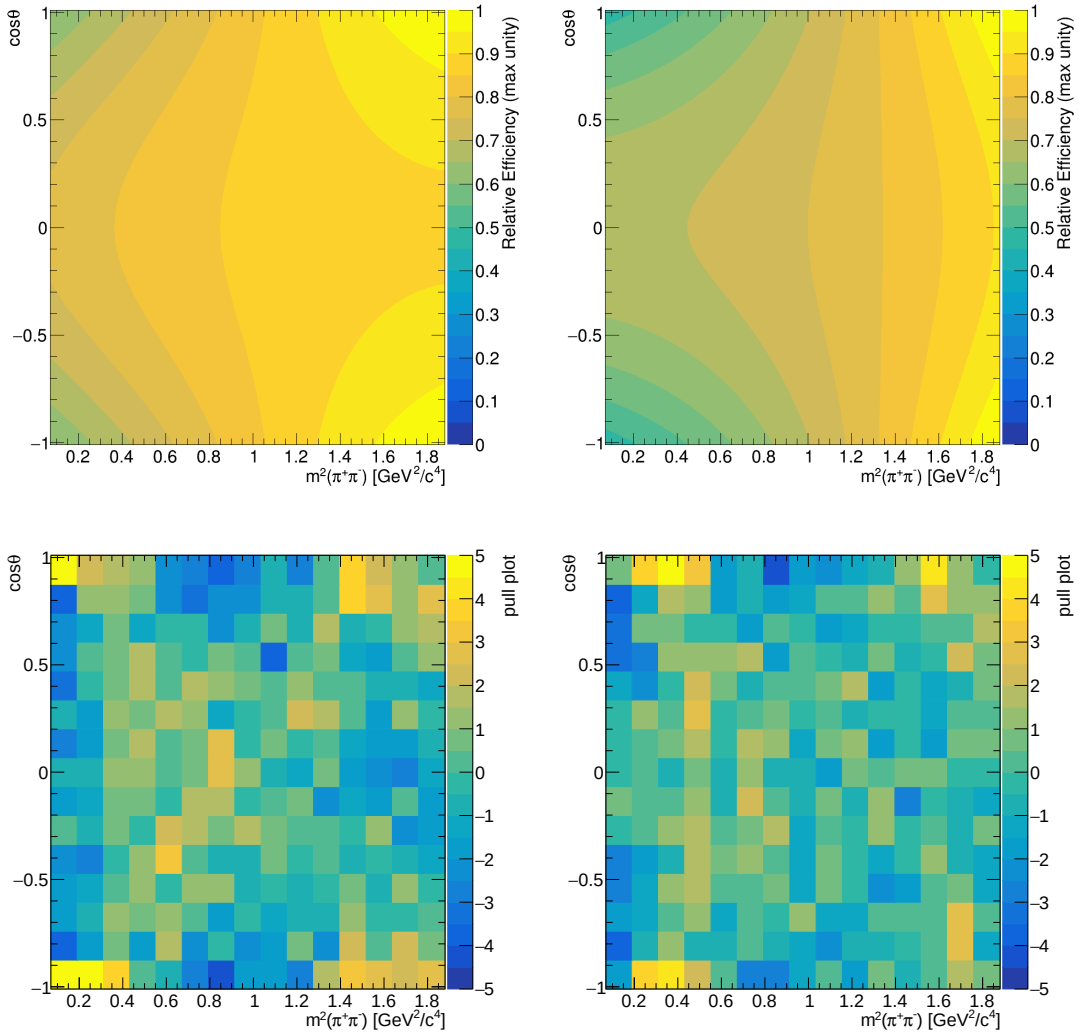

Figure A.4 – (Top) Efficiency function of Equation (4.4) in the plane $(m^2(\pi^+\pi^-), \cos\theta_{\pi^+\pi^-})$ for the parameters of Table 4.2 year 2017 (with $q_5 = q_6 = 0$), separately for reconstructed K_S^0 in the DD (left) and LL (right) categories. (Bottom) Corresponding pull plots with respect to the simulated sample for the 2017 data-taking year.

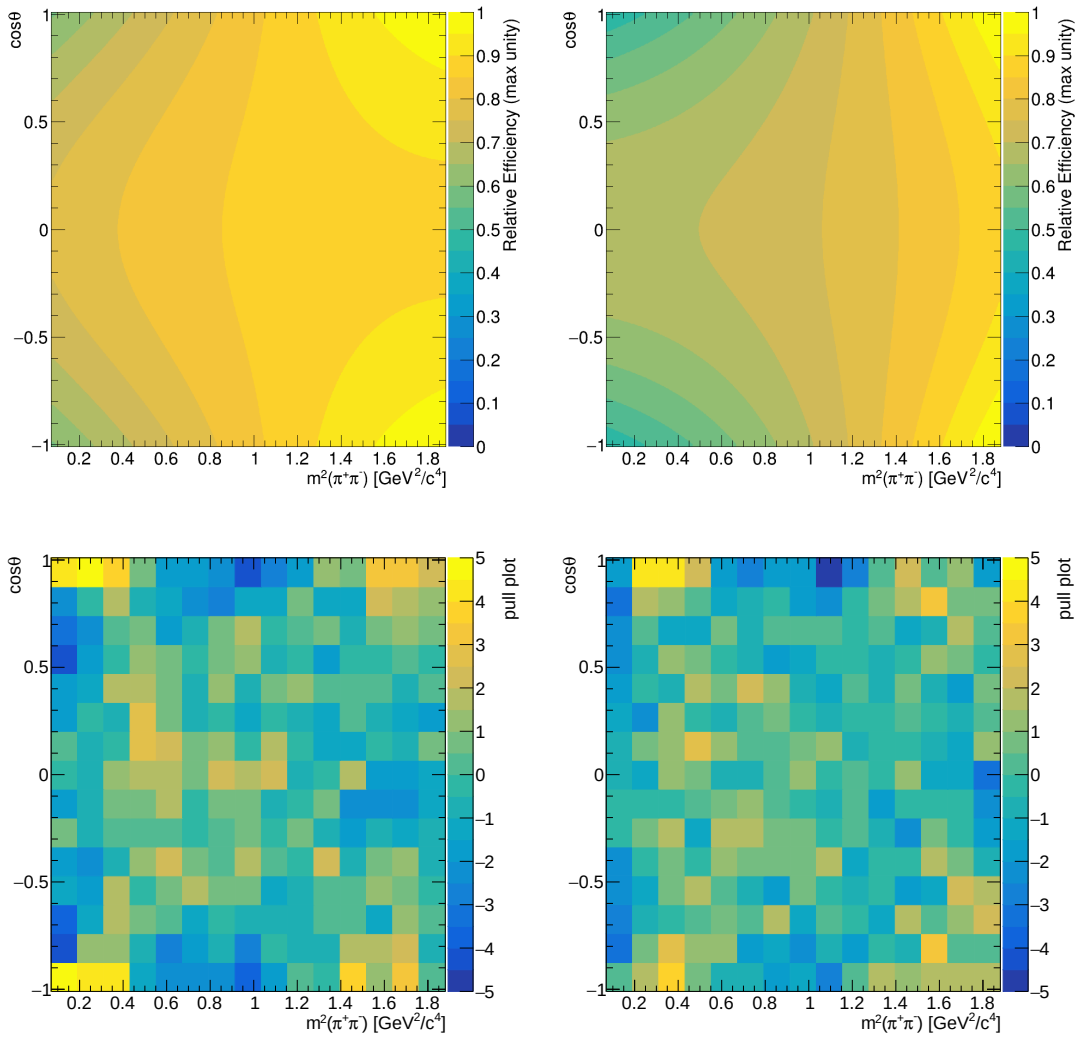

Figure A.5 – (Top) Efficiency function of Equation (4.4) in the plane $(m^2(\pi^+\pi^-), \cos\theta_{\pi^+\pi^-})$ for the parameters of Table 4.2 year 2018 (with $q_5 = q_6 = 0$), separately for reconstructed K_S^0 in the DD (left) and LL (right) categories. (Bottom) Corresponding pull plots with respect to the simulated sample for the 2018 data-taking year.

B Detailed results

B.1 Signal and background yield in each Dalitz and D^0 decay time bins.

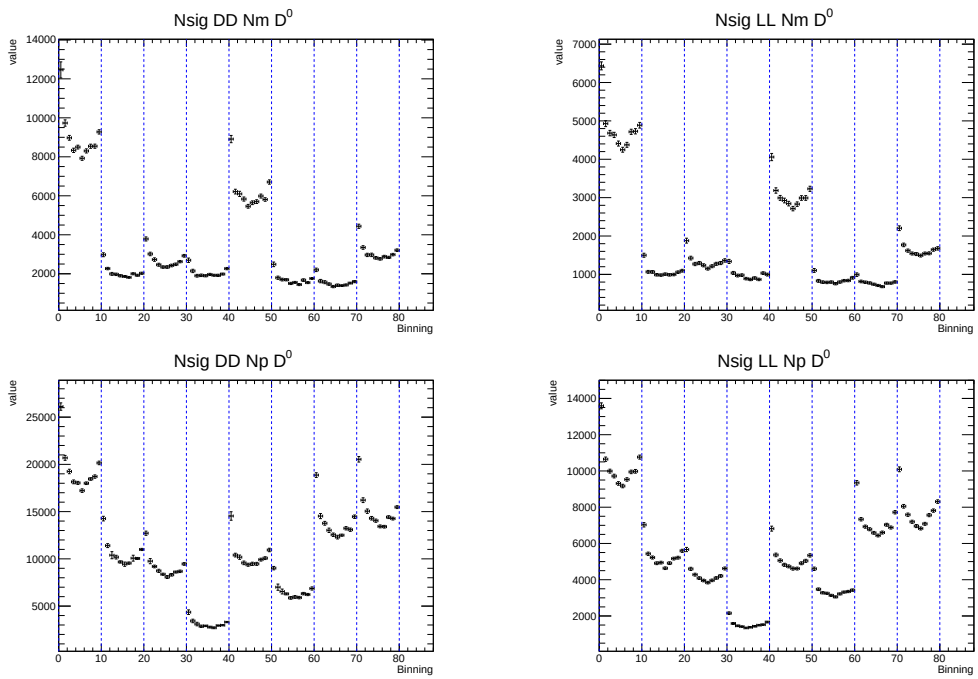

Figure B.1 – D^0 signal yield parameters from fits in (8 Dalitz bins) × (10 decay time bins) for DD (left) and LL (right). Fit on positive (negative) part of the Dalitz plot are denoted as Np (Nm).

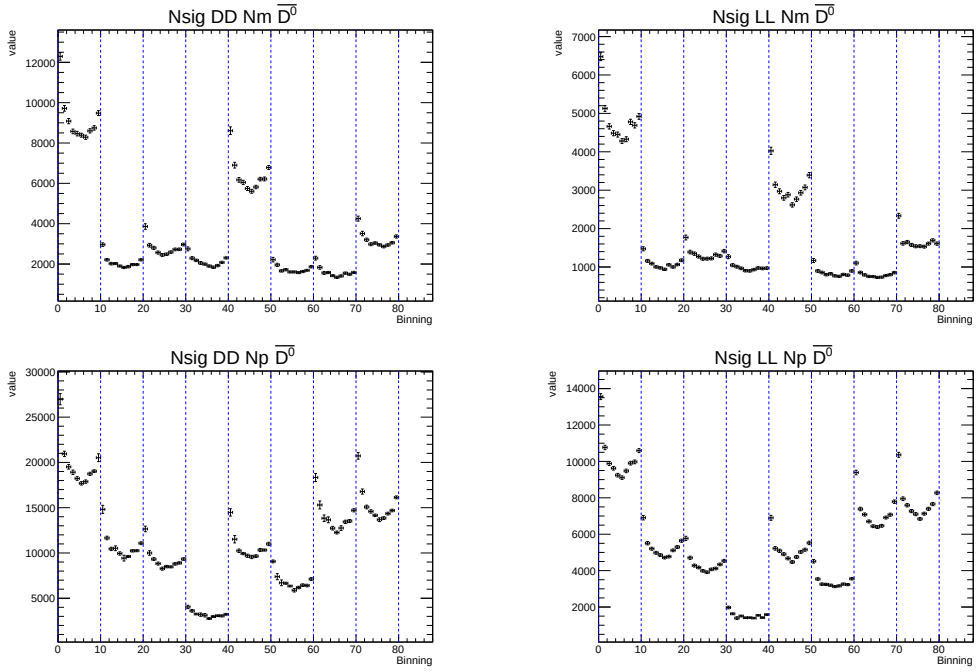

Figure B.2 – $\overline{D}^0$ signal yield parameters from fits in (8 Dalitz bins) × (10 decay time bins) for DD (left) and LL (right). Fit on positive (negative) part of the Dalitz plot are denoted as Np (Nm).

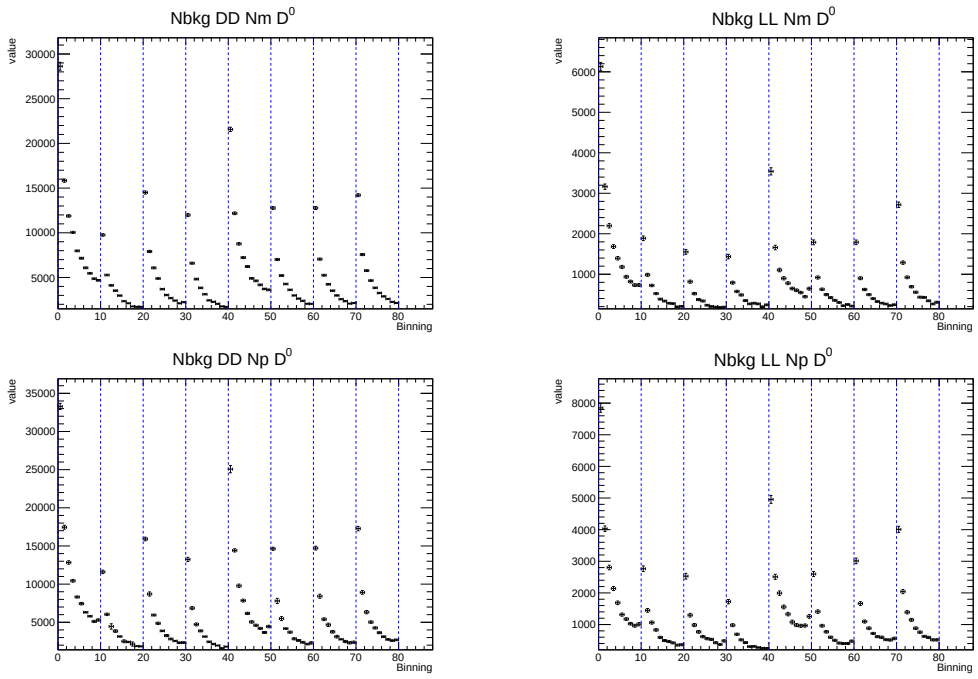

Figure B.3 – D^0 background yield parameters from fits in (8 Dalitz bins) × (10 decay time bins) for DD (left) and LL (right). Fit on positive (negative) part of the Dalitz plot are denoted as Np (Nm).

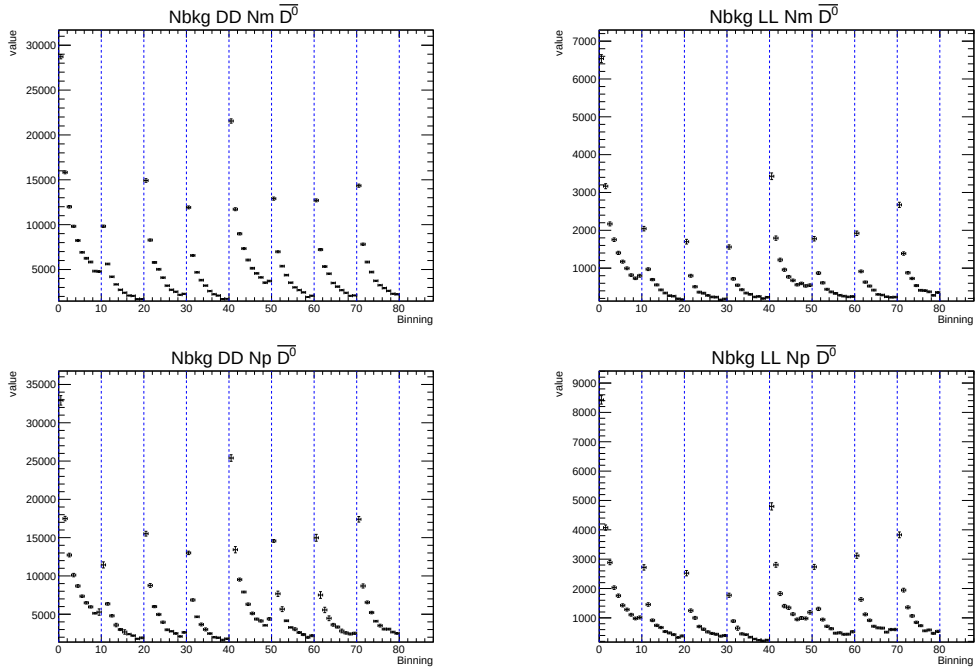

Figure B.4 – $\overline{D}^0$ background yield parameters from fits in (8 Dalitz bins) × (10 decay time bins) for DD (left) and LL (right). Fit on positive (negative) part of the Dalitz plot are denoted as Np (Nm).

B.2 Numerical results with different r_b

Table B.1 – Numerical results from the Binflip fit to the data separately for no CP violation and allowed one. The ratio r_b is different between DD and LL samples.

Parameter	No *CP* violation	Indirect *CP* violation allowed
x_{CP} [10^{-3}]	4.41 ± 1.49	4.41 ± 1.49
y_{CP} [10^{-3}]	11.71 ± 3.12	11.44 ± 3.11
Δx [10^{-3}]	–	-0.80 ± 0.93
Δy [10^{-3}]	–	2.90 ± 1.91
c_1	0.700 ± 0.020	0.700 ± 0.020
c_2	0.643 ± 0.036	0.645 ± 0.036
c_3	0.002 ± 0.047	0.007 ± 0.047
c_4	-0.606 ± 0.052	-0.605 ± 0.052
c_5	-0.955 ± 0.023	-0.954 ± 0.023
c_6	-0.577 ± 0.058	-0.574 ± 0.058
c_7	0.064 ± 0.056	0.071 ± 0.056
c_8	0.412 ± 0.036	0.414 ± 0.036
s_1	0.091 ± 0.062	0.091 ± 0.062
s_2	0.304 ± 0.108	0.309 ± 0.108
s_3	0.996 ± 0.074	1.003 ± 0.074
s_4	0.645 ± 0.122	0.648 ± 0.122
s_5	-0.028 ± 0.068	-0.025 ± 0.068
s_6	-0.547 ± 0.120	-0.543 ± 0.120
s_7	-0.864 ± 0.093	-0.855 ± 0.094
s_8	-0.434 ± 0.082	-0.430 ± 0.082
DD		
r_1	0.4658 ± 0.0020	0.4659 ± 0.0020
r_2	0.1962 ± 0.0017	0.1961 ± 0.0017
r_3	0.2951 ± 0.0025	0.2951 ± 0.0025
r_4	0.6586 ± 0.0072	0.6587 ± 0.0072
r_5	0.5959 ± 0.0036	0.5961 ± 0.0036
r_6	0.2569 ± 0.0027	0.2570 ± 0.0027
r_7	0.1145 ± 0.0012	0.1145 ± 0.0012
r_8	0.2109 ± 0.0014	0.2108 ± 0.0014
LL		
r_1	0.4723 ± 0.0021	0.4723 ± 0.0021
r_2	0.2059 ± 0.0018	0.2058 ± 0.0018
r_3	0.3040 ± 0.0028	0.3040 ± 0.0028
r_4	0.6379 ± 0.0071	0.6380 ± 0.0071
r_5	0.5922 ± 0.0038	0.5923 ± 0.0038
r_6	0.2486 ± 0.0027	0.2486 ± 0.0027
r_7	0.1134 ± 0.0012	0.1134 ± 0.0012
r_8	0.2173 ± 0.0015	0.2172 ± 0.0015

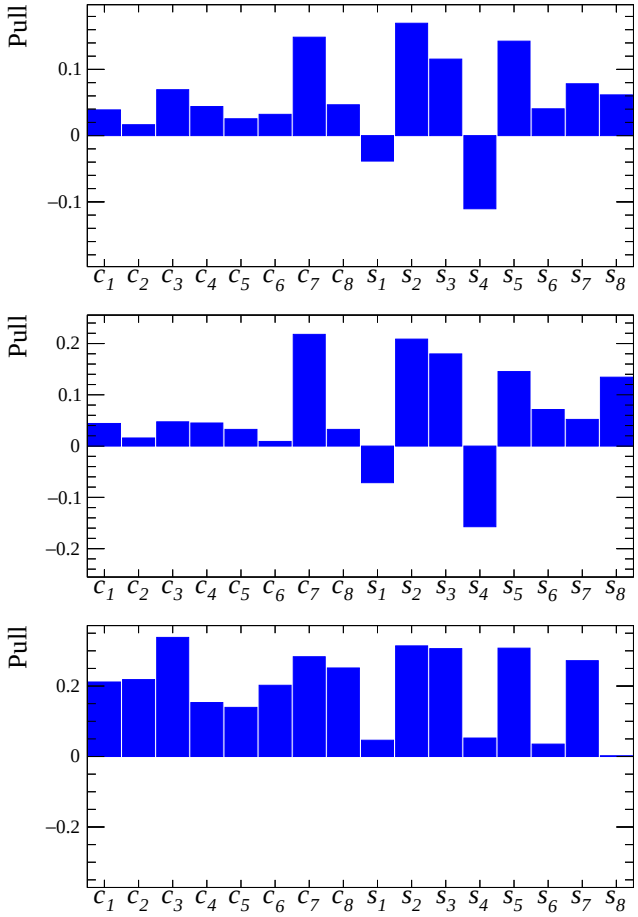

Figure B.5 – Pulls of the measured strong phases with respect to the central values used in the constraints, for fits performed using (top) combined BESIII and CLEO inputs, (middle) BESIII inputs only, (bottom) CLEO inputs only where r_b is not constrained.

C Detection asymmetry by data-taking years

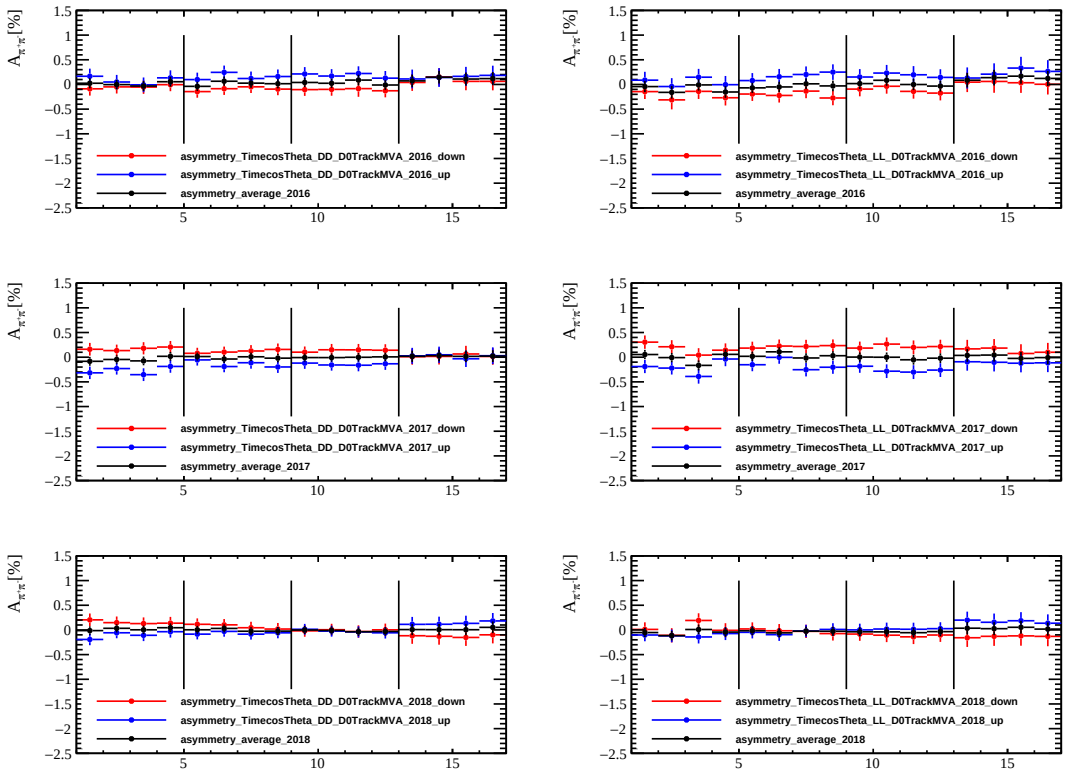

Figure C.1 – Observed tracking detection asymmetry as a function of $(t/\tau_{D^0}, |\cos\theta_{\pi^+\pi^-}|)$ separately for DD (left) and LL (right) from combined data-taking year with averaged magnet polarity.

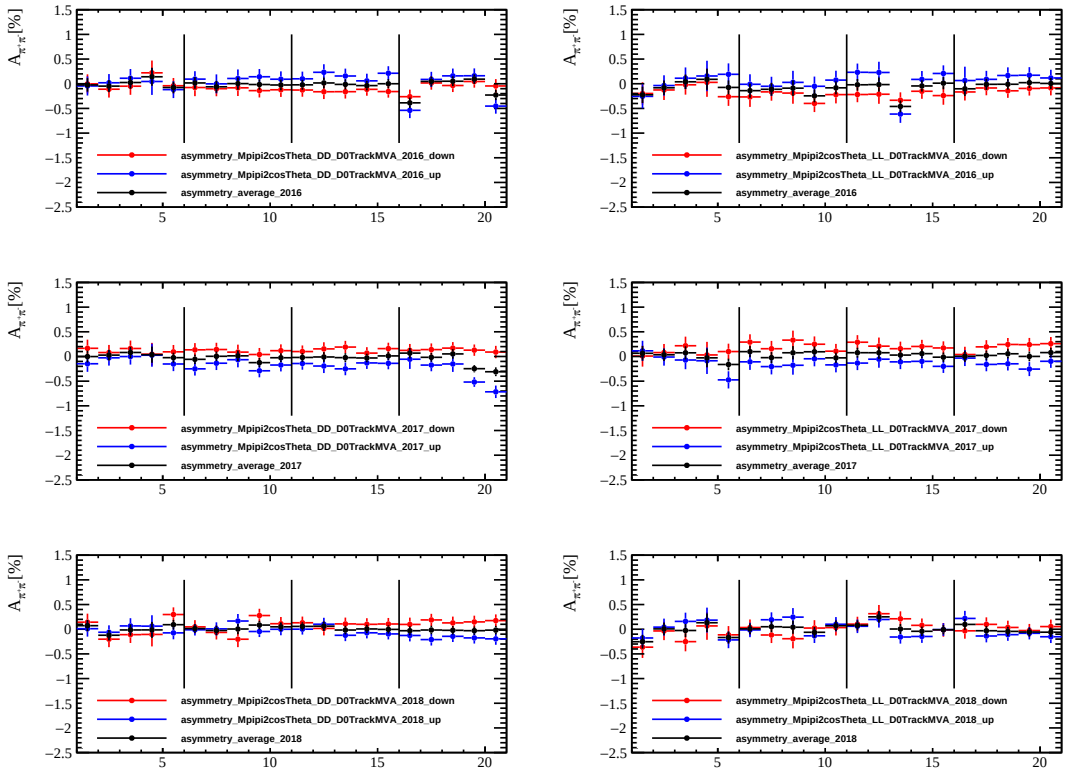

Figure C.2 – Observed tracking detection asymmetry as a function of $(m^2(\pi^+\pi^-), |\cos\theta_{\pi^+\pi^-}|)$ separately for DD (left) and LL (right) from combined data-taking year with averaged magnet polarity.

D Reweight $\overline{B} \to D^0(\to K^-\pi^+)\mu^-\overline{\nu}_\mu X$ to $\overline{B} \to D^0(\to K^0_S\pi^+\pi^-)\mu^-\overline{\nu}_\mu X$

In this section, we are matching the kinematics of the $\overline{B} \to D^0(\to K^-\pi^+)\mu^-\overline{\nu}_\mu X$ decay to that of $\overline{B} \to D^0(\to K^0_S\pi^+\pi^-)\mu^-\overline{\nu}_\mu X$. These two decay modes come from a similar $\overline{B} \to D^0\mu^-\overline{\nu}_\mu X$ reconstruction. The selections are described in Section 6.6.2 where two MVA models trained on different K^0_S categories of the $\overline{B} \to D^0(\to K^0_S\pi^+\pi^-)\mu^-\overline{\nu}_\mu X$ sample are applied on the same $\overline{B} \to D^0(\to K^-\pi^+)\mu^-\overline{\nu}_\mu X$ decay. This leads to two different samples of the $\overline{B} \to D^0(\to K^-\pi^+)\mu^-\overline{\nu}_\mu X$ decay. We denote these two samples as DD and LL similar to the $\overline{B} \to D^0(\to K^0_S\pi^+\pi^-)\mu^-\overline{\nu}_\mu X$ sample described in Chapter 3.

A Gradient Boosting reweighter is used, as explained earlier in Section 6.6. The training variables are the B's decay vertex quality, the D^0 pesudo-rapidity, as well as the D^0 and μ^- transverse momenta. The sample is divided randomly into two subsamples for training and testing, to check further for possible overtraining. These are presented in Figures D.1 and D.3 for DD and LL sample, respectively.

We train two reweighters separately for the DD and LL $\overline{B} \to D^0(\to K^-\pi^+)\mu^-\overline{\nu}_\mu X$ samples until their distributions match the ones in the DD and LL $\overline{B} \to D^0(\to K^0_S\pi^+\pi^-)\mu^-\overline{\nu}_\mu X$ samples, as shown in Figures D.2 and D.4 for DD and LL samples.

After the reweighing procedure, the sample is divided into right sign $\overline{B} \to D^0(\to K^-\pi^+)\mu^-\overline{\nu}_\mu X$ candidates and wrong sign $\overline{B} \to D^0(\to K^-\pi^+)\mu^+\overline{\nu}_\mu X$ candidates based on the charges of the kaon and muon. Yields are extracted from a fit to the $D^0 \to K^-\pi^+$ mass distribution for each decay time bin. The mistag probability is computed as explained in Section 6.6 with Equation (6.11). The effect of known possible mixing and DCS decays is accounted for as a function of decay time [123]. We show the mistag probability as a function of D^0 decay time in Figures D.5 and D.6 for 2017 and 2018 data-taking years.

The mistag probabilities are found to be independent of the D^0 decay time and consistent between these two data-taking years. Note that the 2016 data-taking sample is not available as the TopoMu trigger lines were not applied on that data.

To validate the representativeness of the $\overline{B} \to D^0(\to K^-\pi^+)\mu^-\overline{\nu}_\mu X$ decay mode for $\overline{B} \to D^0(\to$

$K^0_S\pi^+\pi^-)\mu^-\overline{\nu}_\mu X$, we examine the mistag probability of $B \to D^*(\to D^0\pi^+_s)\mu X$ with $D^0 \to K^-\pi^+$ decay mode. The sample is trained similarly to the $\overline{B} \to D^0(\to K^-\pi^+)\mu^-\overline{\nu}_\mu X$ explained earlier. However, because the B vertex is reconstructed differently in this sample, the χ^2 distribution is affected and leading to an incompatibility between DoubleTag and SingleTag.

The training variables of the DoubleTag sample are presented in Figures D.7 and D.8 before and after applying the optimal reweighter on the DD $\overline{B} \to D^0(\to K^-\pi^+)\mu^-\overline{\nu}_\mu X$ sample. Figures D.9 and D.10 show the corresponding distribution for LL $\overline{B} \to D^0(\to K^-\pi^+)\mu^-\overline{\nu}_\mu X$ sample.

Figures D.12–D.13 compare mistag probabilities of $D^0 \to K^-\pi^+$ and $D^0 \to K^0_S\pi^+\pi^-$ decays tagging through the $B \to D^*(\to D^0\pi^+_s)\mu X$ decay. The probabilities are found to be independent of the D^0 decay time, and are slightly higher for the $D^0 \to K^0_S\pi^+\pi^-$ decay mode. Therefore, we estimate the mistag probability in the $\overline{B} \to D^0(\to K^0_S\pi^+\pi^-)\mu^-\overline{\nu}_\mu X$ as the average mistag probability found in the reweighted SingleTag $\overline{B} \to D^0(\to K^-\pi^+)\mu^-\overline{\nu}_\mu X$ sample with a scaling factor from the DoubleTag samples.

We also show the mistag probability measured in the $B \to D^*(\to D^0\pi^+_s)\mu X$ sample with $D^0 \to K^0_S\pi^+\pi^-$ during the 2016 data-taking year as shown in Figure D.11. Its average is consistent with the other years. Although the sample of $D^0 \to K^-\pi^+$ decays mode is not available for this year, the $D^0 \to K^0_S\pi^+\pi^-$ mistag probability is verified to be similar to $D^0 \to K^0_S\pi^+\pi^-$ in the other years.

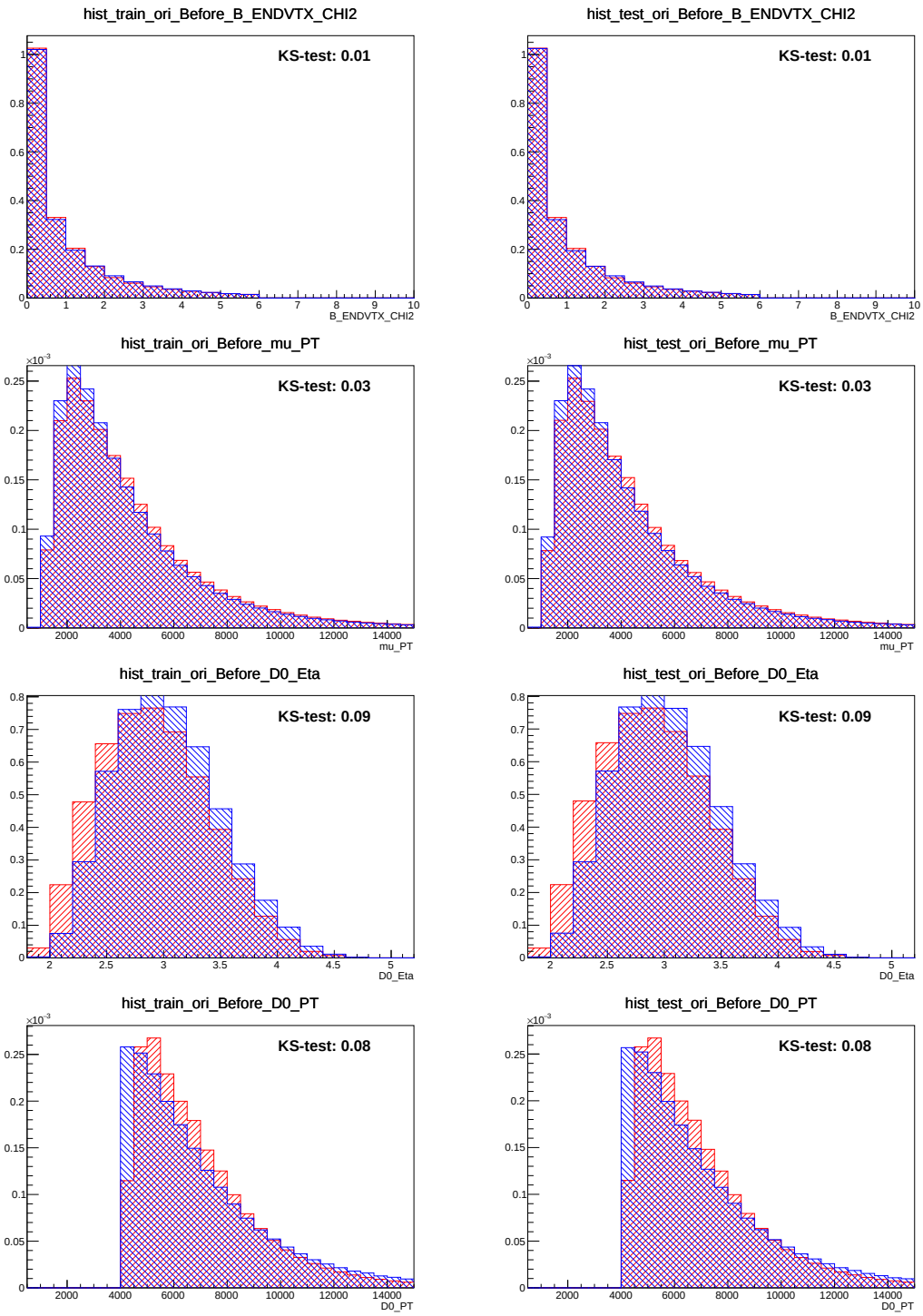

Figure D.1 – Distributions of the variables before reweighting of the (left) training and (right) testing samples. The original sample of $\overline{B} \to D^0(\to K^-\pi^+)\mu^-\overline{\nu}_\mu X$ (red) and the target sample of $\overline{B} \to D^0(\to K^0_S\pi^+\pi^-)\mu^-\overline{\nu}_\mu X$ decays (blue) are shown for the DD samples.

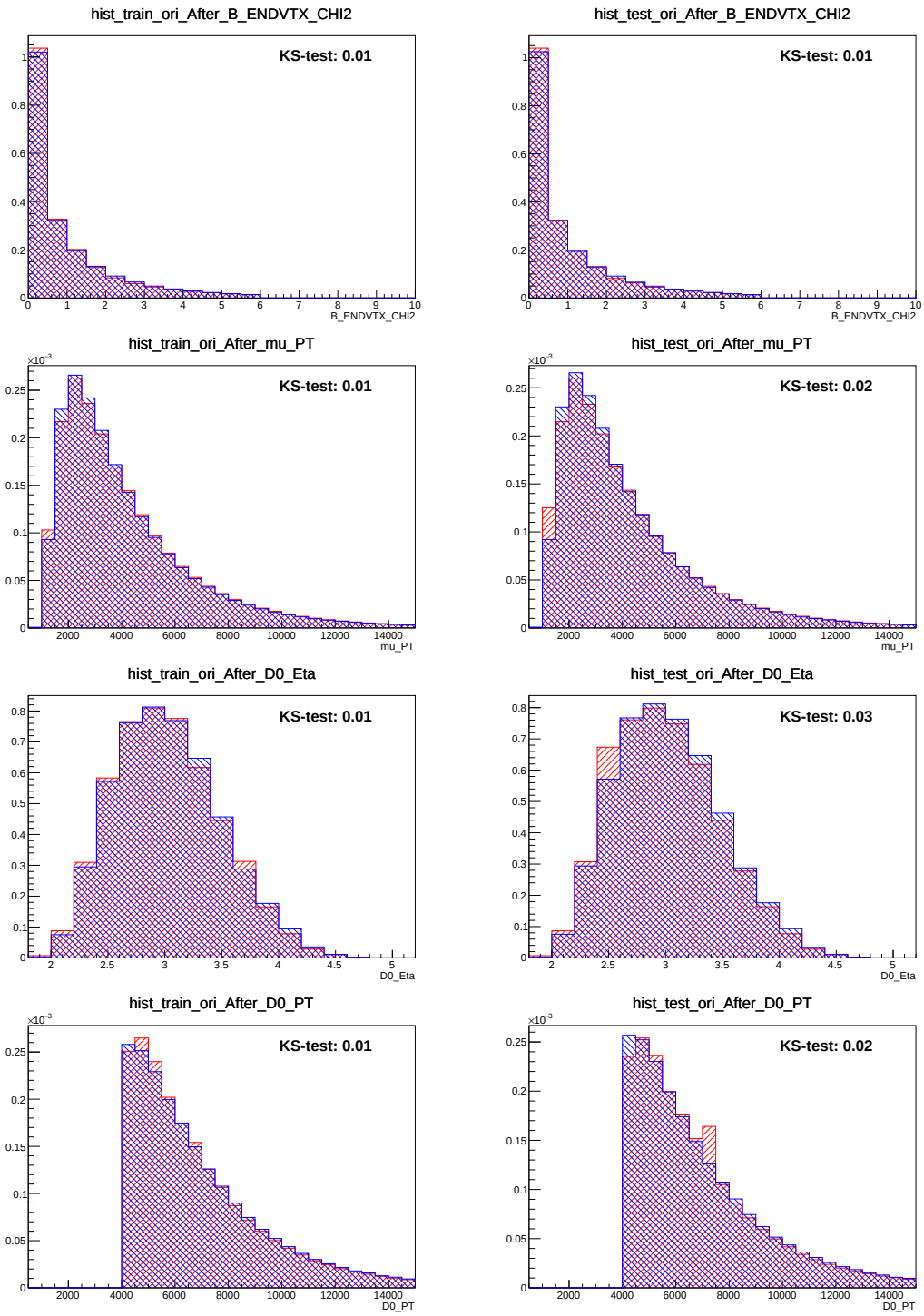

Figure D.2 – Distributions of the variables after reweighting of the (left) training and (right) testing samples. The original sample of $\overline{B} \to D^0(\to K^-\pi^+)\mu^-\overline{\nu}_\mu X$ (red) and the target sample of $\overline{B} \to D^0(\to K^0_S\pi^+\pi^-)\mu^-\overline{\nu}_\mu X$ decays (blue) are shown for the DD samples.

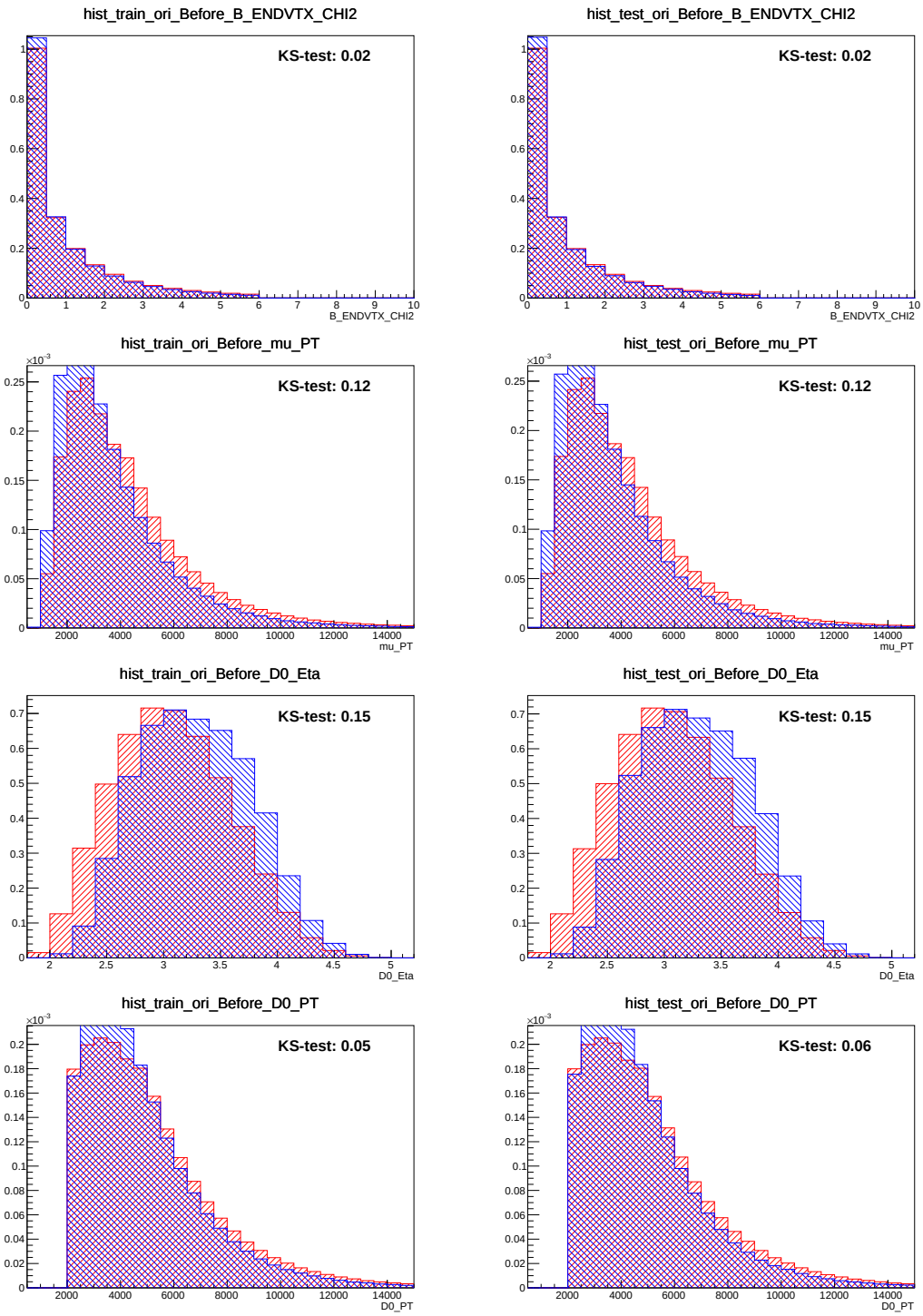

Figure D.3 – Distributions of the variables before reweighting of the (left) training and (right) testing samples. The original sample of $\overline{B} \to D^0(\to K^-\pi^+)\mu^-\overline{\nu}_\mu X$ (red) and the target sample of $\overline{B} \to D^0(\to K^0_S\pi^+\pi^-)\mu^-\overline{\nu}_\mu X$ decays (blue) are shown for the LL samples.

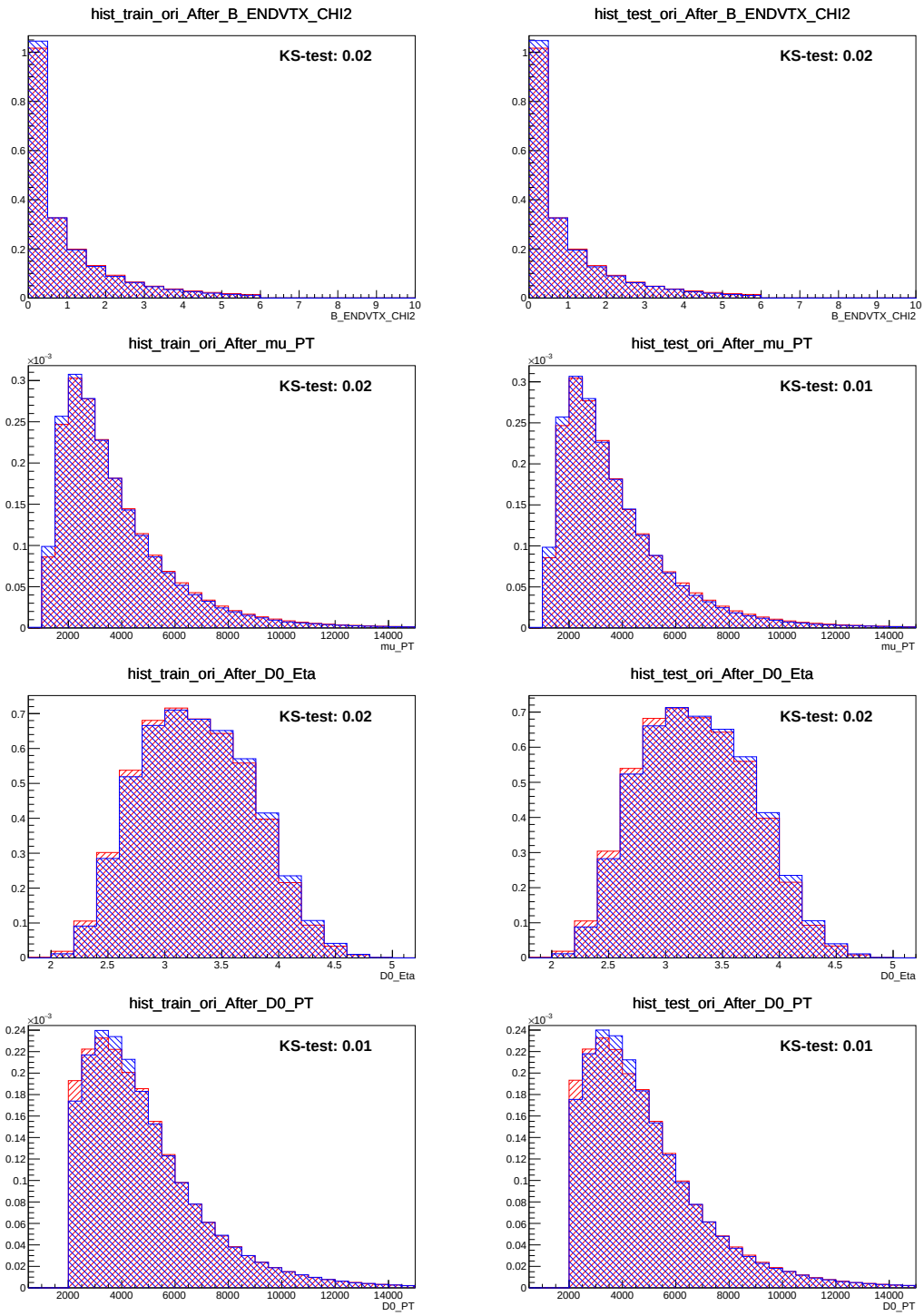

Figure D.4 – Distributions of the variables after reweighting of the (left) training and (right) testing samples. The original sample of $\overline{B} \to D^0(\to K^-\pi^+)\mu^-\overline{\nu}_\mu X$ (red) and the target sample of $\overline{B} \to D^0(\to K^0_S\pi^+\pi^-)\mu^-\overline{\nu}_\mu X$ decays (blue) are shown for the LL samples.

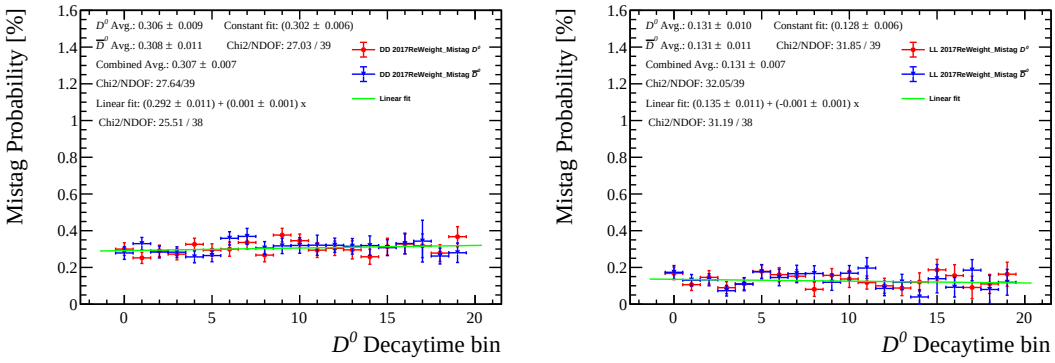

Figure D.5 – Mistag probability as a function of D^0 decay time separately for D^0 and $\overline{D}^0$ in the reweighted $\overline{B} \to D^0(\to K^-\pi^+)\mu^-\overline{\nu}_\mu X$ sample for the 2017 data-taking year. The MVA selection is applied with the model trained on (left) DD and (right) LL $\overline{B} \to D^0(\to K^0_S\pi^+\pi^-)\mu^-\overline{\nu}_\mu X$.

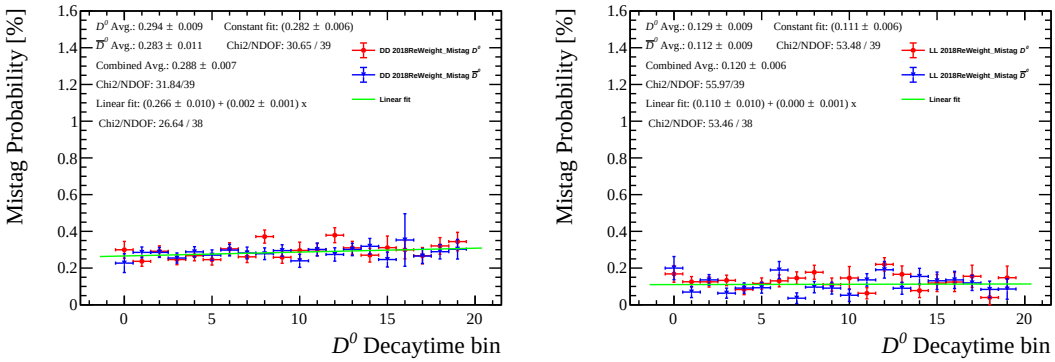

Figure D.6 – Mistag probability as a function of D^0 decay time separately for D^0 and $\overline{D}^0$ in the reweighted $\overline{B} \to D^0(\to K^-\pi^+)\mu^-\overline{\nu}_\mu X$ sample for the 2018 data-taking year. The MVA selection is applied with the model trained on (left) DD and (right) LL $\overline{B} \to D^0(\to K^0_S\pi^+\pi^-)\mu^-\overline{\nu}_\mu X$.

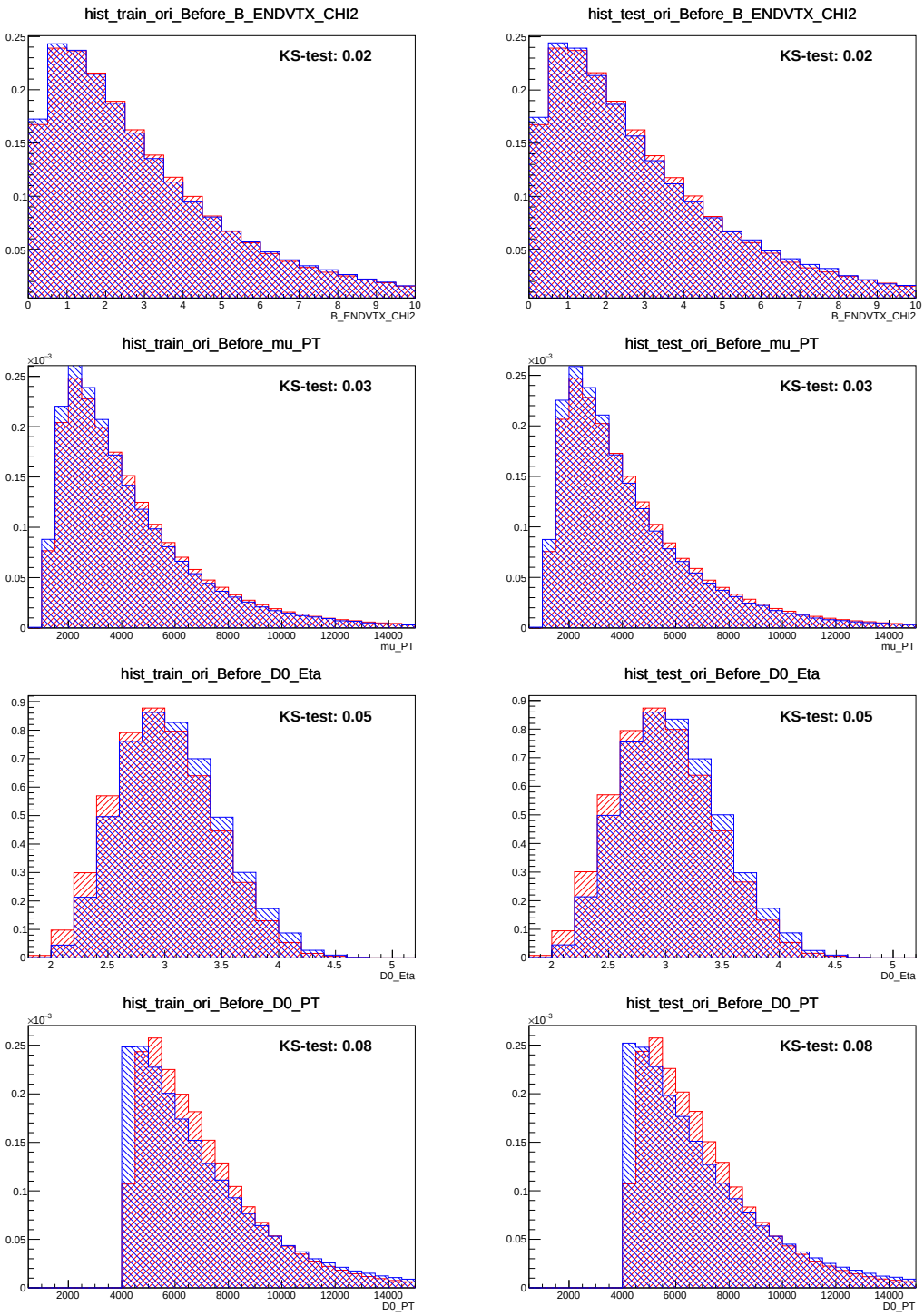

Figure D.7 – Distributions of the variables before reweighing of (Left) training and (Right) testing samples. The original sample $B \to D^*(\to D^0\pi^+_s)\mu X$ with the $D^0 \to K^0_S\pi^+\pi^-$ decay mode (Red) and target of the $D^0 \to K^-\pi^+$ mode (Blue) are showed for K^0_S DD MVA model.

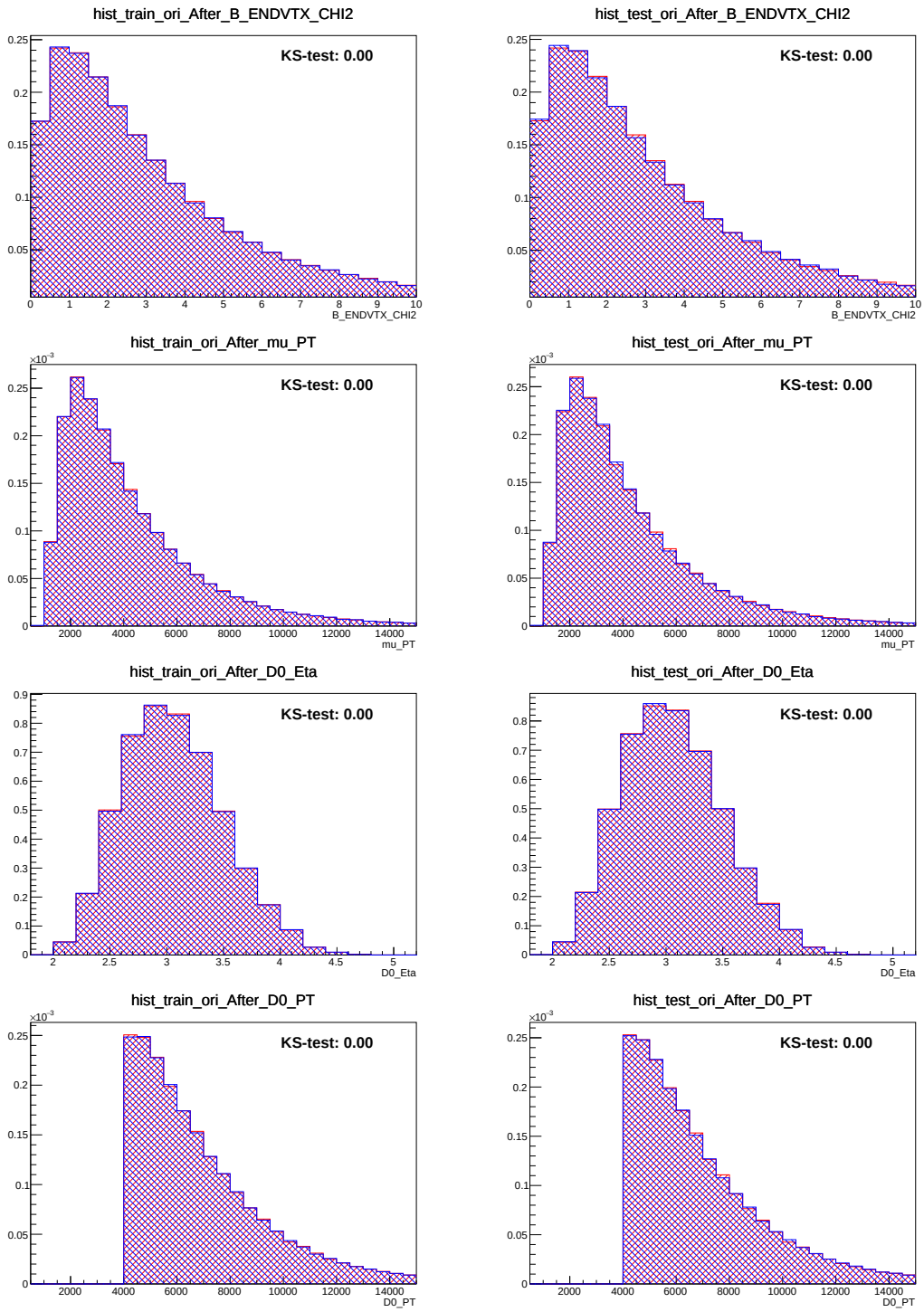

Figure D.8 – Distributions of the variables after reweighing of (Left) training and (Right) testing samples. The original sample $B \to D^*(\to D^0\pi_s^+)\mu X$ with the $D^0 \to K_S^0\pi^+\pi^-$ decay mode (Red) and target of the $D^0 \to K^-\pi^+$ mode (Blue) are showed for K_S^0 DD MVA model.

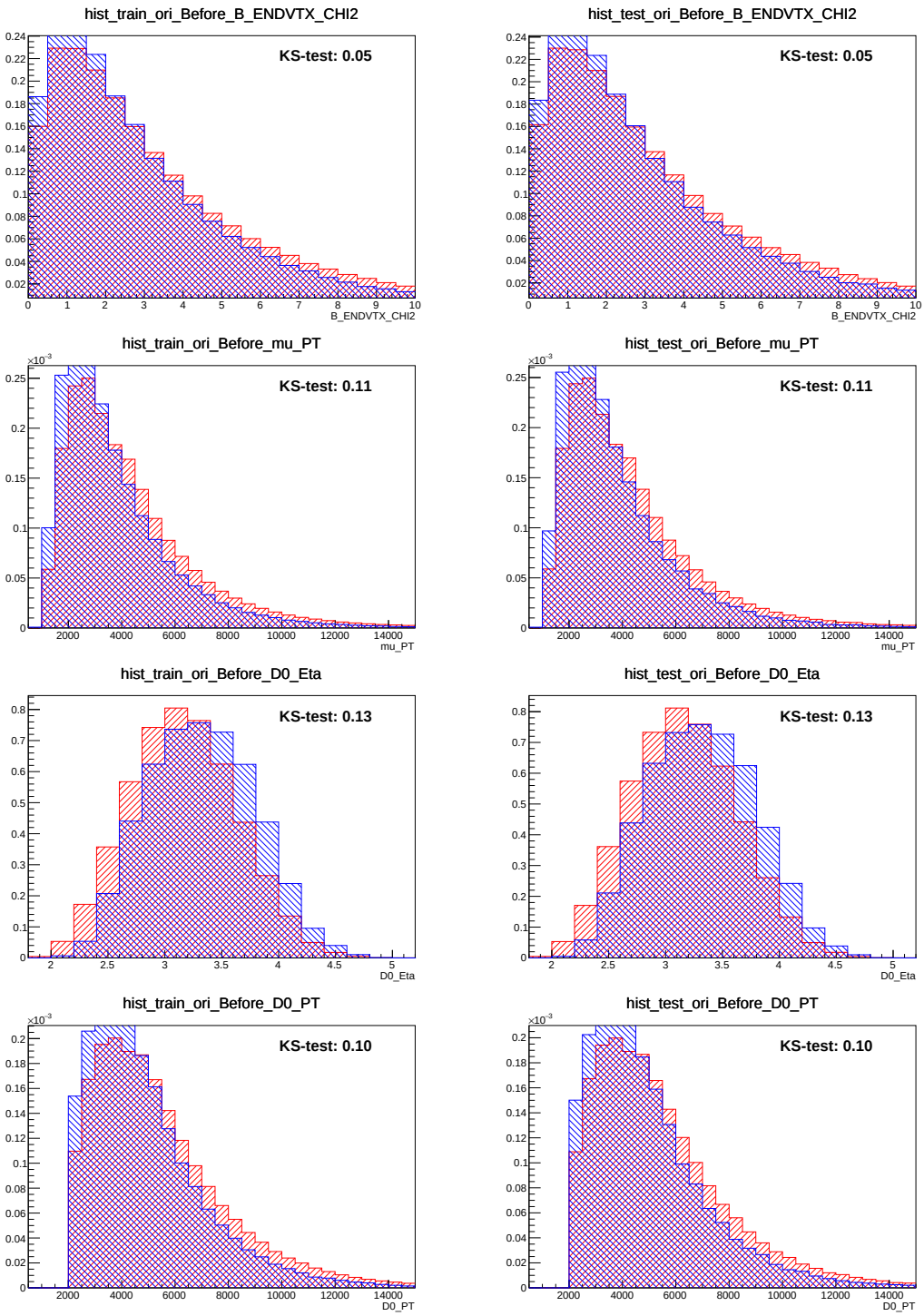

Figure D.9 – Distributions of the variables before reweighing of (Left) training and (Right) testing samples. The original sample $B \to D^*(\to D^0\pi^+_s)\mu X$ with the $D^0 \to K^0_S\pi^+\pi^-$ decay mode (Red) and target of the $D^0 \to K^-\pi^+$ mode (Blue) are showed for K^0_S LL MVA model.

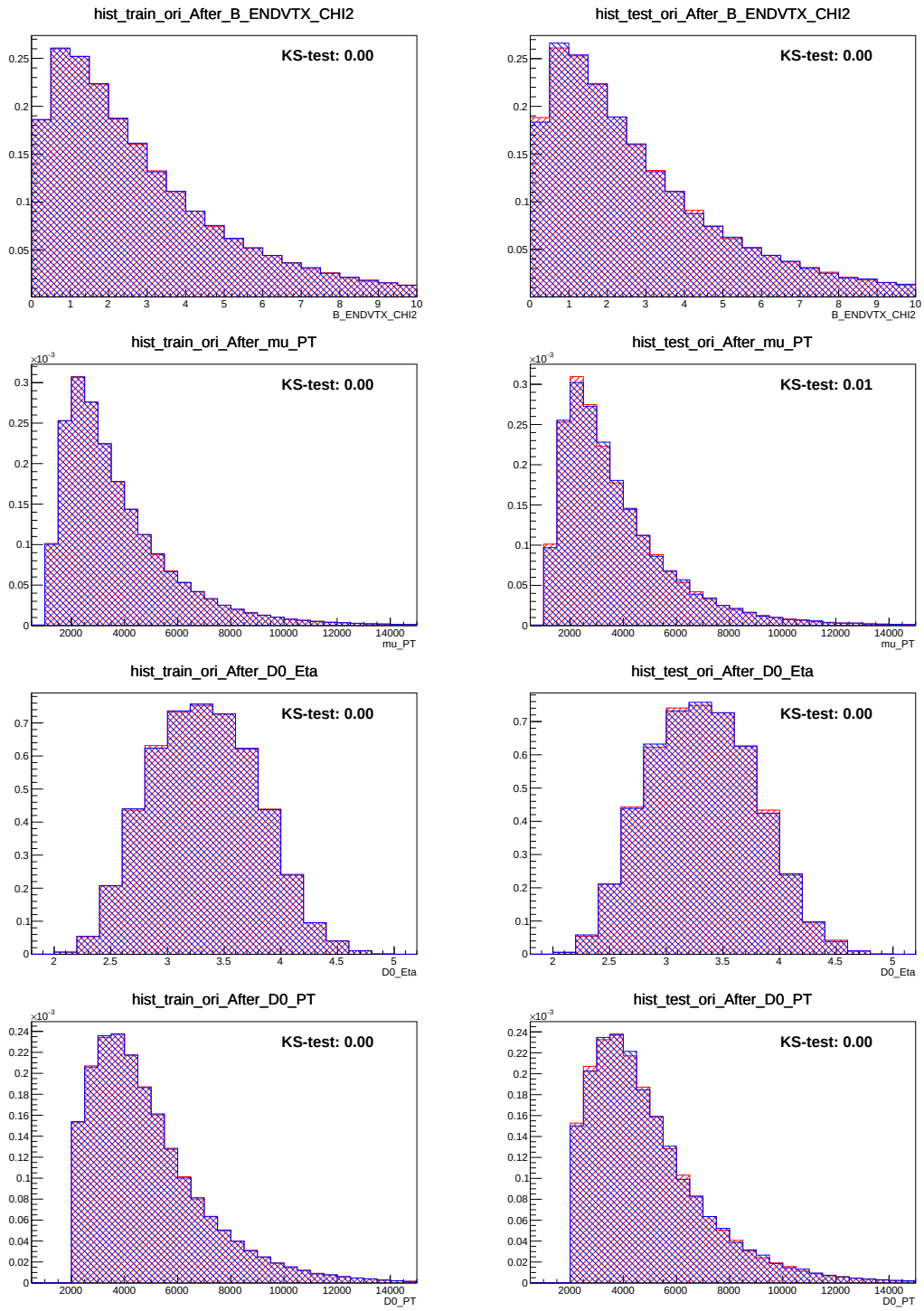

Figure D.10 – Distributions of the variables after reweighing of (Left) training and (Right) testing samples. The original sample $B \to D^*(\to D^0\pi_s^+)\mu X$ with the $D^0 \to K_S^0\pi^+\pi^-$ decay mode (Red) and target of the $D^0 \to K^-\pi^+$ mode (Blue) are showed for K_S^0 LL MVA model.

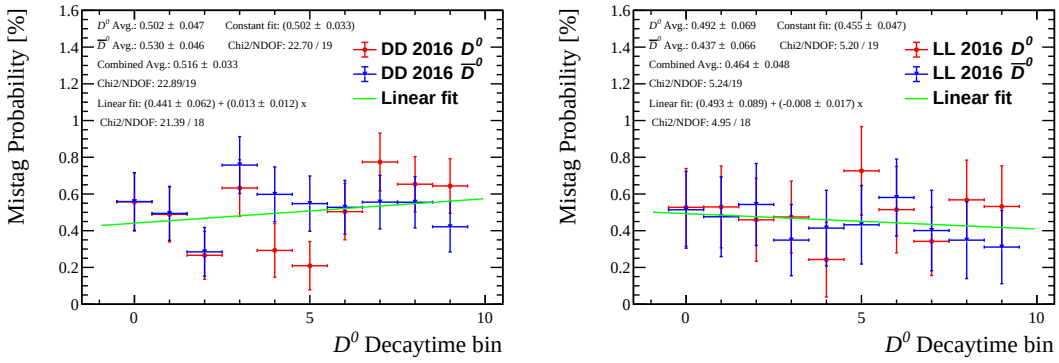

Figure D.11 – Mistag probability as a function of D^0 decay time separately for D^0 and $\overline{D}^0$ in the reweighted $\overline{B}^0 \to D^{*+}(\to D^0\pi^+)\mu^- X$ sample with final state $D^0 \to K^0_S\pi^+\pi^-$: (left) DD, (right) LL samples for the 2016 data-taking year.

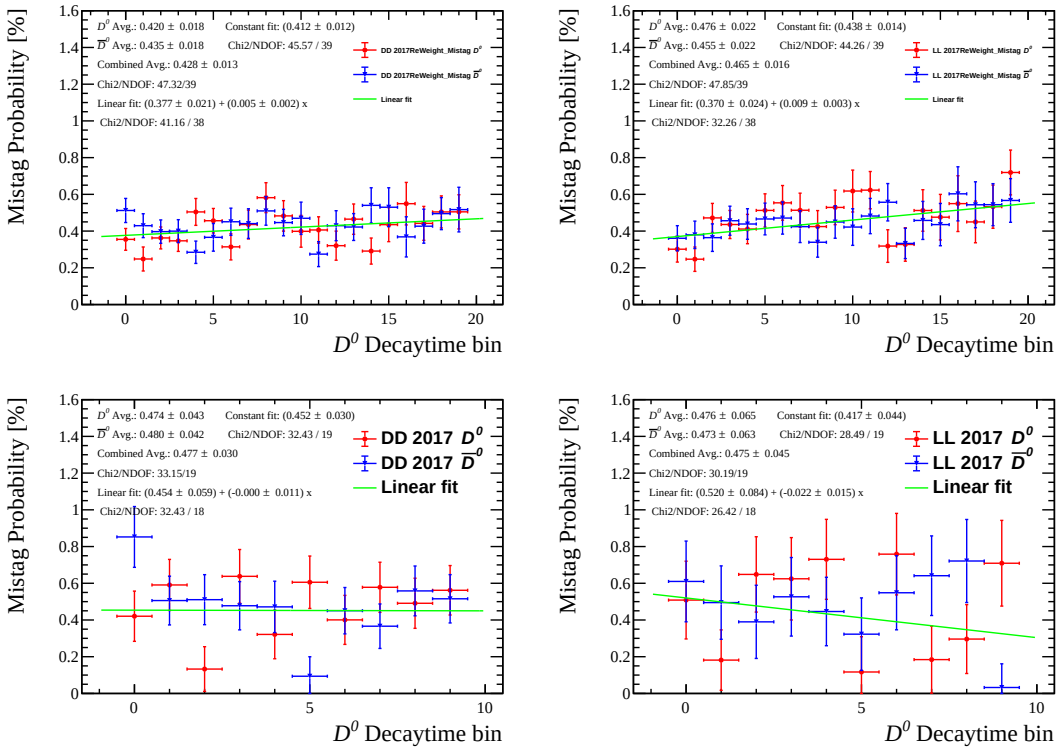

Figure D.12 – Mistag probability as a function of D^0 decay time separately for D^0 and $\overline{D}^0$ in the reweighted $\overline{B}^0 \to D^{*+}(\to D^0\pi^+)\mu^- X$ with final state: (top) $D^0 \to K^-\pi^+$, (bottom) $D^0 \to K^0_S\pi^+\pi^-$, (left) DD, (Right) LL samples for 2017 data-taking year.

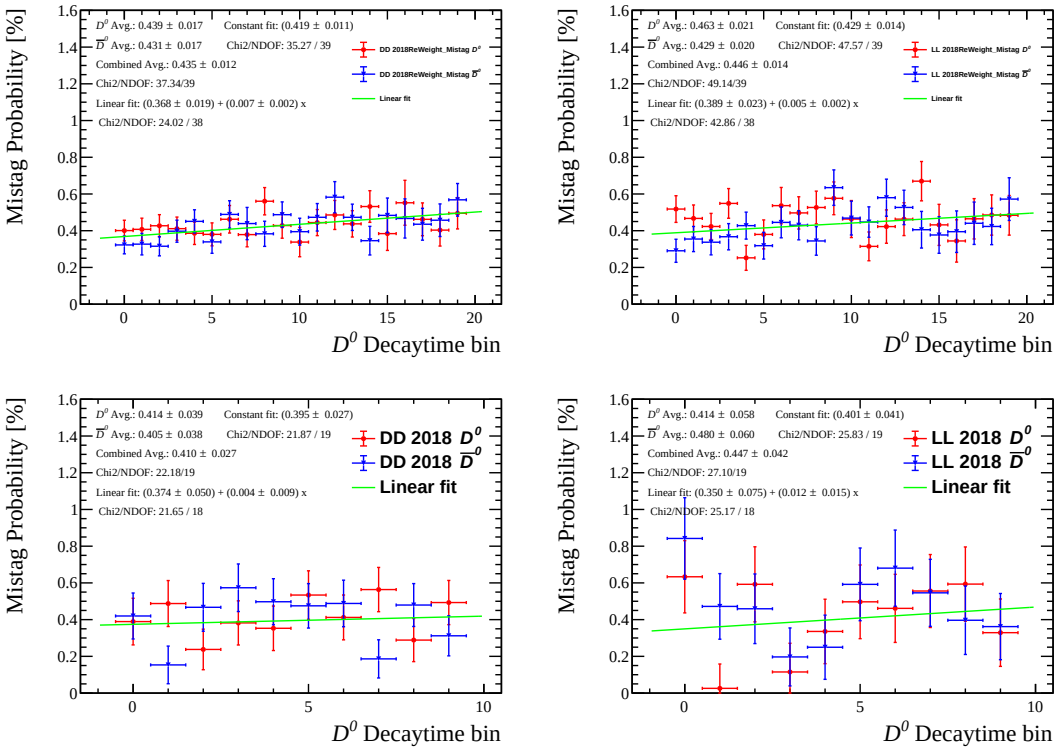

Figure D.13 – Mistag probability as a function of D^0 decay time separately for D^0 and $\overline{D}^0$ in the reweighted $\overline{B}^0 \to D^{*+}(\to D^0\pi^+)\mu^- X$ with final state: (top) $D^0 \to K^-\pi^+$, (bottom) $D^0 \to K_S^0\pi^+\pi^-$, (left) DD, (Right) LL samples for 2018 data-taking year.

Bibliography

[1] LHCb collaboration, R. Aaij *et al.*, *Observation of D^0–$\overline{D}^0$ oscillations*, Phys. Rev. Lett. **110** (2013) 101802, `arXiv:1211.1230`.

[2] S. Ek-In *et al.*, *Run 2 analysis of semileptonic $D^0 \to K^0_S\pi^+\pi^-$ decays with the bin-flip method*, 2020. LHCb-ANA-2020-038.

[3] LHCb collaboration, R. Aaij *et al.*, *Model-independent measurement of charm mixing parameters in $\overline{B} \to D^0(\to K^0_S\pi^+\pi^-)\mu^-\overline{\nu}_\mu X$ decays*, `arXiv:2208.06512`.

[4] A. Di Canto *et al.*, *Run 2 analysis of prompt $D^0 \to K^0_S\pi^+\pi^-$ decays with the bin-flip method*, 2020. LHCb-ANA-2020-020.

[5] LHCb collaboration, R. Aaij *et al.*, *Observation of the mass difference between neutral charm-meson eigenstates*, Phys. Rev. Lett. **127** (2021) 111801, `arXiv:2106.03744`.

[6] M. Hilton *et al.*, *Measurement of charm mixing and CP violation parameters using a time-dependent amplitude analysis of semileptonically-tagged $D^0 \to K^0_S\pi^+\pi^-$ decay.*, LHCb internal analysis note (in preparation).

[7] W. Shen *et al.*, *A silicon photomultiplier readout ASIC for time-of-flight applications using a new time-of-recovery method*, IEEE Trans. Nucl. Sci. **65** (2018) 1196.

[8] M. E. Stramaglia *et al.*, *SHiP_DAQ_run_TB*, https://gitlab.cern.ch/mstramag/SHiP_DAQ_run_TB. Accessed: 2022-05-20.

[9] LHCb collaboration, *Rec package: forward tracking with histograming technique*, https://gitlab.cern.ch/lhcb/Rec/-/tree/dev-hist. Accessed: 2022-05-20.

[10] S. L. Glashow, *Partial symmetries of weak interactions*, Nucl. Phys. **22** (1961) 579.

[11] S. Weinberg, *A Model of Leptons*, Phys. Rev. Lett. **19** (1967) 1264.

[12] A. Salam, *Weak and Electromagnetic Interactions*, Conf. Proc. C **680519** (1968) 367.

[13] C.-N. Yang and R. L. Mills, *Conservation of isotopic spin and isotopic gauge invariance*, Phys. Rev. **96** (1954) 191.

[14] Particle Data Group, P. A. Zyla *et al.*, *Review of particle physics*, Prog. Theor. Exp. Phys. **2020** (2020) 083C01.

[15] E. Siegel, *Ask Ethan: How do quantum fields create particles?*, https://www.forbes.com/sites/startswithabang/2019/01/13/ask-ethan-how-do-quantum-fields-create-particles/?sh=6a1a612330ad, 2019. Accessed: 2022-05-20.

[16] D. Tong, *Line operators in the Standard Model*, JHEP **07** (2017) 104, `arXiv:1705.01853`.

[17] CMS collaboration, S. Chatrchyan *et al.*, *Observation of a new boson at a mass of 125 GeV with the CMS experiment at the LHC*, Phys. Lett. **B716** (2012) 30, `arXiv:1207.7235`.

[18] ATLAS collaboration, G. Aad *et al.*, *Observation of a new particle in the search for the Standard Model Higgs boson with the ATLAS detector at the LHC*, Phys. Lett. **B716** (2012) 1, `arXiv:1207.7214`.

[19] F. Englert and R. Brout, *Broken symmetry and the mass of gauge vector mesons*, Phys. Rev. Lett. **13** (1964) 321.

[20] P. W. Higgs, *Broken symmetries and the masses of gauge bosons*, Phys. Rev. Lett. **13** (1964) 508.

[21] G. S. Guralnik, C. R. Hagen, and T. W. B. Kibble, *Global conservation laws and massless particles*, Phys. Rev. Lett. **13** (1964) 585.

[22] J. Woithe, G. J. Wiener, and F. F. V. der Veken, *Let's have a coffee with the Standard Model of particle physics!*, Physics Education **52** (2017) 034001.

[23] C. Burgard, *Standard Model of physics programmed in TikZ*, https://texample.net/tikz/examples/model-physics/, 2016. Accessed: 2022-05-20.

[24] J. Womersley, *Beyond the Standard Model*, https://web.archive.org/web/20071017160238/http://www.symmetrymagazine.org/pdfs/200502/beyond_the_standard_model.pdf, 2007. Accessed: 2022-05-20.

[25] J. D. Lykken, *Beyond the Standard Model*, `arXiv:1005.1676`, FERMILAB-CONF-10-103-T/CERN-2010-002.101.

[26] T. Mannel, *Theory and phenomenology of CP violation*, Nucl. Phys. Proc. Suppl. **B167** (2007) 115.

[27] L. Canetti, M. Drewes, and M. Shaposhnikov, *Matter and antimatter in the Universe*, New J. Phys. **14** (2012) 095012, `arXiv:1204.4186`.

[28] CERN, *The matter-antimatter asymmetry problem*, https://home.cern/science/physics/matter-antimatter-asymmetry-problem. Accessed: 2022-05-20.

[29] E. Corbelli and P. Salucci, *The extended rotation curve and the Dark Matter halo of M33*, Mon. Not. Roy. Astron. Soc. **311** (2000) 441, `arXiv:astro-ph/9909252`.

[30] Wikipedia, *Dark matter*, https://en.wikipedia.org/wiki/Dark_matter. Accessed: 2022-05-20.

[31] P. J. E. Peebles and B. Ratra, *The cosmological constant and Dark Energy*, Rev. Mod. Phys. **75** (2003) 559, `arXiv:astro-ph/0207347`.

[32] A. D. Sakharov, *Violation of CP in variance, C asymmetry, and baryon asymmetry of the universe*, Soviet Physics Uspekhi **34** (1991) 392.

[33] G. W. S. Hou, *Source of CP violation for the baryon asymmetry of the Universe*, Int. J. Mod. Phys. **D20** (2011) 1521, `arXiv:1101.2161`.

[34] O. W. Greenberg, *CPT violation implies violation of Lorentz invariance*, Phys. Rev. Lett. **89** (2002) 231602, `arXiv:hep-ph/0201258`.

[35] V. A. Kostelecky, *The Status of CPT*, in *5th International WEIN Symposium: A Conference on Physics Beyond the Standard Model (WEIN 98)*, 588–600, 1998, `arXiv:hep-ph/9810365`.

[36] C. S. Wu *et al.*, *Experimental test of parity conservation in β decay*, Phys. Rev. **105** (1957) 1413.

[37] R. G. Sachs, *CP violation in K^0 decays*, Phys. Rev. Lett. **13** (1964) 286.

[38] N. Cabibbo, *Unitary symmetry and leptonic decays*, Phys. Rev. Lett. **10** (1963) 531.

[39] M. Kobayashi and T. Maskawa, *CP-violation in the renormalizable theory of weak interaction*, Prog. Theor. Phys. **49** (1973) 652.

[40] L. Wolfenstein, *Parametrization of the Kobayashi-Maskawa matrix*, Phys. Rev. Lett. **51** (1983) 1945.

[41] CKMfitter group, J. Charles *et al.*, *CP violation and the CKM matrix: Assessing the impact of the asymmetric B factories*, Eur. Phys. J. **C41** (2005) 1, `arXiv:hep-ph/0406184`, updated results and plots available at `http://ckmfitter.in2p3.fr/`.

[42] J. Ellis, *TikZ-Feynman: Feynman diagrams with TikZ*, Comput. Phys. Commun. **210** (2017) 103, `arXiv:1601.05437`.

[43] K. Lande *et al.*, *Observation of long-lived neutral V particles*, Phys. Rev. **103** (1956) 1901.

[44] ARGUS collaboration, H. Albrecht *et al.*, *Observation of B^0–$\overline{B}^0$ mixing*, Phys. Lett. **B192** (1987) 245.

[45] CDF collaboration, A. Abulencia *et al.*, *Observation of B_s^0–$\overline{B}_s^0$ oscillations*, Phys. Rev. Lett. **97** (2006) 242003, `arXiv:hep-ex/0609040`.

[46] BaBar collaboration, B. Aubert *et al.*, *Evidence for D^0–$\overline{D}^0$ mixing*, Phys. Rev. Lett. **98** (2007) 211802, `arXiv:hep-ex/0703020`.

[47] Belle collaboration, M. Starič *et al.*, *Evidence for D^0–$\overline{D}^0$ mixing*, Phys. Rev. Lett. **98** (2007) 211803, `arXiv:hep-ex/0703036`.

[48] J. F. Donoghue, E. Golowich, B. R. Holstein, and J. Trampetic, *Dispersive effects in D^0–$\overline{D}^0$ mixing*, Phys. Rev. D **33** (1986) 179.

[49] E. Golowich and A. A. Petrov, *Short distance analysis of D^0–$\overline{D}^0$ mixing*, Phys. Lett. B **625** (2005) 53, `arXiv:hep-ph/0506185`.

[50] G. Isidori, Y. Nir, and G. Perez, *Flavor physics constraints for physics beyond the Standard Model*, Ann. Rev. Nucl. Part. Sci. **60** (2010) 355, `arXiv:1002.0900`.

[51] BaBar collaboration, B. Aubert *et al.*, *Observation of CP violation in the B^0 meson system*, Phys. Rev. Lett. **87** (2001) 091801, `arXiv:hep-ex/0107013`.

[52] Belle collaboration, K. Abe *et al.*, *Observation of large CP violation in the neutral B meson system*, Phys. Rev. Lett. **87** (2001) 091802, `arXiv:hep-ex/0107061`.

[53] LHCb collaboration, R. Aaij *et al.*, *Observation of CP violation in charm decays*, Phys. Rev. Lett. **122** (2019) 211803, `arXiv:1903.08726`.

[54] Heavy Flavor Averaging Group, Y. Amhis *et al.*, *Global fit for D^0–$\overline{D}^0$ mixing (allowing for CP violation) (updated 28 May 2018)*, https://hflav-eos.web.cern.ch/hflav-eos/charm/CHARM18/results_mix_cpv.html, 2019. Accessed: 2022-05-20.

[55] Heavy Flavor Averaging Group, Y. Amhis *et al.*, *Global fit for D^0–$\overline{D}^0$ mixing (allowing for CP violation) (updated 31 March 2019)*, https://hflav-eos.web.cern.ch/hflav-eos/charm/Moriond19/results_mix_cpv.html, 2019. Accessed: 2022-05-20.

[56] Heavy Flavor Averaging Group, Y. Amhis *et al.*, *Global fit for D^0–$\overline{D}^0$ mixing (allowing for CP violation) (through 21 December 2021)*, https://hflav-eos.web.cern.ch/hflav-eos/charm/CKM21/results_mix_cpv.html, 2021. Accessed: 2022-05-20.

[57] Heavy Flavor Averaging Group, Y. Amhis *et al.*, *Averages of b-hadron, c-hadron, and τ-lepton properties as of 2018*, Eur. Phys. J. **C81** (2021) 226, `arXiv:1909.12524`, updated results and plots available at `https://hflav.web.cern.ch`.

[58] R. H. Dalitz, *Decay of tau mesons of known charge*, Phys. Rev. **94** (1954) 1046.

[59] BaBar collaboration, P. del Amo Sanchez *et al.*, *Measurement of D^0–$\overline{D}^0$ mixing parameters using $D^0 \to K^0_S \pi^+ \pi^-$ and $D^0 \to K^0_S K^+ K^-$ decays*, Phys. Rev. Lett. **105** (2010) 081803, `arXiv:1004.5053`.

[60] CLEO collaboration, J. Libby *et al.*, *Model-independent determination of the strong-phase difference between D^0 and $\overline{D}^0 \to K^0_{S,L} h^+ h^-$ ($h = \pi, K$) and its impact on the measurement of the CKM angle γ/ϕ_3*, Phys. Rev. **D82** (2010) 112006, `arXiv:1010.2817`.

[61] BaBar collaboration, Belle collaboration, I. Adachi *et al.*, *First evidence for* $\cos 2\beta > 0$ *and resolution of the Cabibbo-Kobayashi-Maskawa quark-mixing Unitarity Triangle ambiguity*, Phys. Rev. Lett. **121** (2018) 261801, `arXiv:1804.06152`.

[62] M. Hilton, *Measurement of the mixing parameters of neutral charm mesons and search for indirect CP violation with* $D^0 \to K_S^0\pi^+\pi^-$ *decays at LHCb*, PhD thesis, University of Manchester, 2021, CERN-THESIS-2021-168.

[63] LHCb collaboration, R. Aaij *et al.*, *Measurement of the mass difference between neutral charm-meson eigenstates*, Phys. Rev. Lett. **122** (2019) 231802, `arXiv:1903.03074`.

[64] A. Di Canto *et al.*, *Novel method for measuring charm-mixing parameters using multi-body decays*, Phys. Rev. **D99** (2019) 012007, `arXiv:1811.01032`.

[65] A. Contu *et al.*, *A novel measurement of charm-mixing parameters and CP-violating asymmetries using* $D \to K_S^0\pi^+\pi^-$ *decays*, LHCb-ANA-2015-027.

[66] BESIII collaboration, M. Ablikim *et al.*, *Model-independent determination of the relative strong-phase difference between* D^0 *and* $\overline{D}^0 \to K_{S,L}^0\pi^+\pi^-$ *and its impact on the measurement of the CKM angle* γ/ϕ_3, Phys. Rev. **D101** (2020) 112002, `arXiv:2003.00091`.

[67] E. Mobs, *The CERN accelerator complex - August 2018*, https://cds.cern.ch/record/2636343?ln=fr, 2018. Accessed: 2022-05-20.

[68] CERN Communications and Outreach Group, *FAQ: CERN the guide*, https://cds.cern.ch/record/2255762/files/CERN-Brochure-2017-002-Eng.pdf, 2017. Accessed: 2022-05-20.

[69] CERN, *Restarting the LHC: Why 13 Tev?*, https://home.cern/science/engineering/restarting-lhc-why-13-tev. Accessed: 2022-05-20.

[70] LHCb collaboration, A. A. Alves Jr. *et al.*, *The LHCb detector at the LHC*, JINST **3** (2008) S08005.

[71] F. Follin and D. Jacquet, *Implementation and experience with luminosity levelling with offset beam*, ICFA Mini-Workshop on Beam-Beam Effects in Hadron Colliders (2014) 183, `arXiv:1410.3667`.

[72] LHCb collaboration, *LHCb operation plots webpage*, https://lbgroups.cern.ch/online/OperationsPlots/index.htm, 2018. Accessed: 2022-05-20.

[73] S. Ek-In, *Reconstruction of semileptonic decays and search for* $B_s^0 \to K^{*-}\mu^+\nu_\mu$ *at the LHCb experiment*, PhD thesis, EPFL, 2018, EPFL Master Thesis.

[74] LHCb collaboration, *LHCb VELO (VErtex LOcator): Technical Design Report*, CERN-LHCC-2001-011, 2001.

[75] LHCb collaboration, *VErtex LOcator (VELO)*, https://lhcb-public.web.cern.ch/en/detector/VELO-en.html, 2008. Accessed: 2022-05-20.

[76] C. Abellan Beteta *et al.*, *Monitoring radiation damage in the LHCb Tracker Turicensis*, `arXiv:1809.05063`.

[77] R. Arink *et al.*, *Performance of the LHCb Outer Tracker*, JINST **9** (2014) P01002, `arXiv:1311.3893`.

[78] C. Abellan Beteta *et al.*, *Calibration and performance of the LHCb calorimeters in Run 1 and 2 at the LHC*, `arXiv:2008.11556`, submitted to JINST.

[79] LHCb collaboration, E. Picatoste Olloqui, *LHCb preshower(PS) and scintillating pad detector (SPD): Commissioning, calibration, and monitoring*, J. Phys. Conf. Ser. **160** (2009) 012046.

[80] LHCb collaboration, *Trigger schemes*, https://lhcb.web.cern.ch/speakersbureau/html/TriggerScheme.html, 2015. Accessed: 2022-05-20.

[81] LHCb collaboration, *LHCb computing: Technical Design Report*, CERN-LHCC-2005-019, 2005.

[82] G. Barrand *et al.*, *GAUDI - A software architecture and framework for building HEP data processing applications*, Comput. Phys. Commun. **140** (2001) 45.

[83] R. Brun and F. Rademakers, *ROOT: An object oriented data analysis framework*, Nucl. Instrum. Meth. **A389** (1997) 81.

[84] I. Antcheva *et al.*, *ROOT: A C++ framework for petabyte data storage, statistical analysis and visualization*, Comput. Phys. Commun. **180** (2009) 2499, `arXiv:1508.07749`.

[85] S. Borghi *et al.*, *LHCb offline analysis in Run 3 OATF recommendations* , CERN, Geneva, 2020. LHCb-INT-2020-003.

[86] C. Burr *et al.*, *Data Processing & Analysis (DPA) Project* , CERN, Geneva, 2020. LHCb-INT-2020-009.

[87] LHCb starterkit team, *Analysis Productions*, https://lhcb.github.io/starterkit-lessons/first-analysis-steps/analysis-productions.html, 2020. Accessed: 2022-05-20.

[88] LHCb Trigger collaboration, A. Puig, *The LHCb Turbo stream*, Nucl. Instrum. Meth. **A824** (2016) 38.

[89] J. T. Mościcki *et al.*, *Ganga : A tool for computational-task management and easy access to Grid resources*, Comput. Phys. Commun. **180** (2009) 2303, `arXiv:0902.2685`.

[90] J. Shiers, *The Worldwide LHC Computing Grid (worldwide LCG)*, Comput. Phys. Commun. **177** (2007) 219.

[91] LHCb collaboration, *Analysis Productions*, https://gitlab.cern.ch/lhcb-datapkg/AnalysisProductions/, 2021. Accessed: 2022-05-20.

[92] G. Van Rossum and F. L. Drake, *Python 3 Reference Manual*, CreateSpace, Scotts Valley, CA, 2009. ISBN: 978-1-4414-1269-0.

[93] B. Stroustrup, *C++ (Computer program language)*, Addison-Wesley, 1997. ISBN 0-201-88954-4.

[94] LHCb collaboration, *Code to study $D^0 \to K^0_S \pi^+ \pi^-$ with the binflip method*, https://gitlab.cern.ch/lhcb-charm/D02KsPiPi/. Accessed: 2022-05-20.

[95] LHCb collaboration, *$\pi^+\pi^-$ detection asymmetries*, https://gitlab.cern.ch/ldufour/adetpipi. Accessed: 2022-05-20.

[96] LHCb collaboration, R. Aaij *et al.*, *Measurement of the CKM angle γ from a combination of LHCb results*, JHEP **12** (2016) 087, `arXiv:1611.03076`.

[97] W. Verkerke and D. P. Kirkby, *The RooFit toolkit for data modeling*, eConf **C0303241** (2003) MOLT007, `arXiv:physics/0306116`.

[98] C. R. Harris *et al.*, *Array programming with NumPy*, Nature **585** (2020) 357, `arXiv:2006.10256`.

[99] Wes McKinney, *Data structures for statistical computing in* PYTHON, in *Proceedings of the 9th Python in Science Conference* (Stéfan van der Walt and Jarrod Millman, eds.), 56 – 61, 2010.

[100] J. D. Hunter, *Matplotlib: A 2D Graphics Environment*, Comput. Sci. Eng. **9** (2007) 90.

[101] P. Virtanen *et al.*, *SciPy 1.0–Fundamental Algorithms for Scientific Computing in Python*, Nature Meth. **17** (2020) 261, `arXiv:1907.10121`.

[102] F. Pedregosa *et al.*, *Scikit-learn: Machine learning in Python*, J. Machine Learning Res. **12** (2011) 2825, `arXiv:1201.0490`, and online at `http://scikit-learn.org/stable/`.

[103] A. Rogozhnikov, *Reweighting with Boosted Decision Trees*, J. Phys. Conf. Ser. **762** (2016) 012036, `arXiv:1608.05806`, https://github.com/arogozhnikov/hep_ml.

[104] S. Tolk, J. Albrecht, F. Dettori, and A. Pellegrino, *Data driven trigger efficiency determination at LHCb* , CERN, Geneva, 2014. LHCb-PUB-2014-039.

[105] T. Likhomanenko *et al.*, *LHCb topological trigger reoptimization*, J. Phys. Conf. Ser. **664** (2015) 082025, `arXiv:1510.00572`.

[106] W. D. Hulsbergen, *Decay chain fitting with a Kalman filter*, Nucl. Instrum. Meth. **A552** (2005) 566, `arXiv:physics/0503191`.

[107] N. L. Johnson, *Systems of frequency curves generated by methods of translation*, Biometrika **36** (1949) 149, http://www.jstor.org/stable/2332539.

[108] M. Pivk and F. R. Le Diberder, *sPlot: A statistical tool to unfold data distributions*, Nucl. Instrum. Meth. **A555** (2005) 356, `arXiv:physics/0402083`.

[109] J. H. Friedman, *Greedy function approximation: A gradient boosting machine.*, Annals Statist. **29** (2001) 1189.

[110] J. Stevens and M. Williams, *uBoost: A boosting method for producing uniform selection efficiencies from multivariate classifiers*, JINST **8** (2013) P12013, `arXiv:1305.7248`.

[111] G. Louppe, L. Wehenkel, A. Sutera, and P. Geurts, *Understanding variable importances in forests of randomized trees*, in *Advances in Neural Information Processing Systems 26* (C. J. C. Burges *et al.*, eds.), pp. 431–439. Curran Associates, Inc., 2013. http://papers.nips.cc/paper/4928-understanding-variable-importances-in-forests-of-randomized-trees.pdf.

[112] M. Needham, *Dealing with clones*, https://twiki.cern.ch/twiki/bin/viewauth/LHCbPhysics/CloneCuts, 2011. Accessed: 2022-05-20.

[113] T. Sjöstrand, S. Mrenna, and P. Skands, *A brief introduction to PYTHIA 8.1*, Comput. Phys. Commun. **178** (2008) 852, `arXiv:0710.3820`; T. Sjöstrand, S. Mrenna, and P. Skands, *PYTHIA 6.4 physics and manual*, JHEP **05** (2006) 026, `arXiv:hep-ph/0603175`.

[114] I. Belyaev *et al.*, *Handling of the generation of primary events in Gauss, the LHCb simulation framework*, J. Phys. Conf. Ser. **331** (2011) 032047.

[115] D. J. Lange, *The EvtGen particle decay simulation package*, Nucl. Instrum. Meth. **A462** (2001) 152.

[116] N. Davidson, T. Przedzinski, and Z. Was, *PHOTOS interface in C++: Technical and physics documentation*, Comp. Phys. Comm. **199** (2016) 86, `arXiv:1011.0937`.

[117] Geant4 collaboration, J. Allison *et al.*, *Geant4 developments and applications*, IEEE Trans. Nucl. Sci. **53** (2006) 270; Geant4 collaboration, S. Agostinelli *et al.*, *Geant4: A simulation toolkit*, Nucl. Instrum. Meth. **A506** (2003) 250.

[118] M. Clemencic *et al.*, *The LHCb simulation application, Gauss: Design, evolution and experience*, J. Phys. Conf. Ser. **331** (2011) 032023.

[119] G. Corti *et al.*, *Software for the LHCb experiment*, in *2004 IEEE Nuclear Science Symposium and Medical Imaging Conference*, No. 4, 2048–2052, 2004.

[120] W. S. Cleveland, *Robust locally weighted regression and smoothing scatterplots*, Journal of the American Statistical Association **74** (1979) 829.

[121] L. Anderlini *et al.*, *The PIDCalib package*, LHCb-PUB-2016-021, 2016.

[122] LHCb collaboration, R. Aaij *et al.*, *Updated measurement of decay-time-dependent CP asymmetries in $D^0 \to K^+K^-$ and $D^0 \to \pi^+\pi^-$ decays*, Phys. Rev. **D101** (2020) 012005, `arXiv:1911.01114`.

[123] LHCb collaboration, R. Aaij *et al.*, *Updated determination of D^0–$\overline{D}^0$ mixing and CP violation parameters with $D^0 \to K^+\pi^-$ decays*, Phys. Rev. **D97** (2018) 031101, `arXiv:1712.03220`.

[124] LHCb collaboration, R. Aaij *et al.*, *Measurements of charm mixing and CP violation using $D^0 \to K^\pm\pi^\mp$ decays*, Phys. Rev. **D95** (2017) 052004, erratum ibid. **D96** (2017) 099907, `arXiv:1611.06143`.

[125] A. Davis and M. D. Sokoloff, *Time Dependent D^0 - $\overline{D}^0$ Mixing and CP violation from prompt charm and doubly-tagged semileptonic decay $B \to \mu D^* X$*, 2015. LHCb-ANA-2015-058.

[126] J. A. Nelder and R. Mead, *A simplex method for function minimization*, The Computer Journal **7** (1965) 308, `arXiv:https://academic.oup.com/comjnl/article-pdf/7/4/308/1013182/7-4-308.pdf`.

[127] B. Sen, M. Walker, and M. Woodroofe, *On the unified method with nuisance parameters*, Statistica Sinica **19** (2009) 301.

[128] G. J. Feldman and R. D. Cousins, *A unified approach to the classical statistical analysis of small signals*, Phys. Rev. **D57** (1998) 3873, `arXiv:physics/9711021`.

[129] LHCb collaboration, R. Aaij *et al.*, *Measurement of the CKM angle γ from a combination of $B^\pm \to Dh^\pm$ analyses*, Phys. Lett. **B726** (2013) 151, `arXiv:1305.2050`.

[130] Heavy Flavor Averaging Group, Y. Amhis *et al.*, *Global fit for D^0–$\overline{D}^0$ mixing (allowing for CP violation) (through 1 July 2021)*, https://hflav-eos.web.cern.ch/hflav-eos/charm/CHARM21/results_mix_cpv.html, 2021. Accessed: 2022-05-20.

[131] LHCb collaboration, *Physics case for an LHCb Upgrade II — Opportunities in flavour physics, and beyond, in the HL-LHC era*, `arXiv:1808.08865`.

[132] LHCb Twiki Page, *Isolation tools in the LHCb stripping framework*, https://twiki.cern.ch/twiki/bin/view/LHCb/StrippingIsolationTools, 2014. Accessed: 2022-05-20.

[133] BESIII collaboration, M. Ablikim *et al.*, *Future Physics Programme of BESIII*, Chin. Phys. C **44** (2020) 040001, `arXiv:1912.05983`.

[134] Lucasfilm Ltd. , *Defining moments: twin suns*, https://www.lucasfilm.com/news/defining-moments-twin-suns/, 1977. Accessed: 2022-06-06.

[135] CERN collaboration, M. Brice, *Record luminosity: well done LHC*, https://home.cern/news/news/accelerators/record-luminosity-well-done-lhc, 2017. Accessed: 2022-06-06.

[136] A. Puig Navarro, *First measurements of radiative B decays in LHCb*, PhD thesis, Barcelona U., 2012, CERN-THESIS-2012-025.

[137] CERN, *Illustration of the mass difference between the D1 and D2 mesons*, https://cds.cern.ch/images/CERN-HOMEWEB-PHO-2021-086-1, 2021. Accessed: 2022-06-06.

[138] CERN, *The LHCb detector was opened up in December to make way for LS2 activities.*, https://cerncourier.com/a/lhcbs-momentous-metamorphosis/, 2019. Accessed: 2022-06-06.

[139] M. Brice, *The LHCb electromagnetic calorimeter*, https://cds.cern.ch/record/835712, 2005. Accessed: 2022-06-06.

Surapat Ek-In

Nationality: Thai, Birth date: 3rd of March 1994
Rue de Bassenges 3B, 1024-Ecublens VD, Switzerland
surapat.eki@gmail.com | @surapat01 | in/surapat-ek-in/

Skills

Programming	Bash script, C/C++, Python, SQL, R, Matlab, LaTeX, Mathematica, HTML, CSS, JavaScript
Framework	ROOT/RooFit, Numpy, Pandas, ScikitLearn, PyTorch, Keras, Jupyter, Git (CI/CD), Docker, AWS Cloud, Matplotlib, Seaborn, Dash, Tableau, Google Cloud, Node.js, JIRA
Languages	Thai (mother tongue), English (C1), French (A2), German (A2)

Education

École polytechnique fédérale de Lausanne (EPFL) *Switzerland*
Ph.D. in experimental particle physics *2018 – 2022*
Thesis: Model-independent measurement of charm mixing parameters in $D^0 \to K^0_S \pi^+ \pi^-$ decays.
Thesis director: Prof. Olivier Schneider
Advisors: Dr. Tara Nanut, Dr. Maurizio Martinelli

École polytechnique fédérale de Lausanne (EPFL) *Switzerland*
Master of Science in Physics [GPA 5.07/6.00] *2016 – 2018*
Thesis: Reconstruction of semileptonic decays and search for $B^0_s \to K^{*-}\mu^+\nu_\mu$ at the LHCb experiment.
Thesis director: Prof. Tatsuya Nakada
Advisors: Dr. Michel De Cian

Mahidol University *Thailand*
Bachelor of Science in Physics [GPA 3.86/4.00, First Class Honours] *2012 – 2016*
Thesis: Projected search for physics beyond the Standard Model at the Future Circular Collider.
Thesis director: Prof. David Ruffolo
Advisors: Dr. Norraphat Srimanobhas

Professional Experience

LHCb collaboration, CERN *Switzerland*
Experimental Particle Physicist *2018 – 2022*

- Measurements of mixing and CP-violating parameters in $\overline{B} \to D^0(\to K^0_S\pi^+\pi^-)\mu^-\bar{\nu}_\mu X$. Drive the analysis with various machine learning tools and advanced statistical methods with expertise in Python.
- Explore an alternative approach in a real-time tracking algorithm at the experimental apparatus using strong competence in C++ to improve performance of the algorithm.
- Develop a software to process, reconstruct, and analyse stream of data from STiC readout to monitor and improve performance of the detector during R&D phase.

Altruistic Innovation Limited, UK *Remote*
Data Scientist (Remote - Freelance) *2021 – 2022*

- Data-driven analysis consultant in optimisation on a commercial optical sensor in smart electricity grid monitoring. Successfully deploy a model to achieve the highest precision of measurement on sensors produced at Micatu Inc. (USA).
- Architect cloud-based solutions in AWS using SageMaker, S3, ECR, and EC2. Automate a model pipeline using Gitlab CI/CD. Enable batch model training on different sensors with AWS batch. Develop a dashboard to visualise model performance with plotly Dash and deploy to AWS Fargate.

High Energy Physics Laboratory, EPFL *Switzerland*
Specialisation semester and Master thesis *2017 – 2018*

- Analysis of $B_s^0 \to K^{*-}\mu^+\nu_\mu$. Develop analysis strategy, data engineer and data cleaning on data collected by LHCb using Python. Optimise Boosted decision tree classifier to select physics-related candidates.
- Participate in the development of silicon photomultiplier (SiPM) detector. Perform testing of the detector with a high energy beam at CERN to study its behaviors. Develop and implement a clustering algorithm, anti-kt algorithm, to optimize the resolution of the detector in C++.

Mahidol University *Thailand*
Research Student *2013 – 2016*

- Simulate and analyse magneto-hydrodynamic process to potentially help identify interesting sites at Earth's magnetosphere for Magnetospheric Multiscale (MMS) mission.

Helmholtz-Zentrum Dresden-Rossendorf *Germany*
Internship *2015*

- Investigate magnetic domains on Permalloy for spin-wave transportation using an ion beam implantation with a Kerr Microscope.

Published Documents

Publications

All the LHCb collaboration publications since June 2019
LHCb Collaboration *2019–2022*
A complete list can be found on CERN Document Server. Main contributions are listed as the two following documents.

Model-independent measurement of charm mixing parameters in $\overline{B} \to D^0(\to K_S^0\pi^+\pi^-)\mu^-\bar{\nu}_\mu X$ decays
LHCb Collaboration *2022*
Submitted to Phys. Rev. D., arXiv:2208.06512

Observation of the mass difference between neutral charm-meson eigenstates
LHCb Collaboration *2021*
Phys. Rev. Lett. 127, 111801, 10.1103/PhysRevLett.127.111801

Effects of a Guide Field on the Larmor Electric Field and Upstream Electron Temperature Anisotropy in Collisionless Asymmetric Magnetic Reconnection
S. Ek-In et al. *2017*
The Astrophysical Journal, 845, 113, 10.3847/1538-4357/aa7f2c

Conference talks

Mixing and indirect CP violation in charm mesons at LHCb
S. Ek-In on behalf of the LHCb collaboration *2022*
Talk at International Conference on High Energy Physics (ICHEP) 2022, Bologna (Italy).

Model-independent measurement of charm-mixing parameters in $D^0 \to K_S^0\pi^+\pi^-$
S. Ek-In *2022*
Talk at the Annual Meeting of the Swiss Physical Society 2022, Fribourg, Switzerland.

Charm Physics at LHCb
S. Ek-In on behalf of the LHCb collaboration *2021*
20th Lomonosov Conference on Elementary Particle Physics, Moscow State University (virtual).

Model-independent measurement of charm-mixing parameters in $D^0 \to K_S^0\pi^+\pi^-$
S. Ek-In, T. Nanut, M. Martinelli, and O. Schneider *2019*
Talk at the joint annual meeting of the Swiss Physical Society and Österreichischen Physikalischen Gesellschaft 2019.

Reconstruction of semileptonic decays and search for $B_s^0 \to K^{*-}\mu^+\nu_\mu$ at the LHCb experiment
S. Ek-In, M. De Cian, and T. Nakada *2019*
Poster presentation at the CHIPP Winter School of Particle Physics 2019.

LHCb internal notes

Measurement of charm mixing and CP violation parameters using a time-dependent amplitude analysis of semileptonically-tagged $D^0 \to K_S^0\pi^+\pi^-$ decays
M. Hilton, M. Williams et al. *2021*

Run 2 analysis of semileptonic $D^0 \to K_S^0\pi^+\pi^-$ decays with the bin-flip method
S. Ek-In, T. Nanut, M. Martinelli et al. *2020*

Run 2 analysis of prompt $D^0 \to K_S^0\pi^+\pi^-$ decays with the bin-flip method
A. Di Canto, N. Jurik, S. Stahl et al. *2020*

Awards, & Scholarships

2016–2017	**Excellent Science Student Award 2017**, Mahidol University
2012–2016	**Sri Trang Thong Scholarship**, Mahidol University
2015	**The International Association for the Exchange of Students for Technical Experience (IAESTE)**, Internship at Helmholtz-Zentrum Dresden-Rossendorf, Germany
2015	**CERN Summer Student Programme**, CMS Collaboration, CERN

Teaching Experience

2018–2020	**Physics lab IIIa (PHYS-319)**, Teaching Assistant
2020–2021	**Nuclear and particle physics I**, Teaching Assistant

Outreach & Professional Development

Service and Outreach

2019–2022	**LHCb Collaboration**, LHCb official guide, volunteer in CERN Open Days 2019
2019–2021	**LHCb Collaboration**, Liaison between Run 1–2 performance and LHCb Charm physics working groups
2020	**LHCb Starterkit**, Volunteer for teaching and demonstrating the LHCb software.
2016–2019	**Association of Thai Students in Switzerland (ATSS)**, President (2019), Committee
2019	**EPFL Open Days 2019**, Volunteer at the LPHE stand, EPFL Open Days 2019
2017	**Thai Student Academic Conference (TSAC) Geneva**, Head of Academic Event Management

Certifications

2021	**AWS Certified Cloud Practitioner**, Amazon Web Service
2020	**Certification of Excellence**, 6th Machine learning in High Energy Physics Summer School, Lausanne

Leisures

Hiking and Via-ferrata, Skiing, Certified Advanced SCUBA diving (SSI), Popping dancing